



## **A11L.UAS.96 – A56 Evaluate Unmanned Aircraft Systems (UAS) Electromagnetic Compatibility (EMC)**

September 6, 2023

## **NOTICE**

This document is disseminated under the sponsorship of the U.S. Department of Transportation in the interest of information exchange. The U.S. Government assumes no liability for the contents or use thereof. The U.S. Government does not endorse products or manufacturers. Trade or manufacturers' names appear herein solely because they are considered essential to the objective of this report. The findings and conclusions in this report are those of the author(s) and do not necessarily represent the views of the funding agency. This document does not constitute FAA policy. Consult the FAA sponsoring organization listed on the Technical Documentation page as to its use.

## **LEGAL DISCLAIMER**

The information provided herein may include content supplied by third parties. Although the data and information contained herein has been produced or processed from sources believed to be reliable, the Federal Aviation Administration makes no warranty, expressed or implied, regarding the accuracy, adequacy, completeness, legality, reliability or usefulness of any information, conclusions or recommendations provided herein. Distribution of the information contained herein does not constitute an endorsement or warranty of the data or information provided herein by the Federal Aviation Administration or the U.S. Department of Transportation. Neither the Federal Aviation Administration nor the U.S. Department of Transportation shall be held liable for any improper or incorrect use of the information contained herein and assumes no responsibility for anyone's use of the information. The Federal Aviation Administration and U.S. Department of Transportation shall not be liable for any claim for any loss, harm, or other damages arising from access to or use of data or information, including without limitation any direct, indirect, incidental, exemplary, special or consequential damages, even if advised of the possibility of such damages. The Federal Aviation Administration shall not be liable to anyone for any decision made or action taken, or not taken, in reliance on the information contained herein.

## TECHNICAL REPORT DOCUMENTATION PAGE

*General instructions: To add text, click inside the form field below (will appear as a blue highlighted or outlined box) and begin typing. The instructions will be replaced by the new text. If no text needs to be added, remove the form field and its instructions by clicking inside the field, then pressing the Delete key twice.*

*Please remove this field before completing form.*

<b>1. Report No.</b> A56 – A11L.UAS.96	<b>2. Government Accession No.</b>	<b>3. Recipient’s Catalog No.</b>
<b>4. Title and Subtitle</b> Evaluate Unmanned Aircraft Systems (UAS) Electromagnetic Interference (EMI) Final Report	<b>5. Report Date</b> June 9, 2023	<b>6. Performing Organization Code</b> Enter any/all unique numbers assigned to the performing organization, if applicable.
	<b>7. Author(s)</b> Enter name(s) of person(s) responsible for writing the report, performing the research, or credited with the content of the report. Form of entry is first name, middle initial (if applicable), last name, and any additional qualifiers. Primary author is listed first. After each author name, enter ORCID ( <a href="http://orcid.org">http://orcid.org</a> ) URL, when available. Example: Josiah Carberry, Ph.D. <a href="http://orcid.org/0000-0002-1825-0097">http://orcid.org/0000-0002-1825-0097</a>	<b>8. Performing Organization Report No.</b> Enter any/all unique alphanumeric report numbers assigned by the performing organization, if applicable.
<b>9. Performing Organization Name and Address</b> The University of North Dakota 243 Centennial Drive, Stop 7165 Grand Forks ND 58201  The University of Kansas Center for Remote Sensing of Ice Sheets Nichols Hall 2335 Irving Hill Road Lawrence KS 66045  Drexel University Department of Electrical and Computer Engineering 3141 Chestnut Street Philadelphia PA 19104	<b>10. Work Unit No.</b>	
	<b>11. Contract or Grant No.</b> 15-C-UAS	
<b>12. Sponsoring Agency Name and Address</b>	<b>13. Type of Report and Period Covered</b> Final Report, January 1, 2022 through April 1, 2023	

Federal Aviation Administration 800 Independence Ave, SW Washington DC 20591		<b>14. Sponsoring Agency Code</b> Federal Aviation Administration 5401	
<b>15. Supplementary Notes</b> Conducted in cooperation with the U.S. Department of Transportation, Federal Highway Administration.			
<b>16. Abstract</b> <p>This project characterized the impacts of Electromagnetic Interference small and medium sized Unmanned Aerial Systems. A review of pertinent literature was provided. Test planning was conducted followed by execution of all planned tests. A collection of applicable questions was established, and testing operations addressed each question. Several observations were made from the completed testing, including a strong sensitivity of UAS platforms to very high frequency television signals, there is great benefit to the addition of shielding of critical components, and there is strong sensitivity of the command and control link to 4<sup>th</sup> and 5<sup>th</sup> generation wireless network signals. Several significant recommendations are made to include the need to characterize each UAS model for its sensitivity to very high frequency signals, the maximum magnetic field strength for safe operation is a value higher than 3,000 <math>\mu</math>T, robust automatic gain control circuitry helps improve resilience to electromagnetic interference, and the recommended safe distance for flight in the vicinity of airport surveillance RADAR is 1,200m.</p>			
<b>17. Key Words</b> UAS, EMI, Electromagnetic Interference, Electromagnetic Compatibility, Electric Field, Magnetic Field		<b>18. Distribution Statement</b> No restrictions. This document is available through the National Technical Information Service, Springfield, VA 22161. Enter any other agency mandated distribution statements. Remove NTIS statement if it does not apply.	
<b>19. Security Classification (of this report)</b> Unclassified	<b>20. Security Classification (of this page)</b> Unclassified	<b>21. No. of Pages</b> 185	<b>22. Price</b>

## TABLE OF CONTENTS

NOTICE.....	I
LEGAL DISCLAIMER.....	II
TECHNICAL REPORT DOCUMENTATION PAGE.....	III
TABLE OF FIGURES.....	VII
TABLE OF TABLES.....	XIV
TABLE OF ACRONYMS.....	XV
EXECUTIVE SUMMARY.....	XVII
1 INTRODUCTION & BACKGROUND.....	20
2 STATIC AND LOW FREQUENCY FIELDS: SIMULATION AND LAB TESTING.....	21
2.1 Magnetic field finite-element-analysis (FEA) simulation.....	21
2.1.1 Maxwell simulation of magnetic field for single-phase transmission line.....	21
2.1.2 Maxwell simulation of magnetic field for three-phase transmission line.....	23
2.1.3 Maxwell simulation of magnetic field for lab-based setup (1.7-meter coil).....	26
2.2 Electric field finite-element-analysis (FEA) simulation.....	28
2.2.1 Maxwell simulation of electric field for single-phase transmission line.....	28
2.2.2 Maxwell simulation of electric field for three-phase transmission line.....	29
2.2.3 Maxwell simulation of electric field for lab-based setup (0.9m parallel plates) ....	31
2.3 Lab-based magnetic field testing.....	33
2.3.1 Magnetic field-testing prototype design and construction.....	33
2.3.2 Mavic 2 testing in 7.5-kA solenoid coil.....	38
2.3.3 Mavic 2 testing in 2.2-kA planar coil.....	45
2.3.4 Discrete sensor testing in 5.25-kA solenoid coil.....	53
2.3.5 Mavic 3 carries discrete sensor testing in 2.2-kA planar coil.....	55
2.4 Lab-based electric field testing.....	59
2.4.1 Electric field testing prototype design and construction.....	59
2.4.2 Mavic 2 testing in 2 kV/m electric field.....	60
3 CYBER SECURITY; STATIC & LOW FREQUENCY FLIGHT TEST.....	64
3.1 State-of-the-art summary.....	64
3.1.1 System.....	64
3.1.2 Environmental.....	68
3.1.3 Cyber Security.....	72
3.2 Data Capture /Acquisition Process.....	75

3.2.1	Equipment and Test Site .....	75
3.2.2	Set-up & Mount Orientations.....	81
3.3	Test plan Report Integration.....	85
3.3.1	Observed Electric Fields: 69kV, 145kV, 345kV, 500kV & 250KV DC lines .....	85
3.3.2	Observed Magnetic Fields: 69kV, 145kV, 345kV, 500kV, & 250KV DC lines...	88
3.3.3	Factors Contributing to Choppy Data in UAS Operations Near Transmission Lines 92	
3.3.4	Observed Electric Field Strengths in Microwave Tower.....	93
3.3.5	Observed Magnetic Field Strengths in Microwave Tower .....	94
3.3.6	RF and non-RF Spectrum Analysis .....	96
4	ASSESSMENT OF RFI TO UNMANNED AIRCRAFT SYSTEMS .....	100
4.1	Introduction and Research Objectives.....	100
4.2	Literature Review of RFI to Unmanned Aircraft Systems.....	100
4.3	UAS Models, Test Facility, Equipment, and Procedures.....	101
4.3.1	UAS Models .....	101
4.3.2	Anechoic Chamber.....	102
4.3.3	Antennas .....	102
4.3.4	Test Procedures.....	103
4.4	Laboratory and Anechoic Chamber Testing .....	103
4.4.1	Front-Door RFI Measurements.....	103
4.4.2	Back-Door RFI Measurements .....	106
4.4.3	Main Results and Analysis.....	111
4.5	Flight Tests.....	129
4.5.1	Objectives of Flight Tests .....	129
4.5.2	Flight Test Observations and Analysis .....	133
5	OBSERVATIONS AND RECOMMENDATIONS .....	135
5.1	Observations.....	135
5.1.1	Power Transmission Lines.....	135
5.1.2	RF Signals.....	135
5.2	Recommendations .....	136
6	REFERENCES .....	137
7	APPENDIX A.....	142
8	APPENDIX B.....	147

8.1	Introduction .....	147
8.2	UAS Incidents .....	148
8.3	Sources of EMI.....	153
8.3.1	System.....	153
8.3.2	Environmental.....	159
8.4	Susceptibility.....	174
8.4.1	Radio Frequency .....	174
8.4.2	Low Field Environment .....	176
8.5	Conclusion.....	178
8.6	REFERENCES.....	179

## TABLE OF FIGURES

Figure 2-1.	Maxwell-simulation model of a single-phase transmission line: ideal conductor model and square coil model, which are used to simulate the magnetic field distribution. ....	21
Figure 2-2.	Maxwell-simulated magnetic field distribution with 10-kA high current excitation. Note that the field distribution of these two models are very similar. ....	22
Figure 2-3.	Comparison of Maxwell-simulated magnetic field distribution with 10-kA current excitation in single conductor model and the square coil model, showing the similarity of field strength.....	23
Figure 2-5.	Maxwell-simulated magnetic field distribution of a three-phase transmission system at different current excitation, showing the field strength. ....	24
Figure 2-4.	Maxwell-simulation model of a three-phase transmission system, using three 100-meter-long coils to emulate a practical three-phase system.....	24
Figure 2-6.	Maxwell-simulated magnetic field strength in a three-phase transmission system at different excitation current levels. The 180 $\mu$ T field strength is highlighted as a threshold to define a safety distance. ....	25
Figure 2-7.	180 $\mu$ T threshold magnetic field strength in single- and three-phase systems at different excitations. ....	26
Figure 2-9.	Maxwell-simulated magnetic field attenuation with the distance away from the implemented 1.7-meter square coil. Different excitation currents and the 180 $\mu$ T threshold are considered. ....	27
Figure 2-8.	Maxwell-simulated magnetic field distribution of a 1.7-meter square coil implemented in this project.....	27
Figure 2-10.	Maxwell simulated safety distance of the 1.7-meter square coil, considering 180 $\mu$ T threshold at different magnitudes of the excitation current. ....	28
Figure 2-11.	Maxwell-simulated electric field distribution of a 500-kV single-phase transmission line showing the electric field distribution around a nearby environment.....	29
Figure 2-12.	Illustration of a three-phase transmission system with UAS inspection.....	30
Figure 2-13.	Maxwell-simulated electric field distribution of a 500-kV three-phase transmission system which is excited by a three-phase voltage source. ....	30

Figure 2-14. Maxwell-simulated electric field distribution along the distance to the power line in a 500-kV three-phase transmission system. 2 kV/m is selected as a threshold value as it can be implemented in the laboratory. ....	31
Figure 2-15. Maxwell-simulated distance with 2 kV/m electric field strength in a high-voltage three-phase transmission system when the voltage varies in a wide range. ....	31
Figure 2-16. Proposed parallel-plate structure for implementation to validate the impact of AC electric fields on the performance of a UAS.....	32
Figure 2-17. Electric field distribution in a parallel plate system with 500-kV excitation voltage. ....	32
Figure 2-18. Maxwell-simulated electric field strength between two parallel plates at different excitation voltages. ....	33
Figure 2-20. Circuit topology of the developed DC-AC inverter, which is used to generate current excitation.....	34
Figure 2-19. The implemented high voltage (600V) and high current (46A) 60 Hz AC inverter to provide current excitation for magnetic field testing. Key components are illustrated. ....	34
Figure 2-21. Implemented planar coil and solenoid coil to generate magnetic field to emulate transmission lines and apply effects to the UAS platforms and sensors.....	34
Figure 2-22. Adopted two UAS platforms, MAVIC 2 and MAVIC 3, to study the electromagnetic field impact on UAS performance under various conditions.....	35
Figure 2-23. Implemented sensor platform to study the impact on different systems, including magnetometer, accelerometer, gyroscope, and microcontroller. ....	36
Figure 2-24. Maxwell-simulated magnetic field strength of a solenoid coil with 7.5-kA excitation current to generate a high-concentrated field for UAS testing. ....	38
Figure 2-25. Experimental setup of MAVIC 2 testing in 7.5-kA solenoid coil environment that can generate 60 Hz ac magnetic field up to 1800 $\mu$ T at 0.1m proximity .....	38
Figure 2-26. Built-in sensors in MAVIC 2 UAS, which are used to study the impact of magnetic fields.....	39
Figure 2-27. Experimental testing of Mavic 2 magnetometer signals when it flies over the top of a solenoid coil with 7.5-kA excitation current.....	39
Figure 2-28. Experimental testing of Mavic 2 GPS signals when it flies over the top of a solenoid coil with 7.5-kA excitation current. ....	41
Figure 2-29. Experimental testing of Mavic 2 accelerometer signals when it flies over the top of a solenoid coil with 7.5-kA excitation current.....	41
Figure 2-30. Experimental testing of Mavic 2 gyroscope signals in roll-pitch-yaw three directions when it flies over the top of a solenoid coil with various excitation currents (specifically in an up-and-down movement). ....	42
Figure 2-32. Experimental testing of Mavic 2 motor speed when it flies over the top of a solenoid coil with various excitation currents. ....	43
Figure 2-33. Experimental testing of Mavic 2 motor current and voltage when it flies over the top of a solenoid coil with 7.5-kA excitation current, showing no difference with and without magnetic field. ....	44
Figure 2-34. Experimental testing of MAVIC 2 battery voltage, capacity, and SoC when it flies over the top of a solenoid coil with various excitation currents. ....	44
Figure 2-35. Maxwell-simulated magnetic field strength of a 1.7-meter planar coil with 2.2-kA excitation current to generate a large area of magnetic field for UAS testing.....	45

Figure 2-36. Experimental setup of Mavic 2 testing in 2.2-kA planar coil environment that can generate 60 Hz ac magnetic field up to 3100 $\mu$ T at 0.1m proximity. ....	45
Figure 2-37. Experimental testing of Mavic 2 magnetometer signals when it flies along a planar coil with 2.2-kA excitation current. ....	46
Figure 2-38. Experimental testing of MAVIC 2 magnetometer signals when it flies along a planar coil, comparing with and without 2.2-kA excitation current. ....	47
Figure 2-39. Experimental testing of Mavic 2 GPS longitude signals when it flies along a planar coil, comparing with and without 2.2-kA excitation current. ....	48
Figure 2-40. Experimental testing of Mavic 2 GPS latitude signals when it flies along a planar coil, comparing with and without 2.2-kA excitation current. ....	49
Figure 2-41. Experimental testing of Mavic 2 accelerometer signals when it flies along a planar coil, comparing with and without 2.2-kA excitation current. ....	50
Figure 2-42. Experimental testing of Mavic 2 gyroscope signals when it flies along a planar coil, comparing with and without 2.2-kA excitation current. ....	51
Figure 2-43. Experimental testing of Mavic 2 motor signals when it flies over the top of a planar coil with 2.2-kA excitation current, showing an abnormal spike during the testing process. ....	52
Figure 2-44. Experimental testing of Mavic 2 battery voltage, capacity, and SoC when it flies over the top of a planar coil with and without 2.2-kA excitation current. ....	53
Figure 2-45. Experimental testing platform of discrete sensor board in strong magnetic field generated by a 5.25-kA solenoid coil. ....	53
Figure 2-46. Experimental results of magnetometer data in strong magnetic field generated by a solenoid coil. ....	54
Figure 2-47. Experimental results of accelerometer data in strong magnetic field generated by a solenoid coil. ....	54
Figure 2-48. Experimental results of gyroscope data in strong magnetic field generated by a solenoid coil. ....	55
Figure 2-49. Experimental setup of Mavic 3 with a sensor board payload testing in 2.2-kA planar coil environment that can generate 60 Hz ac magnetic field. ....	55
Figure 2-50. Experimental testing of magnetometer signal in a discrete sensor when it is mounted on Mavic 3 and flies along a planar coil, comparing with and without 2.2-kA excitation current. ....	56
Figure 2-51. Experimental testing of accelerometer x-axis signal in a discrete sensor when it is mounted on Mavic 3 and flies along a planar coil, comparing with and without 2.2-kA excitation current. ....	57
Figure 2-52. Experimental testing of gyroscope x-axis signal in a discrete sensor when it is mounted on Mavic 3 and flies along a planar coil, comparing with and without 2.2-kA excitation current. ....	57
Figure 2-53. Experimental testing of GPS altitude signal in Mavic 3 when it flies along a planar coil, comparing with and without 2.2-kA excitation current. ....	58
Figure 2-54. Experimental testing of gyroscope pitch signal in Mavic 3 when it flies along a planar coil, comparing with and without 2.2-kA excitation current. ....	58
Figure 2-55. Experimental testing of battery status signal in Mavic 3 when it flies along a planar coil, comparing with and without 2.2-kA excitation current. ....	59
Figure 2-56. Experimental setup to generate high voltage electric field for UAS testing. The applied voltage can reach 2000 V through a step-up transformer. ....	59

Figure 2-57. Implemented high voltage transformer to generate 2000 V AC voltage to be applied on the metal plates, including key magnetic core and windings.....	60
Figure 2-58. Experimental setup of high voltage electric field testing of Mavic 2. The field strength can reach 2 kV/m between the plates where the UAS is flying.....	60
Figure 2-59. Experimental testing of Mavic 2 magnetometer signals when it flies between two aluminum plates with 2 kV/m electric field strength.....	61
Figure 2-60. Experimental testing of Mavic 2 GPS signals when it flies between two aluminum plates with 2 kV/m electric field strength.....	62
Figure 2-61. Experimental testing of Mavic 2 accelerometer signals when it flies between two aluminum plates with 2 kV/m electric field strength.....	63
Figure 2-62. Experimental testing of Mavic 2 accelerometer signals when it flies between two aluminum plates with 2 kV/m electric field strength.....	63
Figure 3-1. EMI categories based on system-related, environmental, and cyber causes.....	64
Figure 3-2. DJI Matrice 30T.....	75
Figure 3-3. DJI Mavic 2 Enterprise Advanced (EA).....	76
Figure 3-4. DJI Matrice 300RTK.....	76
Figure 3-5. RF Explorer.....	77
Figure 3-6. FLIR Vue Pro R 640.....	78
Figure 3-7. Digital EMF Meter (EMF-390).....	79
Figure 3-8. Field Strength analyzer (EHP-50F).....	80
Figure 3-9. Microwave tower site.....	80
Figure 3-10. Transmission line sites.....	81
Figure 3-11. Different UAS platforms with sensors mounted.....	81
Figure 3-12. Flight trajectory at various AC transmission lines.....	82
Figure 3-13. Aerial/Ground data acquisition on E and H fields along 500kV AC transmission lines.....	82
Figure 3-14. Flight trajectory (a) above and (b) parallel to 250kV DC transmission line.....	83
Figure 3-15. Aerial and ground data acquisition on E and H fields along 250kV DC transmission line.....	83
Figure 3-17. Electric field strength as a function of distance from conductors along 69kV AC transmission lines.....	86
Figure 3-16. Electric field strength as a function of distance from conductors along 250kV DC transmission lines.....	86
Figure 3-18. Electric field strength as a function of distance from conductors along 230kV AC transmission lines.....	87
Figure 3-19. Electric field strength as a function of distance from conductors of 345kV AC transmission lines.....	87
Figure 3-21. Aggregate measured electric field values across all transmission lines.....	88
Figure 3-20. Electric field strength as a function of distance from conductors along 500kV AC transmission lines.....	88
Figure 3-22. Magnetic field strength as a function of distance from conductors along 250kV AC transmission lines.....	89
Figure 3-23. Magnetic field strength as a function of distance from conductors along 69kV AC transmission lines.....	89

Figure 3-24. Magnetic field strength as a function of distance from conductors along 230kV AC transmission lines.....	90
Figure 3-25. Magnetic field strength as a function of distance from conductors along 345kV AC transmission line. ....	90
Figure 3-26. Magnetic field strength as a function of distance from conductors along 500kV AC transmission lines.....	91
Figure 3-27. Aggregate measured magnetic field values across all transmission lines considered. ....	92
Figure 3-28. Electric field strength as a function of flight duration along a microwave tower. ..	93
Figure 3-29. Magnetic field strength as a function of flight duration along a microwave tower. 94	
Figure 3-30. A comparison of maximum electric field values by UAS model across all test sites. ....	95
Figure 3-31. A comparison of maximum magnetic field value by UAS model across all test sites. ....	95
Figure 3-32. Signal and noise classification from spectrum data. ....	96
Figure 3-33. Received signals near 69kV transmission line.....	97
Figure 3-34. Received signals near 230kV transmission line.....	97
Figure 3-35. Received signals near 345kV transmission line.....	98
Figure 3-36. Received signals near 500kV transmission line.....	98
Figure 3-37. Received signals near 250kV DC transmission line. ....	99
Figure 3-38. Received signals near microwave tower. ....	99
Figure 4-1. UAS models used in testing: Aurelia X6 Standard (left); QwinOut F450 (right) ...	101
Figure 4-3. ADALM-PLUTO SDR.....	102
Figure 4-2. CReSIS anechoic chamber.....	102
Figure 4-4. Antennas used in tests: Q-PAR horn antenna (left), ETS-Lindgren Model 3142C BiConiLog antenna (middle), and ETS-Lindgren Model 3180B antenna(right).....	102
Figure 4-5. Measured spectra of the C2 link signals of Aurelia X6 Standard (blue) and QwinOut F450 (red).....	103
Figure 4-6. Examples of RFI signals in front-door tests. (a) spectrum of a 5G NR baseband waveform; (b) spectrum of simulated RFI signal transmitted by ADALM-PLUTO SDR.....	104
Figure 4-7. Setup in the laboratory for assessment of front-door RFI impacts on UAS .....	105
Figure 4-8. Setup in the anechoic chamber for assessment of front-door RFI impacts on UAS	106
Figure 4-9. Samples of the Z-component from the gyro, accelerometer, and compass of the QwinOut F450 model .....	107
Figure 4-10. The RF spectrum of a TV channel with 6 MHz bandwidth (left) and the spectrum of the ASR long pulse (right) .....	107
Figure 4-11. Example of RFI signal in backdoor tests: the spectrum of a simulated RFI signal transmitted by ADALM-PLUTO SDR with a 1.5 MHz bandwidth centered around 202 MHz	108
Figure 4-12. Setup for back-door RFI test in anechoic chamber at LTE 4G/5G NR and ASR frequencies. The rectangle in the dashed line annotates the chamber enclosure .....	108
Figure 4-13. First setup in chamber for assessment of VHF back-door RFI impacts on UAS. .	109
Figure 4-15. Dedicated calibration setup in chamber to assess VHF backdoor RFI impacts on UAS .....	110
Figure 4-14. Second setup in chamber for assessment of VHF back-door RFI impacts on UAS .....	110

Figure 4-16. RFI barrage of the Herelink C2 across the full bandwidth (left); Spectra of combined C2 link and RFI signals at various ISRs with Aurelia X6 Standard model as the EUT (right)..	111
Figure 4-17. Spectra of combined C2 link and RFI signals at various ISR values with QwinOut F450 model UAS as the EUT .....	112
Figure 4-18. RFI barrage of the sub-bands of Herelink C2 links .....	113
Figure 4-19. Scenario of in-band RFI from Wi-Fi channel 13 .....	115
Figure 4-20. Scenario of adjacent band RFI from 4G LTE/5G NR channel b1/n41.....	116
Figure 4-21. RFI with 112 MHz bandwidth applied to Aurelia X6 Standard for back-door impact evaluation.....	117
Figure 4-22. Output data of the sensors and autopilot of the Aurelia X6 Standard model during No-RFI and RFI periods ( $E = 55$ V/m generated by RFI emissions at $F_c = 2.8$ GHz).....	119
Figure 4-23. Frequency scanning to search for back-door RFI effects.....	120
Figure 4-24. Back-Door effects observed on the C2 links of the Aurelia X6 Standard model around 88 MHz .....	121
Figure 4-25. Back-door effects observed at 198 MHz in the commands of the QwinOut F450 model's remote control.....	122
Figure 4-26. Back-door effects observed at 198 MHz in the compass data (top) and heading (bottom) of the QwinOut F450 model. ....	122
Figure 4-27. Determination of RFI frequency range (top), bandwidth (middle, and power level threshold (bottom) for the Aurelia X6 Standard model. ....	124
Figure 4-28. Determination of RFI frequency range (top), bandwidth (middle), and power level threshold (bottom) for the QwinOut F450 model .....	125
Figure 4-29. Significant back-door RFI effects on the battery current and C2 links of the Aurelia X6 Standard model .....	126
Figure 4-30. Significant back-door RFI effects on the compass, system power, GPS, and C2 links of the QwinOut F450 Standard model .....	127
Figure 4-31. (a) The Herelink box on the Aurelia model; (b) the Herelink box shielded on the Aurelia model; (c) the GPS and compass disk of the QwinOut model shielded; (d) complete shielding of the QwinOut model except its antenna for commands and telemetry; (e) everything shielded except one motor and the antenna. ....	128
Figure 4-32. Calibration setup (also refer to Figure 4-7).....	129
Figure 4-33. Environmental, C2 link, and simulated RFI signals .....	130
Figure 4-34. Calibration before flight tests. Top-left: RFI emissions at different strength levels (cellphones and C2 links turned off). Top-right: linear relation between RFI emissions and received signals. Bottom: Received signals with the presence of both the C2 links and RFI emissions.....	131
Figure 4-35. Determined AGC gains and ISRs versus the SDR's transmit power. ....	132
Figure 4-36. Front-door RFI flight tests. Left: setup (also compare to Figure 4-32). Right: QwinOut F450 model during flight .....	132
Figure 4-37. Data analysis from flight test 1 with $ISR = 3.9$ dB .....	133
Figure 4-38. Data analysis from flight test 3 with $ISR = 0.6$ dB .....	134
Figure 4-39. Data analysis from flight test 4 with $ISR = -3.8$ dB.....	134
Figure 4-40. Time to trigger failsafe versus ISR .....	134

Figure B1. (a) EP control path; (b) Bit errors in SBUS from the aircraft log file of the June 2020 incident showing spikes on the control channels in and out of the autopilot for aileron and rudder. .....	149
Figure B2. EMI categories based on system-related, environmental, and cyber causes. ....	153
Figure B3. UAS Orientation in Space.....	154
Figure B4. Results of Ambient RF Noise Floor Measurements (a) by NOAA; (b) by NASA. .	161
Figure B5. Drones in close proximity to transmission lines for inspection (DJI 2017a).....	162
Figure B6. Drone damaged from physical contact with a powerline (Lee and Choi 2017). ....	163
Figure B7. Drone hits a power line and recovers (D. Chen et al. n.d.).....	163
Figure B8. Drone hits guy tower line (left) and crashes (right) (Dong et al. n.d.). ....	164
Figure B9. Third party drone parachute system ParaZero erroneously deploys. Last frame that was captured from the video feed (left) before the crash (right) (Report Drone Accident 2020b)....	164
Figure B10. Drone is attached to another drone resulting in obstacle avoidance algorithm indefinitely continuing to increase drone altitude until it depletes batteries crashes (Heron 2022). .....	164
Figure B11. Magnetic disturbance due to the planned tall building. (a) Bird’s eye view. (b) xy pane (z=12m). (c) zx plane (y=0m). (d) yz plane (x=0m).....	166
Figure B12. Simulated electric field distribution of 500kV power lines and the effects on drones (D. Chen et al. n.d.).....	169
Figure B13. Simulated electric field distribution considering different power line voltages (W. Zhang et al. n.d.). ....	169
Figure B14. Simulated magnetic field distribution considering different power line voltages (W. Zhang et al. n.d.). ....	170

## TABLE OF TABLES

Table 2-1. Summary of magnetic field strength of single- and three-phase transmission systems. ....	25
Table 2-2. Magnetic field testing and measurements performed in this project. ....	37
Table 3-1. Barometer and magnetometer sensors affected ranges and field strengths. ....	65
Table 3-2. Intentional sources of EMI from common cyber-attacks. ....	74
Table 3-3. List of UAS platforms with specifications used for data capture/acquisition process. ....	75
Table 3-4. Frequency specifications for RF Explorer. ....	79
Table 3-5. Flight trajectory and orientation summary. ....	84
Table 4-1. RFI effects across the C2 link full bandwidth (S, U, D represent stable, Unstable, Disconnection status, respectively). ....	111
Table 4-2. Comparison between laboratory and anechoic chamber measured results with Aurelia X6 Standard UAS model as the EUT (S, U, D represent Stable, Unstable, and Disconnection status, respectively). ....	113
Table 4-3. RFI effects across C2 link sub-bands (S, U, D represent Stable, Unstable, and Disconnection status, respectively). ....	114
Table 4-4. Calculated safe distances of two UAS platforms from RFI sources. ....	118
Table 4-5. Mean and standard deviation of the sensor and autopilot output of the Aurelia X6 Standard model in No-RFI and RFI periods for ASR RFI scenarios. ....	120
Table 4-6. Sumarized findings from VHF RFI and shielding tests. ....	128
Table 4-7. Variable values used in ISR calculation. ....	131
Table 4-8. Summary of calibration and flight test observations. ....	135
Table B1. UAS Accidents compiled from AAIB. ....	150
Table B2. Barometer and magnetometer sensors affected ranges and field strengths. ....	158
Table B3. List of Potential Sources of RFI to UAS. ....	161
Table B4. Examples of drone accidents with involvement of power lines. ....	165
Table B5. Intentional sources of EMI based on system components. ....	170
Table B6. Intentional sources of EMI from common cyber attacks. ....	173
Table B7. Analysis of component susceptibility of transmission line interference. ....	177

## TABLE OF ACRONYMS

4G LTE	Fourth Generation Long Term Evolution
5G NR	Fifth Generation New Radio
AC	Alternating Current
ACK	Acknowledgement
AGC	Automatic Gain Control
AM	Amplitude Modulation
ASR	Airport Surveillance RADAR
AWG	American Wire Gauge
BW	Bandwidth
CReSIS	Center for Remote Sensing and Integrated Systems
DC	Direct Current
DUT	Device Under Test
EF	Electric Field
EMC	Electromagnetic Compatibility
EMF	Electromagnetic Field
EMI	Electromagnetic Interference
ESD	Electro-Static Discharge
FAA	Federal Aviation Administration
FEA	Finite Element Analysis
FLIR	Forward Looking Infra-Red
FM	Frequency Modulation
GPS	Global Positioning System
HEMP	High Altitude Electromagnetic Pulse
HPEM	High Power Electromagnetics
HT	Hardware Trojan
HVDC	High Voltage Direct Current
I2C	Inter-Integrated Circuit
IEMI	Intentional Electromagnetic Interference
IMU	Inertial Measurement Unit
ISM	Industrial, Scientific, and Medical
ISR	Interference to Signal Ratio

LIDAR	Light Detection and Ranging
LiPo	Lithium Polymer
MOSFET	Metal Oxide Semiconductor Field Effect Transistor
NRB	Number of Resource Blocks
OOB	Out-of-Band
PWM	Pulse Width Modulation
QPSK	Quadrature Phase Shift Keying
RADAR	RADio Detection And Ranging
RF	Radio Frequency
RFI	Radio Frequency Interference
RGB	Red-Green-Blue
RSSI	Received Signal Strength Indication
RTL	Return To Launch
SCS	Sub-Carrier Spacing
SDR	Software Defined Radio
SiC	Silicon Carbide
SMA	Sub-Miniature version A
SPWM	Sinusoidal Pulse-Width-Modulation
TED	Transient Electromagnetic Device
TEM	Transverse Electric and Magnetic
TV	TeleVision
UWB	Ultra Wideband
VHF	Very High Frequency
VLf	Very Low Frequency
Wi-Fi	Wireless Fidelity

## EXECUTIVE SUMMARY

This project aims to characterize Electromagnetic Interference impacts on small and medium sized Unmanned Aerial Systems, and to provide recommendations for characterization and mitigation strategies.

The project began with a review of pertinent literature to identify any gaps in testing that may exist in the research community. The team then planned the test scenarios that were needed, and then proceeded with accomplishment of all tests that were planned. Specific research questions that the team focused on were

- How susceptible are UAS to EMI, H fields, and E fields?
- What UAS components are most susceptible to EMI, H fields and E fields?
- How susceptible are UAS to operations near power lines?
- What low cost test methods can be used to evaluate UAS for susceptibility?
- What operational procedures are recommended to mitigate the various risks?

To address these questions, the team performed a variety of test exercises as follows

- Development of an inexpensive laboratory setup to simulate high-voltage power lines, comprised of a large inductive coil, a small solenoidal coil, and large electric field plates, together with appropriate power supplies to drive each at high voltage or high current. This test setup was then used to evaluate the effects of high magnetic and electric fields on multiple flight platforms.
- Real-world flight tests were completed to assess the effects of high-power transmission lines on a collection of UAS platforms. Specific transmission lines include alternating current lines at 69kV, 145kV, 345kV, 500kV and a Direct Current line at 250kV.
- Front-door and back-door Radio Frequency Interference tests were performed on multiple representative flight platforms to assess the sensitivity of the Command and Control link to in-band and adjacent-band interference signals, and to test the sensitivity of critical sensors and systems to signals that are far from the command and control frequency band. These tests were performed in a standard laboratory environment as well as within an anechoic test chamber. Real-world flight tests were performed to test front-door effects in a real-world environment.

Significant observations from this work are summarized below

- All measured platforms exhibited strong sensitivity to television signals in the very high frequency band. However, each platform responded to a different portion of this band and so it is recommended to ensure that each flight platform be tested to identify which portion of the band causes a risk to that platform.
- Shielding of critical components was shown to reduce sensitivity to interference for all models tested. Systems to be shielded should include the command and control system (other than the antenna), global positioning system (other than the antenna), and compass.
- Robust automatic gain control circuitry should be employed in the command and control link to reduce the potential for front-door interference
- Any command and control link that operates in the 2.4 GHz band is likely to be sensitive to radiation from 4<sup>th</sup> or 5<sup>th</sup> generation wireless network signals. When flying in a region

with cellular radiation in the b41 or n41 channels, the safe flight distance must be calculated using the equations contained herein.

Significant recommendations from this work are summarized below

- One of the most significant findings of this work is the sensitivity of both UAS platforms to VHF interference. Because both UAS platforms exhibited sensitivity to different parts of this frequency band, it is necessary to test the C2 link associated with each prospective UAS platform for its sensitivity to VHF signals and to determine its safe distance from TV transmit antennas. This testing must include the entirety of the VHF band as follows:
  - VHF frequency sweep from 60.5 MHz to 335.5 MHz with a 55MHz bandwidth
  - Use a setup shown in Figure 4-15 to assess the sensitivity of each UAS platform to the entire VHF band
  - Once a region of the VHF band is identified as sensitive to RFI, the level of sensitivity should be assessed by varying the RFI power level and investigating signals obtained by the various on-board systems (such as C2 link, compass, GPS receiver, etc.)
- From extensive experimental Measurements in a controlled laboratory setting, it is clear that the commonly held safety level for magnetic fields of 180  $\mu$ T is overly restrictive. The team was not able to rigorously determine the maximum upper field strength for safe flight, the team recommends a threshold of at least 3,000  $\mu$ T.
- All UAS should have adequate shielding of critical components to improve resilience to RFI. Components that require RF shielding include the C2 system (other than the antenna), GPS system (other than the antenna), and the compass.
- Robust AGC circuitry should be employed in the C2 link to reduce the potential for RFI on the front-door C2 link.
- Any C2 links that operate using the 2.4 GHz ISM band is likely to be sensitive to radiation from Wi-Fi access points and should operate with a significant distance from these points according to the results shown in Figure 4-19.
- Any C2 link that operates using the 2.4 GHz ISM band is likely to be sensitive to radiation from 4G LTE or 5G NR using channel b41 or n41. When flying in a region with cellular radiation in these channels, the safe flight distance may be calculated using the Equation (2) and Figure 4-20.
- Recommend a safe distance of at least 1,200 m from operating ASR for general purpose UAS. If closer flight is desired, each UAS platform must be characterized for its tolerance to ASR signals.
- Flight near power lines has significant adverse impacts to compass/magnetometer performance. When a flight near power transmission lines is needed, alternative methods of determining direction than the compass/magnetometer is recommended.
- Affordable laboratory testing setups that could be employed by UAS manufacturers and operators as described in section 2 are recommended to test any possible effects of strong magnetic and electric fields at lower frequencies.

- The effects of the battery current changes due to long-time exposure to the VHF RFI emissions on UAS operation safety and performance need to be further investigated and evaluated.
- Additional investigation into appropriate shielding against back-door signals in the VHF range is warranted.

## 1 INTRODUCTION & BACKGROUND

As the advancement of technology, the use of unmanned aircraft systems has tremendously expanded from military applications to many civilian uses such as aerial photography, scientific survey, infrastructure inspection, forestry, agriculture, disaster relief, search and rescue, policing surveillance, product delivery, public and commercial formation show, sports and recreation. This wide adoption of UAS platforms has led to increasing numbers of small and medium sized UAS platforms that fly at low altitudes with various systems and payload sensors. These systems are often highly integrated into limited avionics space and operate using a variety of frequency bands. At the same time regulatory authorities have worked to assign frequency allocations to support increasingly dense usage models. As a result, the potential of unpredictable behavior and loss of control of UAS increases due to interference from ubiquitous electromagnetic emissions. UAS Electromagnetic Compatibility (EMC) has therefore become a critical consideration in UAS design and operation in order to reduce any potential safety risks [1] [2] [3] [4] [5].

The primary goal of the ASSURE A56 project is to assess the safety risks of Electromagnetic Interference (EMI) on small and medium sized UAS. EMI is a broad category of potential interference and can be broken into two basic categories: (1) Static and Low Frequency Fields, and (2) Radio Frequency Interference (RFI) which occurs at frequencies that typically are used for wireless signal transmission. The first of these categories is addressed through the use of both laboratory-based measurements using simple equipment and components to simulate the effects of high-power transmission lines, and real-world flight tests near established power transmission lines.

For the purpose of this analysis, the two primary fields that are considered are the Electric Field ( $\bar{E}$ ) and the Magnetic Field ( $\bar{H}$ ). These two fields are defined to be the solutions to Maxwell's equations as follows, for source-free space:

$$\begin{aligned}\nabla \times \bar{E} &= -\mu \frac{\partial \bar{H}}{\partial t} \\ \nabla \times \bar{H} &= \varepsilon \frac{\partial \bar{E}}{\partial t} \\ \nabla \cdot \mu \bar{H} &= 0 \\ \nabla \cdot \varepsilon \bar{E} &= 0\end{aligned}$$

For static fields (i.e., when they do not change with time), these equations simplify to the following sets of separated equations:

$$\begin{aligned}\nabla \times \bar{E} &= 0 & \nabla \times \bar{H} &= 0 \\ \nabla \cdot \varepsilon \bar{E} &= 0 & \nabla \cdot \mu \bar{H} &= 0\end{aligned}$$

RFI analysis begins with a survey of likely sources of candidate signals in the United States National Air Space (NAS). This line of inquiry then measured the effects on candidate UAS platforms in scenarios that simulate real-world Radio Frequency (RF) signals to assess the impacts that these signals may have on UAS platforms. Flight tests were then performed to ascertain these potential RFI effects in a realistic environment. Two different UAS models were used in this

analysis: the Aurelia X6 Standard and QwinOut F450. The former model is a high performance commercial UAS platform, and the latter is a do-it-yourself model. Both front-door and back-door RFI effects were assessed across a range of frequencies, power levels, and bandwidths.

The front-door RFI effect assessments focused on Command and Control (C2) links using the Industrial, Scientific, and Medical (ISM) frequency band between 2.4 GHz and 2.5 GHz. In this scenario, the interference-to-signal-ratio (ISR) was identified as an accurate way to determine useful thresholds for stable, unstable, and disrupted C2 link connections for both UAS models. These resulting thresholds were similar for both models after eliminating the effects of on-board automatic gain control. An in-band RFI scenario of Wi-Fi and an adjacent-band RFI scenario of 4G LTE/5G NR were identified to cause disruption to the C2 links of each UAS model under test if the UAS is located too close to the respective emission source.

The back-door RFI effect assessments span frequencies from 60 MHz to 6 GHz. For this scenario, a targeted set of frequency ranges, bandwidths, and threshold of electric field strength that may cause disruptions were identified. The team identified several VHF TeleVision (TV) channel signals that caused disruptions to the C2 links and sensors of each UAS model. Additionally, signals were identified that cause adverse impacts to battery current and motor servo voltages.

The report concludes with a summary of key findings and recommendations for potential steps to take, and additional investigations that would add value to this work.

## 2 STATIC AND LOW FREQUENCY FIELDS: SIMULATION AND LAB TESTING

### 2.1 Magnetic field finite-element-analysis (FEA) simulation

The ANSYS-Maxwell software is used to simulate the electromagnetic field distribution in a high-power transmission line system. In the analysis, the magnetic field and electric field are simulated separately to identify the field strength. In this section, the simulation of magnetic fields is presented, and the details are provided as follows.

#### 2.1.1 Maxwell simulation of magnetic field for single-phase transmission line

An ideal single-phase transmission line is comprised of an infinitely long single wire. Such a structure is impractical to fabricate because of its extremely long length. Thus, practical models

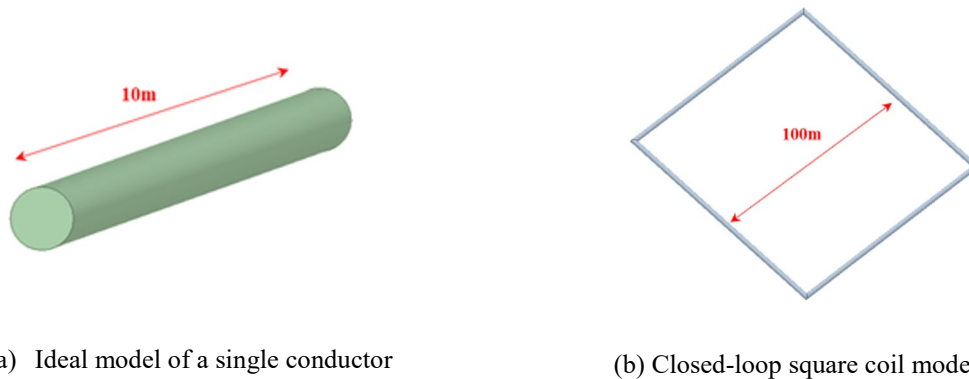
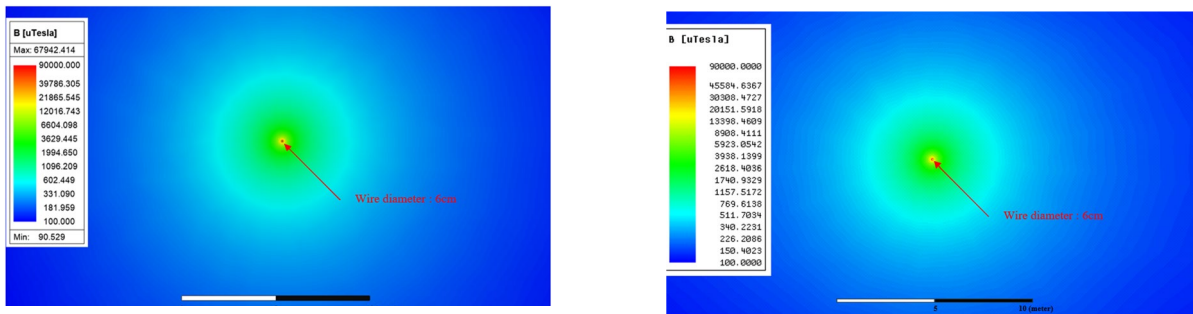


Figure 2-1. Maxwell-simulation model of a single-phase transmission line: ideal conductor model and square coil model, which are used to simulate the magnetic field distribution.

are needed that approximate this ideal structure and provide a reasonable level of accuracy as compared to the ideal. Two such approximate models are shown in Figure 2-1.

In Figure 2-1 (a), the simple model only consists of a single linear conductor to emulate a single-phase transmission line. This model closely resembles a real-world transmission line; however, this model is extremely challenging to build in practice because of the difficulty in applying a meaningful current excitation as it does not allow a return path for current. The model shown in Figure 2-1(b) depicts a square coil built to easily form a closed loop while still providing high accuracy when compared with a real-world transmission line. In this simulation model, the length of each side is set to 100 meters to isolate the fields induced by the current along one side of the square loop from the fields induced by the remaining three sides.

The simulated magnetic field distribution associated with each model with a current excitation of 10-kA applied is shown in Figure 2-2. In Figure 2-2 (a), the single conductor length is set as 10m, and the simulation range is set to 500m for the cross-sectional fields. The excitation current in this single conductor is applied to one end with an amplitude of 10-kA. The simulation result shows a rapidly attenuating field strength as distance increases from the conductor.



(a) Single conductor field simulation

(b) Square closed-loop coil field simulation

Figure 2-2. Maxwell-simulated magnetic field distribution with 10-kA high current excitation. Note that the field distribution of these two models are very similar.

The closed-loop square coil model of Figure 2-1(b) was simulated in Maxwell with results displayed in Figure 2-2(b). The square coil size is 100m on each side, and the simulation range is 500m in all directions to show the cross-sectional fields. The excitation current is applied inside this square coil to form a loop with a magnitude of 10-kA. The simulation result for the square coil is similar to the result for the single wire of Figure 2-2 (a)

A more detailed plot of the fields associated with each model is shown in Figure 2-3, which shows the field strength of both scenarios as a function of distance from the center of each line. Figure 2-3(a) shows the field strength as a function of distance from a single conductor, and Figure 2-3(b) shows the field strength as a function of distance from one side of the square coil structure. A comparison of Figure 2-3(a) and Figure 2-3(b) shows that a large coil of 100m generates field strength that is comparable to that of a single conductor.

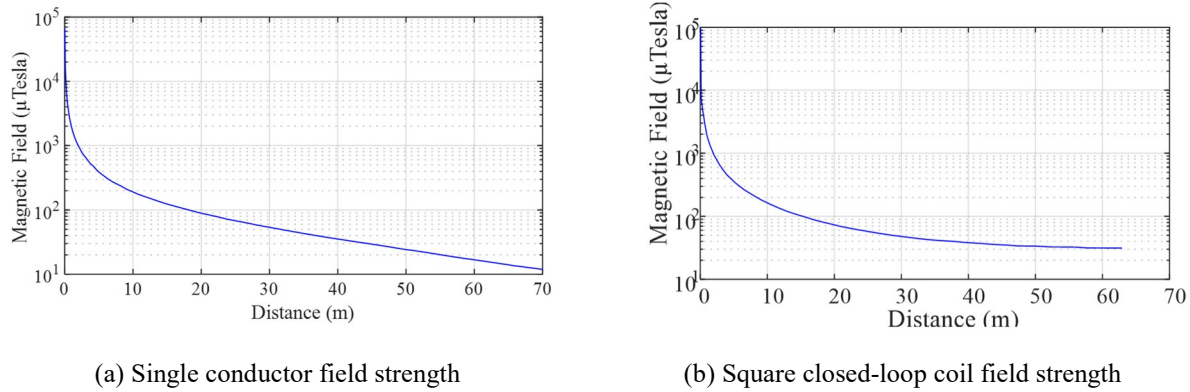


Figure 2-3. Comparison of Maxwell-simulated magnetic field distribution with 10-kA current excitation in single conductor model and the square coil model, showing the similarity of field strength.

### 2.1.2 Maxwell simulation of magnetic field for three-phase transmission line

Since most practical high-power transmission lines utilize a three-phase structure, it is also necessary to study the field distribution of a three-phase transmission system. The Maxwell simulation model of a three-phase transmission system is shown in Figure 2-4.

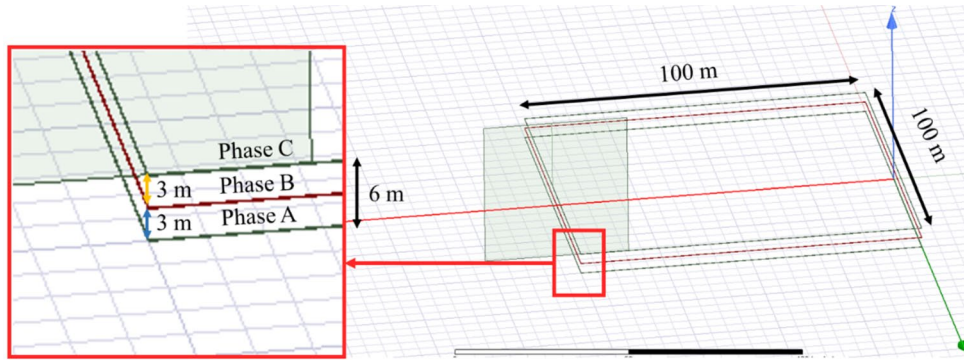
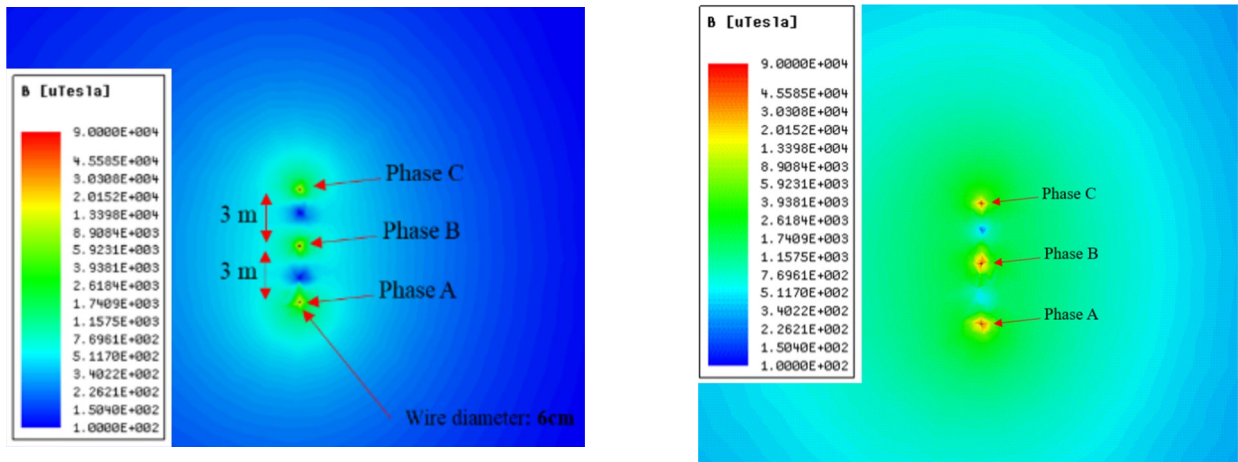


Figure 2-5. Maxwell-simulation model of a three-phase transmission system, using three 100-meter-long coils to emulate a practical three-phase system.

For the purposes of simulation, the simulation structure shown in Figure 2-4 is comprised of a square coil for each phase, each with side length of 100 meters. This structure is a natural extension of the structure of the single-phase coil shown in Figure 2-1(b). To provide results comparable to practical power transmission line structures, the distance between each phase is set to 3 meters. In the simulation, a collection of excitation current values are injected into three coils, and the field simulation result is shown in Figure 2-5.



(a) 1-kA current excitation

(b) 10-kA current excitation

Figure 2-4. Maxwell-simulated magnetic field distribution of a three-phase transmission system at different current excitation, showing the field strength.

In Figure 2-5(a), the excitation current magnitude is 1-kA, and three phases are identical with  $120^\circ$  phase difference between each coil. Similarly, Figure 2-5(b) shows the fields associated with a current excitation of 10-kA with corresponding increase in magnetic field strength. Note here that the fields associated with a 3-phase transmission line of Figure 2-5 are significantly larger than the fields associated with a single-phase transmission line of Figure 2-2. A more detailed plot of the magnetic field strength as a function of distance for the three-phase system shown in Figure 2-4 for a collection of excitation currents is shown in Figure 2-6. Note here that we have used a threshold magnetic field value of  $180 \mu\text{T}$  as a reference “Safe Distance” as

recommended by [6]. This value of safe distance is used here for purposes of discussion; its validity will be addressed later in this report.

Based on the simulation results shown in Figure 2-3 and Figure 2-6, the safety distance for both the single-phase and three-phase system is summarized in Table 2-1 and Figure 2-7.

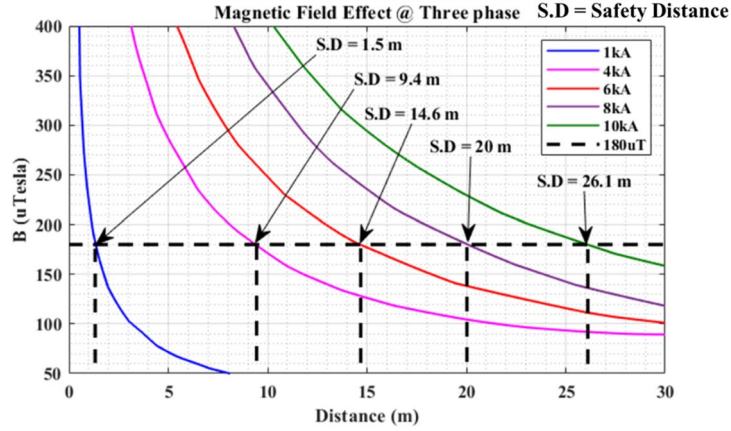


Figure 2-6. Maxwell-simulated magnetic field strength in a three-phase transmission system at different excitation current levels. The 180  $\mu$ T field strength is highlighted as a threshold to define a safety distance.

Table 2-1. Summary of magnetic field strength of single- and three-phase transmission systems.

Current (kA)	Safety Distance (1- $\phi$ )	Safety Distance (3- $\phi$ )	Difference
1	1.08 m	1.5 m	0.42 m
4	4.46 m	9.4 m	4.94 m
6	6.4 m	14.6 m	8.2 m
8	8.48 m	20 m	11.52 m
10	10.52 m	26.1 m	15.58 m

\* 180  $\mu$ T is set as a threshold to define safety distance.

The data in Table 2-1 and Figure 2-7 are consistent and show that when excitation current increases, the magnetic field strength increases, and the safety distance increases as well. The

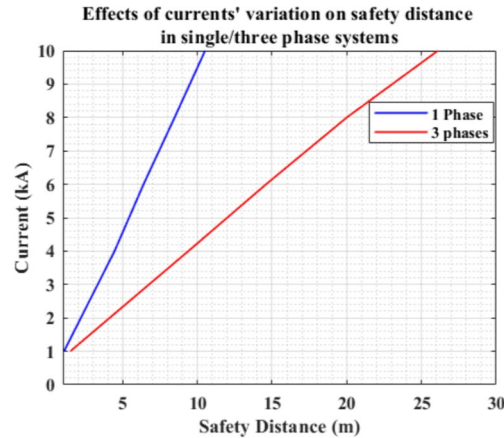


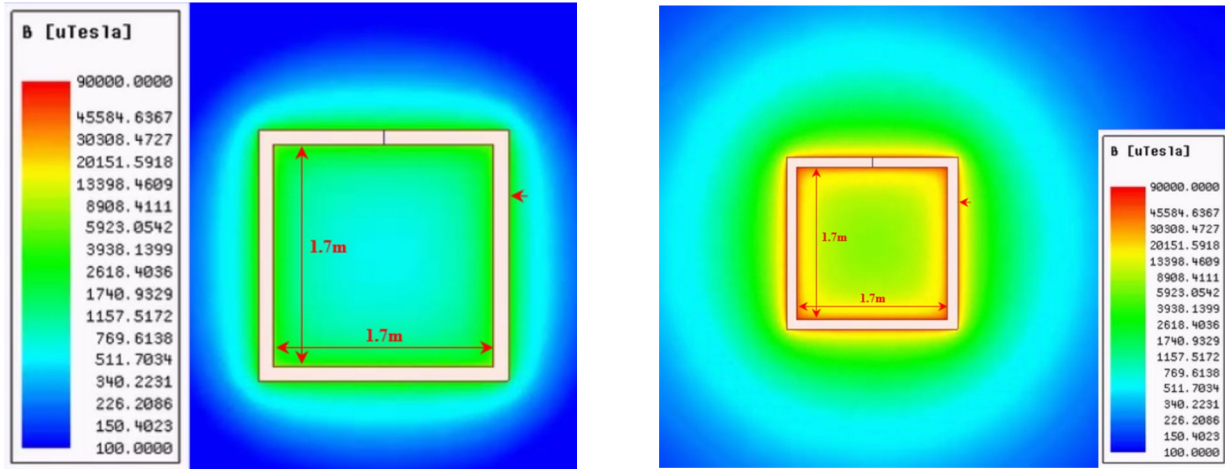
Figure 2-7. 180  $\mu$ T threshold magnetic field strength in single- and three-phase systems at different excitations.

safety distance of a three-phase system is nearly three times larger than the safety distance of a single-phase system.

To illustrate the impacts of this threshold for magnetic field strength, consider a three-phase transmission system with 10 kA current magnitude. This scenario would require the human operator and all electronic devices to be situated at least 26.1 meters (or approximately 85.6 feet) away from the transmission line. This large distance is burdensome for operation, and may prevent adequate inspection, depending on the quality of on-board UAS sensors. Thus, this common threshold should only be enforced if measured results justify its use on safety grounds. The primary purpose of this aspect of the study is to investigate factors such as the 180  $\mu$ T threshold for appropriateness and applicability.

### 2.1.3 Maxwell simulation of magnetic field for lab-based setup (1.7-meter coil)

Based on the analysis presented above, a square coil is used to emulate the field strength of a single-phase transmission line. In this project, a square coil of side length 1.7m was implemented to represent a single-phase transmission line. The magnetic field distribution can be further analyzed through field simulation in Maxwell software, which is shown in Figure 2-8.



(a) 1-kA current excitation

(b) 10-kA current excitation

Figure 2-9. Maxwell-simulated magnetic field distribution of a 1.7-meter square coil implemented in this project.

This 1.7-m square coil was chosen as a trade-off with the system implementation cost and the lab space limitation. A summary of field strength as a function of distance from one coil side for different excitation current values is shown in Figure 2-9.

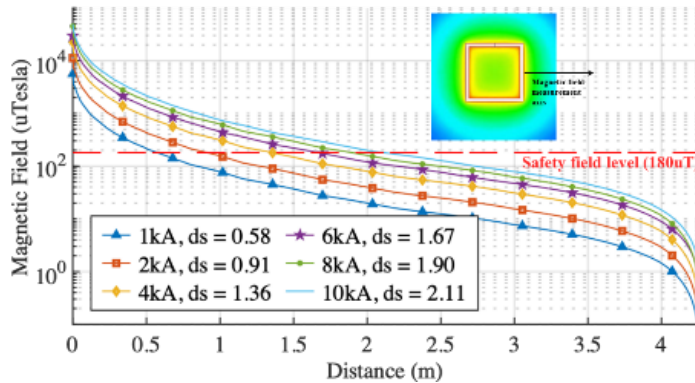


Figure 2-8. Maxwell-simulated magnetic field attenuation with the distance away from the implemented 1.7-meter square coil. Different excitation currents and the 180  $\mu$ T threshold are considered.

It should be noted here that the simulation in Figure 2-9 differs from the results shown in Figure 2-3(b), because the size of the coil is much smaller than 100 meters. Therefore, the fields are much more concentrated in the scenario of Figure 2-9. When the excitation current is 10-kA, the 180  $\mu$ T reference threshold distance is 2.11 meters. Based on this simulation, the safety distance can be further summarized for this 1.7-meter coil as shown in Figure 2-10.

In the laboratory implementation of this coil, the maximum current magnitude flowing through this coil is about 2.5-kA. The data displayed in Figure 2-10 shows that the reference safety distance in this case is about 1m. In subsequent testing, the team will fly the UAS platforms within this 1-meter region to test overall performance. The team will explore potential impacts of

strong magnetic fields in the range of a few hundreds to thousands of  $\mu\text{T}$  on the safe operation of UAS platforms.

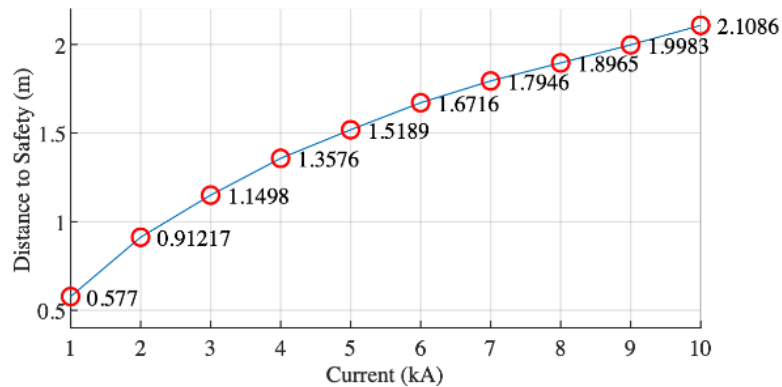


Figure 2-10. Maxwell simulated safety distance of the 1.7-meter square coil, considering  $180 \mu\text{T}$  threshold at different magnitudes of the excitation current.

## 2.2 Electric field finite-element-analysis (FEA) simulation

Maxwell software can also be used to simulate the electric field distribution. In the simulation, an Alternating Current (AC) excitation voltage can be assigned as the source of electric field generation. In this project, both the transmission line and parallel plate based experimental setup are simulated to understand the electric field strength and distribution. The transmission line analysis includes single-phase and three-phase configurations. The parallel plate setup can create a relatively uniform field to simplify testing.

### 2.2.1 Maxwell simulation of electric field for single-phase transmission line

The simulation of transmission lines is relatively straightforward because the high voltage potential is the source of electric field. We do not need to generate any current excitation, and the single-conductor model in Figure 2-1(a) can be used to emulate a single-phase transmission line. In this simulation, we apply 500-kV 60 Hz ac voltage on a single conductor line, and the simulation result of the electric field distribution is shown in Figure 2-11. In this simulation, since the field strength changes with time in this ac field, the peak field transient is captured to illustrate the field impact to the nearby environment.

Figure 2-11 shows that the electric field varies in a wide range at the proximity of a transmission line. When a UAS platform operates near a 500-kV transmission line, the field strength is in the kV/m range. The electric field also attenuates rapidly with increasing distance from the transmission line. When the distance increases to the range of tens of meters, the field reduces to hundreds of V/m. In the simulation, the voltage can also be extended to a higher value (such as 1000 kV). Additionally, a Direct Current (DC) voltage excitation can be applied to emulate a high-power High Voltage Direct Current (HVDC) system. The operating frequency can also be varied as needed. In this project, the team focuses more on the 60 Hz ac test. In future research, with more resources and support, the team also plans to extend the simulation and experimental testing to DC system as well.

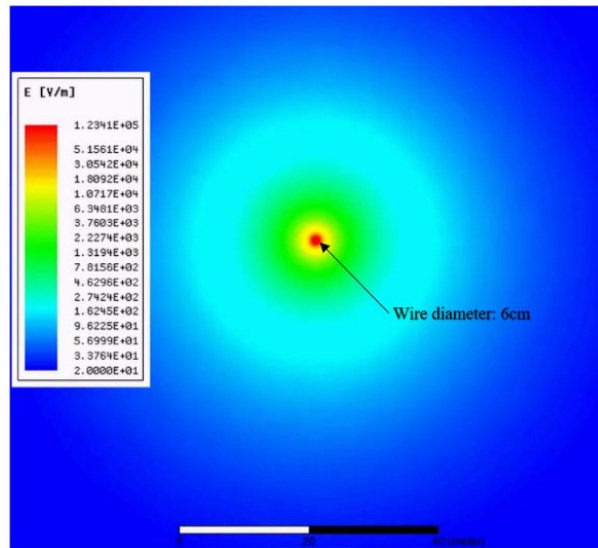


Figure 2-11. Maxwell-simulated electric field distribution of a 500-kV single-phase transmission line showing the electric field distribution around a nearby environment.

### 2.2.2 Maxwell simulation of electric field for three-phase transmission line

Three-phase high voltage transmission system are far more common than single phase transmission structures. A section of three-phase transmission line is illustrated in Figure 2-12. Based on this three-phase transmission system structure, an example of 500-kV simulation of electric field distribution is provided in Figure 2-13.

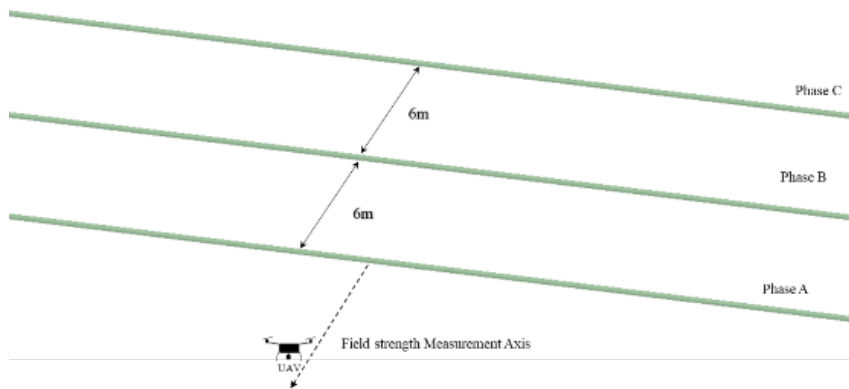


Figure 2-12. Illustration of a three-phase transmission system with UAS inspection.

The three-phase sinusoidal excitation voltage is also presented in this figure, and the peak field transient is captured in Figure 2-13. This figure shows that the three-phase electric field concentrates around the transmission lines, and attenuates with increasing distance. For the three-phase line of Figure 2-13, phase B is situated in the center of the three lines, while phases A and C are positioned on the right and left sides of phase B, respectively. If the drone approaches the powerline from phase A, the most unfavorable scenario arises when phase B reaches its minimum value and phase A reaches its maximum value. For the purpose of the simulation, this specific condition occurs precisely at  $t=0$

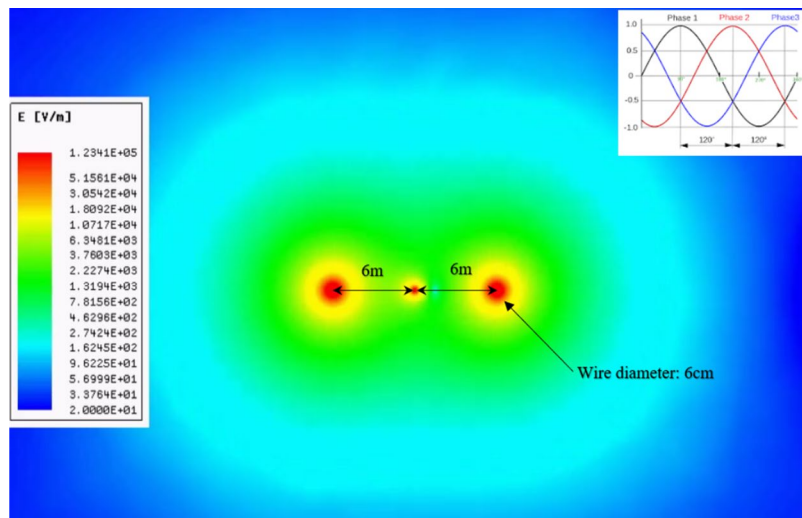


Figure 2-13. Maxwell-simulated electric field distribution of a 500-kV three-phase transmission system which is excited by a three-phase voltage source.

In this project, the implemented experimental setup can achieve a maximum electric field strength of 2 kV/m, so this number is selected as a representative threshold value in our analysis and simulation. The electric field distribution for a three-phase transmission system as a function of distance is shown in Figure 2-14 for a collection of voltage values. Note in this figure that the electric field strength reduces significantly with an increasing distance. For an excitation voltage

of 500-kV, the field reaches a value of 2-kV/m at a distance of 4.1m from the power line. When the distance is closer to the power line, the field strength increases rapidly. These data is derived from distances from the plane of the three lines, as shown in Figure 2-12. Both Figure 2-13 and

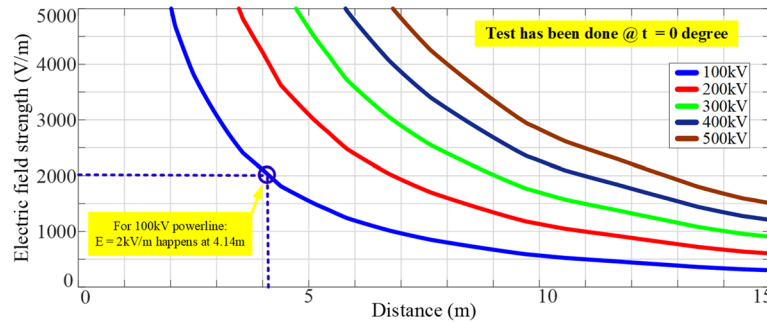


Figure 2-14. Maxwell-simulated electric field distribution along the distance to the power line in a 500-kV three-phase transmission system. 2 kV/m is selected as a threshold value as it can be implemented in the laboratory.

Figure 2-14 show that the electric field strength may be much larger along the line of the three-phase transmission line. While this scenario is not considered in this work, it is a recommended topic of future investigation in lab-based experiments.

Furthermore, the distance at which the field drops to 2-kV/m distance at different excitation voltages is summarized in Figure 2-15. The data shown in this figure can be used as a baseline to evaluate results of practical experiments in the field. Note here that a field test at a voltage level of 2-kV/m is equivalent to a comparable position in a three-phase transmission system. For example, for a 100-kV system, experimental testing at 2 kV/m provides results that are equivalent to performance that is 4.1 meters away from the power line.

In future research, the team plans to further increase the experimental field strength to 10-kV/m or even 100-kV/m with high voltage transformers to emulate a closer position to the high-voltage power line.

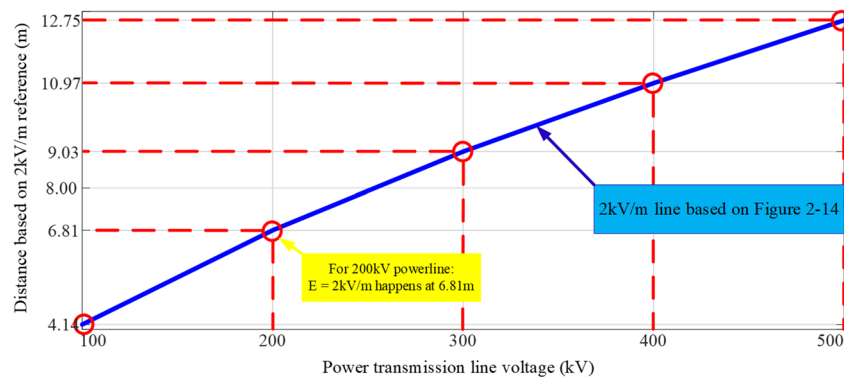


Figure 2-15. Maxwell-simulated distance with 2 kV/m electric field strength in a high-voltage three-phase transmission system when the voltage varies in a wide range.

### 2.2.3 Maxwell simulation of electric field for lab-based setup (0.9m parallel plates)

In the experimental testing process of electric fields, a parallel plate structure is adopted to generate a uniform field distribution for ease of testing. The proposed test structure is shown in

Figure 2-16. The parallel plates shown in this figure were simulated in Maxwell, with results of simulated electric field distribution shown in Figure 2-17.

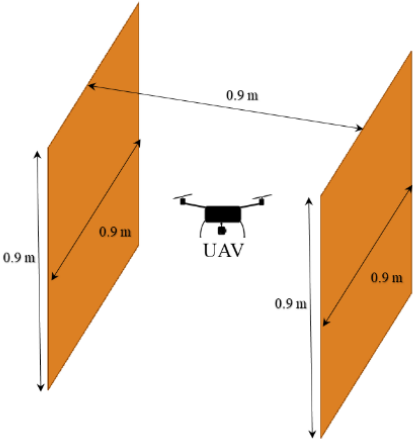


Figure 2-16. Proposed parallel-plate structure for implementation to validate the impact of AC electric fields on the performance of a UAS.

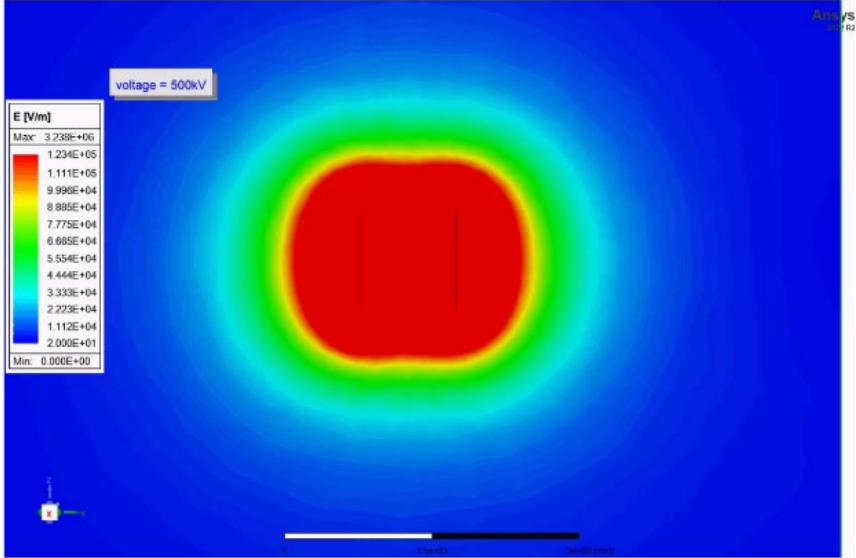


Figure 2-17. Electric field distribution in a parallel plate system with 500-kV excitation voltage.

In this parallel plate system, most of the electric field concentrates between the plates. This structure generates a mostly uniform field in the surrounding environment to accurately quantify any potential impacts to UAS platforms. The electric field distribution between the two plates is further summarized in Figure 2-18 which shows a very small variation in the electric field in the center of the plates with increasing variation closer to each plate.

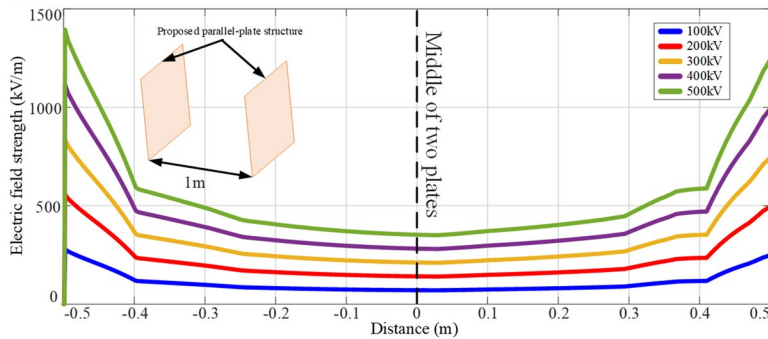


Figure 2-18. Maxwell-simulated electric field strength between two parallel plates at different excitation voltages.

## 2.3 Lab-based magnetic field testing

In the power and energy lab at Drexel University, a high power and high current setup was created to emulate the transmission line system and replicate the electromagnetic field environment that is simulated in software. In this section, magnetic field-testing details are described with test results presented in subsequent sections.

### 2.3.1 Magnetic field-testing prototype design and construction

Precise and large magnetic fields are needed to accurately test each system on board multiple small UAS platforms. To achieve this goal, a custom inverter was developed and implemented to supply the appropriate currents needed for all testing scenarios. Figure 2-19 illustrates the different system that comprise the inverter.

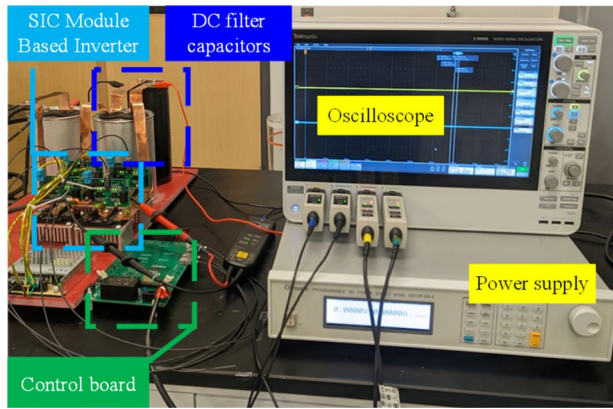


Figure 2-20. The implemented high voltage (600V) and high current (46A) 60 Hz AC inverter to provide current excitation for magnetic field testing. Key components are illustrated.

As shown in Figure 2-19, this inverter has high power capability to support the testing goals of the project. The maximum attainable voltage of this inverter is 600 V, and maximum attainable current is 46 A. The inverter employs sinusoidal pulse-width-modulation (SPWM) to generate 60 Hz AC current. Silicon carbide (SiC) power modules from Wolfspeed are used to provide the switching capability. The circuit topology is shown in Figure 2-20.

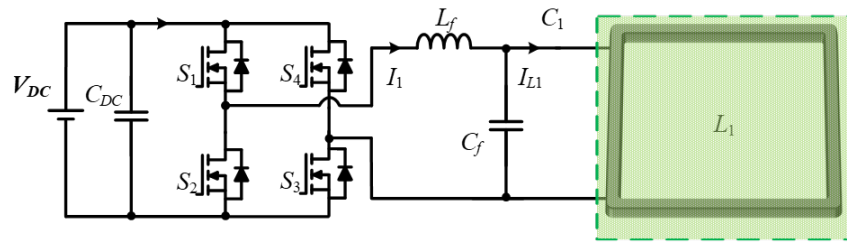


Figure 2-19. Circuit topology of the developed DC-AC inverter, which is used to generate current excitation.

To investigate the potential impact of magnetic fields, two distinct testing platforms were devised and constructed: (a) a large planar coil and (b) a solenoid coil. These platforms are specifically

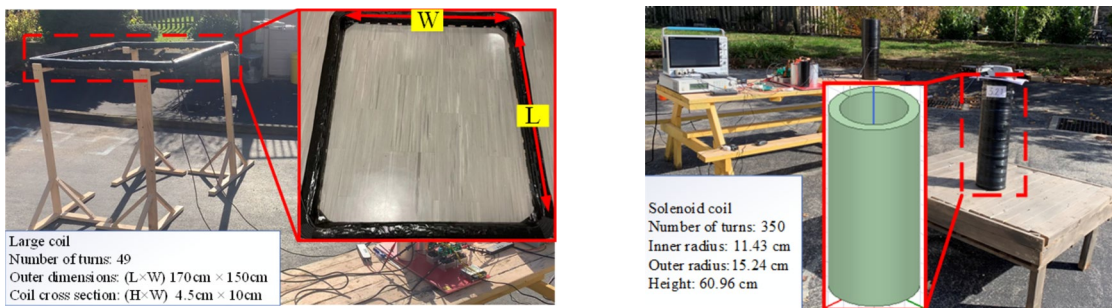


Figure 2-21. Implemented planar coil and solenoid coil to generate magnetic field to emulate transmission lines and apply effects to the UAS platforms and sensors.

designed to facilitate controlled experiments and provide insights into the behavior of the UAS sensors under different magnetic field conditions. Both coils are shown in Figure 2-21.

In Figure 2-21(a), a large planar coil serves as a scaled-down representation of power transmission lines, enabling us to simulate the magnetic fields typically encountered near high-power transmission lines. Each turn of the coil can support a maximum current of  $I_{rms}=46$  A, which results in a maximum equivalent induced current of 2.2 kA, considering the presence of 49 turns as shown in Equation 1. The intensity of magnetic field assuming the coil is 10cm thick in this situation is calculated in Equation 2.

$$I_{coil} = N_{Turn} \times I_{injected\_current} = 49^{Turn} \times 46^A = 2.254kA \quad (1)$$

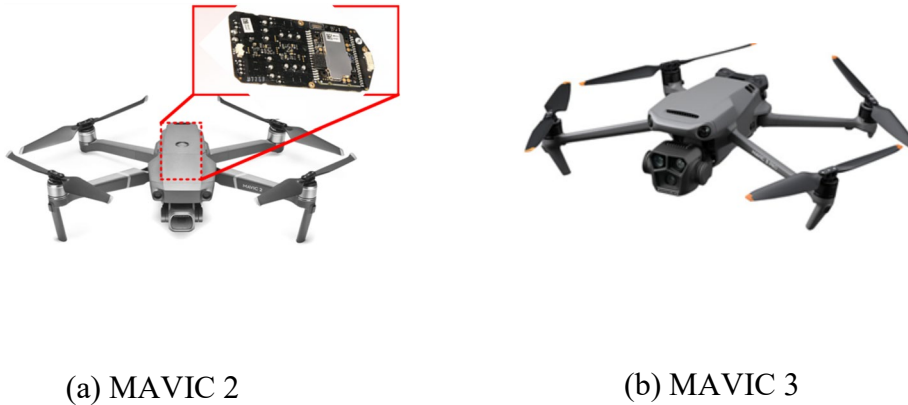
$$B_{Induced} = \frac{\mu_0 \times I_{coil}}{2 \times \pi \times d_{distance\_from\_coil}} = \frac{4 \times \pi \times 10^{-7} \times 2.254^{kA}}{2 \times \pi \times 0.1^{meter}} = 4.508mT \quad (2)$$

In Figure 2-21(b), a long solenoid coil serves as a versatile tool to generate high-intensity magnetic fields, allowing us to conduct a range of tests and analyze the response of the UAS sensors in such extreme conditions. This structure can support a maximum current of approximately  $I_{rms}=22$  A on each turn of the coil which leads to a maximum equivalent current of 7.5-kA on the entire 350 turns of the solenoid.

$$I_{solenoid} = N_{Turn} \times I_{injected\_current} = 350^{Turn} \times 22^A = 7.7kA \quad (3)$$

$$B_{Induced} = \frac{\mu_0 \times I_{solenoid}}{2 \times \pi \times d_{distance\_from\_coil}} = \frac{4 \times \pi \times 10^{-7} \times 7.7^{kA}}{2 \times \pi \times 0.1^{meter}} = 15.4mT \quad (4)$$

This project adopts two different UAS platforms to study the impact of electromagnetic fields: MAVIC 2 and MAVIC 3, as shown in Figure 2-22.



(a) MAVIC 2

(b) MAVIC 3

Figure 2-22. Adopted two UAS platforms, MAVIC 2 and MAVIC 3, to study the electromagnetic field impact on UAS performance under various conditions.

Figure 2-22(a) shows the internal structure of a commercial UAS, which has a built-in controller and sensors that might be affected by the external fields. Figure 2-22(b) shows a more advanced version of UAS (MAVIC 3). Both platforms are made by the same manufacturer but with different

configurations to compare the impact from the fields and also how the manufactures have considered EMC in the design of multiple platforms.

The use of digital and analog filters inside the UAS often complicates the acquisition of raw data. Furthermore, access to certain calculated data may be restricted for UAS users. Even when manufacturers offer data extraction options, understanding the calculation methods and obtaining

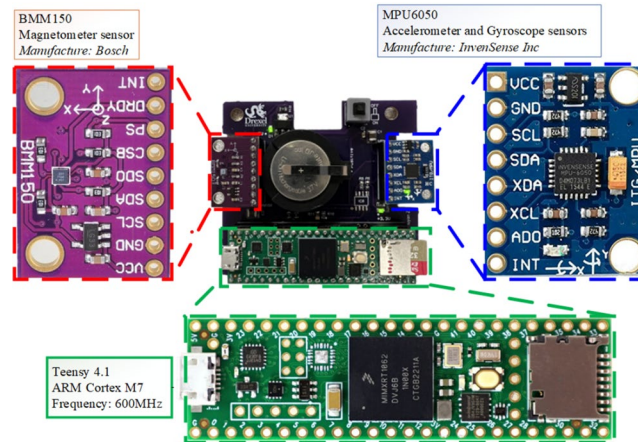


Figure 2-23. Implemented sensor platform to study the impact on different systems, including magnetometer, accelerometer, gyroscope, and microcontroller.

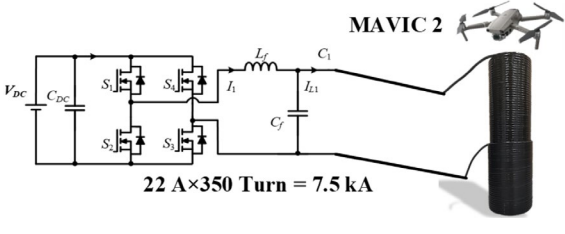
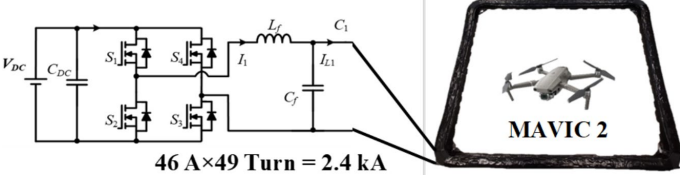
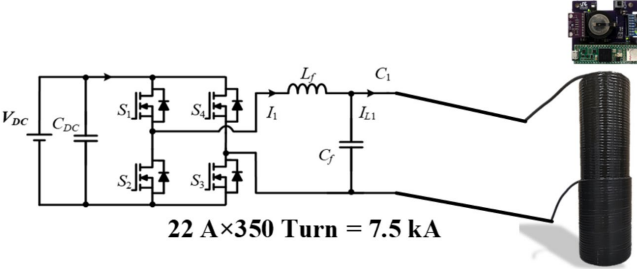
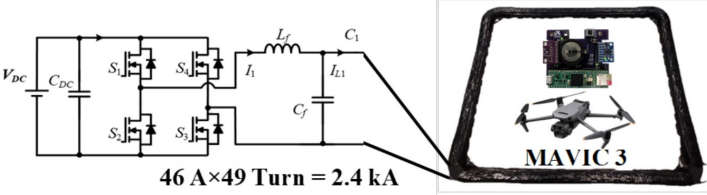
data in its raw form can be challenging. Therefore, there is a need to develop methods that enable unrestricted access to unfiltered data, which would greatly assist engineers in studying the impact of magnetic and electric fields on these integrated sensors. To address this need, a new separate discrete sensor system shown in Figure 2-23 has been created and developed.

In Figure 2-23, the magnetometer BMM 150 is used to measure the magnetic field. Its bandwidth is sufficient to accurately measure the 60 Hz time-varying field generated by both coils. Meanwhile, the accelerometer and gyroscope sensors are integrated on MPU6050, which are part of the inertial measurement units (IMU). All the sensors are managed by the central controller, and their communication is realized through I<sup>2</sup>C. To ensure the reception of each data point, a timestamp is attached to the transmitted data. Furthermore, to safeguard the integrity of the data, two filters have been devised—one at the sensor side and another at the MCU side. These filters collect five sets of data and compute their average, which is then stored in the log file.

This system aims to enhance our understanding of the effects of magnetic and electric fields on each sensor. By utilizing this dedicated sensor system, we can access unfiltered data directly from the sensors, enabling a more comprehensive analysis of the impact of magnetic and electric fields. This facilitates a deeper understanding of the sensor behavior and performance under different field conditions. In this project, the low-cost and fast-speed ARM based Teensy 4.1 microcontroller is utilized, and the team worked on the coding to make sure all the sensors can work properly. The microcontroller plays a vital role in regulating, transmitting, and reporting any incidents that occur during testing. Therefore, it is essential to subject the microcontroller to testing to ascertain its resistance to different magnetic fields.

Based on each experimental setup, there are four categories of magnetic field testing conducted in this project, which are listed in Table 2-2.

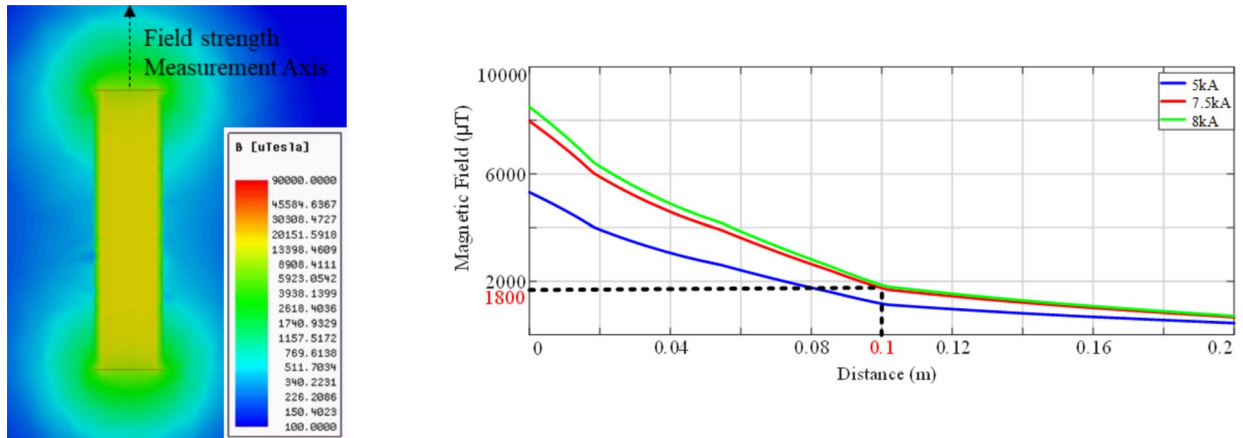
Table 2-2. Magnetic field testing and measurements performed in this project.

Category	Experimental setup	DUT
#1 Mavic 2 in 7.5-kA solenoid coil		 <p>MAVIC 2</p>
#2 Mavic 2 in 2.2-kA planar coil		 <p>MAVIC 2</p>
#3 Sensors in 7.5-kA solenoid coil		
#4 Mavic 3 carrying sensors in 2.2-kA planar coil		  <p>MAVIC 3</p>

As described in Table 2-2, the four experiments cover three devices under test (DUT): Mavic 2 UAS, Mavic 3 UAS, and external circuit board with multiple sensors. All of these test scenarios provide the evaluation of magnetic field impacts from multiple aspects: direct measurement of raw data from sensors and indirect measurement of signal-conditioned data from commercial products.

### 2.3.2 *Mavic 2 testing in 7.5-kA solenoid coil*

The Mavic 2 UAS is selected as the testing device because it is one the most widely used UAS products in the commercial market. Since there are many Mavic 2 flights approaching (or attempting to approach) transmission lines daily, it is meaningful to study its performance in a highly concentrated magnetic field environment.



(a) Magnetic field distribution      (b) Magnetic field strength versus the distance to the solenoid coil

Figure 2-24. Maxwell-simulated magnetic field strength of a solenoid coil with 7.5-kA excitation current to generate a high-concentrated field for UAS testing.

The implemented solenoid coil is very useful to generate high magnetic field strength. When 7.5-kA excitation current is injected, the magnetic field distribution is shown in Figure 2-24 which shows that the magnetic field is very strong at close proximity to the solenoid coil. In the flight test, Mavic 2 can be controlled at a position about 0.1 meter above the top of the coil where the field strength is approximately 1800  $\mu\text{T}$ . In experiments, Mavic 2 position is precisely controlled. The setup is shown in Figure 2-25.

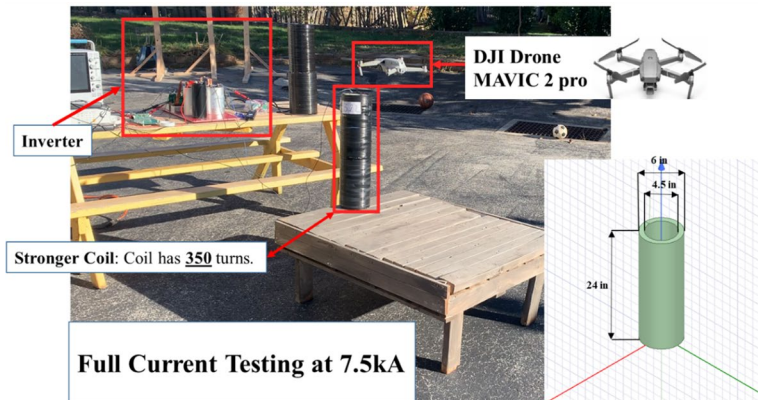


Figure 2-25. Experimental setup of MAVIC 2 testing in 7.5-kA solenoid coil environment that can generate 60 Hz ac magnetic field up to 1800  $\mu\text{T}$  at 0.1m proximity

During the test process, the excitation current magnitude also varies in a wide range, from 0 to 7.5 kA to test the influence of magnetic field strength. The testing time lasts for 20 minutes to observe potential impacts from dwelling in these fields for an extended period of time.

Mavic 2 has onboard sensors, and the data can be accessible after each flight, although some of the data is encrypted and cannot be accessed by users. In this test, after the investigation of the UAS data, the studied built-in sensors include magnetometer, Global Positioning System (GPS), accelerometer, gyroscope, motors, and battery, as shown in Figure 2-26, and measured results are provided below.

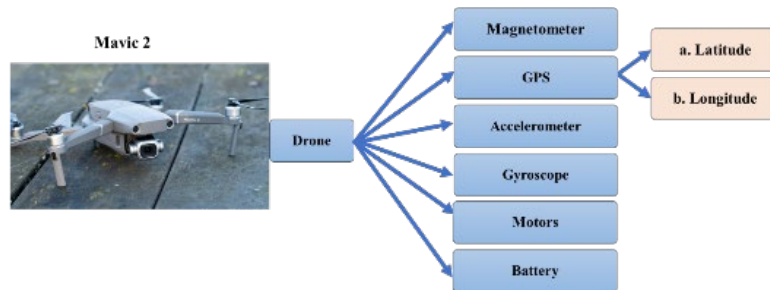
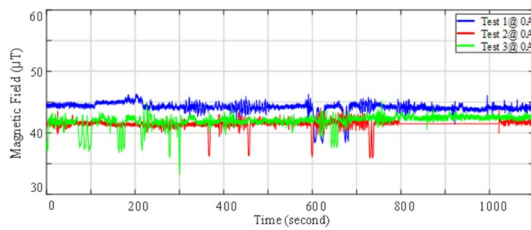


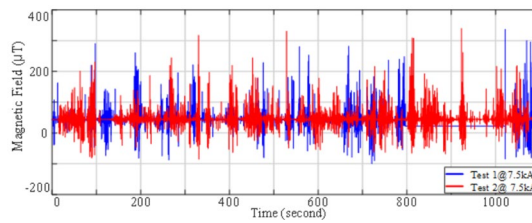
Figure 2-26. Built-in sensors in MAVIC 2 UAS, which are used to study the impact of magnetic fields.

### 2.3.2.1 Magnetometer of Mavic 2 in 7.5-kA solenoid coil

Measured magnetometer signals of Mavic 2 are shown in Figure 2-27.



(a) Measured field at 0A excitation



(b) Measured field at 7.5-kA excitation



(c) Onboard video recording with no warning at far position with 7.5-kA excitation



(d) Onboard video recording with the compass failure warning at near position with 7.5-kA excitation

Figure 2-27. Experimental testing of Mavic 2 magnetometer signals when it flies over the top of a solenoid coil with 7.5-kA excitation current

Figure 2-27(a) shows the magnetometer measurement without any current excitation, which is used as a baseline for comparison. Three additional tests were conducted with favorable results that are consistent with expectation. These data show outcomes that are within an acceptable range, are relatively flat with a slight offset and small ripple within measurement tolerance. In Figure 2-27(b), the results of two additional tests with 7.5-kA excitation are shown. Note that in

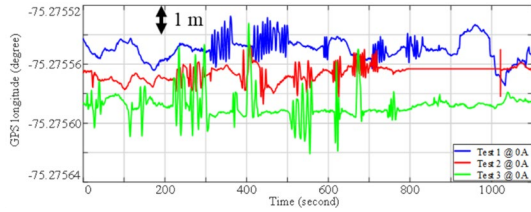
these scenarios the magnetometer results vary widely, approaching the sensor saturation field strength of 400  $\mu\text{T}$ . The spike in data is due to the movement of UAS during flying operations. When the UAS platform drifts closer to the solenoid coil, the measured field strength increases; when the UAS platform moves away, the measured field strength reduces.

During one of the test flights, a warning signal was sent by the UAS to the remote controller when the UAS platform was located a distance of approximately 15cm above the coil. The abnormal and considerably higher field strength compared to the background earth field caused a compass failure, rendering the compass unable to effectively detect direction. As a result, the UAS warned the human operator to conduct compass calibration. Figure 2-27 (c) displays a still image of the onboard video recording when the UAS approached the solenoid coil, while Figure 2-27 (d) shows the warning signal reported on the video screen when the UAS flew directly above the coil, where the magnetic field reached its peak value. Further investigation revealed that the measured magnetic field for the DJI drone is limited to very specific ranges by the manufacturer. If the drone encounters any values outside of these predefined ranges, the UAS assumes the measurement is caused by a calibration issue.

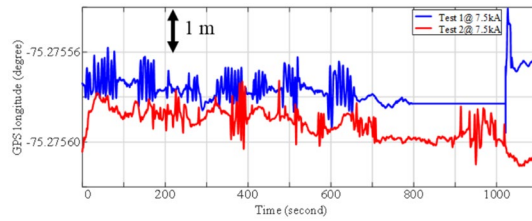
Despite the warning signals, the UAS continued to exhibit normal flight because of the presence of sensor fusion techniques that maintained functionality. However, after prolonged operation, the team did observe a single flight crash that might be related to the compass failure. During this crash, which occurred on November 3, 2022, the Mavic 2 had been operating continuously for 20 minutes, with approximately 15% battery remaining. Apart from the compass failure, there were no specific additional warnings. Fortunately, there was no damage due to the short distance of the fall onto the solenoid coil. Subsequent attempts to replicate the crash during more than 10 tests did not result in a second crash.

### 2.3.2.2 GPS of Mavic 2 in 7.5-kA solenoid coil

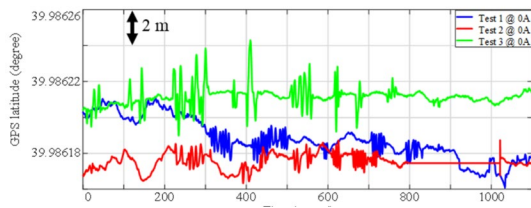
GPS signals from test scenarios are shown in Figure 2-28, including both longitudinal and



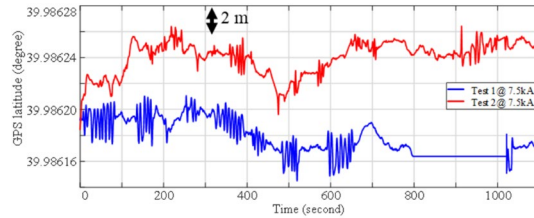
(a) GPS longitude at 0A excitation



(b) GPS longitude at 7.5-kA excitation



(c) GPS latitude at 0A excitation



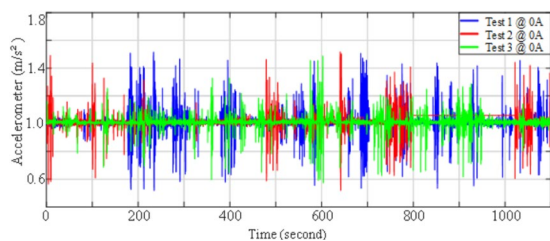
(d) GPS latitude at 7.5-kA excitation

Figure 2-28. Experimental testing of Mavic 2 GPS signals when it flies over the top of a solenoid coil with 7.5-kA excitation current.

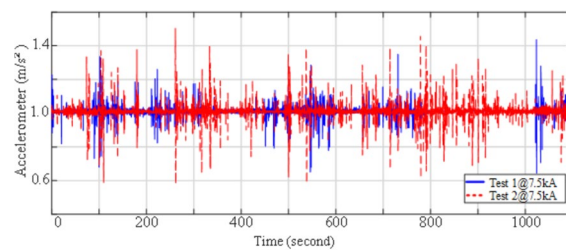
latitudinal signals. When these signals are compared with and without excitation, it is clear that the magnetic field does not affect the GPS measurement. Measurements in different conditions do show some small variations, but all variations fall within the tolerance range (1 or 2 meters) for the GPS sensors on board the UAS.

### 2.3.2.3 Accelerometer of Mavic 2 in 7.5-kA solenoid coil

The accelerometer signals were measured and compared in Figure 2-29.



(a) Accelerometer at 0A excitation



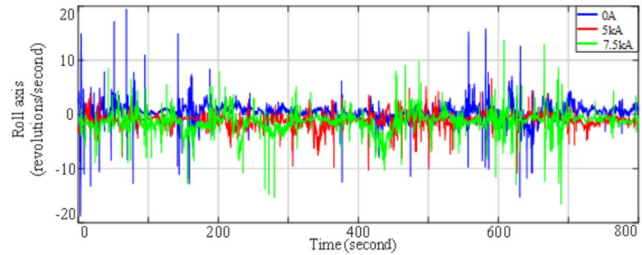
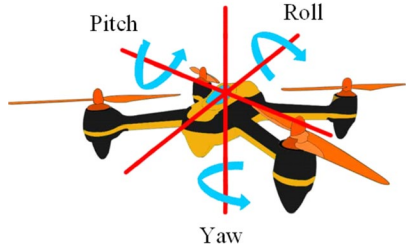
(b) Accelerometer at 7.5-kA excitation

Figure 2-29. Experimental testing of Mavic 2 accelerometer signals when it flies over the top of a solenoid coil with 7.5-kA excitation current.

The comparison in different conditions also indicates that the magnetic field has no impact on the accelerometer measurement results. The data includes an offset of  $1.0 \text{ m/s}^2$  so both the acceleration and deceleration directions are visible on the plot.

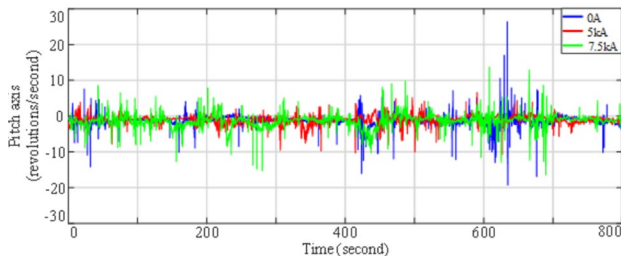
### 2.3.2.4 Gyroscope of Mavic 2 in 7.5-kA solenoid coil

The gyroscope is also a critical component in determining the UAS flight status. The definition of gyroscope measurement is shown in Figure 2-30(a). The measurements in three directions, Roll, Pitch, and Yaw, are presented in Figure 2-30. In this specific test, the UAS moves up and down, and the yaw-direction measurement is relatively stable. For the other two directions, the data corresponds to the flight control. The data distribution is relatively random due to inconsistencies

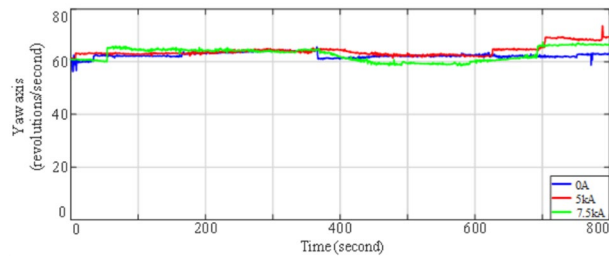


(a) Definition of gyroscope measurement

(b) Roll direction



(c) Pitch direction



(d) Yaw direction

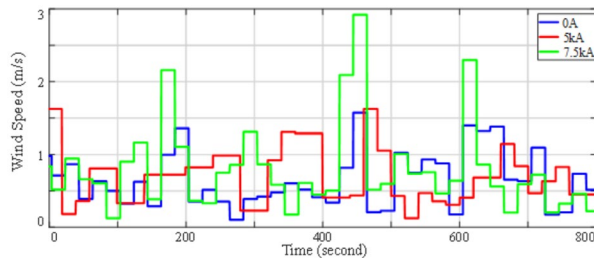
Figure 2-30. Experimental testing of Mavic 2 gyroscope signals in roll-pitch-yaw three directions when it flies over the top of a solenoid coil with various excitation currents (specifically in an up-and-down movement).

in the human operator's commands. Based on Figure 2-30, there is no clear evidence that the excitation current magnitude has any specific influence on the gyroscope data.

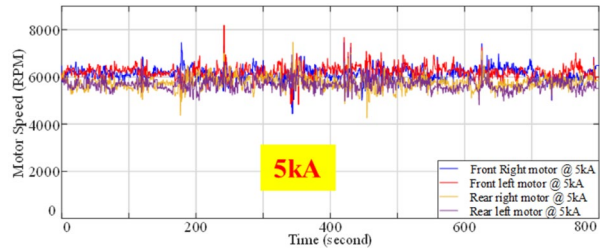
Further flying tests were conducted, and the UAS moves in a relative freestyle around the solenoid coil. Measurement data is shown in Figure 2-31, where the three-direction data are combined to form angular velocity. These data further demonstrate that the excitation current and its magnetic field does not affect the gyroscope measurements in Mavic 2.

### 2.3.2.5 Motors of Mavic 2 in 7.5-kA solenoid coil

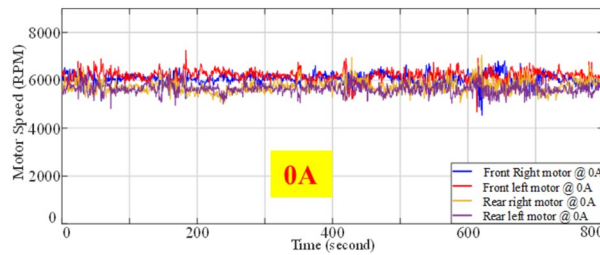
Mavic 2 has four motors that are used to maintain and control flight operations. In real-time, wind is an important disturbance to motor control. Mavic can also measure the wind speed. The



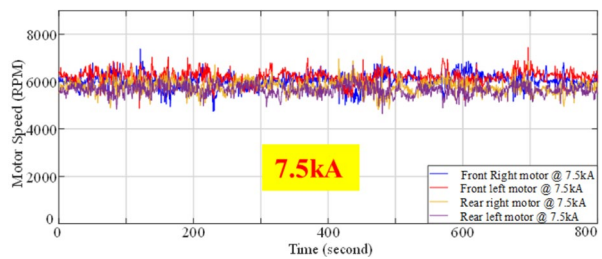
(a) Real-time wind speed



(b) Motor speed at 5-kA excitation



(c) Motor speed at 0 A excitation

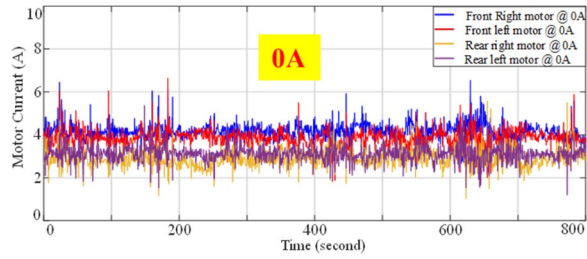


(d) Motor speed at 7.5-kA excitation

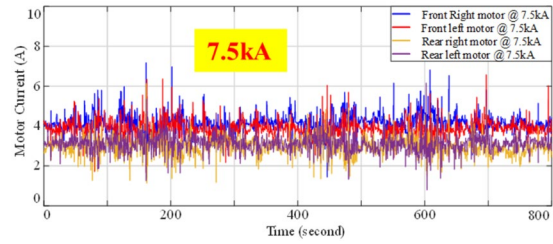
Figure 2-31. Experimental testing of Mavic 2 motor speed when it flies over the top of a solenoid coil with various excitation currents.

comparison of motor speed in different excitation currents is shown in Figure 2-32. These data show that Mavic 2 can maintain a stable motor speed at various wind speeds. When the excitation current varies widely, no significant change is seen on the motor speed. Figure 2-32(a) shows a strong wind during the 7.5-kA excitation test, but the motor speed is still stable as shown in Figure 2-32(d).

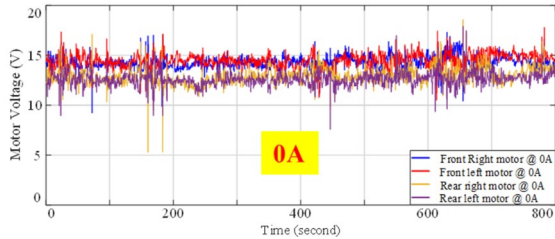
Meanwhile, Mavic 2 can provide insight into the motor drive signals, such as motor current and motor voltage as shown in Figure 2-33. Although there is the presence of noise caused by the switching operation of the motor driver, there is no significant difference in the 7.5-kA excitation test.



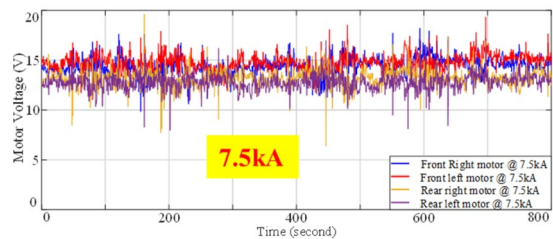
(a) Motor current at 0 A excitation



(b) Motor current at 5-kA excitation



(c) Motor voltage at 0 A excitation



(d) Motor voltage at 7.5-kA excitation

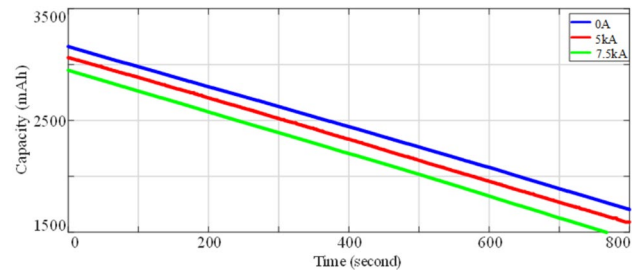
Figure 2-32. Experimental testing of Mavic 2 motor current and voltage when it flies over the top of a solenoid coil with 7.5-kA excitation current, showing no difference with and without magnetic field.

### 2.3.2.6 Battery of Mavic 2 in 7.5-kA solenoid coil

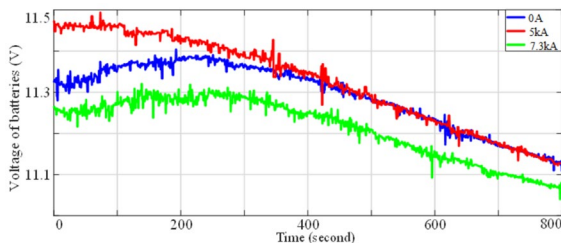
The battery parameters are also measured at different excitation currents as shown in Figure 2-34. During the energy exhaustive test, the UAS is maintained at a stable position immediately above



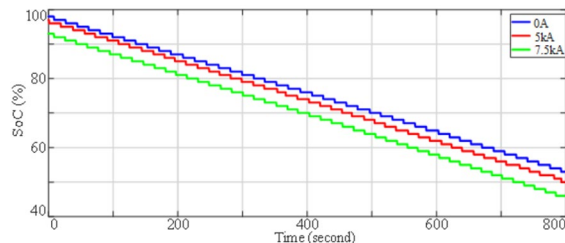
(a) Exhaustive test of UAS on the top of solenoid coil



(b) Battery capacity



(c) Battery voltage



(d) Battery state of charge (SoC)

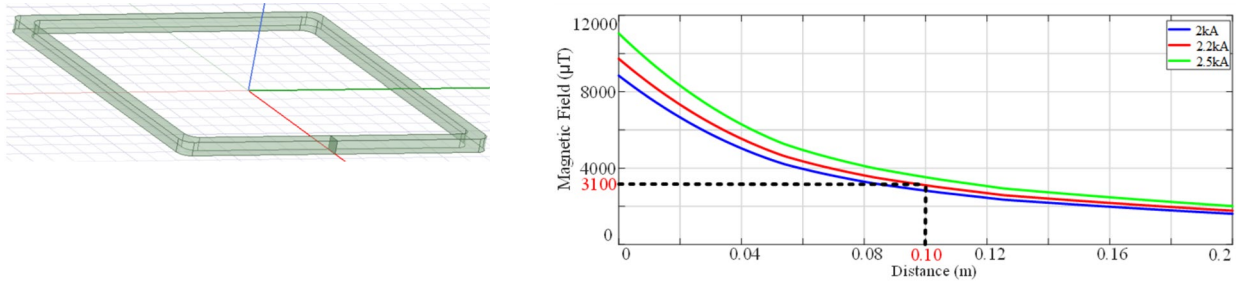
Figure 2-33. Experimental testing of MAVIC 2 battery voltage, capacity, and SoC when it flies over the top of a solenoid coil with various excitation currents.

the solenoid coil. The results show that the rate of battery exhaustion is the same at different

magnetic field strengths. The offset between curves is due to the slight difference in the initial voltage of the battery after it is charged.

### 2.3.3 *Mavic 2 testing in 2.2-kA planar coil*

Mavic 2 is further tested within the 2.2-kA planar coil environment. The coil length is 1.7 meters, which provides sufficient space for the UAS to have a continuous flight with relatively complex actions. The field strength around the planar coil is specified in Figure 2-35.



(a) Planar coil structure

(b) Magnetic field strength versus the distance to planar coil

Figure 2-34. Maxwell-simulated magnetic field strength of a 1.7-meter planar coil with 2.2-kA excitation current to generate a large area of magnetic field for UAS testing.

In Figure 2-35, the magnetic field strength versus the distance to the planar coil is provided. For example, when the UAS flies to 0.1m around the planar coil, the field strength can reach 3100  $\mu\text{T}$ , which is even higher than the solenoid coil in Figure 2-24. It is because this planar coil structure can create a strong field at proximity to its wire, and the solenoid coil field concentrates more inside its cylinder structure.

Using this planar coil, the test platform for the Mavic 2 UAS is shown in Figure 2-36 which shows the planar coil installed on a fixture that is 1.7 meters above ground level. All the equipment and power supply are arranged far from the coil to avoid any influence. The UAS has flexibility to move in a large area to test the acceleration and gyroscope functions. It is also convenient to test the approaching and leaving process of the UAS in the magnetic field. The coil is well insulated. During experiments, the UAS can even land on the coil to study the impact of very strong magnetic fields.

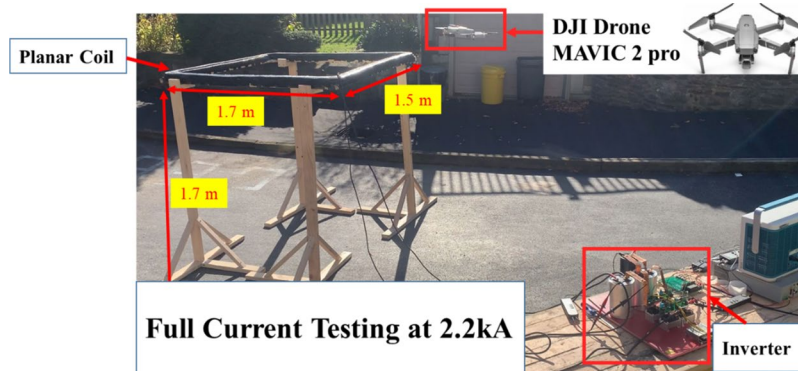
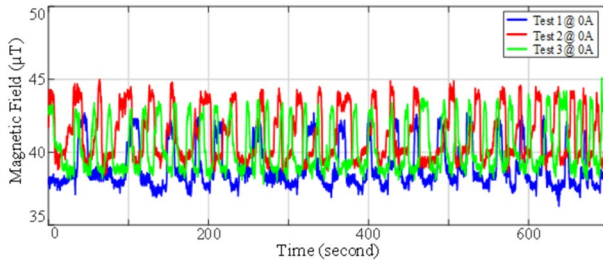


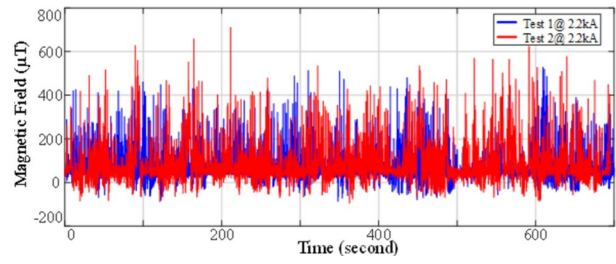
Figure 2-35. Experimental setup of Mavic 2 testing in 2.2-kA planar coil environment that can generate 60 Hz ac magnetic field up to 3100  $\mu\text{T}$  at 0.1m proximity.

### 2.3.3.1 Magnetometer of Mavic 2 in 2.2-kA planar coil

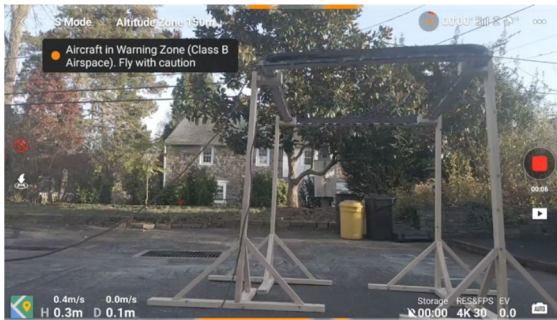
Mavic 2 flies along this planar coil, and the magnetometer signal is shown in Figure 2-37.



(a) Measured magnetic field at 0A excitation



(b) Measured magnetic field at 2.2-kA excitation



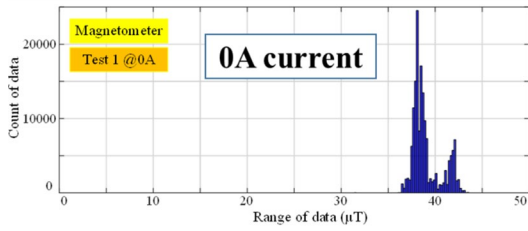
(c) Onboard video recording with no warning at the take-off stage with 2.2-kA excitation



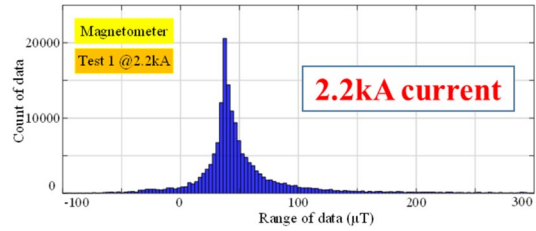
(d) Onboard video recording with the compass failure warning at near position with 2.2-kA excitation

Figure 2-36. Experimental testing of Mavic 2 magnetometer signals when it flies along a planar coil with 2.2-kA excitation current.

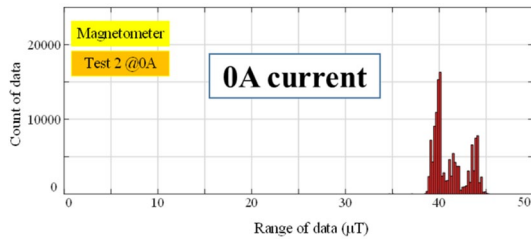
When there is no excitation current, the magnetometer measures the ambient field of the earth; any variation is within the tolerance range. At 2.2-kA excitation current, the field is very high, and the UAS also reports a compass failure. Figure 2-38 shows the measured data in the statistical domain. Statistical domain data is used for various reasons in research, analysis, and decision-making processes. This domain allows effective analysis and interpretation of information. By using statistical methods, patterns, trends, and relationships within the data can be analyzed which leads to meaningful insights. This domain also enables meaningful inferences and generalizations of findings to larger populations or datasets. This approach leads to conclusions beyond the specific data sample and predictions about broader scenarios. The count of data unit in the next figures illustrates the distribution of data during the tests.



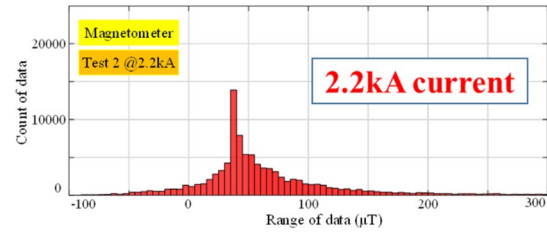
(a) Statistic of magnetometer at 0A current Test 1



(b) Statistic of magnetometer at 2.2 kA current Test 1



(c) Statistic of magnetometer at 0A current Test 2



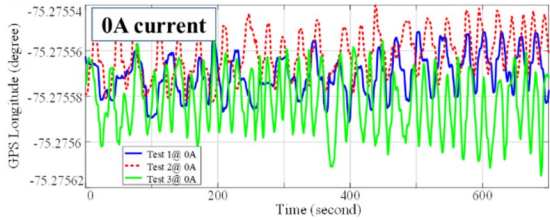
(d) Statistic of magnetometer at 2.2 kA current Test 2

Figure 2-37. Experimental testing of MAVIC 2 magnetometer signals when it flies along a planar coil, comparing with and without 2.2-kA excitation current.

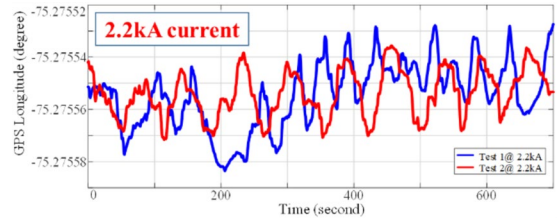
When the excitation current is zero, the magnetic field concentrates around 40  $\mu\text{T}$ , which is consistent with Figure 2-37(a). As the excitation current reaches 2.2 kA, there is a significant increase in noise observed in measured data. This surge in noise suggests that both the magnetometer and the digital and analog filters utilized in the UAS encounter some concerning issues in producing accurate readings. As a result, the controller section of the drone interprets this situation as a need to recalibrate the magnetometer to attain reasonable and reliable values once again. Although Figure 2-38(b) and Figure 2-38(d) represent two different tests, the shape of statistic data is very similar, which validate the impact of magnetic field on magnetometer measurements.

### 2.3.3.2 GPS of Mavic 2 in 2.2-kA planar coil

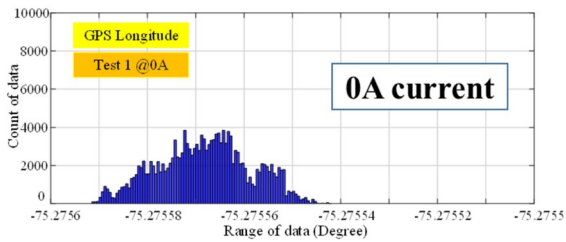
The GPS longitude signals are measured and shown in Figure 2-39. In the time domain, Figure 2-39(a) shows that three measurements at 0 A excitation align well with each other. Figure 2-39(b) shows that two measurements at 2.2-kA excitation also match well. Figure 2-39(c)-(f) provides the statistical domain insight of the measured results. The data distribution is also consistent at different excitation current magnitudes, which shows that the GPS longitude signal is not sensitive to external 60 Hz ac magnetic field.



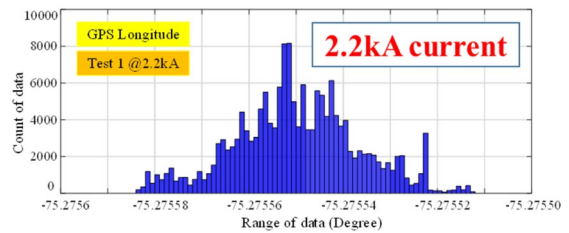
(a) GPS longitude at 0A excitation



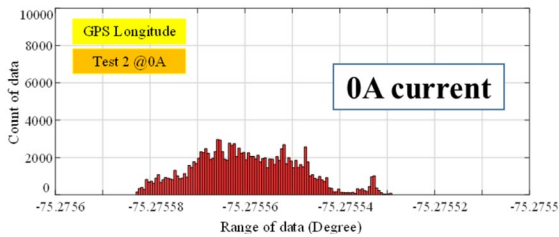
(b) GPS longitude at 2.2-kA excitation



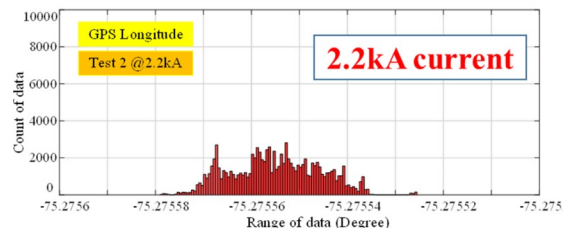
(c) Statistic of GPS longitude at 0A current Test 1



(d) Statistic of GPS longitude at 2.2-kA current Test 1



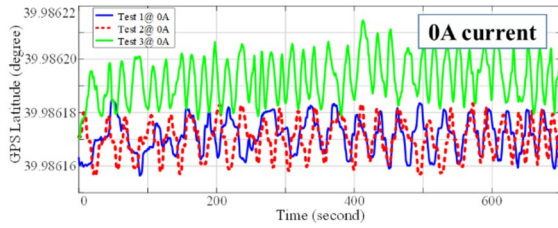
(e) Statistic of GPS longitude at 0A current Test 2



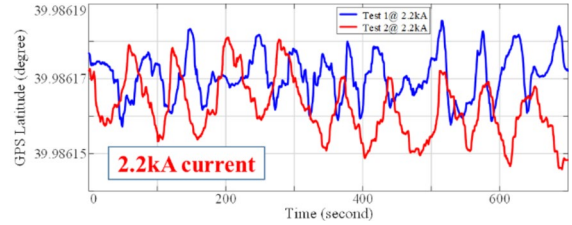
(f) Statistic of GPS longitude at 2.2-kA current Test 2

Figure 2-38. Experimental testing of Mavic 2 GPS longitude signals when it flies along a planar coil, comparing with and without 2.2-kA excitation current.

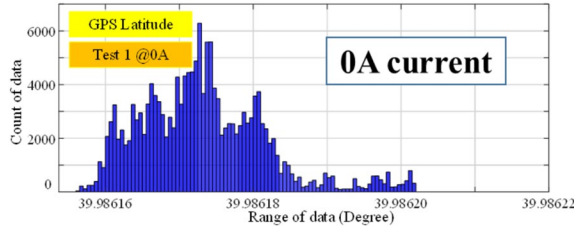
Meanwhile, the GPS latitude signal is also measured and shown in Figure 2-40. The time domain results are presented in Figure 2-40(a) and (b) for both the 0 A and 2.2-kA cases. The statistical domain results are further summarized in Figure 2-40(c)-(f). Similar to the longitude data in Figure 2-39, the comparison in Figure 2-40 shows that the GPS latitude data are not sensitive to magnetic field as well.



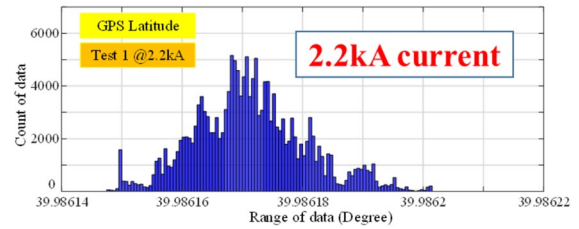
(a) GPS latitude at 0A excitation



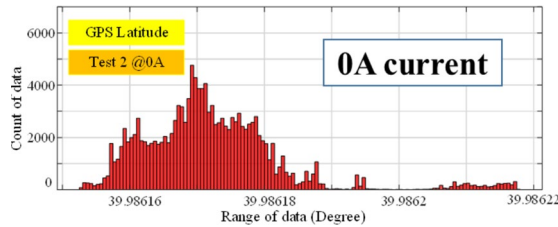
(b) GPS latitude at 2.2-kA excitation



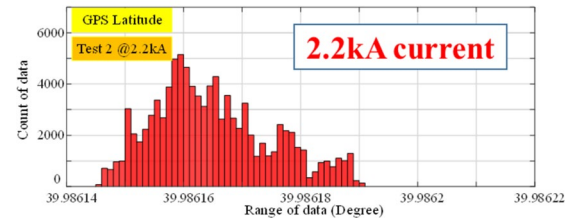
(c)Statistic of GPS latitude at 0A current Test 1



(d) Statistic of GPS latitude at 2.2-kA current Test 1



(e) Statistic of GPS latitude at 0A current Test 2

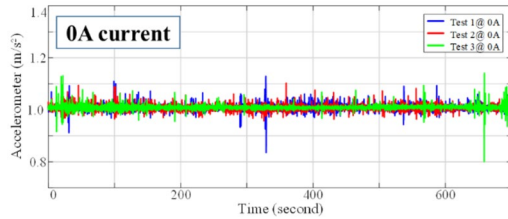


(f) Statistic of GPS latitude at 2.2-kA current Test 2

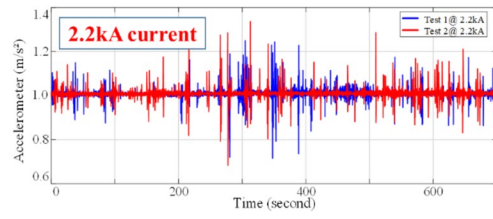
Figure 2-39. Experimental testing of Mavic 2 GPS latitude signals when it flies along a planar coil, comparing with and without 2.2-kA excitation current.

### 2.3.3.3 Accelerometer of Mavic 2 in 2.2-kA planar coil

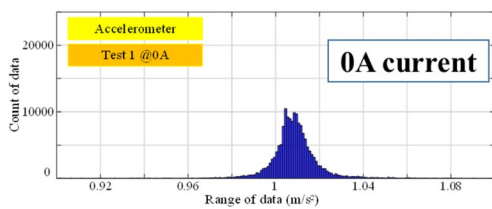
The accelerometer data are measured and compared in Figure 2-41. When the 2.2-kA excitation current is applied, the measured data are not significantly changed. The slight difference in Figure 2-41(a) and Figure 2-41(b) is due to inconsistencies in commands from the human operator during the flying process. The statistical domain results in Figure 2-41(c)-(f) further validate the consistency.



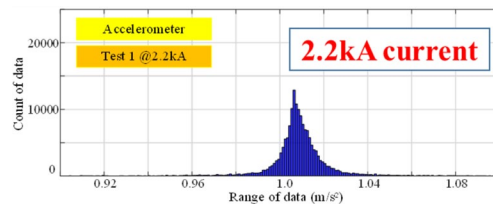
(a) Accelerometer at 0A excitation



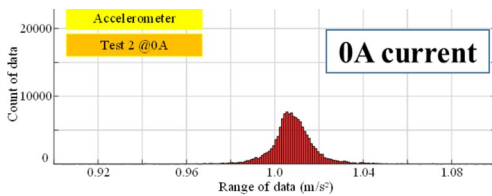
(b) Accelerometer at 2.2-kA excitation



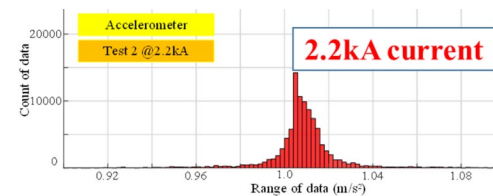
(c) Statistic of accelerometer at 0A current Test 1



(d) Statistic of accelerometer at 2.2-kA current Test 1



(e) Statistic of accelerometer at 0A current Test 2

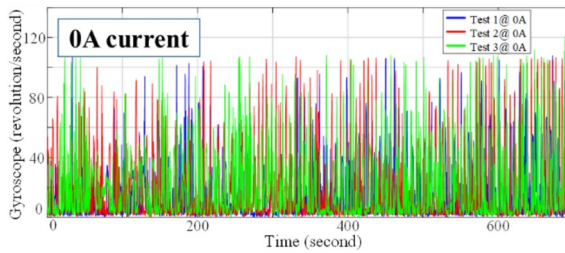


(f) Statistic of accelerometer at 2.2-kA current Test 2

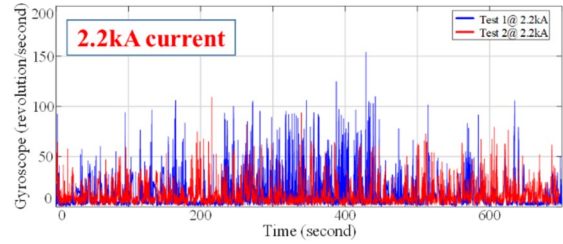
Figure 2-40. Experimental testing of Mavic 2 accelerometer signals when it flies along a planar coil, comparing with and without 2.2-kA excitation current.

### 2.3.3.4 Gyroscope of Mavic 2 in 2.2-kA planar coil

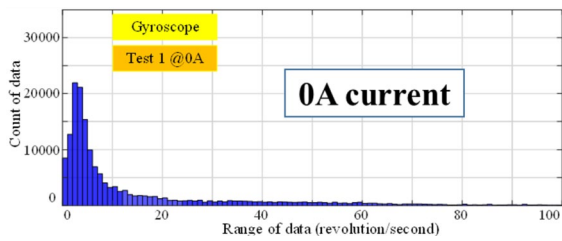
The gyroscope measurement results are presented in Figure 2-42. Similar to previous cases, the gyroscope signals are not affected by the external magnetic field.



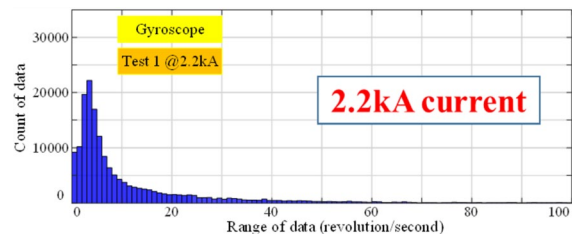
(a) Gyroscope at 0A excitation



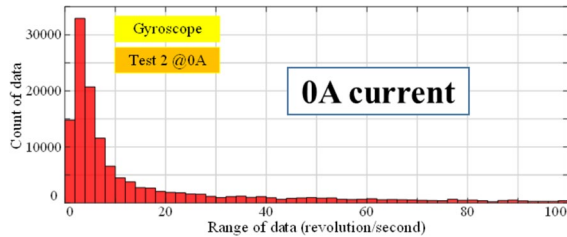
(b) Gyroscope at 2.2-kA excitation



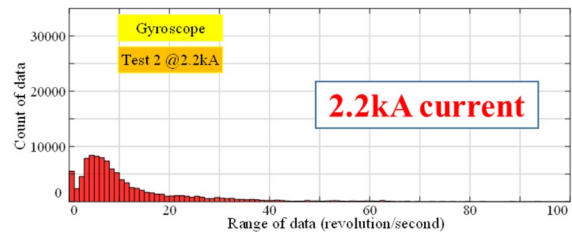
(c) Statistic of gyroscope at 0A current Test 1



(d) Statistic of gyroscope at 2.2-kA current Test 1



(e) Statistic of gyroscope a 0A current Test 2

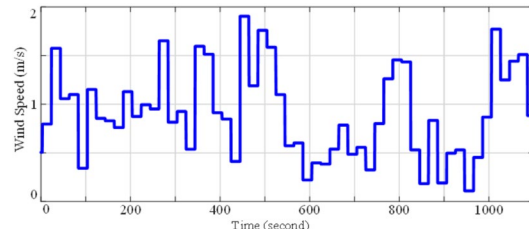


(f) Statistic of gyroscope at 2.2-kA current Test 2

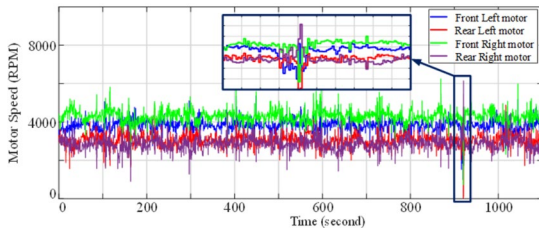
Figure 2-41. Experimental testing of Mavic 2 gyroscope signals when it flies along a planar coil, comparing with and without 2.2-kA excitation current.

### 2.3.3.5 Motor of Mavic 2 in 2.2-kA planar coil

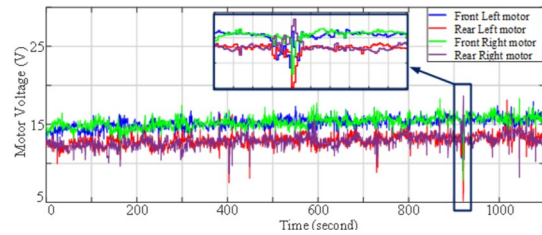
The motor signals are presented in Figure 2-43. In general, these data show that the motor signals are not affected by magnetic field. However, upon careful inspection, there appears to be a sudden drop in the motor speed at around 900 seconds. Further investigation suggests that this drop is seen in the motor voltage, motor current, and motor Pulse Width Modulation (PWM) signals as well. These results suggest that the motor is not under good control during this phase of flight. There is a risk that the motor might stop running and cause a potential crash. Despite this data anomaly, no obvious motion difference in the UAS was observed. In addition, this test was repeated more than 10 times with no similar drop in these signals. Also note here that the wind measurement shown in Figure 2-43(a) suggests that the environmental conditions are normal, and so do not contribute to this observation.



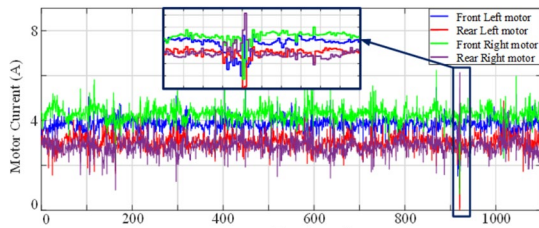
(a) MAVIC 2 measured real-time wind speed



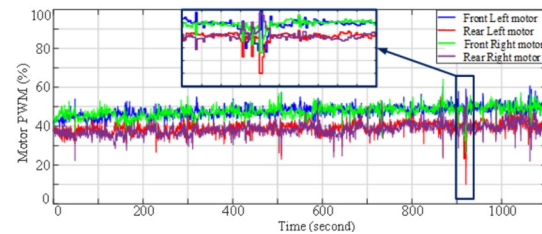
(b) Motor speed at 2.2-kA excitation



(c) Motor voltage at 2.2-kA excitation



(d) Motor current at 2.2-kA excitation



(e) Motor PWM control signal at 2.2-kA excitation

Figure 2-42. Experimental testing of Mavic 2 motor signals when it flies over the top of a planar coil with 2.2-kA excitation current, showing an abnormal spike during the testing process.

### 2.3.3.6 Battery of Mavic 2 in 2.2-kA planar coil

The battery status is monitored as shown in Figure 2-44. The UAS stays close to the planar coil until the battery is exhausted. Comparison of this data shows that the external magnetic field does not affect the exhaustion rate of the battery energy.

### 2.3.4 Discrete sensor testing in 5.25-kA solenoid coil

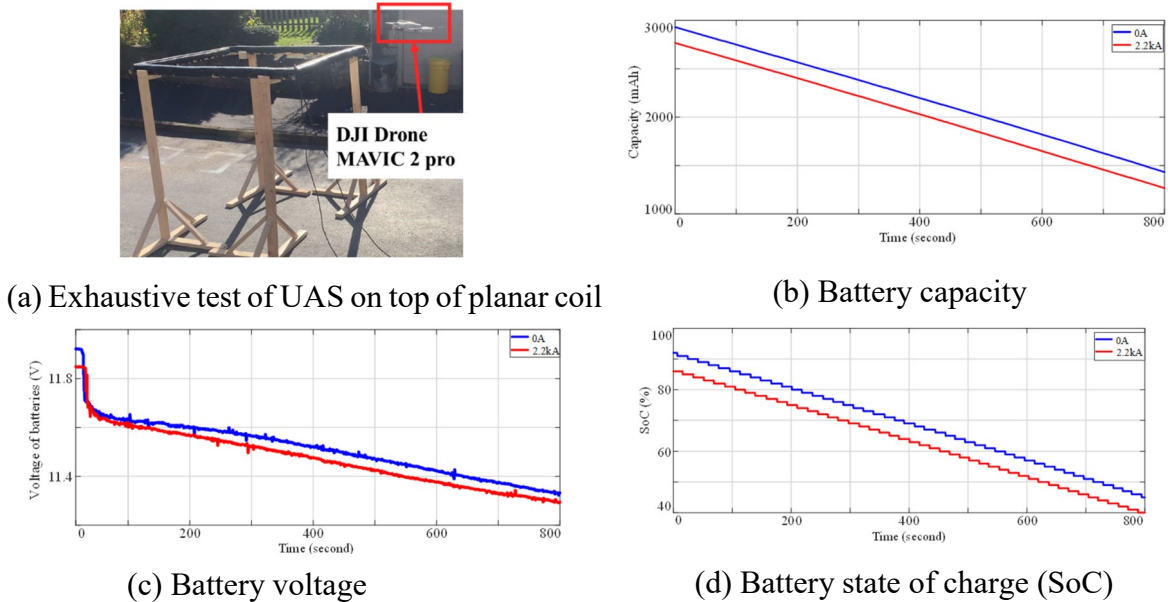


Figure 2-43. Experimental testing of Mavic 2 battery voltage, capacity, and SoC when it flies over the top of a planar coil with and without 2.2-kA excitation current.

In order to test the impact of magnetic field to different sensors, the sensors are placed in the magnetic field generated by a 5.25-kA solenoid coil as shown in Figure 2-45.

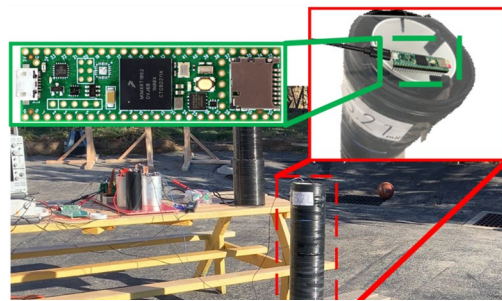


Figure 2-44. Experimental testing platform of discrete sensor board in strong magnetic field generated by a 5.25-kA solenoid coil.

This platform helps to collect the raw data from each sensor. The sensor board implementation is shown in Figure 2-23, including magnetometer, accelerometer, gyroscope, and the microcontroller. Through this test, we can investigate the robustness and capability to withstand 60 Hz ac strong magnetic field. This test is crucial for maintaining accurate and reliable performance during experiments involving strong magnetic field exposure. During the test process, an SD card is integrated with the microcontroller to collect and save the data for further review after the experiment. The SD card capacity is properly selected to ensure continuous saving for at least 20 minutes of operation.

It should be noted that the raw data collected from the sensor board does not have any hardware or software filter integrated. So, these data reflect how the ac magnetic field might adversely impact the sensors. Based on the data, it is also possible to develop potential signal processing methods to improve the data reliability in future research.

#### 2.3.4.1 Magnetometer of discrete sensor in 5.25-kA solenoid coil

The full setup has been tested three times. In test 1, the external current for the solenoid coil is 0

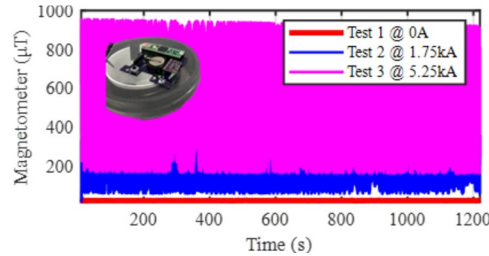


Figure 2-45. Experimental results of magnetometer data in strong magnetic field generated by a solenoid coil.

A, there is no external magnetic field generated, and the sensor board is powered on for 20 minutes. In test 2, the external current is increased to 1.75 kA; the current is further increased to 5.25 kA in test 3. The measured magnetometer results are shown in Figure 2-46 which shows that when the excitation current is zero, the resulting magnetic field is very low and there is no observable noise. When the current is equal to 1.75 kA, the measured magnetic field is around 200  $\mu\text{T}$  with some variation. When the current is equal to 5.25 kA, the measured field approaches 1000  $\mu\text{T}$ . The measured current was not raised beyond this value to avoid damage to the magnetometer sensor. Clearly, a strong external magnetic field can significantly affect the measurement of a magnetometer.

#### 2.3.4.2 Accelerometer of discrete sensor in 5.25-kA solenoid coil

The accelerometer data is collected as shown in Figure 2-47. When the excitation current varies widely, the raw data from the accelerometer is not affected. Figure 2-47 only provide the z-axis

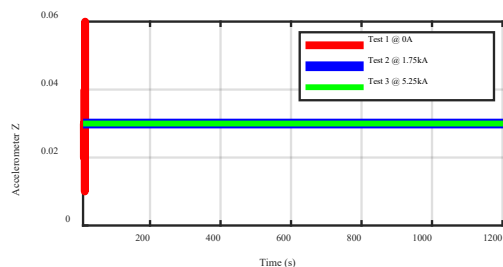


Figure 2-46. Experimental results of accelerometer data in strong magnetic field generated by a solenoid coil.

measurement. The x and y axis measurements are similar, though not shown here. The slight offset in this figure is because the raw data has not been processed to identify the acceleration in both directions.

#### 2.3.4.3 Gyroscope of discrete sensor in 5.25-kA solenoid coil

The gyroscope measured raw data is presented in Figure 2-48. The three axis measurements are similar, and only the x axis result is presented as an example. Since the sensor board is unmoving

in the magnetic field, the gyroscope measure stays at zero. When the current increases to 5.25 kA, the measurement does not change, which validates that the magnetic field cannot affect this

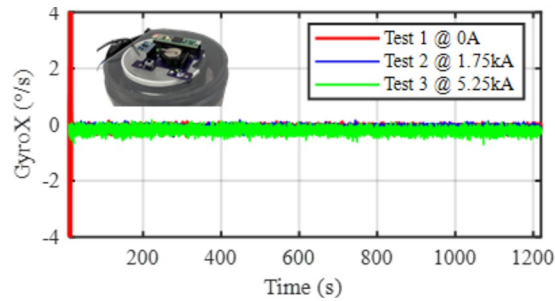


Figure 2-47. Experimental results of gyroscope data in strong magnetic field generated by a solenoid coil.

gyroscope sensor.

### 2.3.5 *Mavic 3 carries discrete sensor testing in 2.2-kA planar coil*

In this test, the sensor circuit board is mounted on Mavic 3 UAS as a payload, and the UAS carries the discrete sensors to fly around the 2.2-kA planar coil as shown in Figure 2-49.

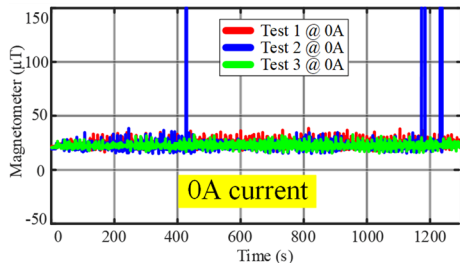


Figure 2-48. Experimental setup of Mavic 3 with a sensor board payload testing in 2.2-kA planar coil environment that can generate 60 Hz ac magnetic field.

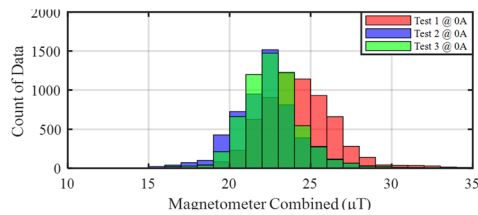
Mavic 3 is a more advanced UAS that can provide professional level inspection and monitoring capabilities. This UAS also has a mechanical structure that can affix an additional circuit board on top. The battery can support longer operating time than the previous Mavic 2 UAS. The external circuit board also has an onboard lithium-ion battery to supply power to sensors, which does not require any power from the UAS. Since the circuit board is very light weight, it does not affect normal flight of the UAS.

### 2.3.5.1 Magnetometer of discrete sensor in 2.2-kA planar coil

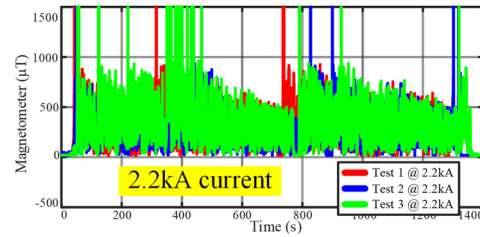
When the UAS moves along the planar coil, the magnetometer on the external circuit board is used to measure the magnetic field, with measured results shown in Figure 2-50. When the excitation current is 0 A, the field strength is low and stable. There are some spikes that are due to measurement noise. As this sensor provides the raw data, there is no built-in filter to smooth the measurement. When the excitation current is 2.2 kA, the field strength significantly increases with a corresponding increase in noise. As expected, the measurement of the magnetometer is strongly impacted by the presence of an external magnetic field.



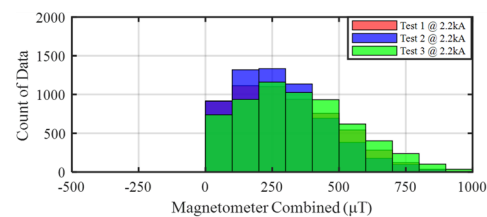
(a) Magnetometer at 0A excitation



(c) Statistic of magnetometer at 0A current



(b) Magnetometer at 2.2-kA excitation

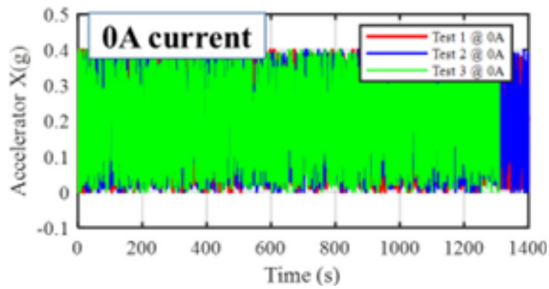


(d) Statistic of magnetometer at 2.2-kA excitation

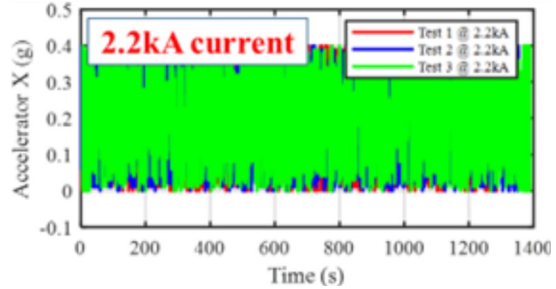
Figure 2-49. Experimental testing of magnetometer signal in a discrete sensor when it is mounted on Mavic 3 and flies along a planar coil, comparing with and without 2.2-kA excitation current.

### 2.3.5.2 Accelerometer of discrete sensor in 2.2-kA planar coil

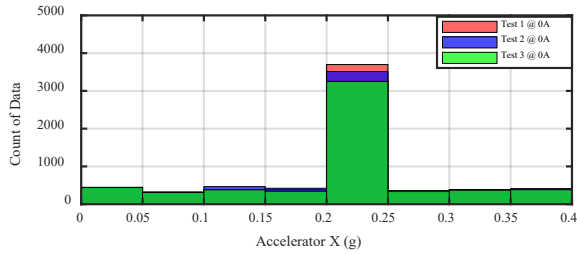
The measurement result of the accelerometer on an external circuit board is shown in Figure 2-51. The accelerometer can measure x, y, and z directions. The measurements are similar, so only the x-direction result is presented here. The results of the accelerometer measurement do not vary with changes to external field strength.



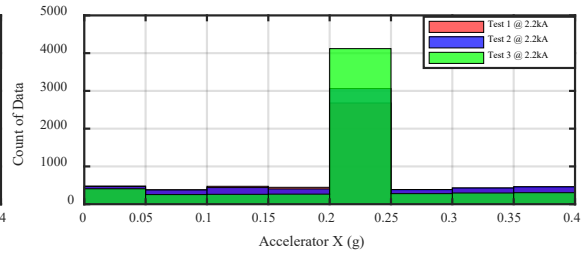
(a) Accelerometer x-axis at 0A excitation



(b) Accelerometer x-axis at 2.2-kA excitation



(c) Statistic of accelerometer x-axis at 0A current

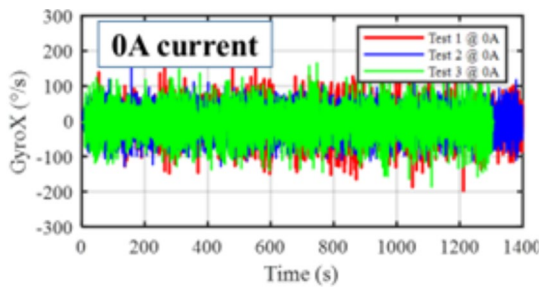


(d) Statistic of accelerometer x-axis at 2.2-kA current

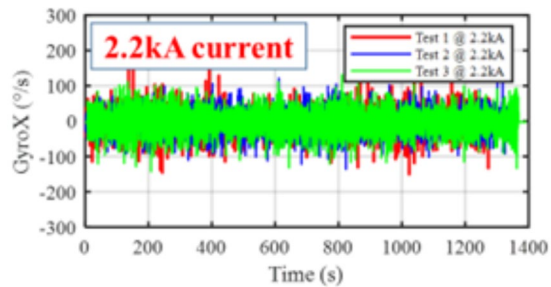
Figure 2-50. Experimental testing of accelerometer x-axis signal in a discrete sensor when it is mounted on Mavic 3 and flies along a planar coil, comparing with and without 2.2-kA excitation current.

### 2.3.5.3 Gyroscope of discrete sensor in 2.2-kA planar coil

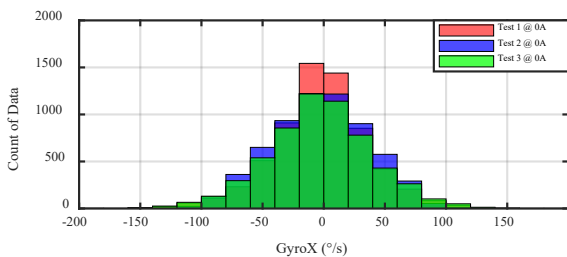
The gyroscope measurement from the discrete sensor is shown in Figure 2-52. The x-axis data is presented as representative of all outputs of the gyroscope. As previously noted, the measurement of the gyroscope is not impacted by significant variations in the external magnetic field.



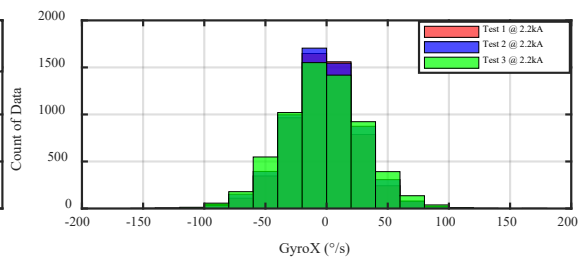
(a) Gyroscope x-axis at 0A excitation



(b) Gyroscope x-axis at 2.2-kA excitation



(c) Statistic of gyroscope x-axis at 0A current



(d) Statistic of gyroscope x-axis at 2.2-kA excitation

Figure 2-51. Experimental testing of gyroscope x-axis signal in a discrete sensor when it is mounted on Mavic 3 and flies along a planar coil, comparing with and without 2.2-kA excitation current.

### 2.3.5.4 GPS altitude of Mavic 3 in 2.2-kA planar coil

Mavic 3 is more advanced, and it can provide the GPS altitude data as shown in Figure 2-53. No significant impact is observed on GPS altitude from a large externally applied magnetic field.

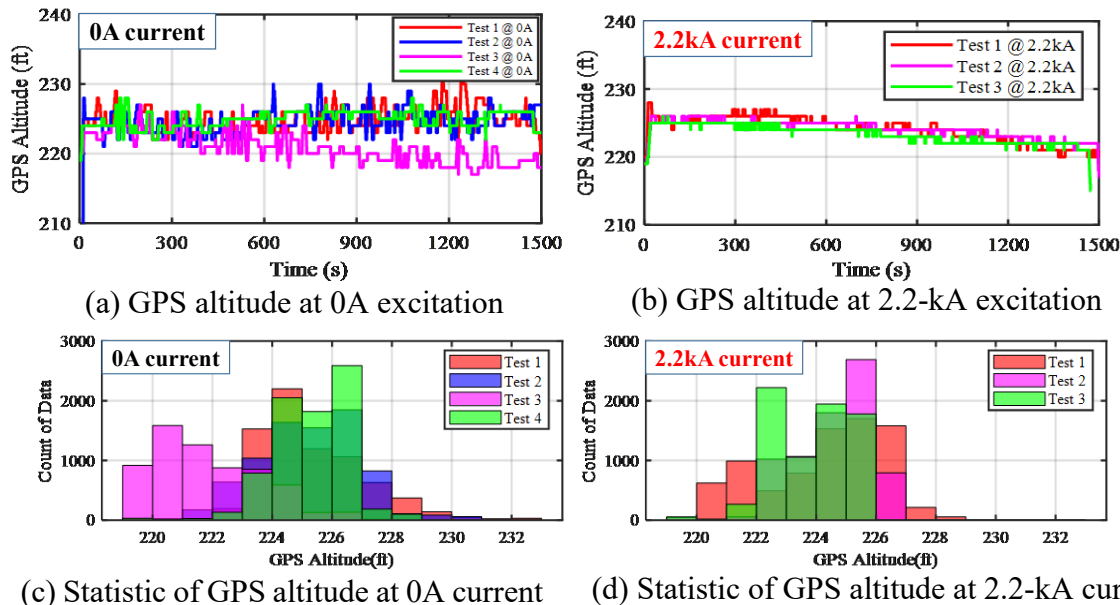


Figure 2-52. Experimental testing of GPS altitude signal in Mavic 3 when it flies along a planar coil, comparing with and without 2.2-kA excitation current.

### 2.3.5.5 Gyroscope of Mavic 3 in 2.2-kA planar coil

The gyroscope measurement from Mavic 3 is shown in Figure 2-54. The pitch angle data is presented as representative of all gyroscope parameters. As before, no noticeable adverse impacts are seen in gyroscope performance as a consequence of an externally applied magnetic field.

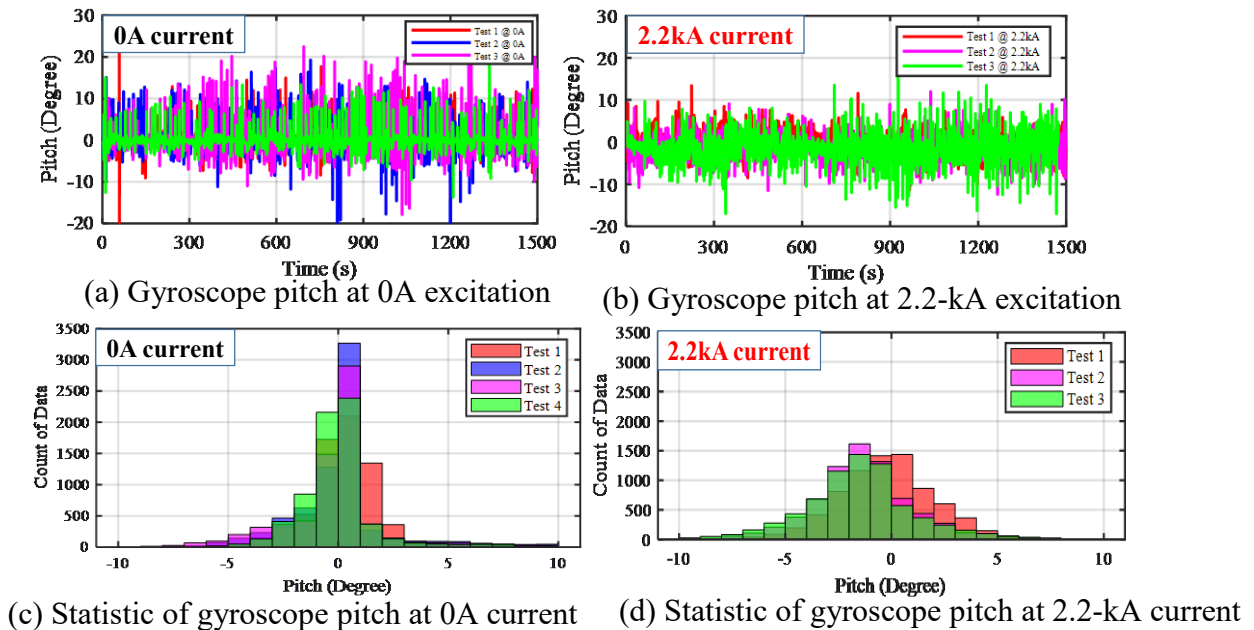


Figure 2-53. Experimental testing of gyroscope pitch signal in Mavic 3 when it flies along a planar coil, comparing with and without 2.2-kA excitation current.

### 2.3.5.6 Battery of Mavic 3 in 2.2-kA planar coil

Mavic 3 can also provide the battery data as shown in Figure 2-55. As before, battery performance is not impacted by large external magnetic fields..

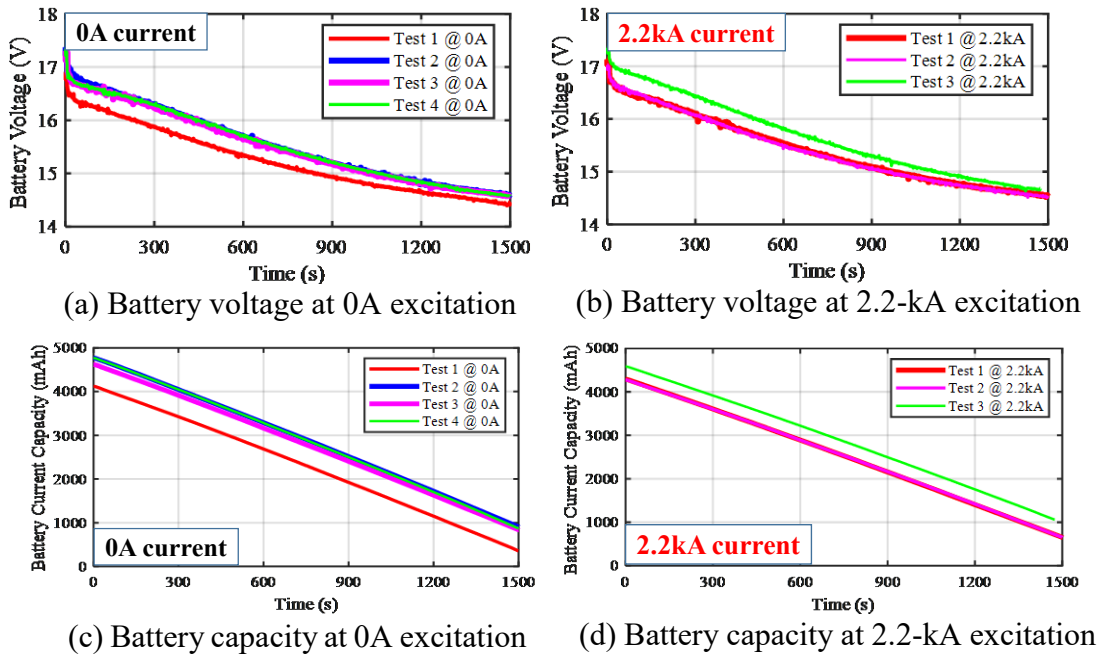


Figure 2-54. Experimental testing of battery status signal in Mavic 3 when it flies along a planar coil, comparing with and without 2.2-kA excitation current.

## 2.4 Lab-based electric field testing

### 2.4.1 Electric field testing prototype design and construction

In the lab environment, the electric field impact is also tested. The experimental testing platform is shown in Figure 2-56.

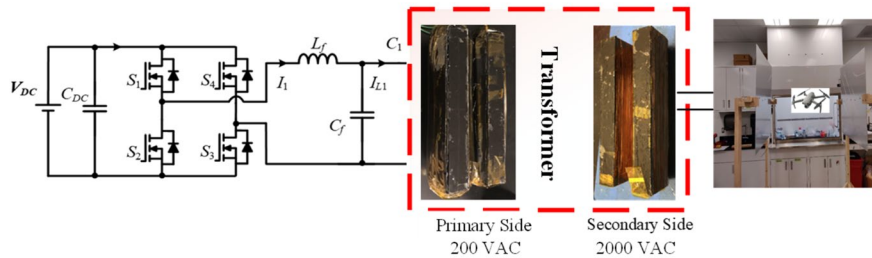


Figure 2-55. Experimental setup to generate high voltage electric field for UAS testing. The applied voltage can reach 2000 V through a step-up transformer.

The inverter provides 200 V ac input voltage to a transformer, which is used to step up the voltage to 2000 V. This high voltage is applied on two parallel aluminum plates to generate a uniform electric field. The UAS can fly in the space between two plates.

The transformer design is critical, which is shown in Figure 2-57. The magnetic core from Hitachi is used to build the transformer core. This product has the benefit of high saturation that can support high voltage conversion. Considering that the maximum current induced in this wire is below 1A, American Wire Gauge (AWG) 30 wire is appropriate to form the transformer windings. Meanwhile, the insulation between windings and magnetic core should be paid extra attention to withstand the high voltage inside this transformer.

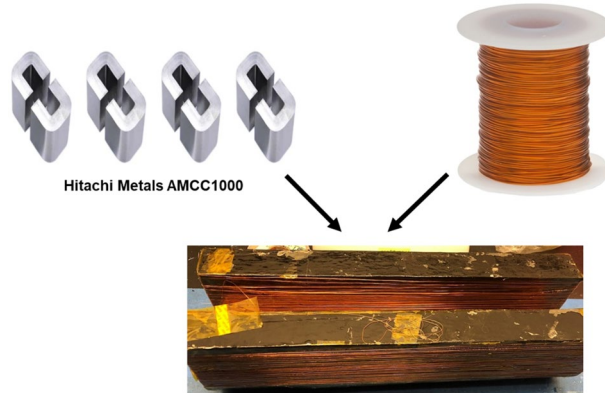


Figure 2-56. Implemented high voltage transformer to generate 2000 V AC voltage to be applied on the metal plates, including key magnetic core and windings.

#### 2.4.2 Mavic 2 testing in 2 kV/m electric field

The Mavic 2 UAS is tested in the generated electric field as shown in Figure 2-58.

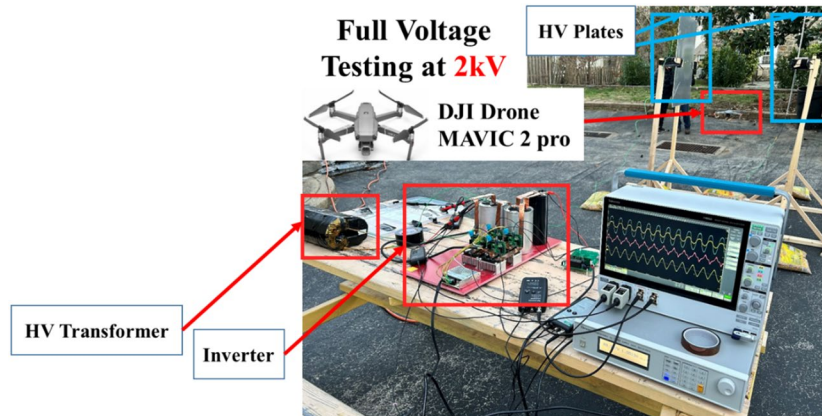
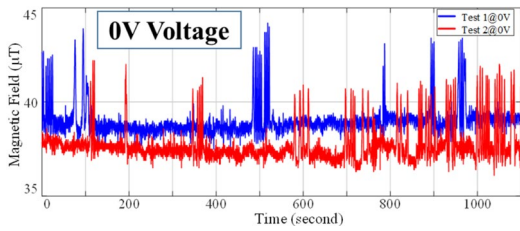


Figure 2-57. Experimental setup of high voltage electric field testing of Mavic 2. The field strength can reach 2 kV/m between the plates where the UAS is flying.

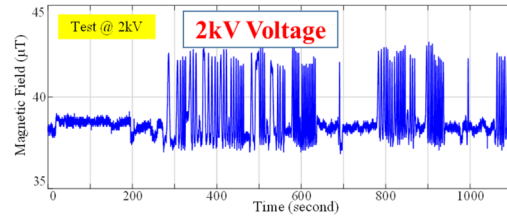
The distance between two parallel plates is about 1 meter, creating a field strength of 2 kV/m for the UAS to fly. The testing equipment is far from the electric field to mitigate any potential impact on the electronic devices. During the testing process, the flight data is recorded by Mavic 2, which is presented as follows.

##### 2.4.2.1 Magnetometer of Mavic 2 in 2 kV/m electric field

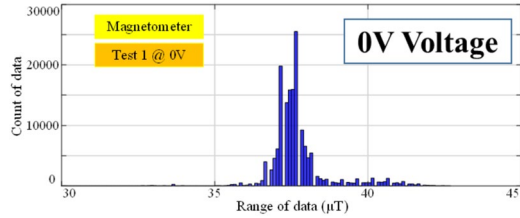
The magnetometer measurement results are shown in Figure 2-59.



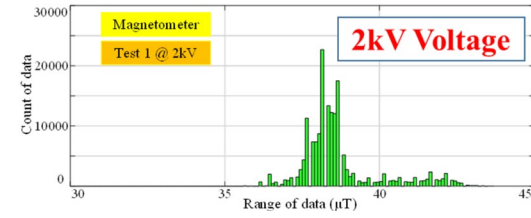
(a) Magnetometer at 0V excitation



(b) Magnetometer at 2 kV excitation



(c) Statistic of magnetometer at 0V excitation



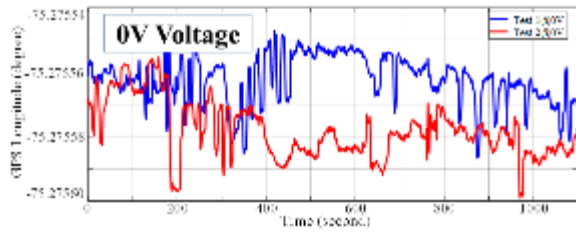
(d) Statistic of magnetometer at 2 kV excitation

Figure 2-58. Experimental testing of Mavic 2 magnetometer signals when it flies between two aluminum plates with 2 kV/m electric field strength.

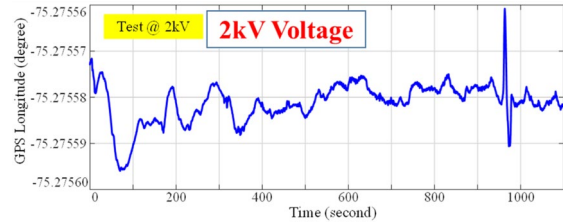
In Figure 2-59(a) and (c), the excitation voltage is zero. Two tests are conducted as a baseline for comparison. From these plots, the background magnetic field strength is around 40  $\mu\text{T}$ , which is consistent with the field of the earth. There are some offsets between the two tests as well as some ripple in both tests, which are mainly caused by the measurement tolerance. Figure 2-59(b) and (d) show the test results when the excitation voltage increases to 2 kV. The magnetometer measurement is not affected by the electric field. It is still close to 40  $\mu\text{T}$  with some ripples as expected.

#### 2.4.2.2 GPS of Mavic 2 in 2 kV/m electric field

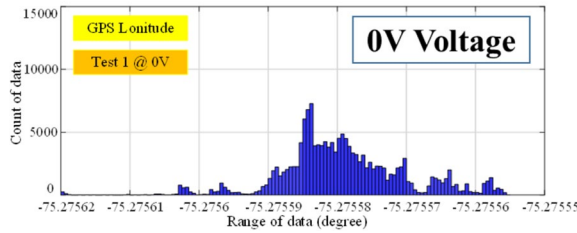
The GPS signals are also measured in electric field, and the results are shown in Figure 2-60. Both the time domain and statistical domain data are presented to illustrate the similarity and differences. This data shows that, in both the longitude and latitude directions, the electric field has no impact to the GPS signals.



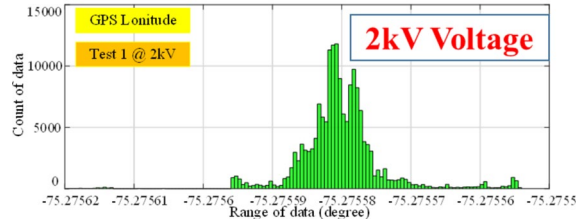
(a) GPS longitude at 0V excitation



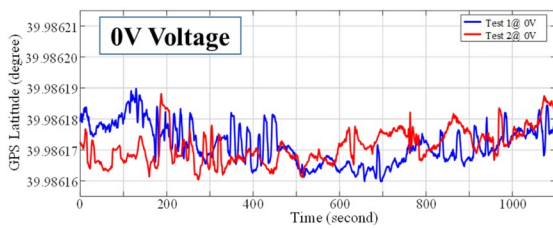
(b) GPS longitude at 2 kV excitation



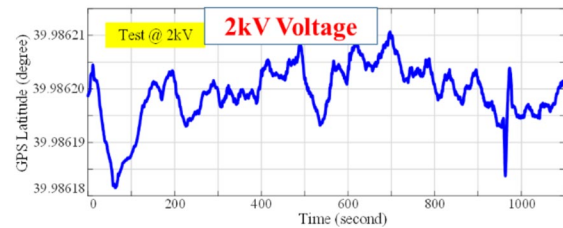
(c) Statistic of GPS longitude at 0V excitation



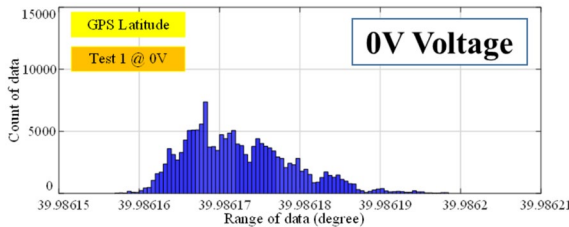
(d) Statistic of GPS longitude at 2 kV excitation



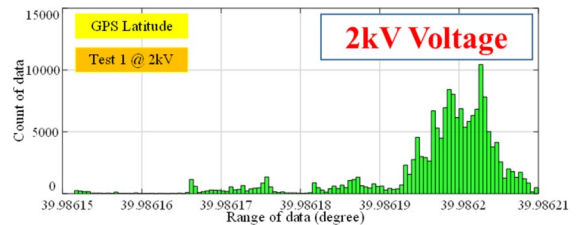
(e) GPS latitude at 0V excitation



(f) GPS latitude at 2kV excitation



(g) Statistic of GPS latitude at 0V excitation

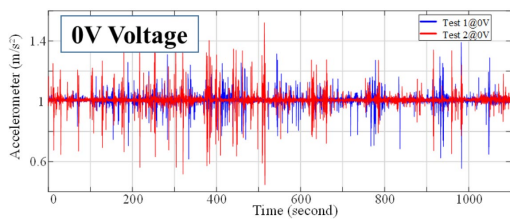


(h) Statistic of GPS latitude at 2 kV excitation

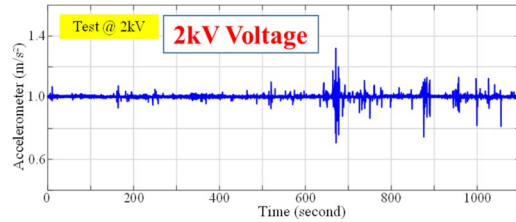
Figure 2-59. Experimental testing of Mavic 2 GPS signals when it flies between two aluminum plates with 2 kV/m electric field strength.

### 2.4.2.3 Accelerometer of Mavic 2 in 2 kV/m electric field

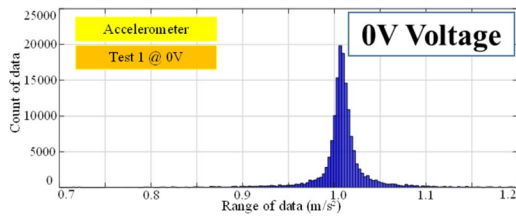
The accelerometer data is shown in Figure 2-61. The slight difference in Figure 2-61(a) and (b) is caused by human operator command variations. The statistical domain comparison in Figure 2-61(c) and (d) further demonstrates that the electric field has no impact on accelerometer measurement.



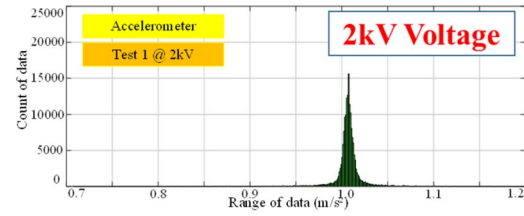
(a) Accelerometer at 0V excitation



(b) Accelerometer at 2kV excitation



(c) Statistic of accelerometer at 0V excitation

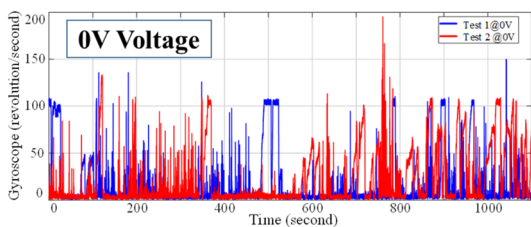


(d) Statistic of accelerometer at 2kV excitation

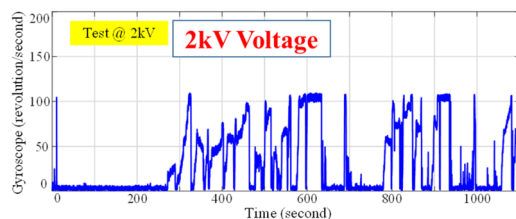
Figure 2-60. Experimental testing of Mavic 2 accelerometer signals when it flies between two aluminum plates with 2 kV/m electric field strength.

#### 2.4.2.4 Gyroscope of Mavic 2 in 2 kV/m electric field

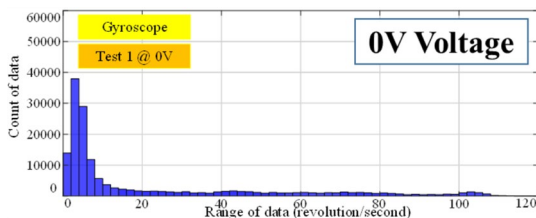
Similarly, Figure 2-62 shows the test results of the gyroscope in electric field, which validates that the electric field does not affect gyroscope measurement.



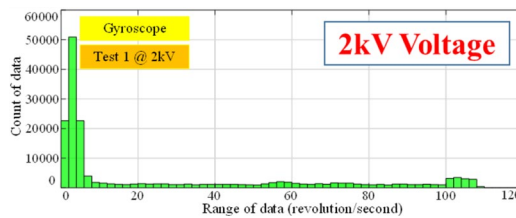
(a) Accelerometer at 0V excitation



(b) Accelerometer at 2kV excitation



(c) Statistic of accelerometer at 0V excitation



(d) Statistic of accelerometer at 2kV excitation

Figure 2-61. Experimental testing of Mavic 2 accelerometer signals when it flies between two aluminum plates with 2 kV/m electric field strength.

### 3 CYBER SECURITY; STATIC & LOW FREQUENCY FLIGHT TEST

#### 3.1 State-of-the-art summary

The team has captured the state-of-the-art work on sources of electric and magnetic field strengths and its impact on UAS under three categories: System, Environmental and Cyber Security related themes. See Figure 3-1. The former two categories can be considered as unintentional sources of interference, while the latter addresses intentional sources of interference.

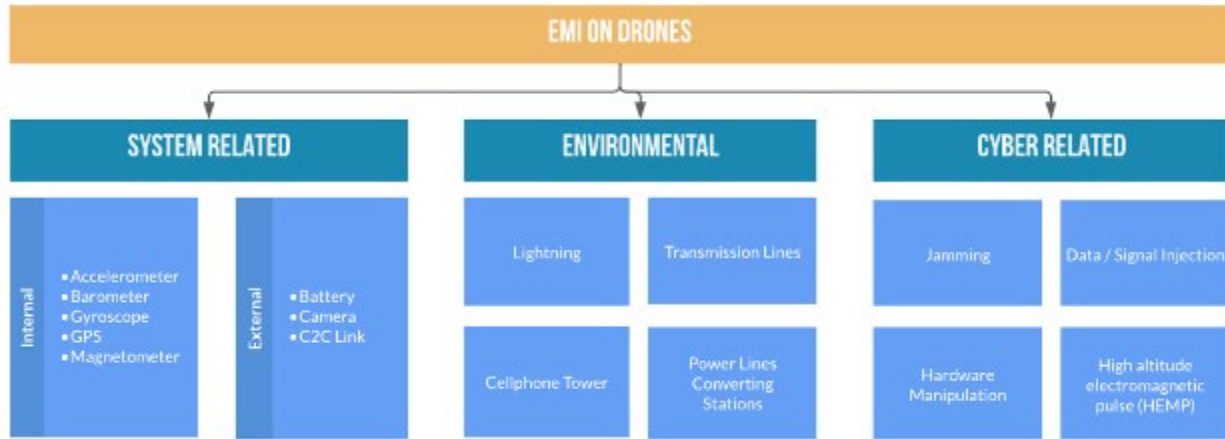


Figure 3-1. EMI categories based on system-related, environmental, and cyber causes.

##### 3.1.1 System

UAS often employ an IMU consisting typically of 1) gyroscope; 2) accelerometer; and 3) magnetometer to help determine the position in space and its orientation. Some difficulties in using IMU sensors for position determination are similar to those experienced in orientation determination. However, while position finding can rely at least in part on the GPS, orientation, often referred to as attitude and heading, can't be determined using GPS at least for relatively small aircraft. A brief overview below describes some general features and difficulties in the navigation based on IMU using orientation determination as an example. Similar difficulties exist in using IMU for position finding.

Electromagnetic interference (EMI) is a form of radiation that covers the electromagnetic spectrum and is comprised of alternating electrical and magnetic fields. EMI is distinct from RFI as the latter is produced by frequencies in the radio spectrum and comprises of a portion of the electromagnetic spectrum. Depending on the application, radio frequencies used for communication will vary from magnitudes of a few kHz to larger GHz [7]. EMI can be produced intentionally by malicious threat actors (i.e., intentional EMI) or by external factors (i.e., unintentional EMI). This report classifies unintentional sources of EMI under system-related and environmental factors and intentional sources of EMI from cyber threats.

Because of the limited space available, it can be difficult to design and operate a UAS for a variety of tasks. The carrier is more susceptible to electromagnetic compatibility concerns due to the physical proximity of the onboard components. UAS electronic systems causing inadvertent interference are a major issue because they occur within the navigation bands. The electromagnetic interference caused by onboard components is discussed in a later section.

### 3.1.1.1 Internal Components

Barometer & Magnetometer Sensor: Lavau et al. [8] quantified the susceptibility of these sensors within certain limits set by IEC 61000-4-20 by connecting the barometer and magnetometer sensors to the same microprocessor and enclosing them in an open TEM (Transverse Electric and Magnetic) cell. Because the TEM waveguide can only illuminate one electromagnetic field polarization, the DUT must be rotated to investigate others. Continuous Wave signals with a frequency range of 10 MHz–7.5 GHz were transmitted with a one-second interval and a step size of 10 MHz and gradually incremented. The RF source was turned off for about five seconds to observe the behavior of these sensors under EMI exposure as well as comparison with normal conditions. The magnetometer sensor was affected by EMI signals that operate over the range of 300–500 MHz, according to the findings. The temperature readings from the barometer sensor were incorrect at various frequencies, while the pressure displayed similar behavior with small variations at the same frequencies [9]. The summary of frequency ranges affected are listed Table 3-1.

Table 3-1. Barometer and magnetometer sensors affected ranges and field strengths.

Sensor	Frequency Range (in MHz)	Field Strength (V/m)
<b>Barometer</b>	500	80
	800-1200	160
	2500-2800	100
	5600-6500	100
	7200-7400	100
<b>Magnetometer</b>	300-500	50
	1800-1900	300

Accelerometer & Gyroscope Sensor: The accelerometer can estimate the tilt by measuring the direction of gravity relative to the sensor (pitch and roll). A gyroscope, on the other hand, keeps the UAS balanced by measuring the rate of rotation. Gyroscopes are mechanical devices in which a mounted wheel spins on an axis that can move in any direction. They are used to keep a reference point or provide stability. The interference susceptibility of two sensors (accelerometer and gyroscope) was investigated. In an FCC-TEM-JM1 cell [10], an Arduino board (GY-521) with MPU6050 (3-axis accelerometer and 3-axis gyroscope) was set up. The sensor and Arduino board were both reset before the measurement. After 15 minutes, the signal generator is turned on, with a 10 dBm output and a sine wave of the selected frequency between 5 MHz and 1 GHz.

In the frequency range between 280 MHz and 330 MHz, an occasional failure occurred during the establishing of data communication (i.e., missing Acknowledgement bit (ACK bit) where sensors do not reach to Inter-Integrated Circuit (I2C) communication). In the same frequency range, the Arduino got crashed occasionally [11].

GPS Sensor: The GPS module is one of several that aid in the transmission of position and altitude data, both of which are necessary for the UAS to function properly. Because the GPS module is more sensitive, a lower electro-static discharge (ESD) voltage interference could cause the GPS module to fail or even be damaged. Induced EMI is one of the side effects of an ESD. Data errors,

and temporary resets can be caused by ESD-induced EMI in the presence of mission critical equipment.

Electromagnetic Interference (EMI) arises from various sources, including lightning, radio transmitters, and radar systems, causing disruptions on electronic devices and systems through electromagnetic fields. EMI can be classified into radiated EMI (propagation of unguided electromagnetic waves) and conducted EMI (transmission through wires and cables). Electrostatic Discharge (ESD) involves a sudden flow of electric current between objects with different potentials and poses a threat to sensitive electronic components in Unmanned Aircraft Systems (UAS) and other applications [12]. ESD testing and protective measures, such as grounding and shielding, are essential to mitigate risks. Additionally, ESD events can generate radiated fields that may contribute to EMI impacts to nearby electronic sensors and systems. Addressing both EMI and ESD concerns is vital to ensure reliable and optimal performance of electronic equipment in diverse settings.

The experiment was carried out in a shielded room with a GPS receiving antenna on the outside and a GPS transmitting antenna on the inside, with the GPS enhanced transmitting device having a GPS receiving antenna on the outside and a GPS transmitting antenna on the inside. The first GPS receiving antenna receives GPS signals, while the second GPS transmitting antenna sends them out, and the two antennas are connected by Sub-Miniature version A (SMA) coaxial cables. This method boosts the GPS signal's strength in the shielded room. The GPS module (uBlox - NEO-M8N chip) and propeller blades are removed from the UAS and placed on a rubber table. An ESD simulator model NSG437 was used to simulate the actual electrostatic discharge. The charge on the GPS module decays to less than 10% of the peak value when the discharge mode and number of discharges are set to repeat discharge and 10 times, respectively, and the discharge interval is greater than 1 second [13].

Another experiment was carried out with three GPS module chips chosen and given the numbers 1519, 6248, and 6656, respectively. The ESD Generator was set to repeat mode, with the discharge interval set to 1s and the number of discharges set to 10, and it was discovered that the ESD threshold of the GPS module is below 3500V for the Chip #1519. The ESD threshold of the GPS module is around 3200V, according to chips #6248 and #6656. The UAS system behaves abnormally when exposed to a 3100V electrostatic discharge voltage [13].

Kai He and colleagues [14] conducted a series of immunity tests on GPS modules using the Bulk Current Injection (BCI) method bounded by the test environment. According to ISO 11452-4 and IEC 62132-3, BCI tests should be conducted in a shielding room with the UAS remaining stationary. The GPS module (uBlox - NEO-M8N chip) was tested according to the IEC 62132-3 standards and the results show that the GPS positioning module is sensitive in the 450MHz to 800MHz range [14].

### **3.1.1.2 External Components**

**Battery:** UAS batteries are responsible for the operation and have a significant impact on their overall performance because some of the functions performed by a UAS requires a lot of energy. As a result, UAS batteries are just as important as the UAS build and capabilities. The two most common lithium compounds are lithium polymer (LiPo) and lithium-ion.

EMI from a lithium-ion battery-powered UAS can be classified into two types: i) EMI unrelated to UAS maneuver and ii) EMI connected to UAS maneuver. High-frequency EMI from airborne electronic equipment is the main cause of the former. The latter refers to the electricity-generated low-frequency electromagnetic field, which includes EMI from wires and lithium batteries. Through low EMI design, the average EMI generated by lithium battery is 177.3 nT. In terms of the UAS itself, flight heading, and throttle can have an impact on EMI at the magnetic compass. During the flight [15], the EMI of UAS is continuous in the time domain and overlapping in the frequency domain. The parts such as the lithium-powered battery (Assuming that UAS uses one 6S lithium battery) and electrified wires related to UAS maneuver appears as low-frequency interference in the frequency domain, When the EMI is greater than 50nT, it will affect the magnetic compass, which in turn will affect the flight trajectory of the system, resulting in heading measurement error cause collision [15].

When lithium-ion batteries are exposed to extremely high temperatures (above 70 °C) or extremely cold temperatures (below 25 °C), their lifetime and discharging capacity can be severely reduced or even destroyed [16].

Camera: UAS cameras are useful for surveillance, crowd monitoring, and even threat detection. This type of surveillance is also necessary for border surveillance to prevent criminal activity and alert authorities. One of the sources of interference in the carrier is imaging systems in unmanned applications. Light Detection and Ranging (LIDAR) + Red-Green-Blue (RGB) cameras, Full Frame aerial cameras, and thermal cameras are the most often utilized cameras for power line inspection. The navigation antenna is frequently located with other electronics in the carrier that are less than 3 meters away from the camera, which is prone to digital noise [17] in terms of shot noise affecting the image quality. When the receiver's gain was adjusted and the camera was turned on, the in-band noise reported by the receiver rose by 12 dB.

Adjacent RF Channel - Differential and Common-Mode Coupling: Unintentional electromagnetic coupling is troublesome. It can result in electromagnetic interferences—both external and internal interference. In electromagnetic coupling causing interference, the source components conduct or radiate electromagnetic signals to interfere with components in the same circuit or neighboring circuit. At high frequencies, the common-mode coupling is more active.

- Various EMI shielding techniques, such as Faraday cages, are introduced in RF and microwave circuits to reduce electromagnetic coupling between circuit components.
- Conductors and cables connected will be sharing a common mode impedance, then voltage drops can interfere with the electronic components and cause Electromagnetic disturbances [18].

Hardware manipulation: Though not a source of Intentional Electromagnetic Interference (IEMI), hardwired attacks can exacerbate or amplify the power of external EMI carried out locally on the hardware by inserting a malicious component onboard the UAS that weakens the system. For instance, Kaji et al. [19] insert a hardware trojan (HT) on an IC to create a zone of heightened receptivity to electromagnetic waves which are about 1/100th of the electric power of a conventional High Power Electromagnetics (HPEM). The insertion of this HT weakens the device immunity, induces electromagnetic waves of a specific frequency, and paves the way for attacks like arbitrary data injection. If electromagnetic waves similar to an HPEM is produced from outside the device/system, a current or voltage is induced at zones with weakened immunity.

According to the authors, the time required to mount this HT onto a target device like a UAS's flight computer is approximately 3 minutes for an experienced attacker.

### **3.1.2 Environmental**

#### **3.1.2.1 Low Frequency**

##### *3.1.2.1.1 EMI from Indirect Lightning Strikes*

EMI produced from external environmental conditions such as lightning are associated with electricity and are a type of low-frequency interference that does not ionize the surrounding fluid (air). Lightning produces an electric current between the sky and the ground and this produces an electromagnetic field (United States Environmental Protection Agency 2022) that can make onboard components susceptible to transients (or oscillations) [20]. Depending on the external material of the aircraft, lightning strikes can either cause significant damage only at the point of contact, or to the entire aircraft and on-board components. According to Petrov and Stancheva [21], 20% of unprotected aircrafts that do not have any type of lightning protection reported seeing major failures of electrical components compared to just 3% of aircrafts that do have a lightning protection mechanism in place. One standard that addresses the induced (indirect) effects of lightning on avionics and airborne equipment is the RTCA DO-160 [22]. The tests in DO-160 standard assess how damage- and upset-tolerant avionics are to lightning-induced transients.

Findings from research literature have attempted to quantify the indirect effects of lightning on avionics. Rimal and colleagues [23] have shown that induced currents and voltages generated by two lightning waveforms with a "level 4 amplitude" on Metal Oxide Semiconductor Field Effect Transistor (MOSFET), diodes, and inductors can easily exceed the tolerable limits for each component; this can upset or damage the equipment.

Lightning can have significant effects on both UAS and grid operations.

#### **Lightning Effects on Unmanned Aircraft Systems**

- a) **Direct Strikes:** If a UAS is struck by lightning directly, it can cause severe damage to the aircraft's structure and electronics. The high current and voltage associated with lightning can overload and destroy sensitive components, including avionics, communication systems, and power systems [24].
- b) **Indirect Effects:** Even if a UAS is not directly hit by lightning, it can still experience adverse effects. Lightning produces strong electromagnetic fields during its discharge, and these electromagnetic pulses can induce electrical currents in nearby conductive materials, including the metal components of a UAS. These induced currents can interfere with the aircraft's electronic systems, leading to glitches, malfunctions, or temporary loss of control [25].
- c) **Safety Concerns:** Lightning strikes can pose safety risks to UAS operators and nearby personnel. Depending on the size and material composition of the UAS, it may attract lightning and become more susceptible to strikes. This can be particularly concerning in areas with frequent thunderstorms or where UAS are used for critical operations.

To mitigate the impact of lightning on UAS, manufacturers and operators implement various protective measures, such as lightning conductive paths, shielding, and surge protection. Additionally, UAS operators often monitor weather conditions to avoid flying in areas with high

lightning activity during thunderstorms. Safe distance operations during thunderstorms need to be studied as there is very limited literature on this topic.

### **Lightning Effects on Power Grid Assets**

- a) **Direct Strikes:** Lightning strikes on power grid assets, such as transmission towers, substations, and power lines, can cause significant damage. The high current flow from a lightning strike can cause structural damage, equipment failure, and even fires. These incidents can result in power outages, disruption of electrical supply, and damage to equipment that requires expensive repairs [26] [27] [28] [29] [30].
- b) **Indirect Effects:** Similar to UAS, power grid assets can also experience induced currents from nearby lightning strikes. These induced currents can damage transformers, circuit breakers, and other equipment, leading to system failures and blackouts [31].
- c) **Ground Potential Rise (GPR):** Lightning strikes can create a Ground Potential Rise (GPR) effect. When lightning hits the ground or a structure, it induces a voltage potential that can affect nearby power lines and substations. GPR can lead to overvoltage and damage sensitive equipment in the power grid [32].

To protect power grid assets from lightning, various measures are implemented, such as installing lightning arrestors, surge protectors, and grounding systems [33] [34]. Additionally, regular inspections and maintenance are performed to ensure the integrity of the power grid infrastructure. In both cases, understanding and mitigating the effects of lightning are essential to ensure the safety and reliable operation of UAS and power grid assets.

### **3.1.2.2 Magnetic**

#### *3.1.2.2.1 EMI from converter stations*

**Origin/Cause:** The major component of a high voltage direct current (HVDC) transmission system is the converter station. Its function is to complete the interface between AC and DC power systems. The switching of the converter station's valves (power electronics converter) is the principal source of electromagnetic emission from the HVDC converter station. When the converter valves are working, they open and close in an alternate, causing rapid transients in the switching voltage and internal current of the valves. The transmission of energy spreads a wide and continuous spectrum of noise characterized as electromagnetic emission [35].

**Effects/Impacts:** The data link allows the UAS to interact with the ground control terminal and exchange information. Through the uplink remote control link, the control terminal transmits control commands to the UAS, and through the downlink telemetry link, the UAS status parameters and task collection information are relayed back to the control terminal. Lock-state refers to the state in which a UAS's data link is operational. The lock-state is interrupted during exposure to large external EMI, and this is known as a lost-link situation [36].

#### a) On UAS Data Link Communication

A UAS was flown in a microwave anechoic chamber to conduct a radiation interference experiment. When the interference field strength reaches 10 V/m at frequencies of 80 MHz to 1000 MHz and 1000 MHz to 2750 MHz, communication between the UAS and the ground is disrupted, and the controller is unable to control the steering stepper motor [37].

Another experiment was carried out on a UAS as a continuous radiation of IEMI radiated susceptibility test. The results show that when the frequency of the radiated continuous wave is the same as or close to the frequency of the UAS data link, even if the radiated electric field is less than 1 V/m, the data link of the UAS used to communicate with the ground control station can be disrupted. Harmonics produced by nonlinear units, such as amplifiers, in the continuous wave emission system produce sensitive frequencies such as 1/2, 1/3, 1/4, and 1/5 times the working frequency, causing the data link to be disrupted [9].

#### b) On UAS Navigation and Positioning System

The GPS positioning accuracy of line-following UAS platforms will be affected by corona discharge, insulator pollution flashover, and electromagnetic scattering in the environment of HVDC converter stations. Polluted insulators have a partial discharge frequency range of 1 MHz to 10,000 MHz, which overlaps with the GPS L1 and L2 frequency bands [38]. The partial discharge power of contaminated insulators ranges from -70 dBm to -10 dBm. GPS positioning accuracy is under the L1 and L2 frequency bands, and it will suffer obvious interference if the power exceeds -40 dBm. When an abnormal discharge occurs in power equipment (such as corona discharge [39] or flashover discharge), co-channel interference [40] will degrade GPS positioning accuracy if the generated electromagnetic wave signal frequency is the same as the GPS signal frequency and reaches a certain signal strength.

##### 3.1.2.2.2 *EMI from Transmission Lines*

#### a) Electric Field on UAS

Experimentation was conducted with a quadrotor UAS inspection model on 500 kV and 220 kV high-voltage overhead transmission lines and simulated experiments. The patrol UAS maximum field strength is scanned at a distance of 0.5–12 meters from the wire in the experiment. The maximum field strength of the surface of the 220 kV voltage class overhead transmission line is reduced as the distance from the conductor increases, and the field strength and distance are nearly inversely proportional. The distortion field strength varies similarly to the distance between the edge conductor's outer side and the middle line.

At a distance of 1 m, the maximum field strength had an amplitude of about 150 kV/m, and at a distance of 3.5 m, the field strength is attenuated to 40 kV/m. The maximum field strength and field strength change rate of the UAS surface gradually decreases as the distance between the UAS and the 500 kV voltage class overhead transmission line increases.

The maximum field strength is 180 kV/m when the UAS is 1 m away from the side conductor, and it is attenuated to 50 kV/m when the distance is 5 m. The electric field distortion of the 500 kV voltage level has a greater influence on the surface of the UAS than the 220 kV voltage level, but the variation of the field strength with distance and the rate of change of the field strength are similar [41].

The maximum electric field strength that can resist electromagnetic interference in the electronic components that make up the UAS flight control system and inspection system, as well as the sensor's conditioning circuit and protection circuit, is generally 50 kV/m [42] [43]. As a result, the maximum electric field strength of the UAS surface must be less than 50 kV/m to operate the UAS

and collect normal environmental data. This electric field strength value is used as the normal inspection operation of the unmanned aerial vehicle's safety field strength threshold in this paper.

### **3.1.2.3 High-Intensity Radiated Fields (HIRF)**

High-Intensity Radiated Fields (HIRF) refers to the exposure of electronic and electrical systems to electromagnetic fields of high intensity. These fields can come from various sources, both natural and man-made. Here are some examples of HIRF-related exposure:

- a) **Lightning Strikes:** Lightning discharges during thunderstorms produce extremely high electromagnetic fields that can affect nearby electronic and electrical systems [44]. This includes both direct strikes on equipment and induced currents in nearby conductive structures.
- b) **High-Power Radio Transmitters:** Powerful radio transmitters, such as those used in broadcasting, radar systems, and satellite communication, can generate intense electromagnetic fields that may impact nearby electronic devices and systems.
- c) **Radar Systems:** Radar installations, including ground-based and airborne radars, emit high-power electromagnetic waves for detection and tracking purposes. Electronic systems operating in the vicinity of radar installations can be exposed to HIRF.
- d) **High-Power Communication Towers:** Communication towers, such as cellular and broadcasting towers, emit electromagnetic waves to carry signals over long distances. Equipment located near these towers may experience HIRF exposure.
- e) **Electromagnetic Pulse (EMP):** EMPs can be generated by nuclear explosions or high-altitude bursts, causing a burst of electromagnetic energy that can damage or disrupt electronic systems over a wide area.
- f) **High-Voltage Power Lines:** High-voltage power lines can produce electromagnetic fields due to the flow of current through the transmission lines. Electronic equipment near these power lines may experience HIRF effects.
- g) **Solar Flares and Geomagnetic Storms:** Solar flares and geomagnetic storms, caused by disturbances in the Earth's magnetic field from solar activity, can induce strong electromagnetic fields that may impact electronic systems.
- h) **Transient Electromagnetic Sources:** Various transient electromagnetic sources, such as lightning discharges from volcanic eruptions (Volcanic Lightning), can produce intense electromagnetic fields with HIRF effects.

To protect electronic and electrical systems from HIRF-related exposure, manufacturers and designers implement appropriate shielding, grounding, and surge protection techniques. Additionally, further research warranted to inform regulatory bodies to revisit existing or establish standards and guidelines to ensure that electronic systems can withstand or mitigate the effects of HIRF exposure, especially in critical applications such as aviation, aerospace, and defense.

Cellular towers, also known as cell towers or base stations, are an integral part of mobile communication networks. They transmit and receive radio signals to facilitate communication between mobile devices, such as cell phones, and the core network.

The HIRF exposure from cellular towers can occur in two main ways:

### Transmitting Antennas (Radiated Fields):

Cellular towers are equipped with transmitting antennas that radiate electromagnetic signals to establish communication with mobile devices. These antennas emit radiofrequency (RF) waves, which carry voice and data signals. The radiated fields from these transmitting antennas can be considered HIRF when examined in the context of the relatively high power levels used for long-range communication.

### Electromagnetic Interference (EMI):

Cellular towers, due to their high power and RF radiation, can potentially cause electromagnetic interference (EMI) with nearby electronic devices. EMI occurs when the electromagnetic fields emitted by the tower affect the proper functioning of sensitive electronic equipment, such as radio receivers, TVs, radios, or even medical devices, in close proximity to the tower.

To mitigate the HIRF-related effects of cellular towers, the following measures are commonly taken:

- a) **Antenna Placement and Orientation:** Cellular towers are designed to optimize their coverage and minimize HIRF exposure in specific directions. The antennas are often tilted or directed to provide better signal coverage in designated areas while reducing radiation in undesired directions.
- b) **Power Control:** Cellular towers use power control mechanisms to adjust the transmit power based on the distance and signal quality to the mobile devices. By optimizing the power levels, HIRF exposure to both users and surrounding areas can be managed.
- c) **Compliance with Standards and Guidelines:** Regulatory bodies and industry organizations set specific standards and guidelines to limit HIRF exposure levels from cellular towers. Tower operators must adhere to these regulations to ensure public safety and compliance with electromagnetic radiation limits.
- d) **Site Selection:** When planning new cellular tower installations, site selection is crucial to minimize HIRF exposure to sensitive areas, such as schools, hospitals, and residential neighborhoods.

Overall, cellular towers are designed and operated to strike a balance between providing reliable communication services and managing potential HIRF exposure to the public and surrounding electronic equipment. By adhering to best practices and regulatory guidelines, the impact of HIRF from cellular towers can be effectively managed and mitigated. As more and more 5G/6G deployments are happening, further research warranted on HIRF emission and its effects due to cellular tower.

### **3.1.3 Cyber Security**

EMI is produced by alternating electric and magnetic fields. Typical sources of interference include onboard UAS components (camera, rotors, flight controller) and environmental causes (cellphone towers, emissions from power lines). These sources come under a broader category of unintentional EMI. However, IEMI from threats external to the unmanned aerial system (UAS) also exists as any communication system using wireless links (i.e., full duplex communication in the case of UAS) is susceptible to EMI. As defined by a report from Metatech Corporation [45], IEMI is the “intentional malicious generation of electromagnetic energy introducing noise or signals into electric and electronic systems, thus disrupting, confusing or damaging these systems

for terrorist or criminal purposes”. Sources of IEMI are small, highly mobile, and freely available in the commercial market and are not easy to detect as they don’t leave verifiable traces; the complexity of internal circuitry adds to the latter issue, and users of systems under IEMI attacks are likely to attribute the interference to faulty hardware [46]. IEMI attacks can have either of the following two characteristics:

- a) Narrowband: Narrowband attacks use frequencies that are close to the center frequency, typically with a bandwidth within 1% of the center frequency [47] and are powerful.
- b) Wideband: Wideband or ultra-wideband (UWB) attacks are based on the use of short, non-continuous pulses spread across a range of frequencies. Though not as powerful as narrowband signals, they can be used to find a system’s vulnerability to different frequencies.

Through these attacks means, IEMI can be maliciously targeted at a UAS via the following attacks:

i) High-altitude electromagnetic pulses (HEMP)

Although much less likely than other IEMI attacks, HEMPs are electromagnetic pulses that produced a nuclear event outside the earth’s atmosphere, typically above an altitude of 30 km [48]. These pulses come under the category of HEMP where electromagnetic signals are channeled at peak strength. Radasky and colleagues [47] state that computers and other systems using microprocessors appear to be vulnerable to radiated EMI that have amplitudes of 30 V/m or above in the narrowband fields. In addition to being fairly easy to produce, narrowband interference is a greater threat to UAS platforms than wideband frequencies as since a narrowband waveform is close to the center frequency, the electrical energy is delivered in a substantially small frequency and is thus of greater power. Of course, the experiment setups and quality of equipment shielding/enclosures will to some degree determine how these systems would respond to such interference.

ii) Jamming

Any system that relies on electronic hardware can be damaged or disrupted by electromagnetic signals given that these signals are powerful enough. The antennae on terminal equipment such as the ground station controllers and the UAS itself serve as easy entry points for IEMI. When IEMI is coupled via an antenna, it is termed as front door coupling. Experiments performed by Beek and Leferink [49] shows that regardless of any base station or wireless receiver that is equipped with a bandpass filter, front door coupled EMI that is produced by IEMI sources that are from out-of-band frequencies (OOB) (i.e., frequencies that are outside the passband of the front-end filter) need to be at a certain magnitude to cause receiver saturation. However, in-band frequencies from an IEMI source can saturate the front end of a receiver and lead to decreased signal sensitivity. Jamming attacks can use narrowband or wideband frequencies [50]. An example of a wideband interference weapon is the transient electromagnetic device (TEDs). TEDs do not work with a specific frequency but rather operate in a wide spectrum range and are attractive options to an attacker as they don’t require much skill to build, require much less power to operate, and are smaller in size than narrowband weapons [51].

iii) Data/Signal injection

Analog sensors such as temperature or air quality sensors that can be deployed onboard a UAS can serve as an entry point for attacks like a signal injection. Analog sensors that operate on circuits in the order of a few millivolts and produce signals in the very low frequency (VLF) band (1 Hz – 30 kHz) are vulnerable to interference and signal injection at much lower power levels. According to Kune and colleagues [52], manipulating sensor readings with EMI-based sources requires an adversary to identify a suitable emission frequency as each component has a certain frequency by which a signal can pass with little attenuation. Another side-effect of EMI to analog sensor circuits is the loss of accuracy in sensor readings [4]. Narrowband frequencies can damage modern electronic equipment at amplitudes of 0.5kV/m for a frequency of 1 GHz [45].

Table 3-2 summarizes the common cyber-attacks that cause EMI. Occurrences are assigned based on the ease by which components can be obtained and attacks can be executed.

Table 3-2. Intentional sources of EMI from common cyber-attacks.

Attack	Remark	Affected Range	Occurrence	References
<b>High-altitude electromagnetic pulse (HEMP)</b>	Typically produced by super high-power, high-energy emissions such as those from nuclear detonation.	Narrowband frequencies of < 1 Hz.	Low <sup>1</sup>	[45] [47] [48]
<b>Jamming</b>	Antennae onboard UAS and a source of IEMI that targets these antennae (front door coupling) using in-band operating frequencies.	Deployed using wideband frequencies.	Medium <sup>2</sup>	[49] [50] [51]Click or tap here to enter text.
<b>Data/Signal injection</b>	EMI is ‘injected’ in analog sensors as they are sensitive to EMI due to heightened sensor receptivity (mV-level sensitivity).	Wideband frequencies or narrowband frequencies of 1 GHz.	Medium <sup>2</sup>	[45] [52] [4]

<b>Hardware manipulation</b>	Insertion of malicious hardware component(s) amplifies EMI to the entire system	-	<b>Low-Medium</b>	[53]
------------------------------	---	---	-------------------	------

<sup>1</sup>Low – Likely to be used in military-level situations that call for high impact weaponry. There is a fairly high degree of complexity for execution.

<sup>2</sup>Medium – Subject to use in situations where components are easy to obtain. There is a low complexity for execution.

### 3.2 Data Capture /Acquisition Process

#### 3.2.1 Equipment and Test Site

A variety of testing has been accomplished in, and around multiple testing sites. Coordination of testing has been completed in the planning, testing and analysis phase for several months. In this section all the equipment and sites used throughout the data capture/ acquisition process is discussed.

##### 3.2.1.1 UAS Platforms

Table 3-3 lists three UAS models that were used for flight testing. More information for these UAS platforms can be found by navigating to the hyperlinks in the “UAS Model” column.

Table 3-3. List of UAS platforms with specifications used for data capture/acquisition process.

UAS Model	Specifications	UAS Image
<i>DJI Matrice 30T</i> <a href="#">(Link)</a>	<ul style="list-style-type: none"> <li>• 41-minute flight time</li> <li>• Width: 585 mm</li> <li>• Height: 215 mm</li> <li>• Weight 3770g</li> <li>• Max flight speed 6m/s</li> <li>• Max wind resistance 15m/s</li> <li>• Max flight altitude 1676ft.</li> <li>• Operating frequency 2.400-2.4835 GHz</li> </ul>	

Figure 3-2. DJI Matrice 30T.

- 
- DJI Mavic 2 EA* • 31-minute flight time  
([Link](#))
- Width: 242mm
  - Height: 114 mm
  - Weight 1100g
  - Max flight speed 50-72kph
  - Max wind resistance 10m/s
  - Max flight altitude
  - Operating frequency 2.400-2.4835 GHz; 5.725-5.850 GHz



Figure 3-3. DJI Mavic 2 Enterprise Advanced (EA).

- 
- DJI Matrice 300 RTK* ([Link](#))
- 55-minute flight time
  - Width: 670mm
  - Height: 430mm
  - Weight 6300g (with two TB60 batteries)
  - Max flight speed 23m/s
  - Max wind resistance 15m/s
  - Operating frequency 2.400-2.4835 GHz; 5.725-5.850 GHz



Figure 3-4. DJI Matrice 300RTK.

---

### 3.2.1.2 Non-UAS Test Equipment

The test apparatus and their relevance to data collection are as follows:

1. RF Spectrum Analyzer – Captured real-time measurements of RF signals at and above ground-level from a sweep of frequencies from 50 Hz to 6.1 GHz. Data logging was enabled to record as many measurements as possible up to approximately 8,000 total samples at a rate of 1 sample every 1 second.
2. Electromagnetic Field (EMF) logger – EMF loggers produced insights into the field strengths, radio frequency strengths, and electric field strengths at and above ground-level.
3. Thermal imaging – Forward looking infrared (FLIR) or thermal imaging was captured aerially in real-time to quantify the thermal heat map of deployed UAS platforms.

#### 3.2.1.2.1 RF Spectrum Analyzer

RF Explorer is a portable RF spectrum analyzer that is available in a variety of frequency ranges from 50Hz to 6.1GHz (Figure 3-5). This RF analyzer can be used as a standalone device or can connect to a computer running analysis software via Universal Serial Bus (USB). Six RF Spectrum Analyzers with a center frequency from 480 Hz to 5980 Hz were mounted on M300 drones to

record wideband RF data. Later the USB port on the RF Explorer was used to extract the data and perform further analysis. The specifications for this analyzer are as follows:

- Graphics Liquid Crystal Display 128x64 pixels, great visibility outdoors.
- Spectrum Analyzer mode - Peak Max and Hold, Normal, Overwrite and Averaging modes.
- Lithium-ion polymer internal battery with a life of 16 hours of continuous operation
- Wideband coverage that includes: all popular sub-1GHz ISM bands, 2.4x GHz ISM band (WiFi, Bluetooth, Zigbee), 5.x GHz ISM band (WiFi) - with maximum frequency of 6.1 GHz.



Figure 3-5. RF Explorer.

#### 3.2.1.2.2 Thermal Imaging Sensor

The FLIR Vue Pro R 640, 69° FOV, 9mm, 30Hz is 640 × 512-pixel thermal imaging resolution camera module shown in Figure 3-6. It empowers UAS operators and certified thermographers to acquire precise, non-contact temperature measurements from an aerial vantage point. Each captured still image by the Vue Pro R includes meticulously calibrated temperature data embedded within every pixel, enhancing the value of your sUAS (small unmanned aircraft system) operations and services significantly. By incorporating fully radiometric data-gathering capabilities, the Vue Pro R extends its applicability to a range of sUAS applications, such as building and roof inspections, power grid assessments, infrastructure analysis, precision agriculture, and public safety. The specification of the thermal imaging sensor is as follows:

- Weight - 92-113 grams
- Dimensions - 57.4 mmx 44.5mm (including lens)
- Sensor - CMOS 1/2,8" 2MP 23mm F2,8
- Frame Rate - 30 Hz (NTSC); 25 Hz (PAL)
- Thermal Imager - Uncooled VOx Microbolometer
- HDMI Output - 1280x720 @ 50hz, 60hz

- IR Camera Resolution -  $640 \times 512$



Figure 3-6. FLIR Vue Pro R 640.

### 3.2.1.2.3 EMF Logger

Two different EMF logger was used while capturing the data. Initially a portable EMF logger was used which was carried by the UAS platforms to log in flight EMF strength data. The other one was not a portable one which was used to capture ground EMF strength. Details regarding these two EMF logger are discussed in next two subsections.

#### 3.2.1.2.3.1 EMF-390

The EMF-390 digital multi-function EMF meter is a portable device (Figure 3-7). EMF, Electric Field (EF), RF, and Radio Spectrum Power Analyzer are among the device's integrated testing features. The meter can identify common sources of EMF, such as power lines, WiFi, and so on, based on the EMF measured. It can detect and monitor EMF, EF, RF, and 5G networks both indoors and outdoors (protected), as well as other similar environments. It has the ability to continuously monitor radiation. When the device is connected to a computer, software can download measurement data to the computer, which the user can then analyze later. A high contrast black/white Liquid Crystal Display module and one front light emitting diode indicator were also installed on the device. The specifications are as follows:

#### EMF (Magnetic Field)

- Triple axis (X, Y, Z) Detectable low frequency: 0.5Hz to 150Khz
- Range: 0.0~500mG
- Resolution: 0.1/1 mG

#### EF (Electric Field)

- Range: 0V/m to 1000V/m
- Resolution: 1 V/m

#### RF (Radio Frequency)

- Detectable Radio frequency: 10Mhz to 10GHz

#### RF Spectrum Power Analyzer

Table 3-4. Frequency specifications for RF Explorer.

Frequency Band	Frequency Step	Frequency Span
<b>Band 1 – 50 MHz to 65MHz</b>	100KHz	100KHz
<b>Band 2 – 65MHz to 76MHz</b>	100KHz	100KHz
<b>Band 3 – 76MHz to 108MHz</b>	100KHz	100KHz
<b>Band 4 – 240MHz to 1040MHz</b>	1KHz to 10KHz	50KHz to 4000KHz
<b>Band 5 – 240GHz to 2.5GHz</b>	25KHz to 405KHz	58KHz to 812KHz

- Operating temperature & humidity: 5 to 40-degree C, below 80% RH
- Working Voltage: 3.6-3.7V
- Power Consumption: 25mW to 125mW (backlight dependent)
- Power: Supply 3.7V Li-Ion battery / USB power
- Dimensions 135 x 78 x 25 mm (5.25'x 3' x 1')



Figure 3-7. Digital EMF Meter (EMF-390).

### 3.2.1.2.3.2 EHP-50F field strength analyzer

EMF-390 EMF reader having 1000V/m max range we used EHP-50F shown in Figure 3-8 for capturing higher E field data. Which does isotropic measurement of electric and magnetic extremely low frequency fields. It uses the Weighted Peak method for standard-compliant measurement of complex signals.

- Frequency range: 1 Hz to 400 kHz
- Dynamic range: >105 dB
- Measurement range, E field: 5 mV/m to 100 kV/m
- Measurement range, H field: 0.3 nT to 10 mT
- Temperature range: -20 °C to +55 °C

- Weight: 550 g
- Dimensions: 92 mm x 92 mm x 109 mm



Figure 3-8. Field Strength analyzer (EHP-50F).

### 3.2.1.3 Transmission Line and Microwave tower sites

Multiple flight tests were conducted at five high voltage transmission lines, four AC and one DC transmission line, and one microwave tower sites. Figure 3-10 represents all the transmission line sites and microwave tower site can be seen in Figure 3-9.

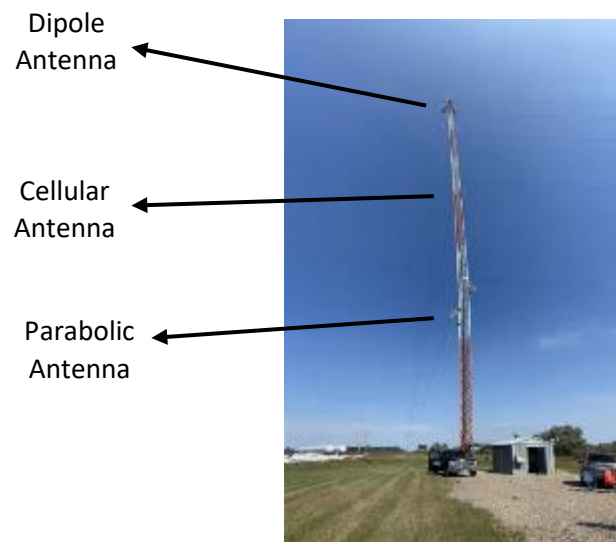


Figure 3-9. Microwave tower site.

### 3.2.2 Set-up & Mount Orientations

From Figure 3-11, we can see the EMF and RF reader set-up for different UAS platforms. The smallest UAS (M2EA) was carrying one EMF reader and one RF Explorer each. While M30T UAS, the midsize one was carrying one EMF reader one RF explorer and Thermal Camera. M300 on the other hand being the largest carried six RF Explorer and one EMF reader.

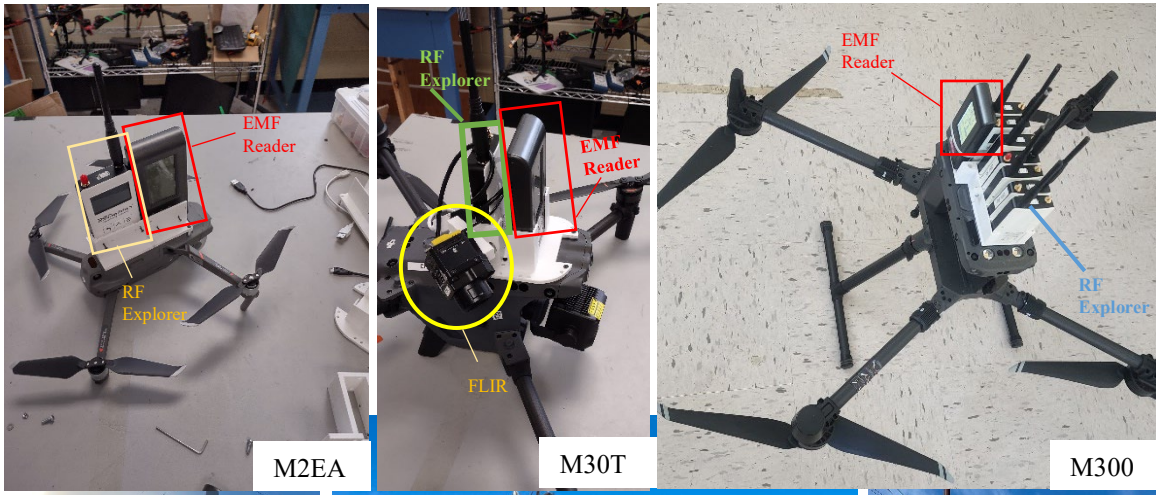


Figure 3-11. Different UAS platforms with sensors mounted.

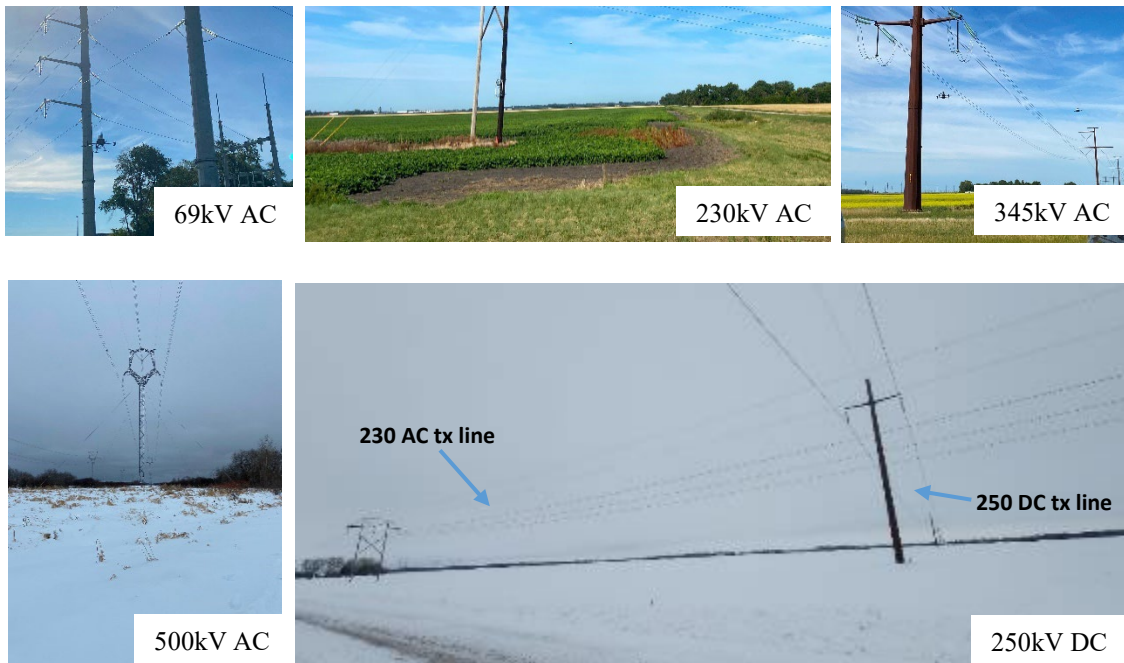


Figure 3-10. Transmission line sites.

Multiple flights were performed by each UAS in each transmission line site. Flights were performed at different orientations (above and parallel) to the transmission lines and at different distances (7.62m, 9.14m, 10.67m, 12.19m) from the transmission lines. Figure 3-12 to Figure 3-15 show the flight trajectory at different test sites.

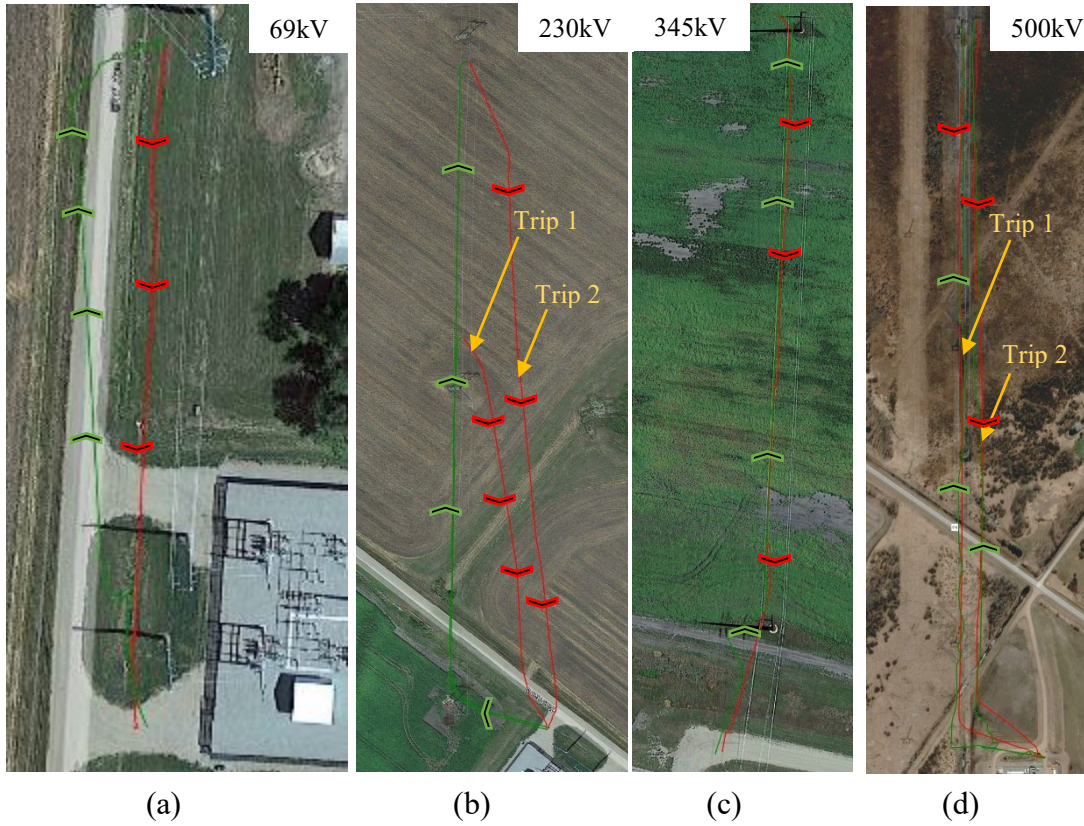


Figure 3-12. Flight trajectory at various AC transmission lines.

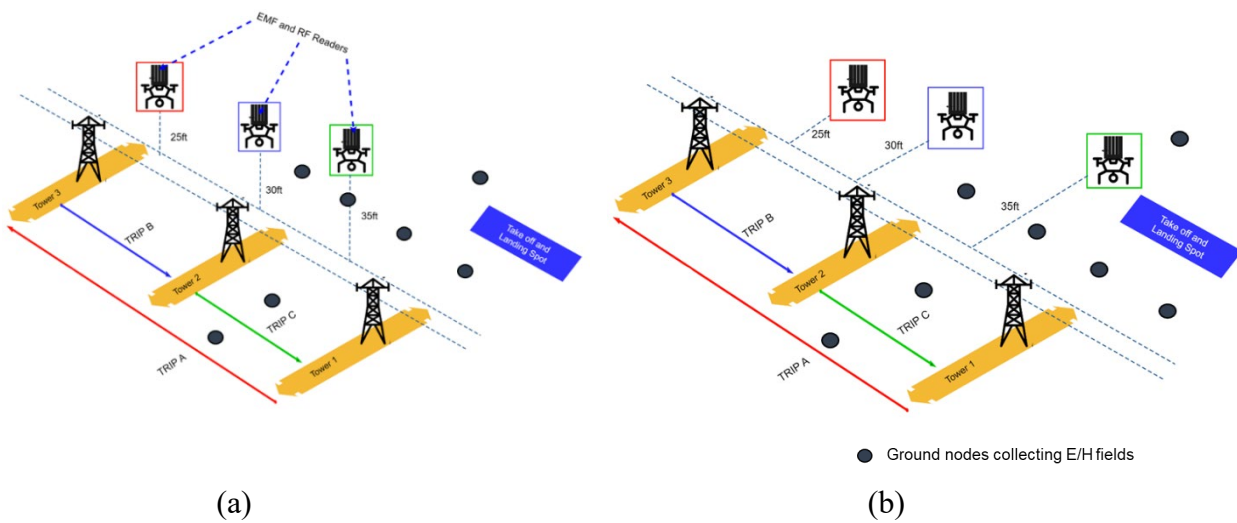


Figure 3-13. Aerial/Ground data acquisition on E and H fields along 500kV AC transmission lines.



Figure 3-14. Flight trajectory (a) above and (b) parallel to 250kV DC transmission line.

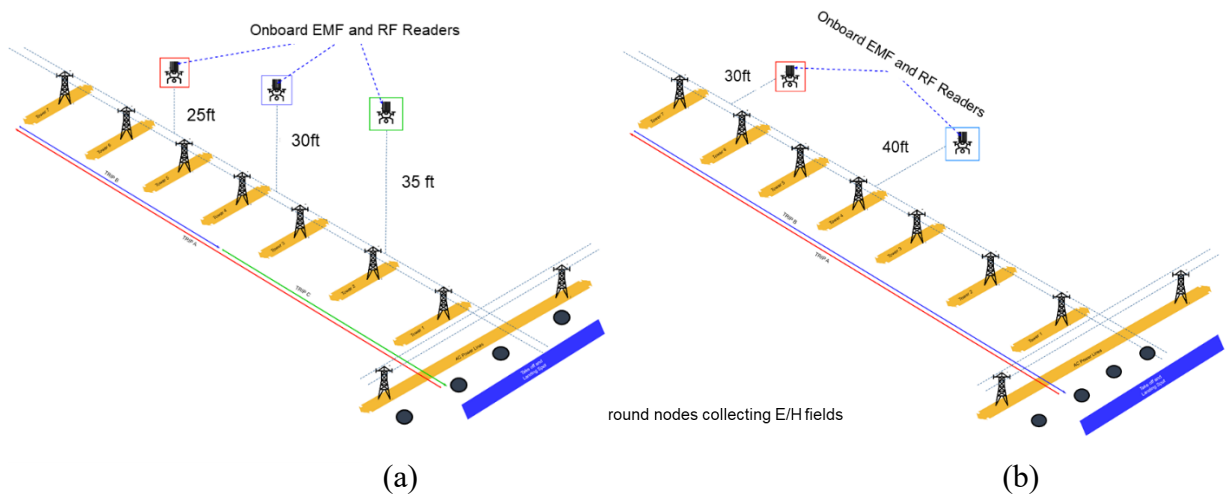


Figure 3-15. Aerial and ground data acquisition on E and H fields along 250kV DC transmission line.

The flight paths and UAS orientations with reference to the transmission lines are summarized in Table 3-5. It lists the various transmission line locations, the corresponding UAS models that were employed, the flight paths taken, and the orientations of the UAS platforms while in flight.

Table 3-5. Flight trajectory and orientation summary.

Test site /UAS	Microwave tower	6 230kV AC	345kV AC	500kV AC	250kV DC		
M2EA	✗ <sup>1</sup>	✗ <sup>1</sup>	Bellow & Parallel	Bellow & Parallel	✗ <sup>2</sup>		
M30T	Parallel	3.05m 4.6m	Bellow & Parallel	Bellow & Parallel	Above & Parallel	7.6m	7.6m 9.1m 10.7m
		6.1m				9.1m 10.7m	Parallel
M300	Parallel	3.05m 4.6m	Bellow & Parallel	Bellow & Parallel	Above & Parallel	7.6m	7.6m 9.1m 10.7m

	o Paralle		v
	w l		e
6.1m	&	9.1m	P 9.1m
	P	10.7m	a 12.2m
	a		r
	r		a
	a		l
	l		l
	l		e
	e		l
	l		

<sup>1</sup> DJI M2EA was not flown as it was in a non-approved zone

<sup>2</sup> DJI M2EA was not flown due to high wind velocity

### 3.3 Test plan Report Integration

#### 3.3.1 Observed Electric Fields: 69kV, 145kV, 345kV, 500kV & 250KV DC lines

Figure 3-16 to Figure 3-20 collectively demonstrate a consistent trend where the electric field (E-field) strength decreases as the distance from the transmission lines increases. This pattern holds true regardless of the voltage rating of the transmission lines, the flight direction (above or parallel), or the orientation of the sensor. However, for the 250kV DC and 69kV AC transmission lines, there is not a substantial change in the E-field strength as the distance increases. Nevertheless, it is worth noting that even at the farthest distance from the transmission lines, the E-field strength is significantly lower compared to when the UAS platforms were flying in close proximity to the lines.

Further analysis reveals that the increase in E-field strength fluctuates between 25% and 50% for every 3.05m increase in distance. This variation is consistent with theory.

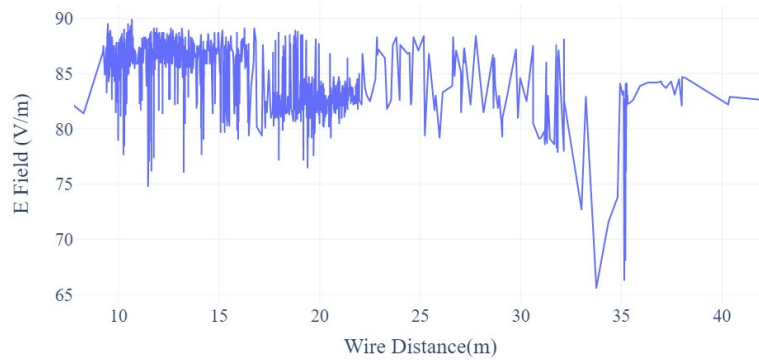


Figure 3-17. Electric field strength as a function of distance from conductors along 250kV DC transmission lines.

Figure 3-16 depicts the relationship between the electric field (E-field) strength and distance from 250kV DC transmission lines. The plot reveals that the E-field strength remains relatively constant and low, fluctuating between 75V/m and 90V/m, regardless of the varying distance from the transmission lines. This observation suggests a consistent and relatively low E-field strength near 250kV DC transmission lines.

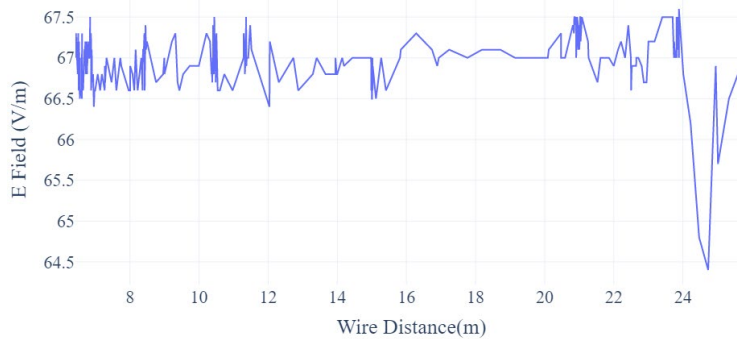


Figure 3-16. Electric field strength as a function of distance from conductors along 69kV AC transmission lines.

Figure 3-17 displays the relationship between the electric field (E-field) strength to distance from wire for 69kV AC transmission lines. The plot reveals that the E-field strength remains relatively constant, ranging from around 66.5V/m to 67.5V/m, regardless of the distance from the transmission lines. This observation indicates a consistent E-field strength level throughout the varying distances from the 69kV AC transmission lines.

Figure 3-18 illustrates the relationship between the electric field (E-field) strength and distance for 230kV AC transmission lines. The plot indicates that within a distance of up to 18m from the lines, there is a high E-field<sup>1</sup> strength reaching 1000V/m. Beyond this distance, the E-field strength

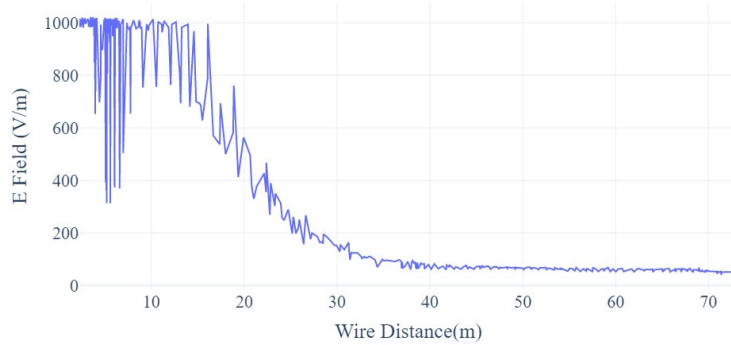


Figure 3-18. Electric field strength as a function of distance from conductors along 230kV AC transmission lines.

gradually decreases as the distance increases. This observation suggests a significant drop in the E-field strength beyond the initial 18m distance from the 230kV AC transmission lines.

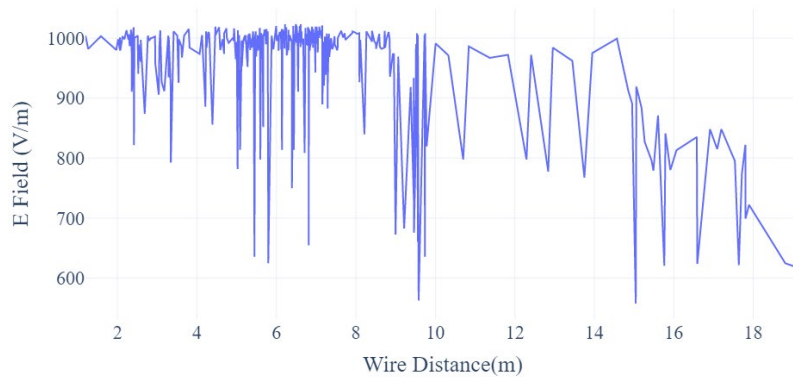


Figure 3-19. Electric field strength as a function of distance from conductors of 345kV AC transmission lines.

Similar to the behavior observed in 230kV AC transmission lines, the E-field strength for 345kV AC transmission lines exhibits a higher magnitude within a distance of up to 18m from the conductors. As the distance increases beyond this point, the E-field strength gradually decreases. This trend suggests a comparable pattern in the E-field behavior for both 230kV and 345kV AC transmission lines, where the maximum E-field strength is observed in close proximity to the conductors and diminishes with increasing distance.

Figure 3-20 depicts the electric field (E-field) strength for 500KV AC transmission lines. The trend observed in this figure is similar to that of 230kV and 345kV AC transmission lines, indicating a decrease in E-field strength with increasing distance. However, it is important to note that the average E-field strength for the 500KV AC transmission lines is lower compared to the other voltage ratings.

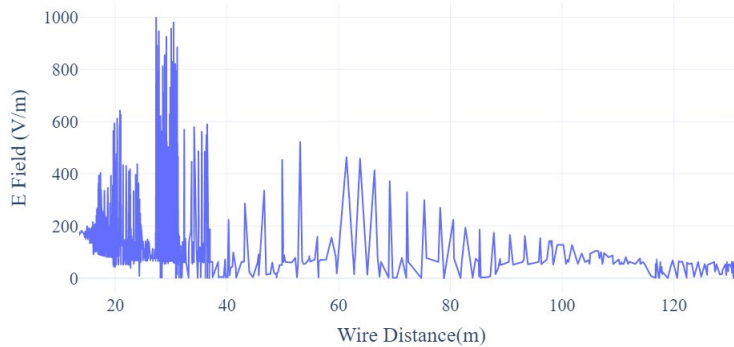


Figure 3-21. Electric field strength as a function of distance from conductors along 500kV AC transmission lines.

Furthermore, it is worth mentioning that the flight test for the 500KV AC transmission lines was specifically conducted during the winter season at a temperature of 20°F (-6.7°C). This temperature falls outside the operating temperature envelope of the EMF 390 equipment, suggesting that the measurements were taken under conditions that may not fully align with the device's specified operating range.

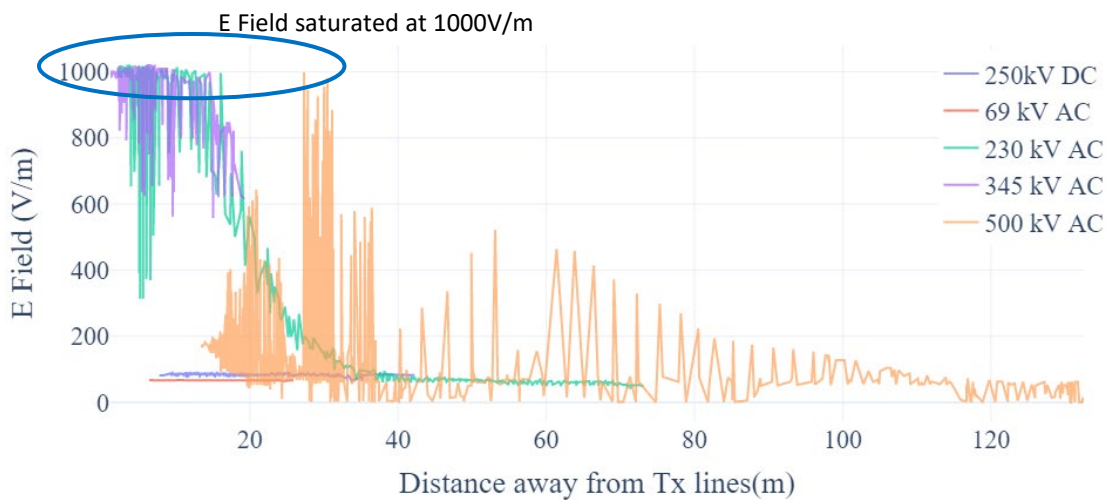


Figure 3-20. Aggregate measured electric field values across all transmission lines.

Figure 3-21 represents the combined plot of Figure 16 through Figure 20. This aggregated plot reveals two significant findings. Firstly, as the distance from the transmission lines increases, the electric field (E-field) strength decreases. Secondly, within a distance of approximately 50ft from the transmission lines, the E-field strength exceeds 1000V/m, indicating higher levels of electromagnetic field exposure in close proximity to the lines.

### 3.3.2 Observed Magnetic Fields: 69kV, 145kV, 345kV, 500kV, & 250KV DC lines

Figure 3-22 to Figure 3-26 indicate that the magnetic field decreases with the increase in distance from the transmission line. The maximum magnetic field captured for 250kV DC and 69kV AC

transmission lines is 1.8mG, which is very low compared to other transmission lines. The changes to H field with increasing distance is likely, and but yielded significantly lower value.

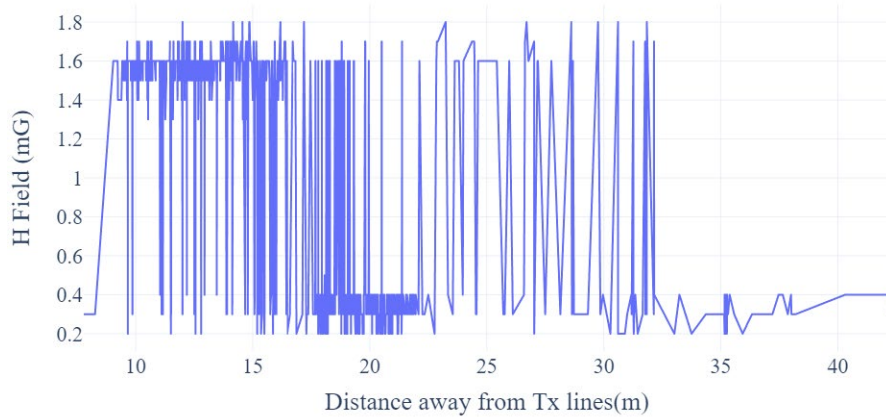


Figure 3-22. Magnetic field strength as a function of distance from conductors along 250kV AC transmission lines.

Figure 3-22 illustrates the relationship between the magnetic field (H-field) strength to distance from 250kV DC transmission lines. The plot demonstrates a similar trend as observed in Figure 16 for the electric field (E-field) strength. Both the E-field and H-field strengths exhibit a relatively constant and low pattern with increasing distance, fluctuating between 0.2mG to 1.8mG. This observation indicates a consistent and relatively low H-field strength in the vicinity of 250kV DC transmission lines.

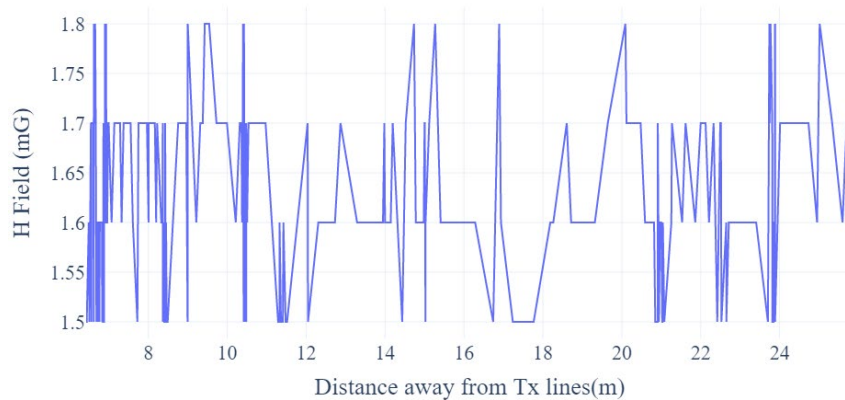


Figure 3-23. Magnetic field strength as a function of distance from conductors along 69kV AC transmission lines.

Figure 3-23 exhibits similar trends to Figure 3-17, where the magnetic field (H-field) strength remains relatively constant and low. The H-field strength ranges from approximately 1.5mG to

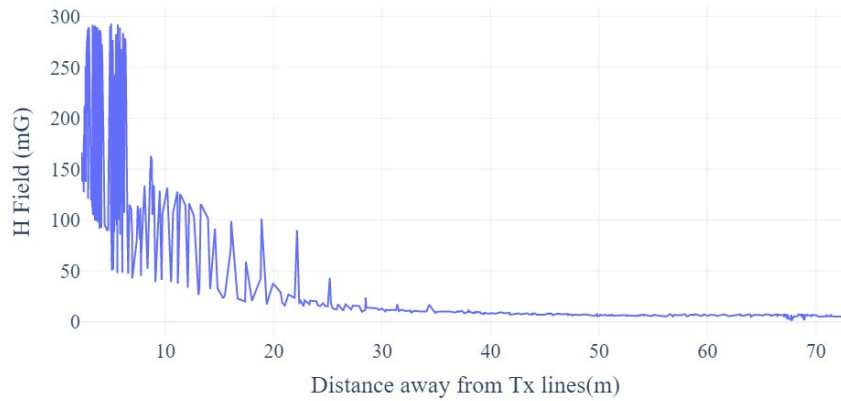


Figure 3-24. Magnetic field strength as a function of distance from conductors along 230kV AC transmission lines.

1.8mG, irrespective of the distance from the 69kV AC transmission lines. This observation suggests a consistently low H-field strength level throughout the varying distances from the 69kV AC transmission lines.

Figure 3-24 and Figure 3-18 exhibit similar trends, indicating a significant decrease in field strength with increasing distance. Within a distance of up to 6.5m or 21ft from the wires, there is a high magnetic field strength of approximately 295mG. Beyond this point, the field strength decreases noticeably as the distance increases. Specifically, from 6.1m to 9.14m, the magnetic field strength decreases to 160.5mG, representing a reduction of 45.5%.

Continuing with consecutive 10ft increases in distance, the magnetic field strength further decreases to 116mG (28%), 73mG (37%), 42mG (42%), and 26mG (38%), respectively. These

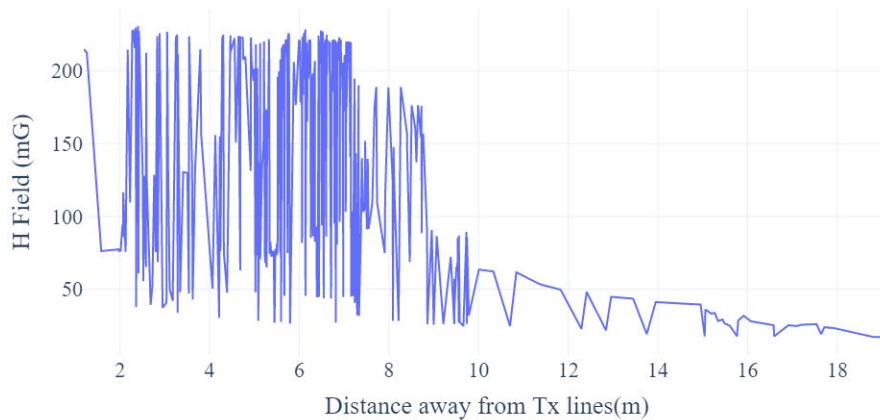


Figure 3-25. Magnetic field strength as a function of distance from conductors along 345kV AC transmission line.

observations indicate a consistent and substantial decrease in magnetic field strength with increasing distance from the wires.

Similarly, to the pattern observed in Figure 3-24, Figure 3-25 shows a higher magnitude of H-field strength, reaching approximately 230mG, within a distance of up to 7.5m/7.6m from the conductors. Beyond this distance, as the measurement points progress from 7.6m to 10.7m, the magnetic field strength gradually diminishes, resulting in a decrease to 96.3mG. This reduction accounts for a significant 58.1% decrease in the magnetic field strength

With each consecutive 10ft increase in distance, the magnetic field strength progressively decreases. At 45ft, the strength drops to 68.8mG, reflecting a 28.6% reduction compared to the previous measurement. Further, at 55ft, the magnetic field strength decreases to 33.7mG, marking a significant 50.8% decrease compared to the preceding measurement.

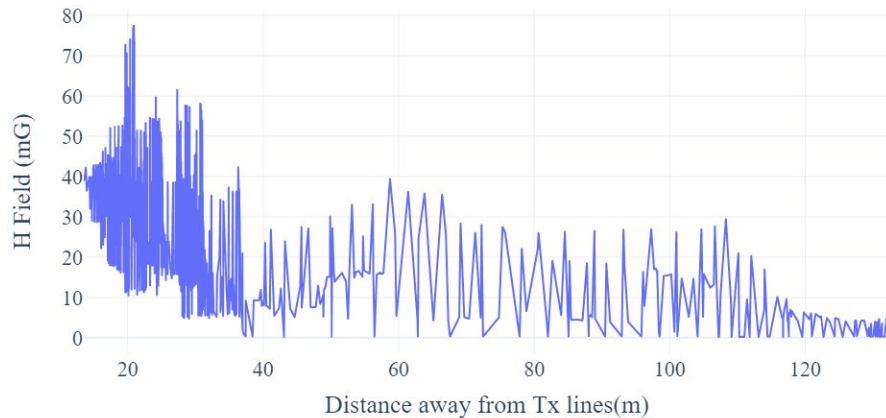


Figure 3-26. Magnetic field strength as a function of distance from conductors along 500kV AC transmission lines.

Figure 3-26 displays the trend of the magnetic field (H-field) strength associated with 500kV AC transmission lines. The observed pattern in this figure is comparable to that of 230kV and 345kV AC transmission lines, demonstrating a decrease in H-field strength as the distance from the lines increases. The average H-field strength for the 500kV AC transmission lines captured is lower compared to the other voltage ratings due to the test site temperature mentioned above.

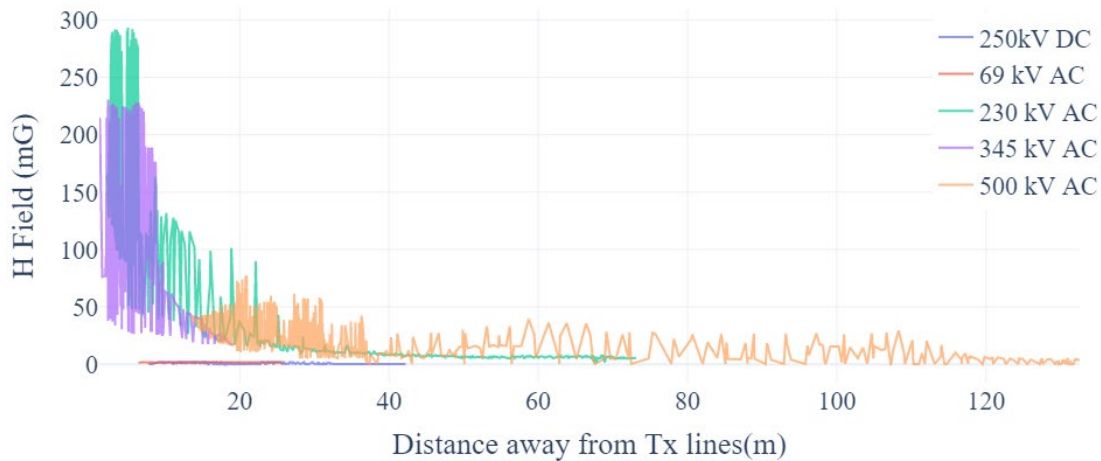


Figure 3-27. Aggregate measured magnetic field values across all transmission lines considered.

Figure 3-27 represents the combined plot of Figure 3-22 through Figure 3-26. This aggregated plot reveals two significant findings. Firstly, as the distance from the transmission lines increases, the magnetic field (H-field) strength decreases. Secondly, within a distance of approximately 9.14m from the transmission lines, the H-field strength is above 250mG, indicating higher levels of electromagnetic field exposure in close proximity to the lines.

### 3.3.3 Factors Contributing to Choppy Data in UAS Operations Near Transmission Lines

There are a variety of reasons why choppy data occurs in these measurements, and it is difficult to point out the exact causes. Some possible causes of this behavior includes:

1. Electromagnetic Interference (EMI):

The large fields associated with high power transmission lines can lead to EMI impacts on the measurement systems that are used to gather the data. While the UAS platform may experience no adverse impacts as a consequence of the large fields, the testing equipment used to detect these signals may experience adverse impacts.

2. Sample Rate and Data Processing:

The UAS's sample rate, which determines how often data is collected from sensors, can impact the smoothness of the recorded data. If the sample rate is too low, the data might not capture rapid changes or fluctuations, resulting in choppy data.

3. Flight Stability and Environmental Factors:

The proximity to high-voltage transmission lines can subject the UAS to challenging environmental conditions, such as turbulence and wind gusts, which could affect the stability of aircraft flight during data collection. In turn, this instability can lead to choppy data.

4. Hardware or Software Issues:

Choppy data may also arise from hardware or software malfunctions within the UAS. Faulty sensors, communication modules, or data storage systems can all contribute to data irregularities.

To address the choppy data issue when operating UAS near transmission lines, the following measures can be considered:

- a) Use Shielding: Shield sensitive electronic components on the UAS to minimize the impact of electromagnetic fields from transmission lines.
- b) Increase Sample Rate: Adjust the UAS's sample rate to capture data more frequently and accurately.
- c) Optimize Flight Path: Plan flight paths that maintain a safe distance from transmission lines and avoid areas with potential interference.
- d) Conduct Pre-flight Checks: Perform thorough pre-flight checks to ensure that all hardware and software components of the UAS are functioning correctly.
- e) Analyze Data Post-Flight: Examine the collected data after each flight to identify any anomalies or irregularities that could indicate potential interference issues.

By considering these factors and implementing appropriate measures, operators can improve data quality and reliability when conducting UAS operations near transmission lines or other potential sources of interference

### 3.3.4 Observed Electric Field Strengths in Microwave Tower

Figure 3-28 represents that the E field strength was almost constant and significantly low near microwave tower. Irrespective to the height and distance from the tower. E field reached at 454V/m at 430<sup>th</sup> second as the UAS was near to the ground control room of the microwave tower.

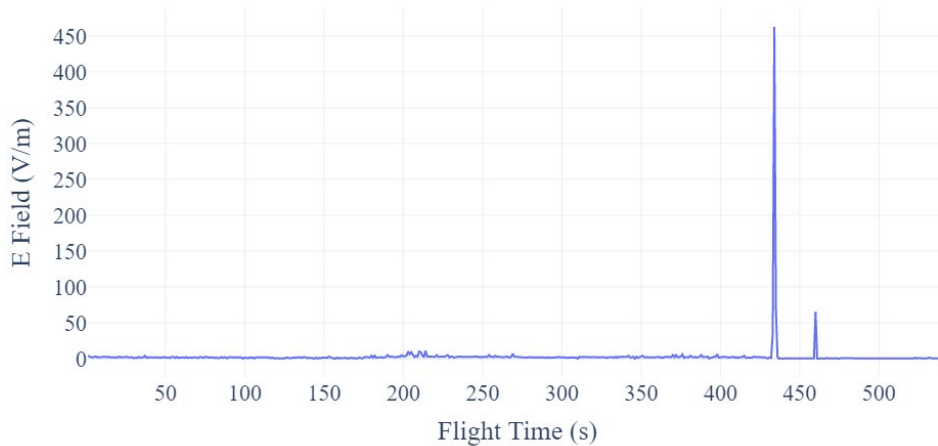


Figure 3-28. Electric field strength as a function of flight duration along a microwave tower.

### 3.3.5 Observed Magnetic Field Strengths in Microwave Tower

Figure 3-29 represents the H field strength with respect to flight duration. Similar to E field, H field was almost constant and significantly low near microwave tower irrespective to the height and distance from the tower.

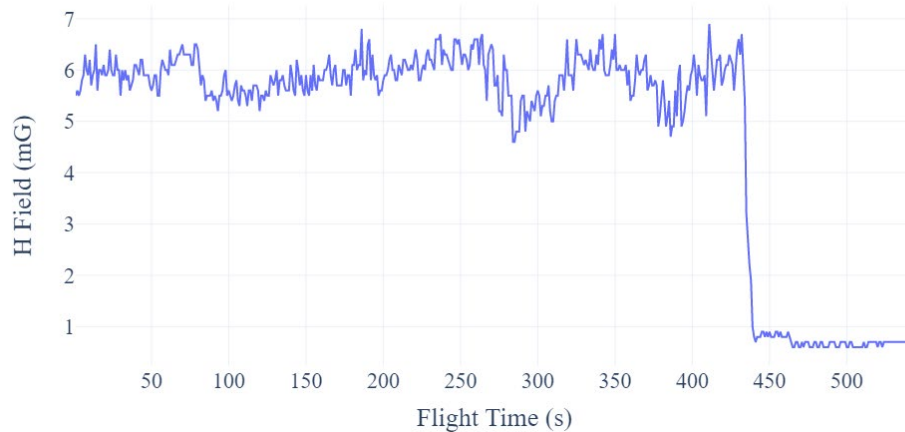


Figure 3-29. Magnetic field strength as a function of flight duration along a microwave tower.

Figure 3-30 and Figure 3-31 summarize a comparison of max E & H field values captured by UAS types across all critical infrastructures. Overall, 250kV DC lines has very low E&H field strengths comparing to AC transmission lines. E field maxed out at 1000v/m for 69kV, 230kV and 345kV lines both during Ground and Aerial observation.

For 500kV AC lines, while flying above the transmission line, E field is 23% more compared to flying parallel path, H field is 25.9% more while flying in parallel.

For 230kv and 345kv lines H field has increased significantly considering ground versus aerial measurements (e.g., 570%– 640% @15ft from line).

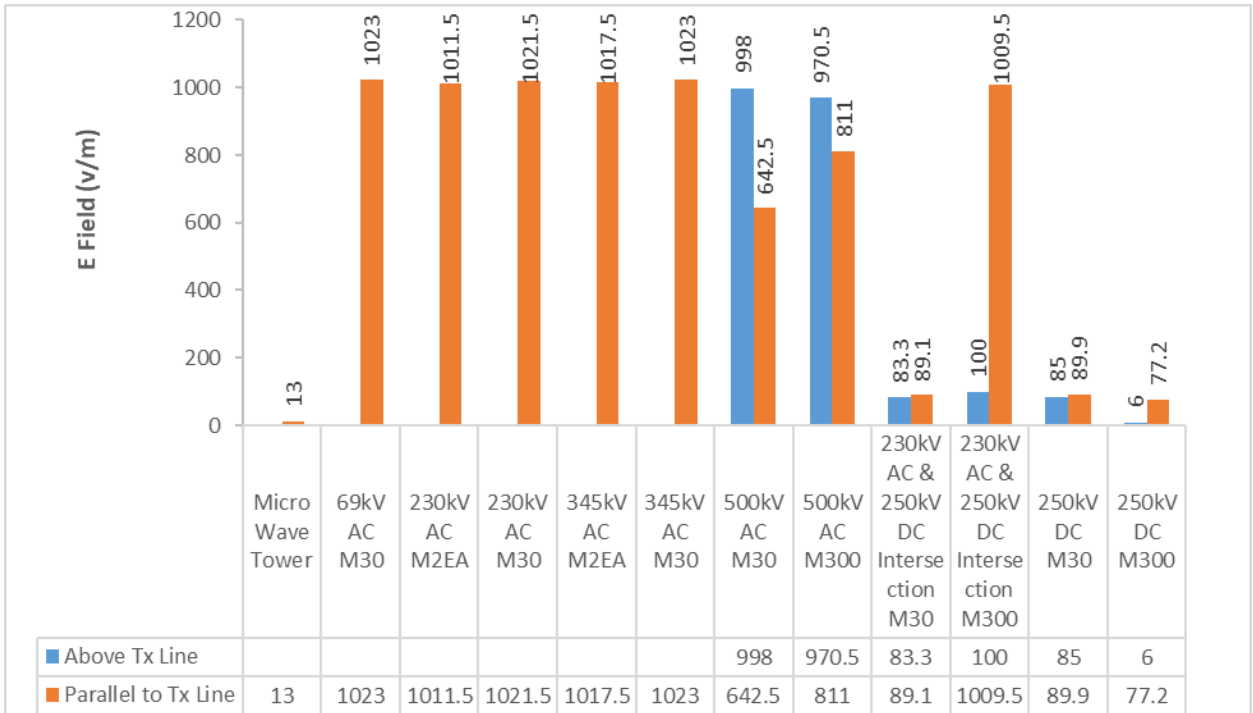


Figure 3-30. A comparison of maximum electric field values by UAS model across all test sites.

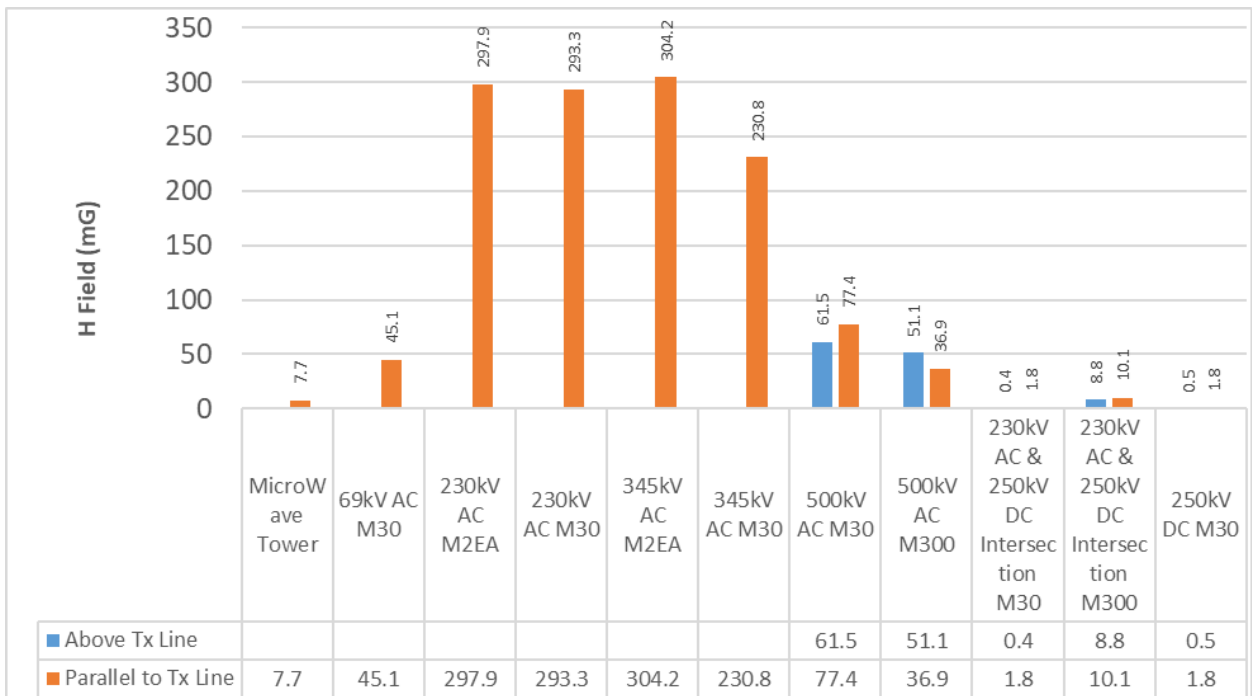


Figure 3-31. A comparison of maximum magnetic field value by UAS model across all test sites.

### 3.3.6 RF and non-RF Spectrum Analysis

RF-Explorer 6G Plus spectrum analyzers were used to monitor RF signals near transmission lines and a microwave tower. These devices can collect a frequency sweep over a range 960 MHz per collection and have a minimum and maximum frequency of 0.05 MHz and 6.1 GHz, respectively. Three DJI UAS platforms were used for data collection: an M300, M30T, and Mavic 2 Enterprise. The M300 could support a payload consisting of seven RF-explorer devices enabling it to capture the entire frequency range of the devices (0.05 MHz and 6.1 GHz) in a single flight. The M30T and Mavic 2 enterprise could only support a single device, resulting in a frequency range limit of 960 MHz, with the center frequency chosen at time of launch.

Data was extracted from the RF-Explorer devices as CSV files using “RF explorer suite for windows” after data collection. To distinguish real signals from noise, a custom python program was written to 1) label the noise floor for each sweep with a spline, 2) calculate the standard deviation of the differences between the measured received power and the noise floor at each frequency, and 3) aggregate real signals defined as having a received power greater than twice the standard deviation plus the noise floor. Figure 3-32 provides two examples of noise and signal classification using this algorithm.

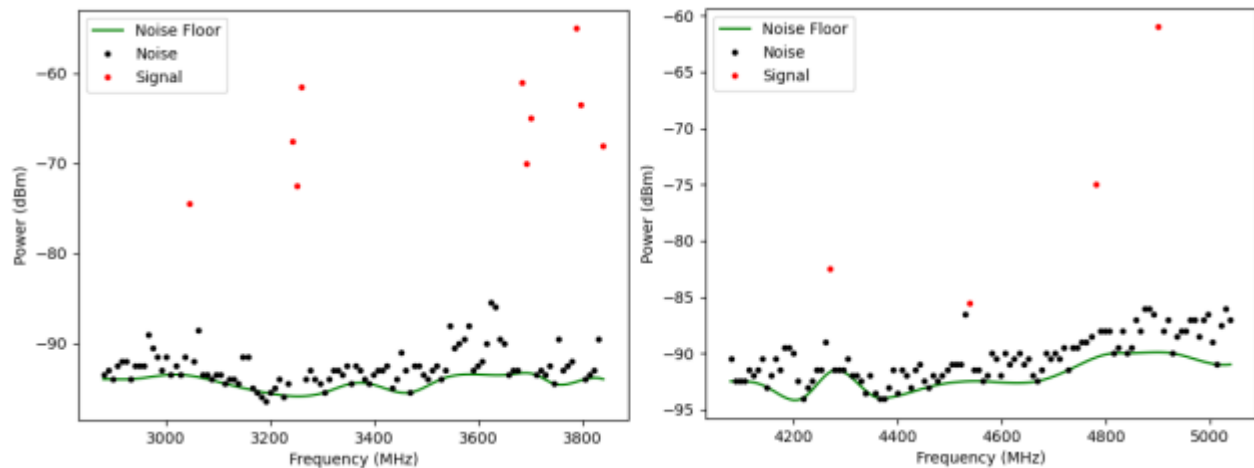


Figure 3-32. Signal and noise classification from spectrum data.

**Transmission Lines:** Data was collected near 5 transmission lines which consisted of 69 kV, 230 kV, 345 kV, and 500 kV AC power lines and one 250 kV DC power line. The 69 kV, 230 kV, and 345 kV power lines were located in Grand Forks, ND. The 500 kV AC line was located in Warroad, MN, and the DC power line was near Kindred, ND. Figure 3-33 through Figure 3-37 show histograms of captured signals at each transmission line with bin sizes of approximately 10 MHz. Note that for the DC power line data collection, data from the device set to record a 960 MHz range centered on 1.44 GHz was not recoverable, which is the reason for the gap. Additionally, the RF-Explorer devices captured sweeps more rapidly (i.e., collected more data points) when set to record higher frequencies which partially explains the significantly higher peak at approximately 5.8 GHz in the histograms for the 69, 230, and 345 kV lines. This dependency of recording speed on the frequency setting was accounted for in the device settings for the 500 kV AC and 250 kV DC data collections. This data shows that channels near 5.7-5.8 GHz and 1.8-2.0 GHz have the most activity, where “counts” refers to individual instances of the signal detections depicted in Figure 3-32 during the data collection period.

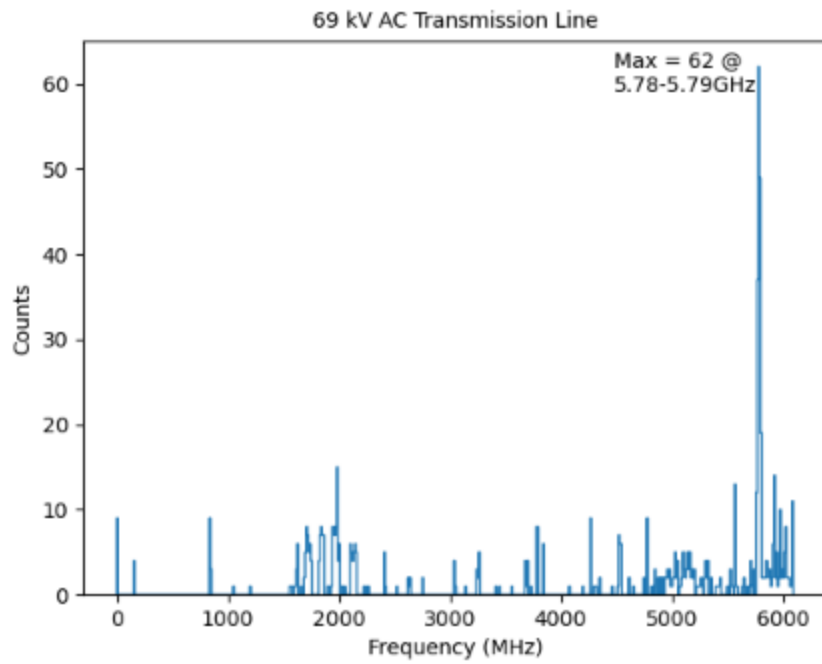


Figure 3-33. Received signals near 69kV transmission line.

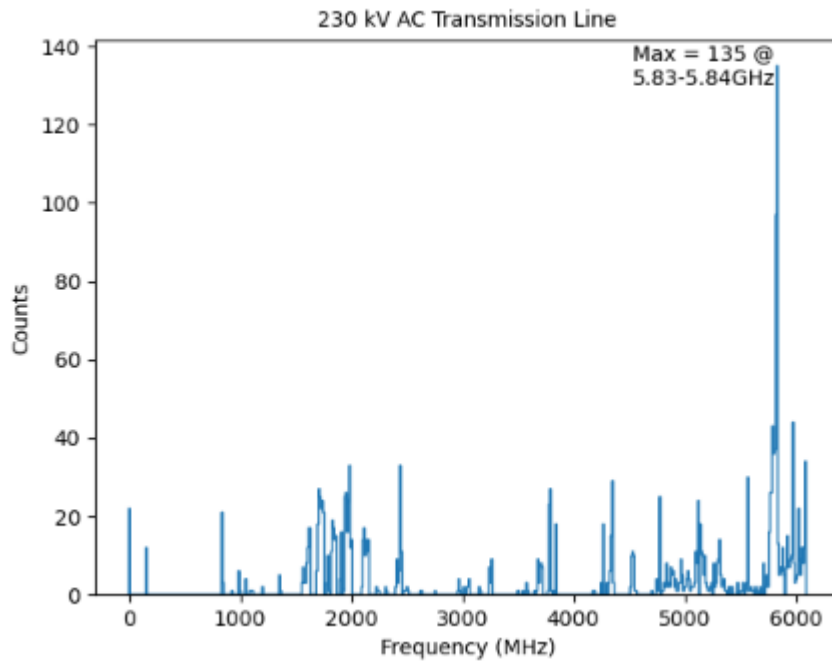


Figure 3-34. Received signals near 230kV transmission line.

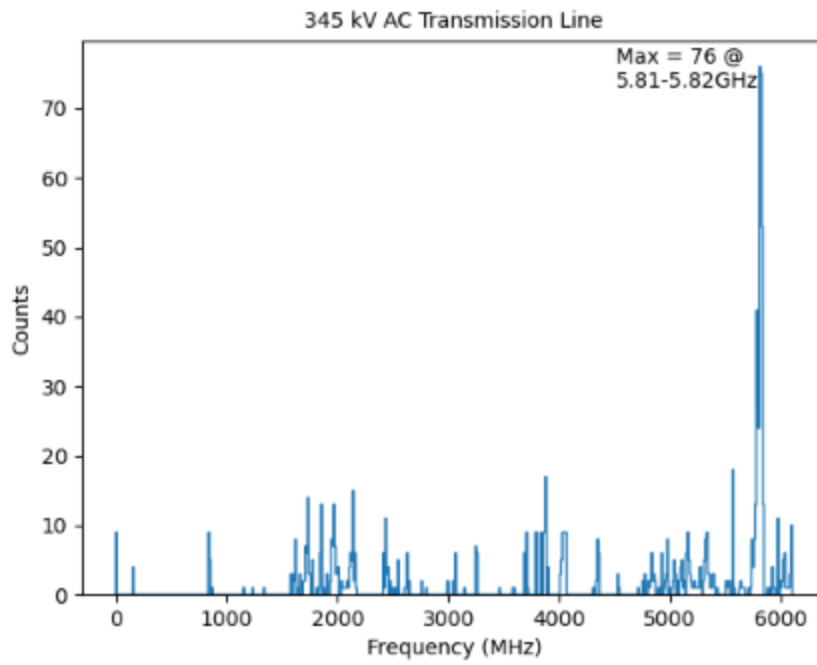


Figure 3-35. Received signals near 345kV transmission line.

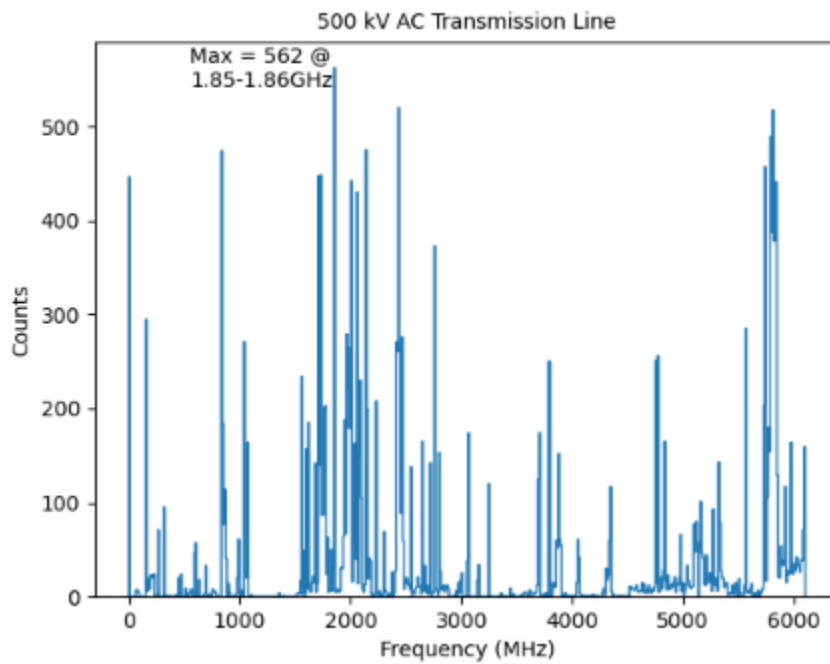


Figure 3-36. Received signals near 500kV transmission line.

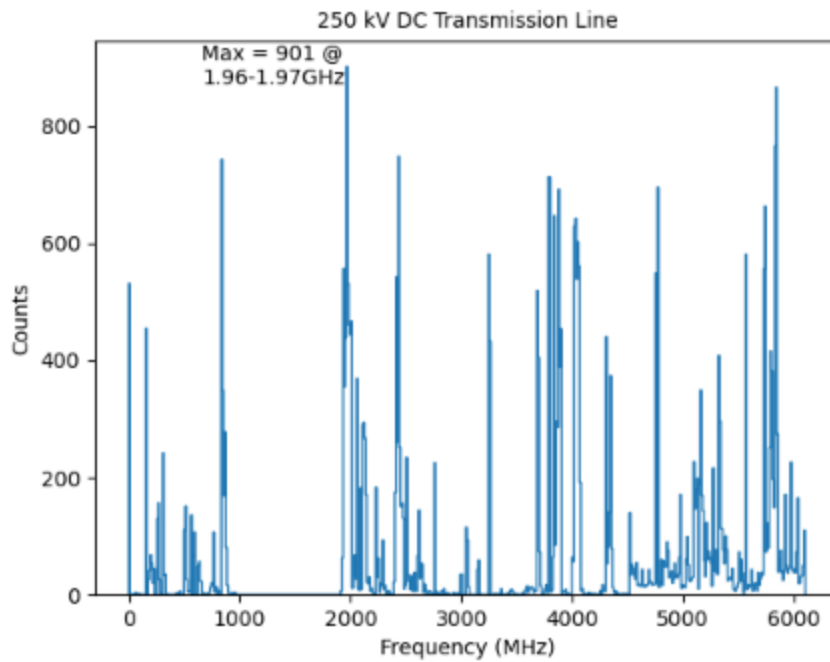


Figure 3-37. Received signals near 250kV DC transmission line.

**Microwave Tower:** Spectral data was also collected near a microwave tower. However, during the data capture process, data from only three devices was able to be collected. These are shown in Figure 3-38 with center frequencies of 2.40, 3.36, and 5.28 GHz. One notable difference between this data set and the ones for the transmission lines is the range having the most activity near 3.8 GHz.

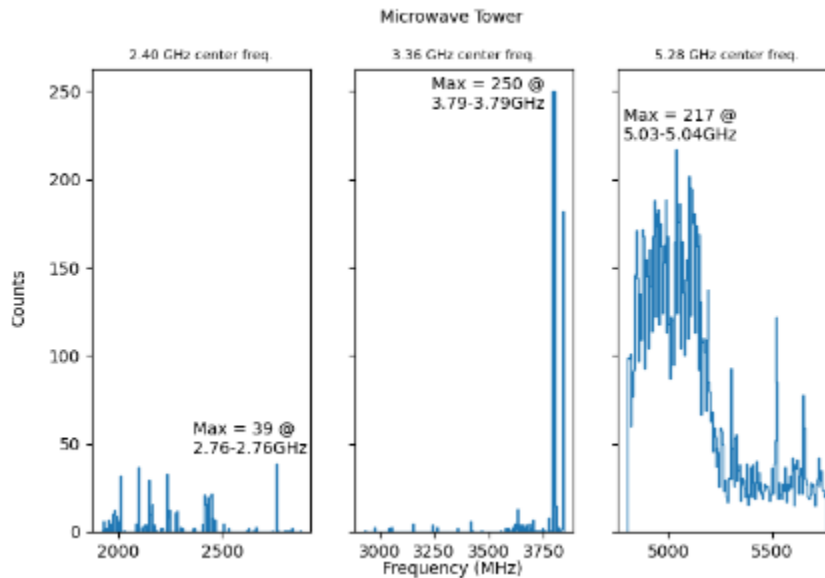


Figure 3-38. Received signals near microwave tower.

## 4 ASSESSMENT OF RFI TO UNMANNED AIRCRAFT SYSTEMS

### 4.1 Introduction and Research Objectives

As overall technology has advanced, the use of UAS has expanded significantly from primarily military applications to many non-military uses such as aerial photography, scientific survey, infrastructure inspection, forestry, agriculture, disaster relief, search and rescue, police surveillance, product delivery, public and commercial formation shows, sports and recreation. Increasing numbers of small and medium sized UAS platforms fly at low altitudes with various systems and payload sensors that are highly integrated into limited avionics space and utilize different frequency bands. At the same time, regulatory authorities are limiting frequency allocations. As a result, the possibility of unpredictable performance and even loss of control of UAS due to interference from ubiquitous electromagnetic emissions increases. UAS electromagnetic compatibility has therefore become a critical consideration in UAS design and operation to reduce any potential safety risks [54] [2] [5] [3] [55]

RFI, such as from cellular phone towers, broadcast of TV, Amplitude Modulation (AM) and Frequency Modulation (FM) radios, two-way radios, Wireless Fidelity (Wi-Fi) hotspots, various Radio Detection and Ranging (RADAR) systems, telemetry, etc., is a subset of a wider range of electromagnetic emissions that may lead to unpredictable performance and even loss of control of unmanned aircraft systems (UAS). Through literature review and tests, this research aims to identify sources of RFI in the NAS, summarize any impacts of these RFI sources on UAS safety and operations, propose risk mitigation solutions, and make recommendations for further research through simulation and testing for the ultimate goal to inform FAA decisions and UAS industry standards.

RFI can be divided into the two categories of front-door RFI and back-door RFI [54] based on the pathway by which RFI enters the circuits of UAS electronics. Front-door RFI occurs when an UAS suffers interference from RF sources that enters through a component that is designed to receive RF energy, such as an antenna/receiver. Back-door RFI occurs when an UAS receives RF energy through other means, such as through capacitive or inductive coupling of RF fields. Because the electronics of small UAS are lightweight and inexpensive, back-door RFI is possible if the UAS is close to RF sources with high field strength. Both front-door and back-door RFI impacts on UAS were evaluated in this project.

This section is organized as follows: Section 4.2 provides a brief description of literature review activities that relate to RFI; Section 4.3 lists the UAS models, test facility, equipment, and procedures that we adopted throughout this research; Section 4.4 provides the details of static tests on front-door and backdoor RFI effects in lab and chamber, and the analysis of the collected data; and Section 4.5 presents the outdoor flight tests and data analysis.

### 4.2 Literature Review of RFI to Unmanned Aircraft Systems

The literature review began with the Air Accident Monthly Bulletins (AAIB) published by the government of the United Kingdom [56] between the years 2018 and 2021. As shown in Table A1 in the Appendix, a listing of UAS accidents with field investigation reports was compiled. Information gathered for the purposes of this effort includes report publication date, accident date, UAS model involved in the accident, and the identified accident cause. AAIB published 55 field investigation reports for UAS accidents that occurred between May 22, 2018 and November 21, 2021. A variety of UAS models were involved in these accidents. Potential RFI source information

was then collected (see Table A2 in Appendix A) and the UAS risk evaluation to RFI source was performed (see Table A3 and A4 in Appendix A).

### **4.3 UAS Models, Test Facility, Equipment, and Procedures**

The UAS models, test facility, equipment and procedures adopted in test are briefly described below:

#### **4.3.1 UAS Models**

To adequately assess RFI across a sampling of UAS platforms, two very different UAS architectures were selected, as shown in Figure 4-1. These models were selected as representative samples to assess RFI impact on small UAS broadly.

##### **4.3.1.1 Aurelia X6 Standard**

The first, Aurelia X6 Standard, is a high-performance commercial model that uses the 2.4 GHz remote controller Herelink and the Cube Orange autopilot with three redundant Inertial Management Units (IMU), two barometers and one magnetometer. This model is also equipped with Light Detection and Ranging (LiDAR), Global Positioning System (GPS), and compass modules.

##### **4.3.1.2 QwinOut F450**

The QwinOut F450, is a do-it-yourself model that uses an AT9S Pro remote controller operating in the 2.4 GHz band, a PX4 autopilot with a single IMU, GPS, one barometer and one magnetometer. The drone also has a combined GPS/compass module.



Figure 4-1. UAS models used in testing: Aurelia X6 Standard (left); QwinOut F450 (right)

### 4.3.2 Anechoic Chamber

Many tests were performed in the Center for Remote Sensing and Integrated Systems (CReSIS) anechoic test chamber, as shown in Figure 4-2, to exclude any unwanted radio emissions from the environment. The chamber's interior dimensions are 11.58m x 7.29m x 7.36m with 0.4m raised floor. The chamber is capable of measuring electromagnetic fields from 30 MHz to 18 GHz with a maximum range length of 10m. The chamber can accommodate small and medium sized UAS



Figure 4-3. CReSIS anechoic chamber



Figure 4-2. ADALM-PLUTO SDR

up to 1,100 lbs and has approximately 100 dB shielding from the external environment.

Two ADALM-PLUTO Software Defined Radios (SDR) from Analog Devices were used to generate RFI signals. The SDR, as shown in Figure 4-3, can be configured to run with a 56 MHz bandwidth and a tuning range from 70 MHz to 6 GHz.

### 4.3.3 Antennas

The antennas used for RFI signal generation and detection include two Q-PAR horn antennas, one ETS-Lindgren Model 3142C BiConiLog antenna, and one ETS-Lindgren Model 3180B antenna, as shown in Figure 4-4. The horn antenna's operating frequencies extend from 2 GHz to 18 GHz. One horn antenna was used to transmit RFI signals between 2 GHz and 6 GHz, and the other was used to receive RFI signals for power calibration during testing. The operating frequencies of the ETS-Lindgren Model 3142C BiConiLog antenna extend from 26 MHz to 3 GHz. This antenna



Figure 4-4. Antennas used in tests: Q-PAR horn antenna (left), ETS-Lindgren Model 3142C BiConiLog antenna (middle), and ETS-Lindgren Model 3180B antenna(right)

was used to transmit RFI signals in the Very High Frequency (VHF) band from 80 MHz to 300 MHz. The operating frequencies of the ETS-Lindgren Model 3180B antenna extend from 30 MHz to 3 GHz. This antenna was used to receive RFI signals transmitted in the range from 30 MHz to 300 MHz for power calibration during the tests.

#### 4.3.4 Test Procedures

The test approach followed the IEEE standard ANSI C63 [57] to evaluate RFI effects on the safety and performance of the two UAS platforms under the scenarios that were previously identified. This approach includes

- 1) Specify the RFI scenario
- 2) Specify the intended signal
- 3) Specify the interference signal
- 4) Specify the Equipment Under Test (EUT)
- 5) Specify the susceptibility and functional performance
- 6) Specify the chamber test setup

The details of the above steps are given for specific scenarios and tests in Sections 4.4 and 4.5. In general, front-door RFI evaluations in the ISM frequency band were first tested in a laboratory environment outside the anechoic chamber for convenience of rapid setup. These laboratory findings were verified inside the anechoic chamber to exclude any unwanted radio frequency emissions from the environment. These findings were further verified through real-world outdoor flight testing. For back-door RFI evaluations, all tests were completed inside the anechoic chamber because of the high-power levels required.

### 4.4 Laboratory and Anechoic Chamber Testing

#### 4.4.1 Front-Door RFI Measurements

Front-door RFI effect assessments focus on the UAS C2 links using the ISM frequency band from 2.4 GHz to 2.5 GHz. The selected scenarios of front-door RFI include UAS flying near cellular

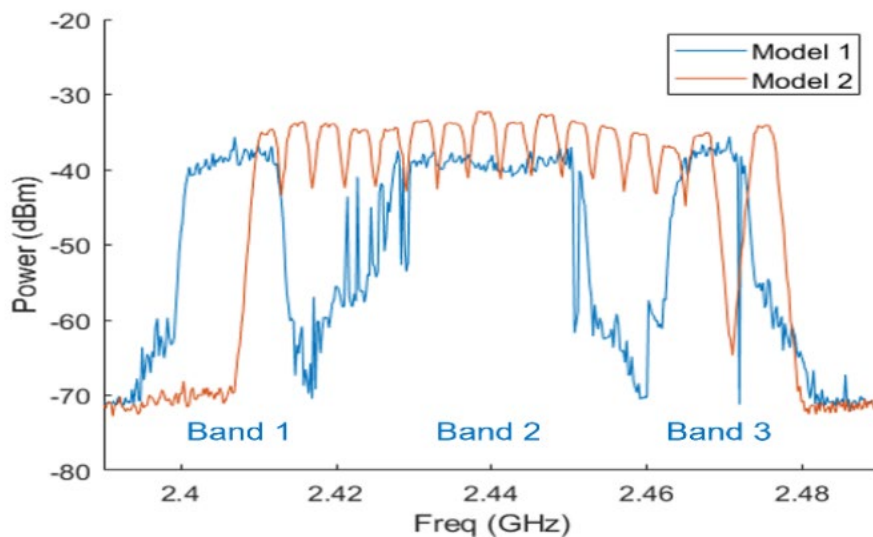


Figure 4-5. Measured spectra of the C2 link signals of Aurelia X6 Standard (blue) and QwinOut F450 (red)

telephone base stations and Wi-Fi hotspots. The intended signals in this case include communication between the UAS and its controller. Figure 4-5 presents the measured frequency spectra of the C2 uplink signals of Aurelia X6 Standard and the QwinOut F450, respectively, using a spectrum analyzer. The spectrum occupied by the control signals sent to Aurelia X6 Standard extends from 2.4 GHz to 2.48 GHz with frequency hopping in three bands centered around 2.405 GHz, 2.44 GHz, and 2.468 GHz. The spectrum occupied by the control signals sent to QwinOut F450 is evenly distributed between 2.41 GHz and 2.48 GHz.

The interference signals in these scenarios are Fourth Generation Long-Term Evolution (4G LTE)/Fifth Generation New Radio (5G NR) transmitted from cellular telephone base stations through downlink channels and Wi-Fi signals. Simulated signals that have similar power levels and spectrum characteristics were used in all tests. Figure 4-6(a) shows an example of the spectrum of replicated 5G NR waveform (Sub-Carrier Spacing (SCS) = 15 kHz, Bandwidth (BW) = 50 MHz, Number of Resource Blocks (NRB) = 270, Modulation=Quadrature Phase Shift Keying (QPSK)) using the MATLAB Wireless Waveform Generator. Figure 4-6(b) shows an example of the spectrum of a transmitted RFI signal of width 56 MHz centered around 2.4764 GHz by ADALM-PLUTO SDR.

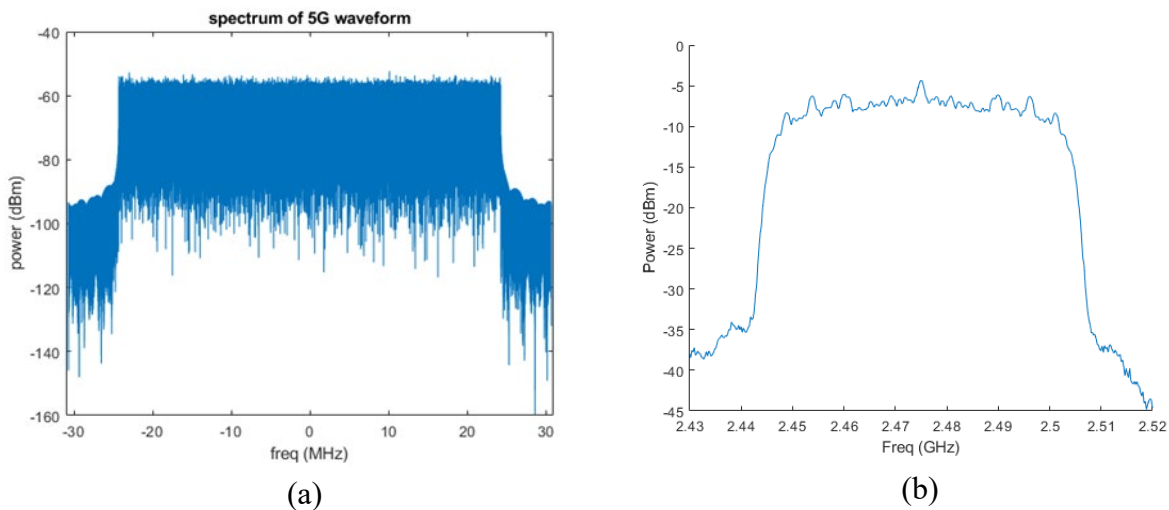


Figure 4-6. Examples of RFI signals in front-door tests. (a) spectrum of a 5G NR baseband waveform; (b) spectrum of simulated RFI signal transmitted by ADALM-PLUTO SDR.

ISR was adopted as an indicator of RFI susceptibility of C2 links to evaluate its functional performance in terms of stable connection, unstable connection, or disconnection. The test setups are shown in Figure 4-7 and Figure 4-8 for tests in the laboratory and in the anechoic chamber, respectively. As illustrated in Figure 4-7, two ADALM-PLUTO SDR devices were programmed to accept the baseband RFI signals through their receive ports from the laptop and to emit RFI signals at selected amplitudes and frequencies through their transmit ports. The SDR devices were configured to run with a 56 MHz bandwidth and a local oscillator tuning frequency range from 70 MHz to 6 GHz. The two RFI signals from the SDRs, each with a bandwidth of 56 MHz and centered at 2.418 GHz and 2.472 GHz, respectively, were coupled using a combiner to create an RFI signal that spans the C2 link spectra of both UAS models at frequencies between 2.39 GHz and 2.5 GHz. The transmit and receive antennas are identical horn antennas that operate in the 2-

18 GHz frequency range. The combined RFI signal was amplified and fed into the transmit antenna, which was positioned a distance from the receive antenna and UAS so both systems receive the RFI signal at the same strength. The receive antenna is also arranged to detect uplink signals from the UAS controller sent to the UAS platforms during testing. The spectrum characteristics and the power level of the received signals were displayed and recorded by the spectrum analyzer attached to the receive antenna. The setup in the chamber is essentially identical to the setup in the laboratory, except the isolation granted by the anechoic chamber itself.

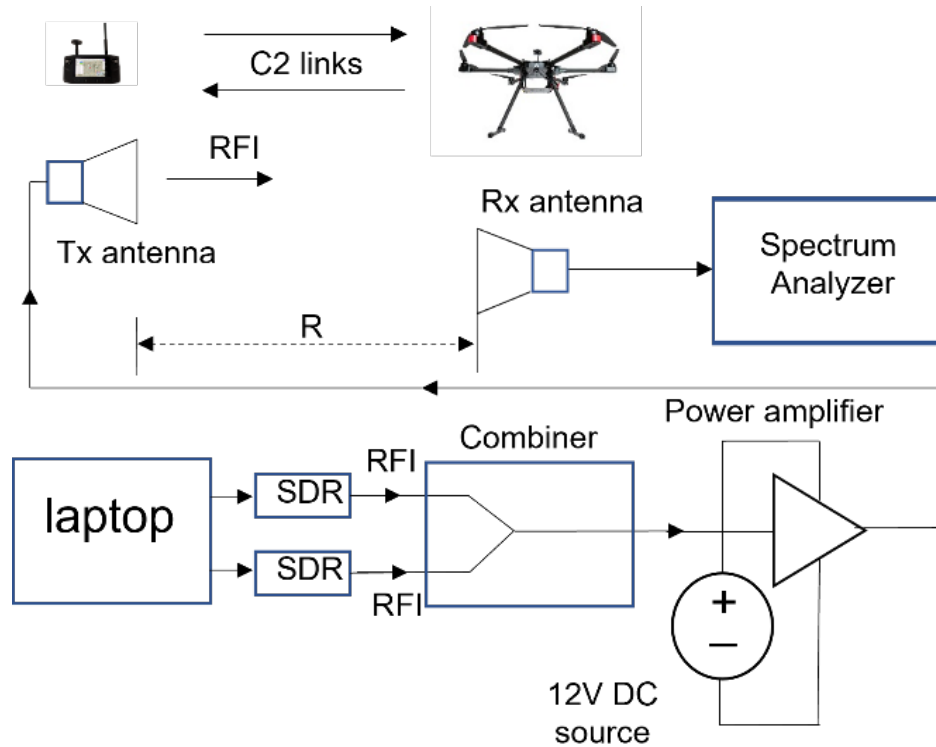


Figure 4-7. Setup in the laboratory for assessment of front-door RFI impacts on UAS

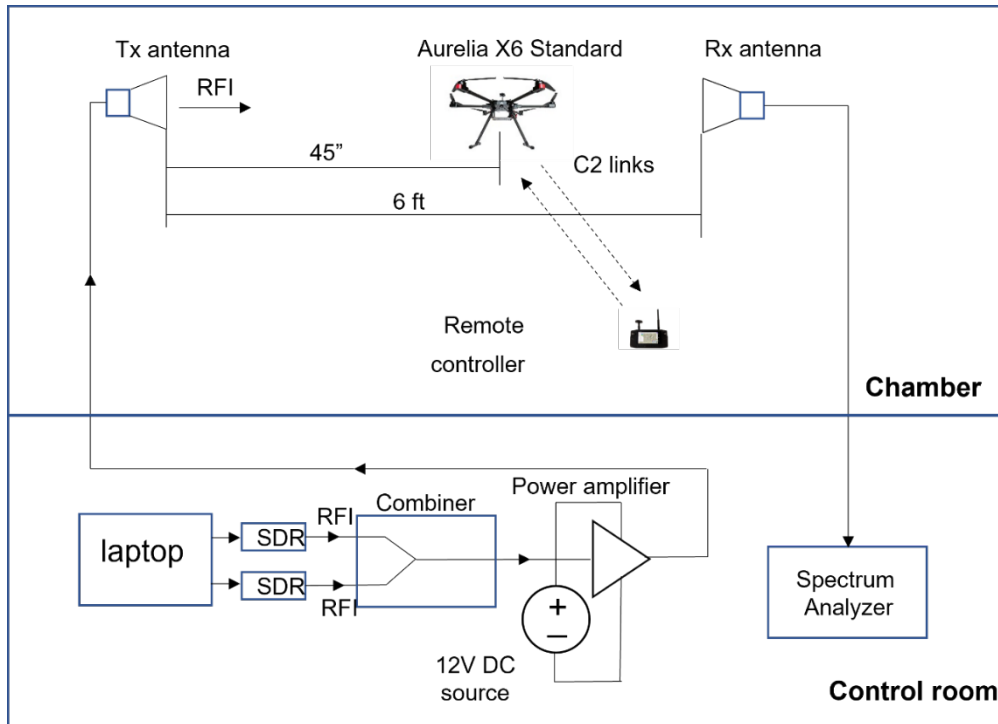


Figure 4-8. Setup in the anechoic chamber for assessment of front-door RFI impacts on UAS

#### 4.4.2 Back-Door RFI Measurements

Back-door RFI assessments span frequencies from 80 MHz to 6 GHz. The selected scenarios of back-door RFI include UAS flying near FM Radio and TV broadcast towers and Airport Surveillance RADAR (ASR). The intended signals in this case are all derived from data that is saved in log files such as battery current and voltage, the outputs from all sensors, autopilot, and remote controller. Figure 4-9 represents an example of the raw signal from the gyroscope, accelerometer, and compass of the QwinOut F450 model without the presence of RFI emissions. Differences in these data in the presence of RFI emissions suggests the possibility of adverse impacts due to back-door RFI. Interference signals in these selected back-door scenarios are simulated signals transmitted from FM Radio and TV broadcast towers as well as ASR antennas (see Figure 4-10 for examples of the spectra associated with these RFI sources). The RFI signals generated for these tests were chosen to have power levels and spectrum characteristics similar to those of the real-world sources (see Figure 4-11 for one example).

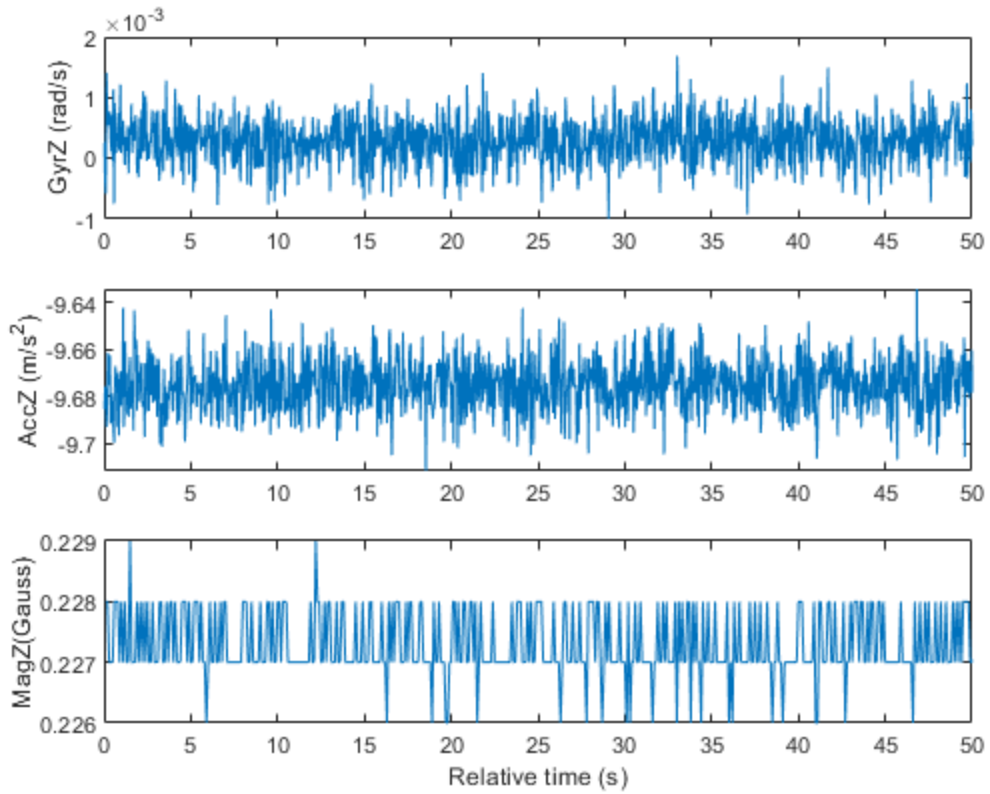


Figure 4-9. Samples of the Z-component from the gyro, accelerometer, and compass of the QwinOut F450 model

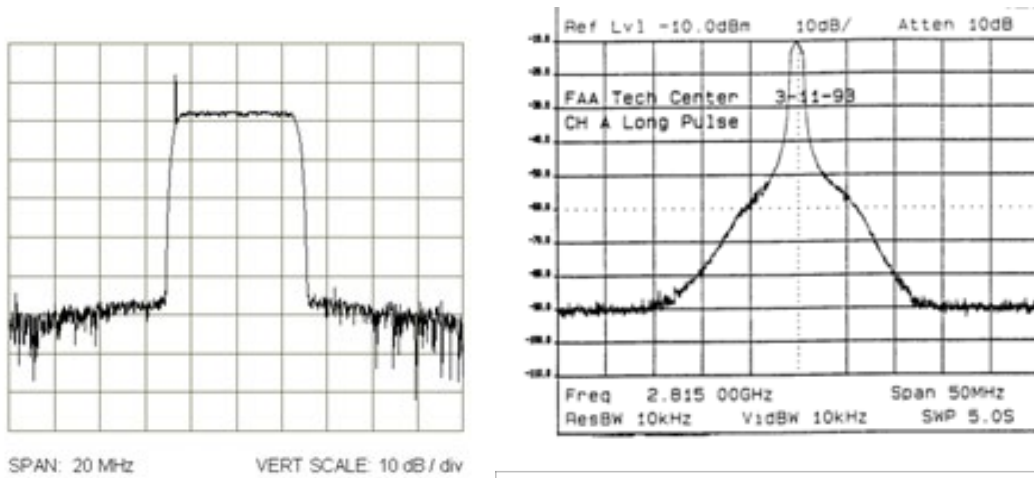


Figure 4-10. The RF spectrum of a TV channel with 6 MHz bandwidth (left) and the spectrum of the ASR long pulse (right)

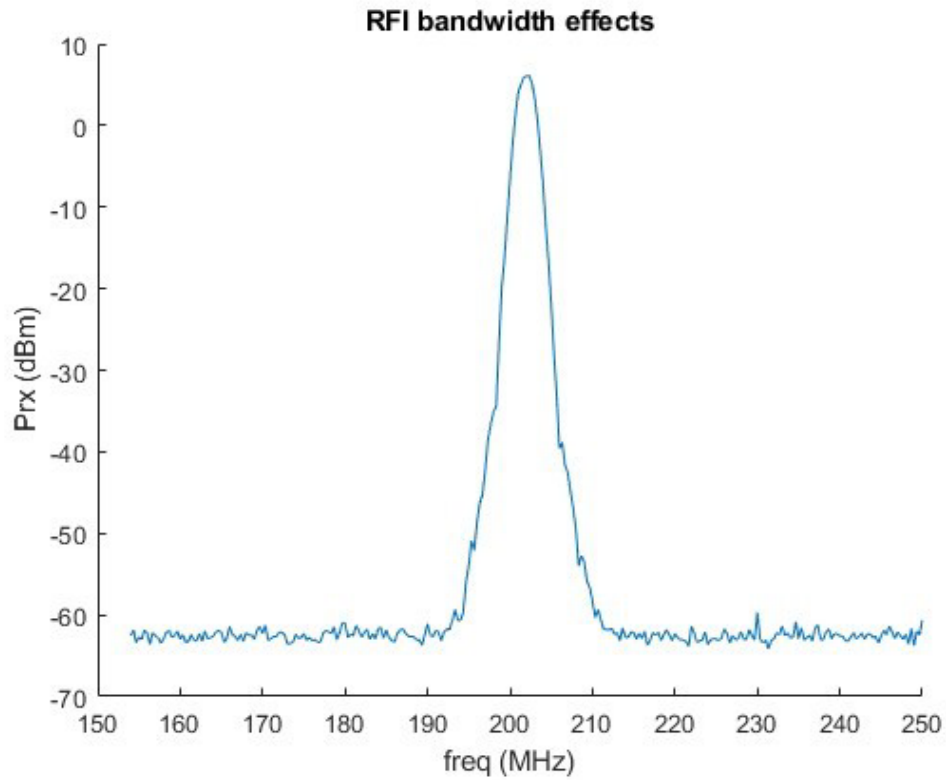


Figure 4-11. Example of RFI signal in backdoor tests: the spectrum of a simulated RFI signal transmitted by ADALM-PLUTO SDR with a 1.5 MHz bandwidth centered around 202 MHz

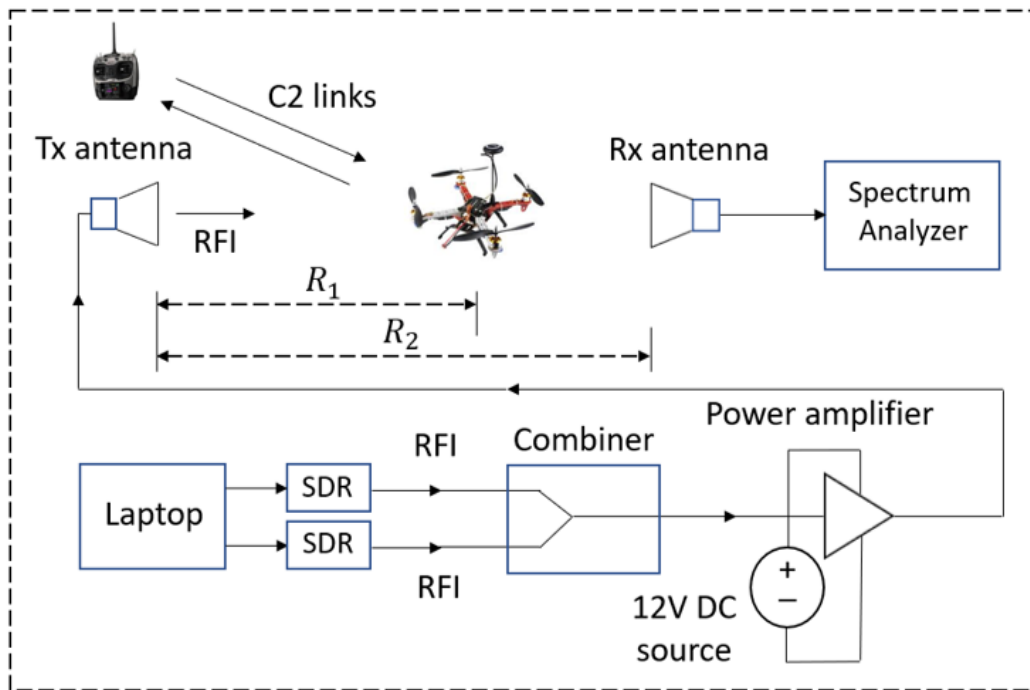


Figure 4-12. Setup for back-door RFI test in anechoic chamber at LTE 4G/5G NR and ASR frequencies. The rectangle in the dashed line annotates the chamber enclosure

Electric field strength,  $E$ , (in V/m) was chosen as an indicator of RFI susceptibility of each UAS sensor. The setup for back-door RFI assessment at frequencies associated with 4G LTE/5G NR and ASR is shown in Figure 4-12. This setup is similar to that in Figure 4-8, but with the following adjustments to achieve the highest electric field strength at the UAS under test: 1) the laptop, combiner, power amplifier and spectrum analyzer were moved from the separated control room into the chamber so that antenna cable losses were small by using short cables (at 2.45 GHz, the transmit cable loss was reduced to 0.6 dB from 5.8 dB, and the receive cable loss was reduced to 2.2 dB from 8.5 dB); 2) high gain power amplifiers (around 36 dB) were employed in the RFI signal transmit path. The test setups for VHF (30 MHz to 300 MHz) back-door RFI effect assessment tests in the chamber are shown in Figure 4-13, Figure 4-14, and Figure 4-15. Only one SDR was used in this scenario, and multiple power amplifiers were used in a cascaded configuration. In the first setup, as illustrated in Figure 4-13, the UAS under test was placed between the transmit and receive antennas. This setup allows the RFI effects on the UAS and the data for electric field strength calibration to be recorded simultaneously. However, the calibration for this setup is not as accurate as in the second setup, shown in Figure 4-15, where field strength calibration is recorded separately to avoid the scattering and blocking effects by the UAS on the power received by the antenna. The first setup in back-door RFI tests was used to quickly identify frequency ranges with significant effects and the second setup was used to confirm findings with accurate electric field strength calibration.

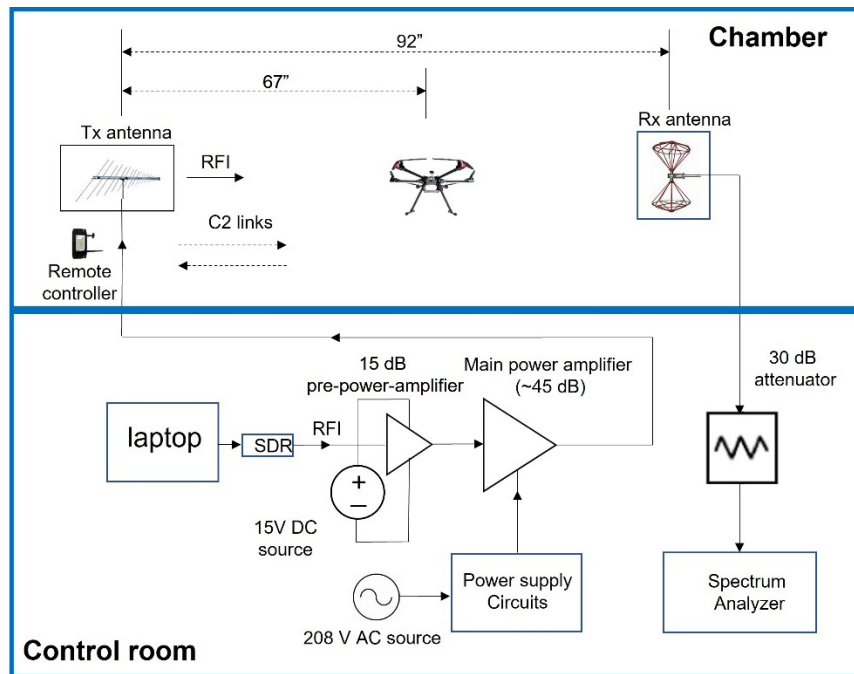


Figure 4-13. First setup in chamber for assessment of VHF back-door RFI impacts on UAS.

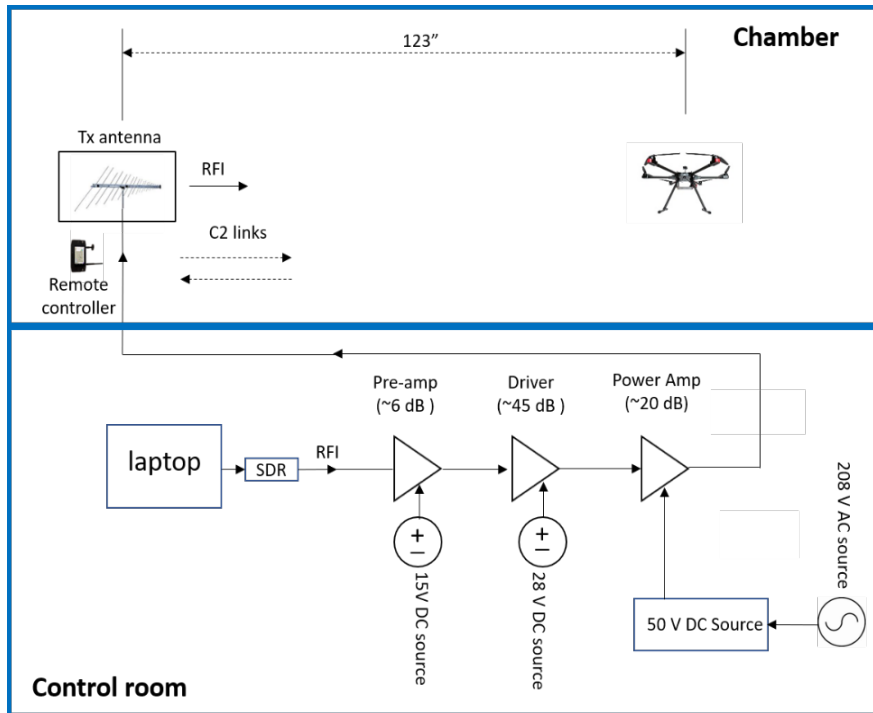


Figure 4-15. Second setup in chamber for assessment of VHF back-door RFI impacts on UAS

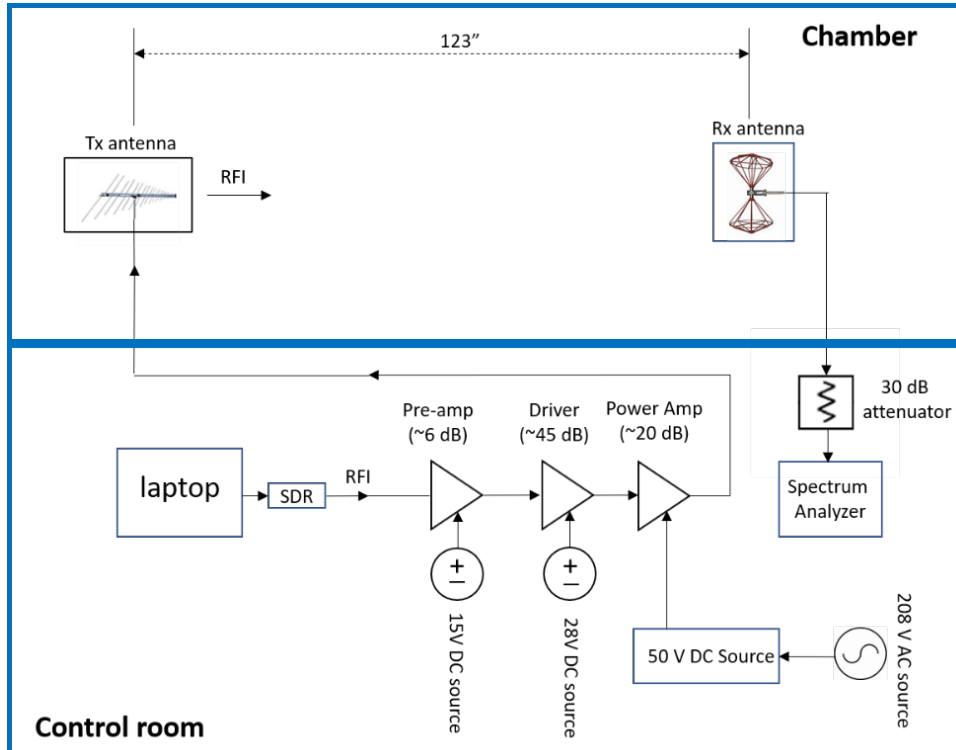


Figure 4-14. Dedicated calibration setup in chamber to assess VHF backdoor RFI impacts on UAS

### 4.4.3 Main Results and Analysis

#### 4.4.3.1 Results of Front-Door RFI Measurements

For both the Aurelia X6 Standard and QwinOut F450 models, in-band RFI effects on C2 links were assessed both in the laboratory and in the anechoic chamber. RFI signals were transmitted with a bandwidth of 112 MHz at various power levels to emulate a barrage scenario.

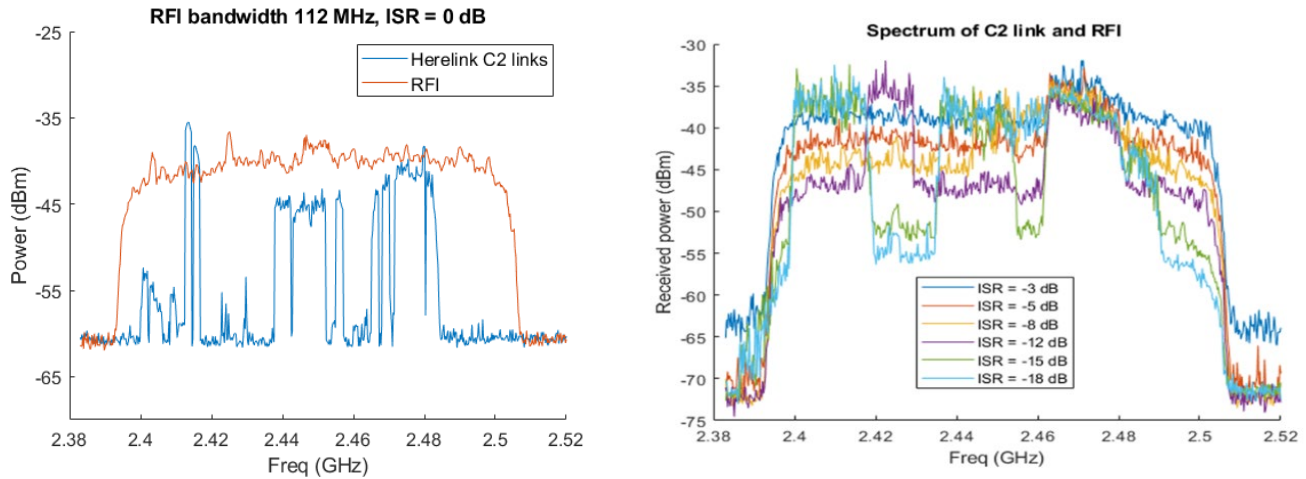


Figure 4-16. RFI barrage of the Herelink C2 across the full bandwidth (left); Spectra of combined C2 link and RFI signals at various ISRs with Aurelia X6 Standard model as the EUT (right)

Table 4-1. RFI effects across the C2 link full bandwidth (S, U, D represent stable, Unstable, Disconnection status, respectively)

Aurelia	ISR (dB)	-12	-9	-6	-3	0
	C2 link Status	S	U	U	U	D
QwinOut	Offset ISR (dB)	12	13	15	16	17
	Actual ISR (dB)	-5	-4	-2	-1	0
	C2 link Status	S	U	U	U	D

Figure 4-16 presents an example showing the RFI spectrum (in red) over the Herelink C2 spectrum (in blue) at  $ISR = 0$  dB and the spectra of the combined C2 link and RFI signals at various ISR levels from -18 dB to -3 dB. This figure shows how the three sub-bands of Aurelia's C2 link signals are gradually overwhelmed by increasing RFI signal strength. The ISR thresholds for stable (S), unstable (U), and disconnected (D) connection were determined by increasing the ISR signal strength with results summarized in Table 4-1. For the Aurelia model UAS, the C2 link maintained a consistent connection whenever the RFI ISR was less than or equal to -12 dB and abruptly disconnected when RFI ISR surpassed 0 dB. RFI ISR values between -12 dB and 0 dB caused intermittent C2 link; the desired signal would occasionally disconnect, then reconnect, then disconnect again, and so on. For the QwinOut model, the C2 link maintained consistent connection for RFI ISR values less than or equal to +12 dB and abruptly disconnected for RFI ISR beyond +17 dB. RFI ISR values between +12 dB and +17 dB caused an inconsistent C2 link. These

results demonstrate that ISR thresholds for the C2 link are distinct for two models. It should be noted that while RFI ISR values for the Aurelia model represent the actual interference-to-signal ratios, those for the QwinOut model are offset in Table 4-1. The C2 link associated with the Aurelia model could not be disabled in the anechoic chamber without overloading the transmitter's Automatic Gain Control (AGC). To ensure that the transmitter emitted at its maximum strength and was not able to increase transmit power with increasing RFI signal level, the controller was placed as far as possible from the UAS and covered with a layer of RF absorber. Similar tests for the QwinOut model were accomplished directly without overloading the transmitter's AGC; the ISR was calibrated at 0 dB. As can be seen in Figure 4-17, AGC greatly boosted the C2 link signal level when the interference signal level was raised from 3 dB to 6 dB. It should be noted that there were no significant AGC effects observed for  $ISR < 3$  dB since the amount of frequency hopping of the C2 link signals maintained the same level for  $ISR = 0$  dB and  $ISR = 3$  dB; only the noise or interference signals increased 3 dB in the case of  $ISR = 3$  dB. After examining the spectra in Figure 4-17, the offset ISR values in Table 4-1 were appropriately adjusted to reflect the actual ISR values for this UAS platform. A method to accurately estimate the AGC effects was given in section 4.5.1.

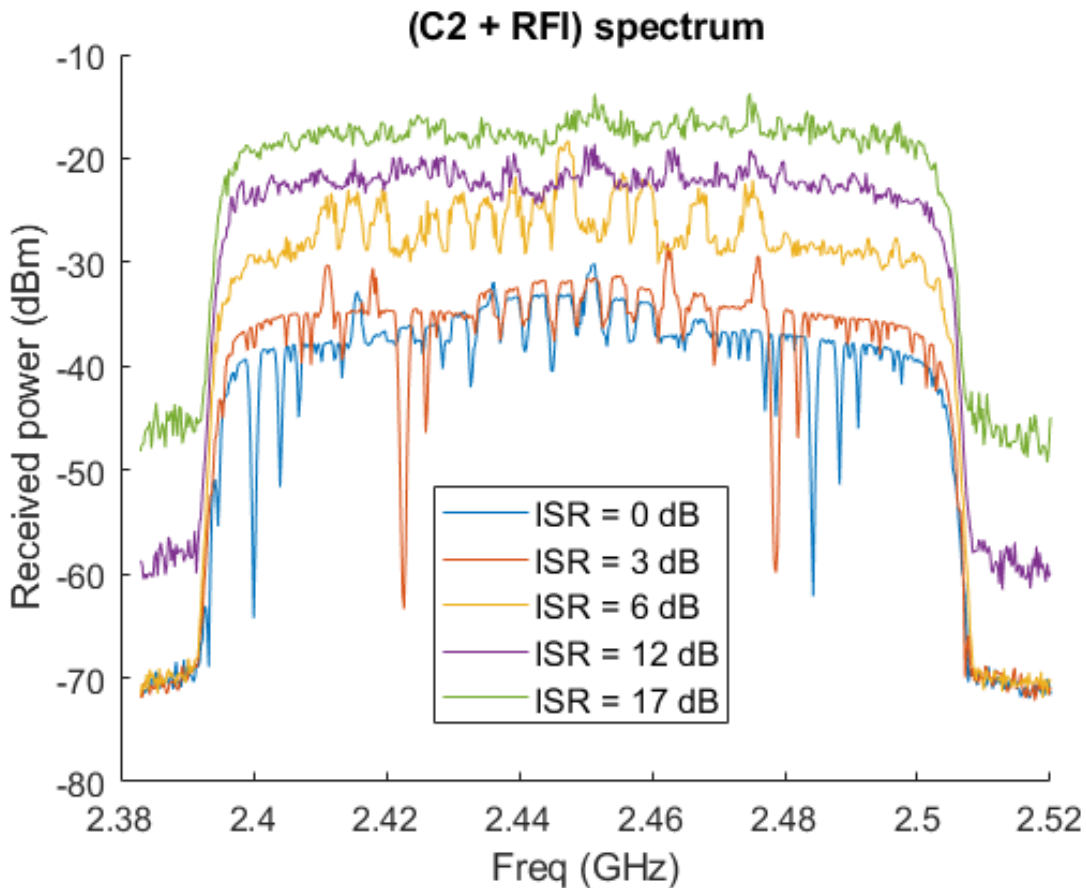


Figure 4-17. Spectra of combined C2 link and RFI signals at various ISR values with QwinOut F450 model UAS as the EUT

As shown in Table 4-2, the ISR ranges identified for stable connection, unstable connection, and disconnection in the laboratory and anechoic chamber measurements match very closely.

Table 4-2. Comparison between laboratory and anechoic chamber measured results with Aurelia X6 Standard UAS model as the EUT (S, U, D represent Stable, Unstable, and Disconnection status, respectively)

Lab	RFI ISR	-12	-9	-6	-3	0
	C2 link status	S	U	U	U	D
Chamber	RFI ISR	-12	-8	-5	-3	0
	C2 link status	S	U	U	D	D

As shown in Figure 4-5, the Herelink C2 link spectrum has three sub-bands with bandwidths of approximately 15 MHz, 20 MHz, and 15 MHz, respectively. To examine the effects of external signals on each channel of this C2 link, RFI signals with an absolute bandwidth of 20 MHz were used across a range of ISR levels and swept across the entire C2 link spectrum. When compared with the full-bandwidth test performed previously, this more focused test is more likely to occur in practice as numerous scenarios exist whereby a 20 MHz signal in this band may unexpectedly be present. For example, if a small UAS operates near a Wi-Fi access point or cellular telephone base station, both Wi-Fi and cellular signals emit energy in this spectrum with bandwidths on the order of 20 MHz. Figure 4-18 displays one example of this scenario where the RFI spectrum is shown in red and the Herelink C2 signal is shown in blue. The results of this measurement are summarized in Table 4-3.

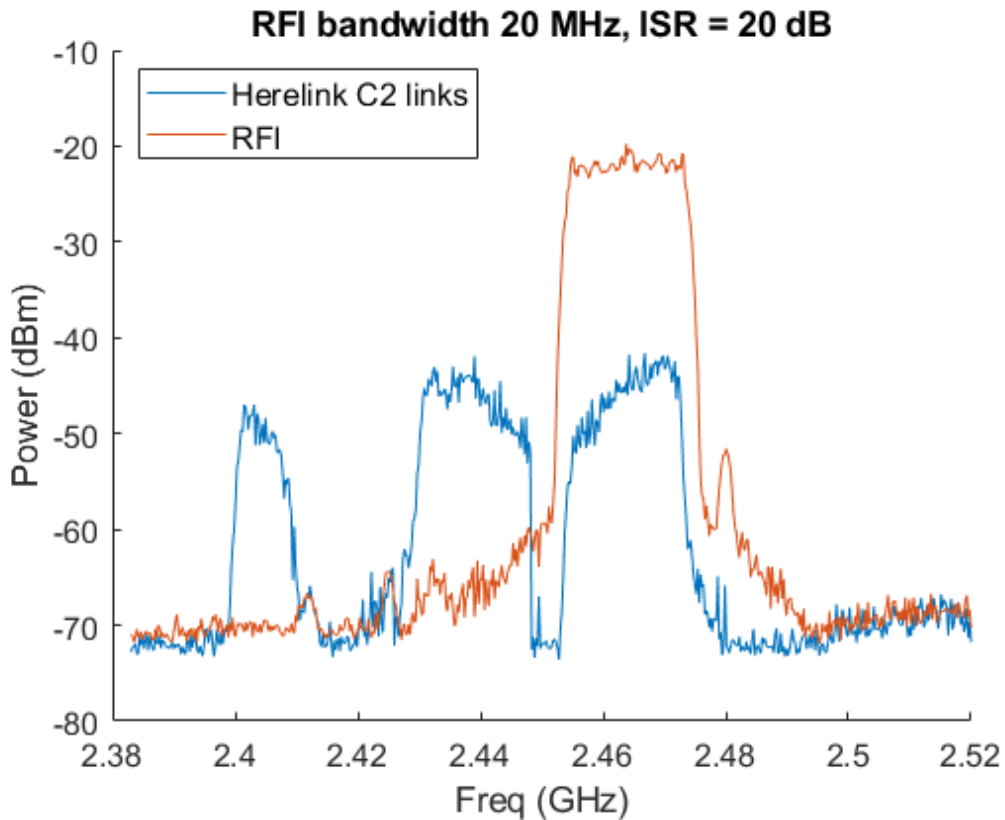


Figure 4-18. RFI barrage of the sub-bands of Herelink C2 links

Note here that whenever Band 1 or Band 2 is masked by RFI signals the C2 link connection remained stable for RFI ISR as high as 20 dB. However, band 3 experienced an unstable connection for interfering signal ISR between 2 dB and 11 dB, and full disconnection for interfering signal ISR greater than or equal to 11 dB.

Table 4-3. RFI effects across C2 link sub-bands (S, U, D represent Stable, Unstable, and Disconnection status, respectively)

	<b>RFI ISR (dB)</b>	<b>20</b>	<b>11</b>	<b>8</b>	<b>5</b>	<b>2</b>
<b>C2 link Status</b>	Band 1	S	S	S	S	S
	Band 2	S	S	S	S	S
	Band 3	D	D	U	U	S

The frequency range of the Herelink band 3 overlaps with Wi-Fi channel 13, which is utilized in the majority of the world, but is not permitted in the United States at high transmitter power levels. Therefore, it is conceivable in other nations for the Aurelia C2 links to be interrupted when the UAS operates near a Wi-Fi access point outside of the United States. This in-band RFI scenario is illustrated in Figure 4-19, along with a safety analysis. Assume that in this instance, the remote controller and the Wi-Fi access point are simultaneously transmitting, with the remote controller transmitting  $P_{tx1}$  Watts at a distance of  $R_1$  from the UAS and the Wi-Fi access point transmits  $P_{tx2}$  Watts at a distance of  $R_2$  from the UAS. The transmit power ratio and range ratio thus define the ISR as

$$ISR = \frac{P_{tx2}}{P_{tx1}} \Big|_{dB} - 20 \log_{10} \frac{R_2}{R_1} \quad (1)$$

The safety threshold RFI ISR should not exceed 2 dB in order to achieve a stable C2 link connection, according to Table 4-3 from measurements. The image in Figure 4-19 depicts the safe and unsafe areas as a function of transmit power and range ratios, with the unsafe region marked by blue points and the RFI ISR scale shown on the color bar. Two particular coordinates represent extreme situations

- 1)  $\frac{R_2}{R_1} = 0.1, \frac{P_{tx2}}{P_{tx1}} = -17 \text{ dB}$ : This point is located at the bottom-left of the data shown in Figure 4-19. This point represents the scenario when the Wi-Fi access point is 10 times closer to the UAS than the remote controller. In this case, the Wi-Fi transmit power must be 17 dB lower than the remote controller power in order to assure a stable connection
- 2)  $\frac{R_2}{R_1} = 2.5, \frac{P_{tx2}}{P_{tx1}} = +10 \text{ dB}$ : This point is located at the top-right of the data shown in Figure 4-19. This point represents the scenario when the Wi-Fi transmit power is 10 dB greater than the power of the remote controller. In this case, the distance from the Wi-Fi access

point to the UAS must be 2.5 times greater than the distance from the remote controller to the UAS.

The next adjacent frequency band to Herelink’s band 3 is 2496 MHz to 2690 MHz, which is the downlink frequency spectrum for 5G NR band n41 and 4G LTE channel b41. If the UAS approaches a b41/n41 base station, the unwanted emissions from the base station could overwhelm the C2 link.

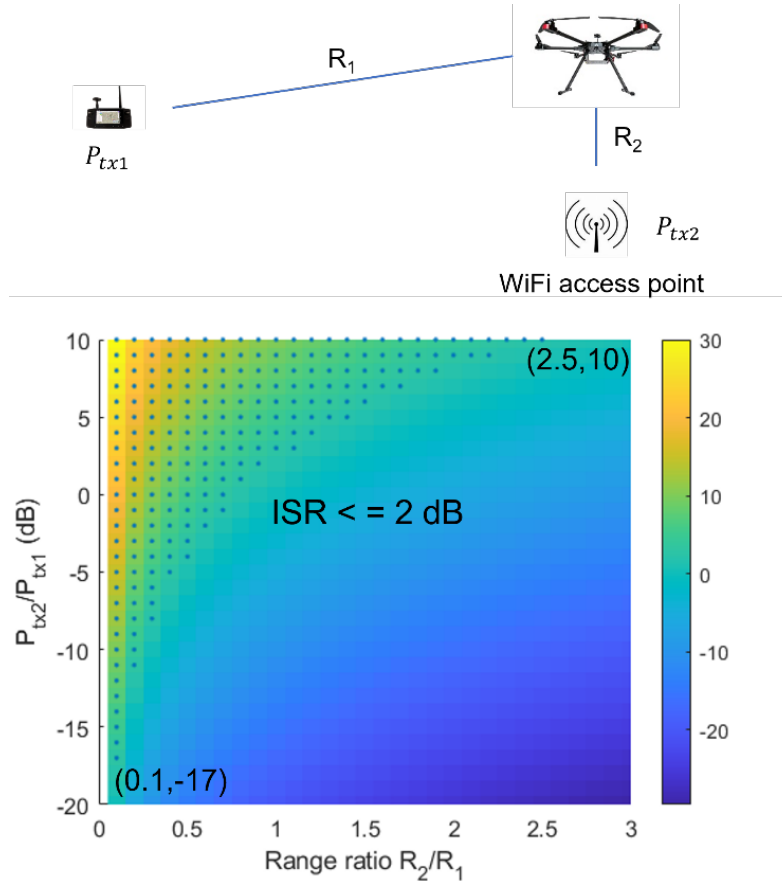


Figure 4-19. Scenario of in-band RFI from Wi-Fi channel 13

To examine this adjacent band RFI scenario, relevant regulations and technological requirements regarding unwanted radio emissions and out-of-band emissions must be considered. The former emissions are produced by the modulation process and non-linearity in the transmitter. These emissions occur immediately outside the channel bandwidth. The latter emissions are caused by unintended transmitter effects like harmonic emission, parasitic emission, intermodulation products, and frequency conversion products. The maximum permissible unwanted emissions of b41/n41 across the Herelink band 3 are allowed to be -13 dBm in accordance with the base station unwanted emission restrictions for 20 MHz channel indicated in ETSI TS 136 141 V15.4.0 (2018-10). As with the previous scenario, the controller and base station are assumed to transmit with respective transmit powers of  $P_{tx1}$  and  $P_{tx2}$  at distances of  $R_1$  and  $R_2$  from the UAS. If the maximum transmit power of the controller is  $P_{tx1} = 20$  dBm and the base station power is  $P_{tx2} = -13$  dBm, then the RFI ISR can be estimated according to Equation (2).

$$ISR = \frac{P_{tx2,unwanted\ emissions}}{P_{tx1}} \Big|_{dB} - 20\log_{10} \frac{R_2}{R_1} = -33 - 20\log_{10} \frac{R_2}{R_1} \quad (2)$$

The RFI ISR power as a function of  $R_2/R_1$  is plotted in Figure 4-20 according to Equation (2). The red vertical line separates the area into safe and unsafe zones using a RFI ISR value of 2 dB as the threshold at which  $\frac{R_2}{R_1} = 0.017$ . When  $\frac{R_2}{R_1} < 0.017$ , the UAS is approximately 60 times closer to the base station than from its controller and there is a strong likelihood that the UAS C2 link could become unstable or disconnected.

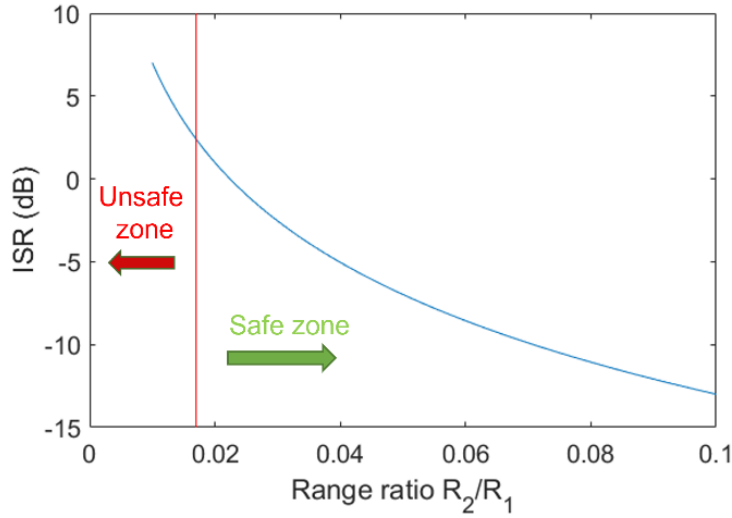


Figure 4-20. Scenario of adjacent band RFI from 4G LTE/5G NR channel b1/n41.

Front-door RFI impacts on the C2 downlink of UAS platforms using the setup as that of Figure 4-7 was also investigated, but with the placements of the remote controller and the UAS exchanged. The C2 downlink spectra of this scenario resemble those in Figure 4-5. However, the C2 downlink of the Aurelia model did not disconnect for the downlink as it did for the uplink when only band 3 was obscured by RFI signals at high ISR levels.

#### 4.4.3.2 Results of Back-Door RFI Measurements

##### 4.4.3.2.1 Tests at 4G LTE/5G NR and ASR Frequencies

For the Aurelia UAS platform, back-door RFI effects were assessed at four frequencies 1.73 GHz, 2.8 GHz, 4.5 GHz, and 5.8 GHz using the setup in Figure 4-12. As shown in Figure 4-21, the received power displayed on the spectrum analyzer was  $P_{sp} = -8.6\text{ dBm}$ ,  $+0.9\text{ dBm}$ ,  $-8.4\text{ dBm}$ , and  $-11\text{ dBm}$  respectively for the RFI signal transmitted toward the UAS at these frequencies. With the known distances between the transmit and receive antennas ( $R_{tx-rx} = 6\text{ ft}$ ), the distance between transmit antenna and UAS ( $R_{tx-UAS} = 16\text{ in}$ ), the receive antenna gain ( $G_{rx} = 7.5\text{ dB}$ ) and cable loss ( $L_{cbrx} = 2.2\text{ dB}$ ), the electric field strength at the UAS is estimated according to:

$$E = \left(\frac{F_c}{c}\right) \left(\frac{R_{tx-rx}}{R_{tx-UAS}}\right) \sqrt{\frac{4\pi Z_0 P_{sp}}{L_{cbrx} G_{rx}}} \quad (3)$$

Where  $F_c$  is the center frequency,  $c$  the speed of light in vacuum, and  $Z_0 = 377\ \Omega$  the characteristic impedance of vacuum.

For the QwinOut model, the back-door RFI effects were assessed at 5 frequencies of 1.96, 2.13, 2.55, 2.8, and 3.8 GHz using the setup in Figure 4-12. As shown in Figure 4-21, the received power displayed on the spectrum analyzer  $P_{sp}$  was 2.99, 2.95, 2.86 dBm, 2.81 dBm, and 2.6 dBm, respectively for the RFI transmitted to the UAS at these frequencies. The distances between the transmit and receive antennas was  $R_{tx-rx} = 5 ft$ , and the distance between the transmit antenna and UAS was  $R_{tx-UAS} = 24in$ .

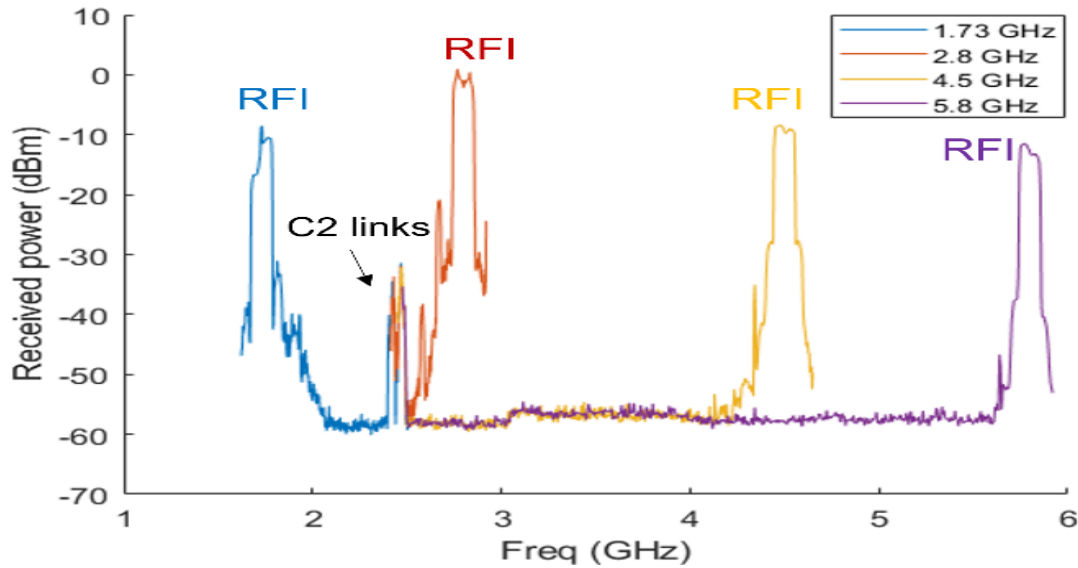


Figure 4-21. RFI with 112 MHz bandwidth applied to Aurelia X6 Standard for back-door impact evaluation

The electric field strength estimated according to Equation (3) is given in Table 4-4, along with the potential RFI sources such as ASR, the 4G LTE/5G NR band downlinks at the measurement frequencies (except for 1.73 GHz, which is the b4/n4 band uplink). The maximum and minimum electric field strength are about 55 V/m and 11.5 V/m for ASR and b3/n3 bands respectively. The electric field strength is substantially smaller at 1.73 GHz due to the transmit antenna gain loss this far outside of its operating frequency band. The back-door RFI impacts on both UAS platforms were assessed by comparing the raw data of the UAS sensors and its autopilot outputs in terms of their mean value and variance during the no-RFI and with-RFI periods. The raw data from the Aurelia UAS accelerometer, gyroscope, and magnetometer measurements in the z-axis, as well as the autopilot readings for pitch, roll and yaw angles, are plotted in Figure 4-22 as an illustration of this comparison for the ASR scenario. The values of mean and standard deviation in this scenario are listed in Table 4-5.

For both UAS platforms, no significant back-door impacts were observed due to these RFI electric field strengths at the measurement frequencies.  $R_s$  in Table 4-4 is the safe distances for the UAS from the RFI sources (cellphone base station and ASR) estimated according to Equation (4) based on typical transmit power  $P_{tx}$  and antenna gain  $G_{tx}$  of each RFI source, where values are taken from [54] and included in the table. The values of  $R_s$  provided are conservative because even at higher electric field strengths, which we could not achieve with our equipment, the UAS might still not be affected and may be able to fly closer to the RFI sources without impact.

Table 4-4. Calculated safe distances of two UAS platforms from RFI sources

RFI source	Aurelia X6 Standard				QwinOut F450				
	b4/n4	ASR	n79	n46	b2/n2	b4/n4	b41/n41	ASR	n77
<b>Fc (GHz)</b>	1.73	2.8	4.5	5.8	1.96	2.13	2.55	2.8	3.8
<b>Psp (dBm)</b>	-8.55	0.89	-8.38	-11.45	2.99	2.95	2.86	2.81	2.60
<b>E (V/m)</b>	11.47	55.02	30.41	27.53	27.25	29.49	34.94	38.08	50.48
<b>Ptx (W)</b>	NA	25000	30	30	30	30	30	25000	30
<b>Gtx (dB)</b>	NA	34	18	18	18	18	18	34	18
<b><math>R_s</math> (m)</b>	NA	789	8	9	9	8	7	1140	5

$$R_s = \sqrt{\frac{Z_0 P_{tx} G_{tx}}{4\pi E^2}} \quad (4)$$

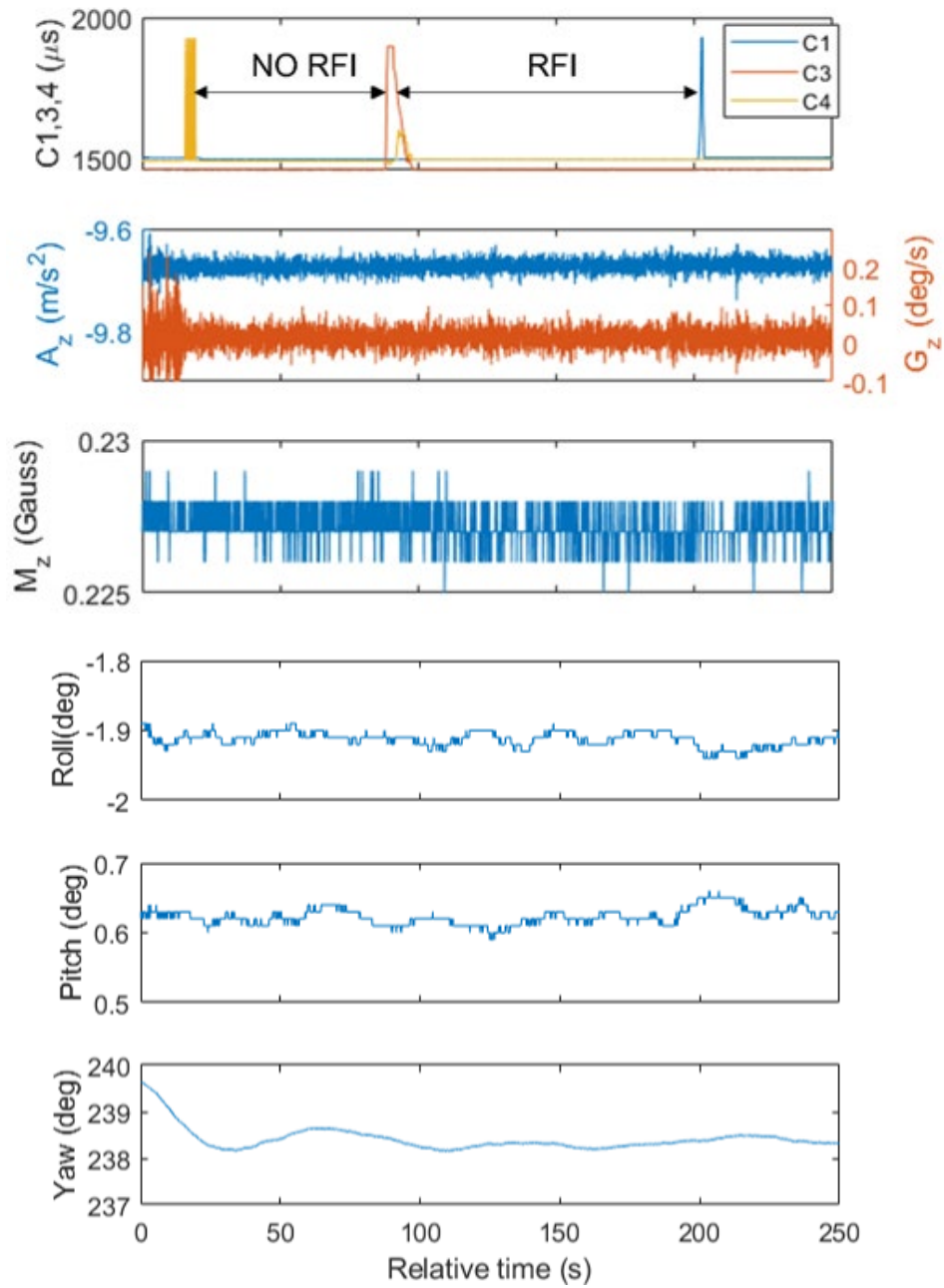


Figure 4-22. Output data of the sensors and autopilot of the Aurelia X6 Standard model during No-RFI and RFI periods ( $E = 55 \text{ V/m}$  generated by RFI emissions at  $F_c = 2.8 \text{ GHz}$ ).

Table 4-5. Mean and standard deviation of the sensor and autopilot output of the Aurelia X6 Standard model in No-RFI and RFI periods for ASR RFI scenarios

		IMU		MAG	Attitude		
		GryZ (rad/s)	AccZ (m/s <sup>2</sup> )	MagZ (Gauss)	Roll (deg)	Pitch (deg)	Yaw (deg)
<b>No RFI</b>	mean	2.78e-04	-9.67	0.227	-1.91	0.62	238.43
	std	3.89e-04	0.0113	5.741e-04	0.0072	0.0096	0.1624
<b>With RFI</b>	mean	2.52e-04	-9.67	0.227	-1.91	0.62	238.27
	std	3.93e-4	0.0117	5.743e-04	0.0094	0.0098	0.0577
$\Delta$	mean	-2.58e-05	0.0026	-2.87e-04	-0.0034	-0.0040	-0.16
	std	4.44e-06	3.54e-04	1.69e-04	0.0023	2.10e-04	-0.10

#### 4.4.3.2.2 Tests at VHF Frequencies

The VHF frequency band contains signals transmitted by FM radio and TV broadcast which have very high transmitter power. The test setup shown in Figure 4-13 was initially used together with RFI signals having 55 MHz bandwidth to assess their effects on both UAS platforms. As shown in Figure 4-23, the frequencies were scanned from 60.5 MHz to 335.5 MHz to search for any significant back-door RFI effects.

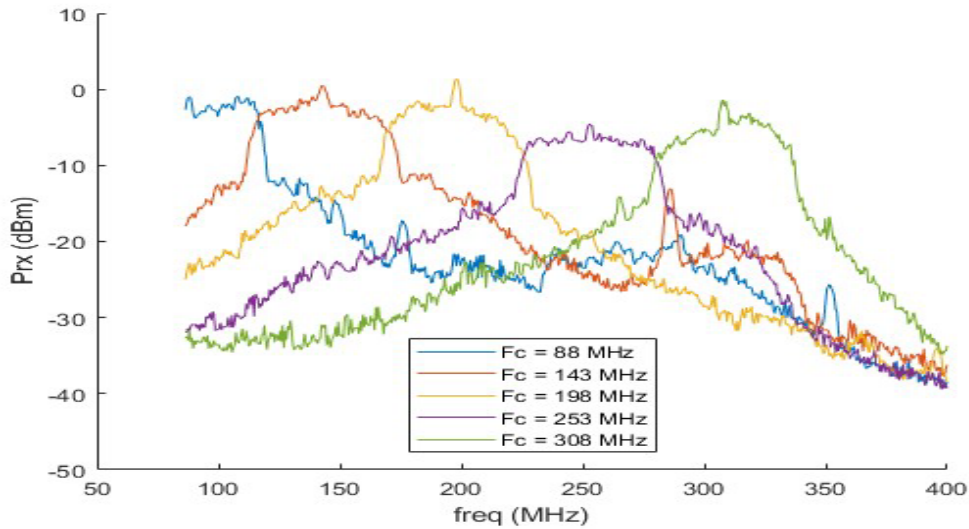


Figure 4-23. Frequency scanning to search for back-door RFI effects

Because only two power amplifiers were used with gain of +15 dB and +45 dB, respectively, the electric field strength was limited to 23-24 V/m at the UAS. For the Aurelia model, two C2 links were affected by RFI emissions centered around 88 MHz. The top panel of Figure 4-24 depicts several abrupt changes in Received Signal Strength Indication (RSSI) during RFI emissions, and

the bottom panel presents the subsystem error information recorded in the log file, indicating that the UAS lost the connection with its remote controller four times.

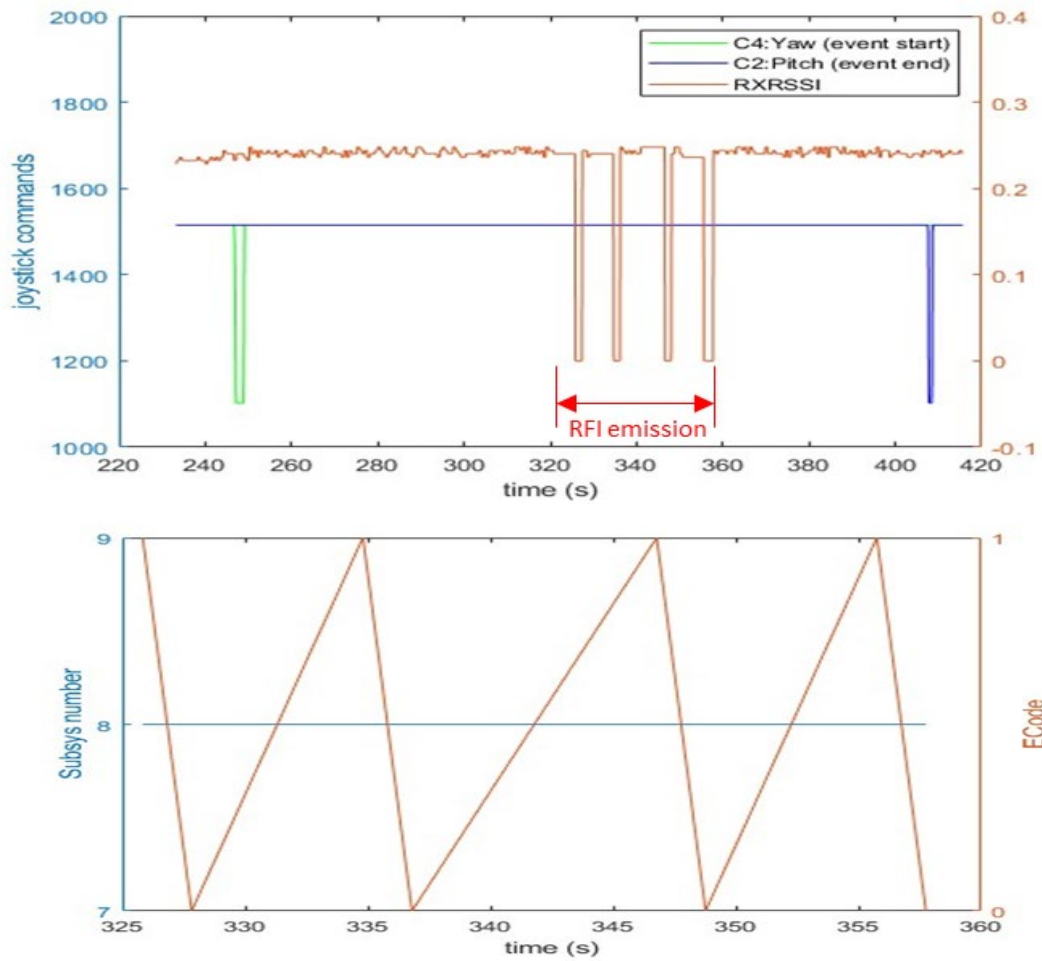


Figure 4-24. Back-Door effects observed on the C2 links of the Aurelia X6 Standard model around 88 MHz

For the QwinOut F450 model, significant back-door effects were observed at center frequencies of 143 MHz, 198 MHz, and 253 MHz. The effects include interruptions to the C2 link and inaccurate compass readings. Figure 4-25 presents the remote controller input commands recorded in the log file. The roll, pitch, yaw, and throttle input should all be flat without any variations because the controls were not moved during this period. However, with RFI emission, ripples were observed in roll, pitch and yaw commands, and abrupt changes in throttle commands, caused by back-door coupling. Figure 4-26 presents the UAS compass data and heading angle recorded in the log file. During the RFI emission period, we observed abrupt changes in compass data (Figure 4-26 top), and divergence in heading (Figure 4-26 bottom). No back-door effects were observed in the data associated with the barometer, accelerometer, and gyroscope.

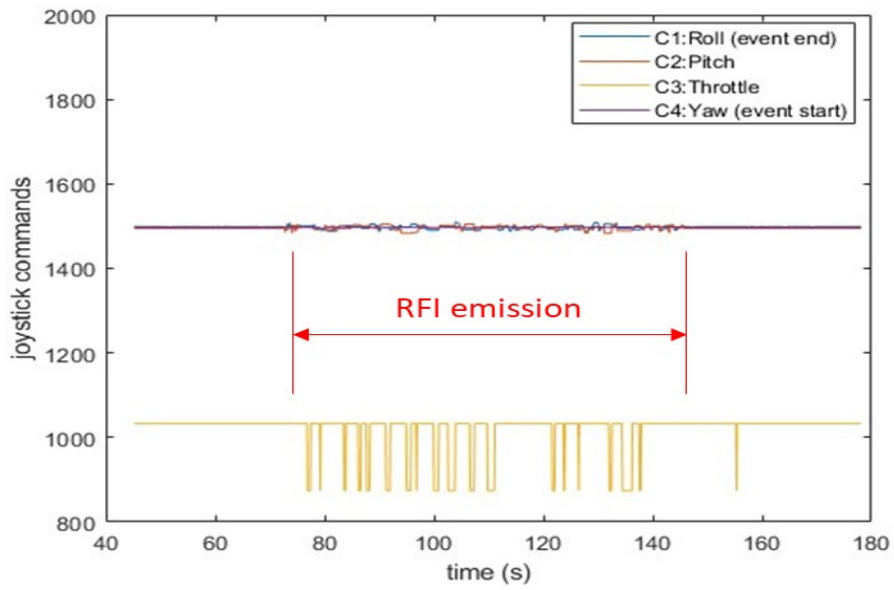


Figure 4-25. Back-door effects observed at 198 MHz in the commands of the QwinOut F450 model's remote control

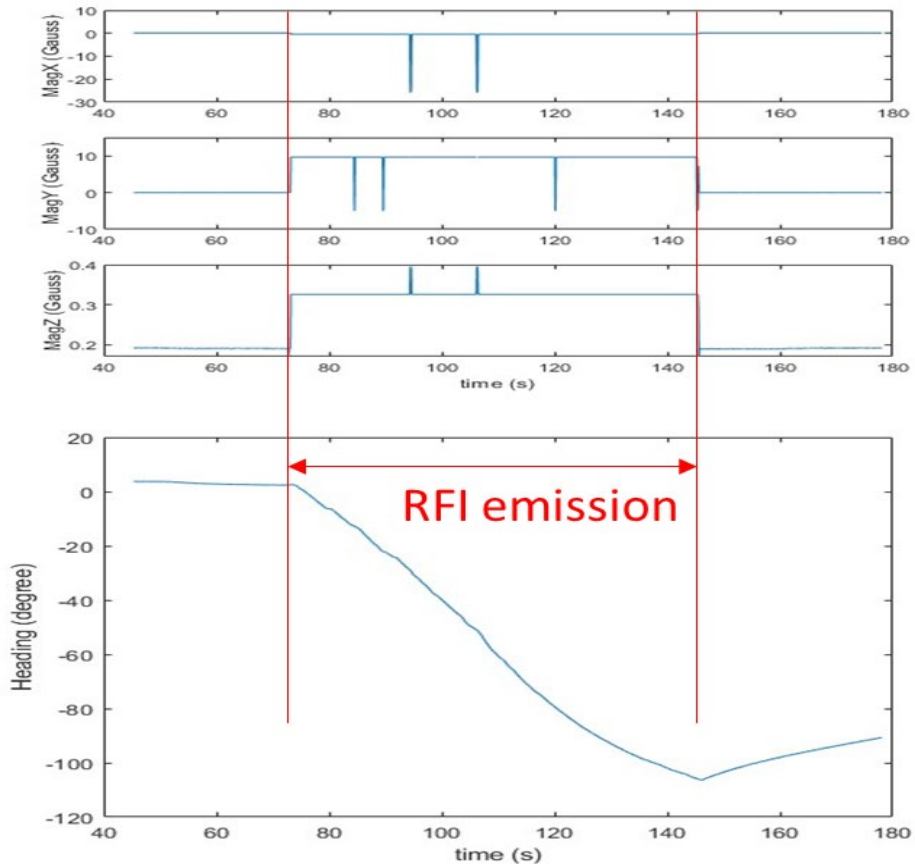


Figure 4-26. Back-door effects observed at 198 MHz in the compass data (top) and heading (bottom) of the QwinOut F450 model.

Based on the above findings, additional tests were performed to pinpoint the frequency bands, power level thresholds and bandwidth effects of RFI within the VHF frequency band on the Aurelia X6 standard and QwinOut F450 models. Test setups were modified from the setup shown in Figure 4-14 and Figure 4-15 to provide more accurate measurement results. Three modifications were made to these setups: 1) The RFI measurements and calibration measurements were taken separately so that they would not affect each other; 2) The UAS platforms were moved farther from the transmit antenna to meet the far-field condition; and 3) Three power amplifiers were cascaded (Gain~6, ~45, ~20 dB, respectively) to compensate for the increased distance between UAS platforms and the transmit antenna.

For the Aurelia model, 44 combinations of RFI frequency, bandwidth, and power levels (See Table A5 in Appendix for some of these combinations) were tested with calibration completed for each combination. The spectrum of some of the tested combinations is shown in Figure 4-27.

For the QwinOut model, 81 combinations of RFI frequency, bandwidth, and power levels (See Table A6 in Appendix for some of these combinations) were tested with calibration for each combination. The spectrum of some of the tested combinations is shown in Figure 4-28.

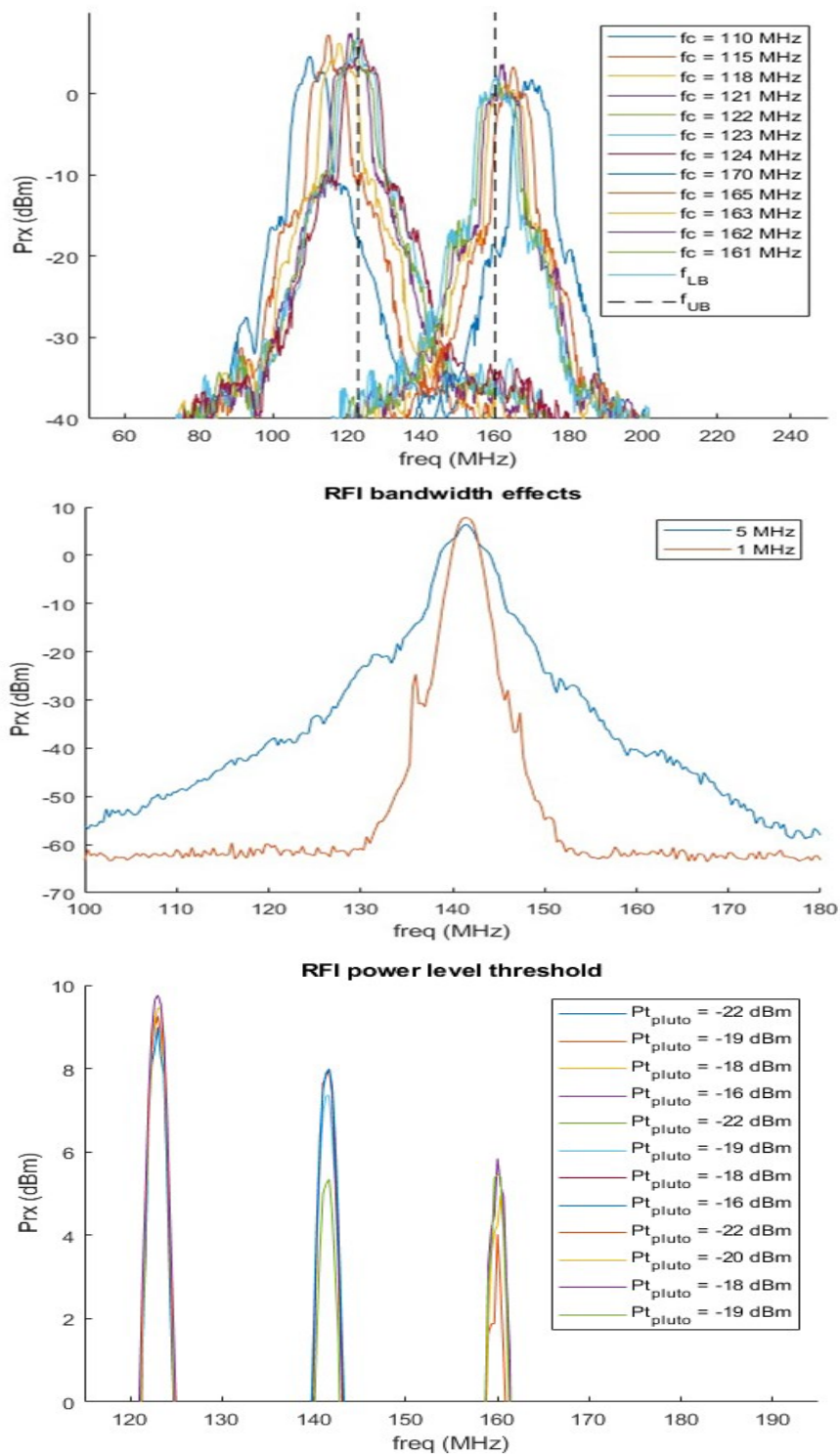


Figure 4-27. Determination of RFI frequency range (top), bandwidth (middle, and power level threshold (bottom) for the Aurelia X6 Standard model.

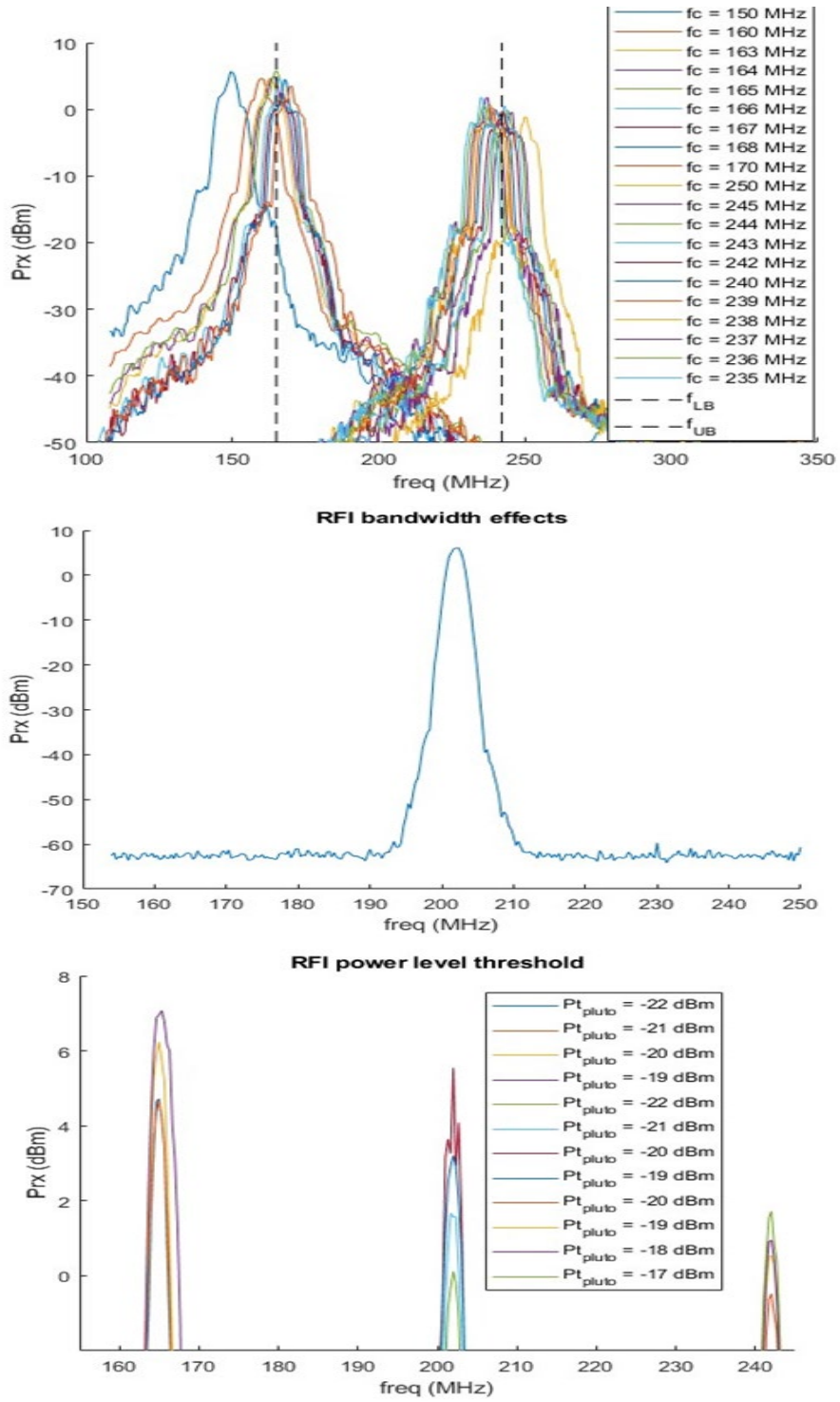


Figure 4-28. Determination of RFI frequency range (top), bandwidth (middle), and power level threshold (bottom) for the QwinOut F450 model

The frequency range that caused significant RFI effects on the Aurelia model's C2 links was determined to extend from 123 MHz to 160 MHz with measurement resolution of 1 MHz. Figure 4-29 presents an example from Event# 6 in Table A5 in the Appendix under the "Frequency range search". The battery current values (Curr) changed whenever the simulated VHF interference signals were transmitting. This current variable serves as a very good indicator for RFI transmission (the effects on battery current variation due to long-time exposure to VHF RFI emissions should be further investigated and evaluated). As the RFI effects became significant, we can observe that the RSSI, the received signal strength indicator for the remote control abruptly dropped to zero sporadically, indicating that the C2 links were disrupted.

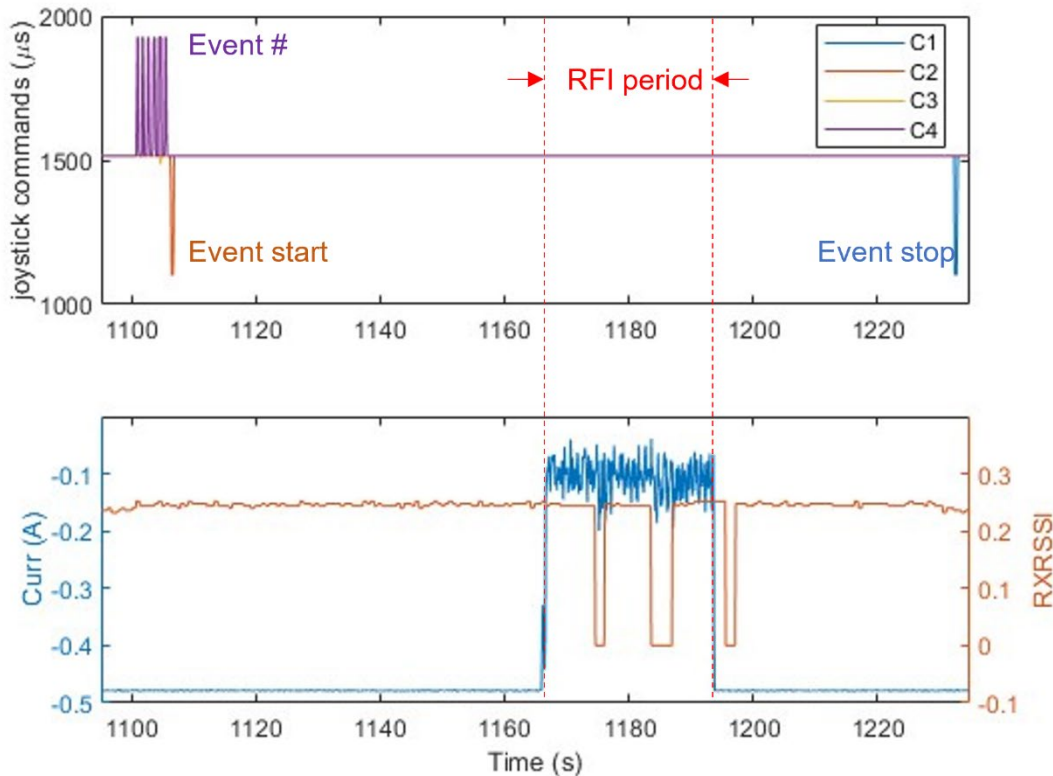


Figure 4-29. Significant back-door RFI effects on the battery current and C2 links of the Aurelia X6 Standard model

The frequency range that caused significant RFI effects on the QwinOut model's C2 links, compass and GPS was determined to be from 165 MHz to 242 MHz with measurement resolution of 1 MHz. Figure 4-30 presents two examples. The first example (the top two panels) corresponds to Event# 9 in Table A6 in the Appendix under the "Power level determination". We see the "Event stop" marker sent by radio channel C1 did not get recorded in the log file because the C2 links were disrupted by RFI signals. We also see that the disk compass output in z-axis jumped from the normal value 0.18 Gauss to a mean value of 0.231 Gauss with a standard deviation of 0.0045 Gauss. After the RFI emission stopped, the compass output did not get back to the normal value, but rather stayed at the mean value of 0.231 Gauss with a smaller standard deviation of 0.0008 Gauss. The servo rail voltage remained at a constant value without any variations due to the back-

door RFI effects. The testing conditions of the second example (the bottom panel) are the same as that for the first example except the SDR transmit power was 3dB higher. We see that in this case, the disk compass output in z-axis jumped from the normal value to a higher mean value of 0.256 Gauss with a higher standard deviation of 0.0077 Gauss. After the RFI emission stopped, the compass output did not return to the normal value but dropped slightly to a mean value of 0.234 Gauss with a standard deviation of 0.0010 Gauss. In addition, due to higher RFI intensity, the value of GPS accuracy parameter Horizontal Dilution of Precision (HDop) was changed from 99.99 (normal value when no satellites were visible in the chamber) to -0.01. It should be noted that the outputs of the compass inside in the PX4 autopilot box were not significantly affected in both examples.

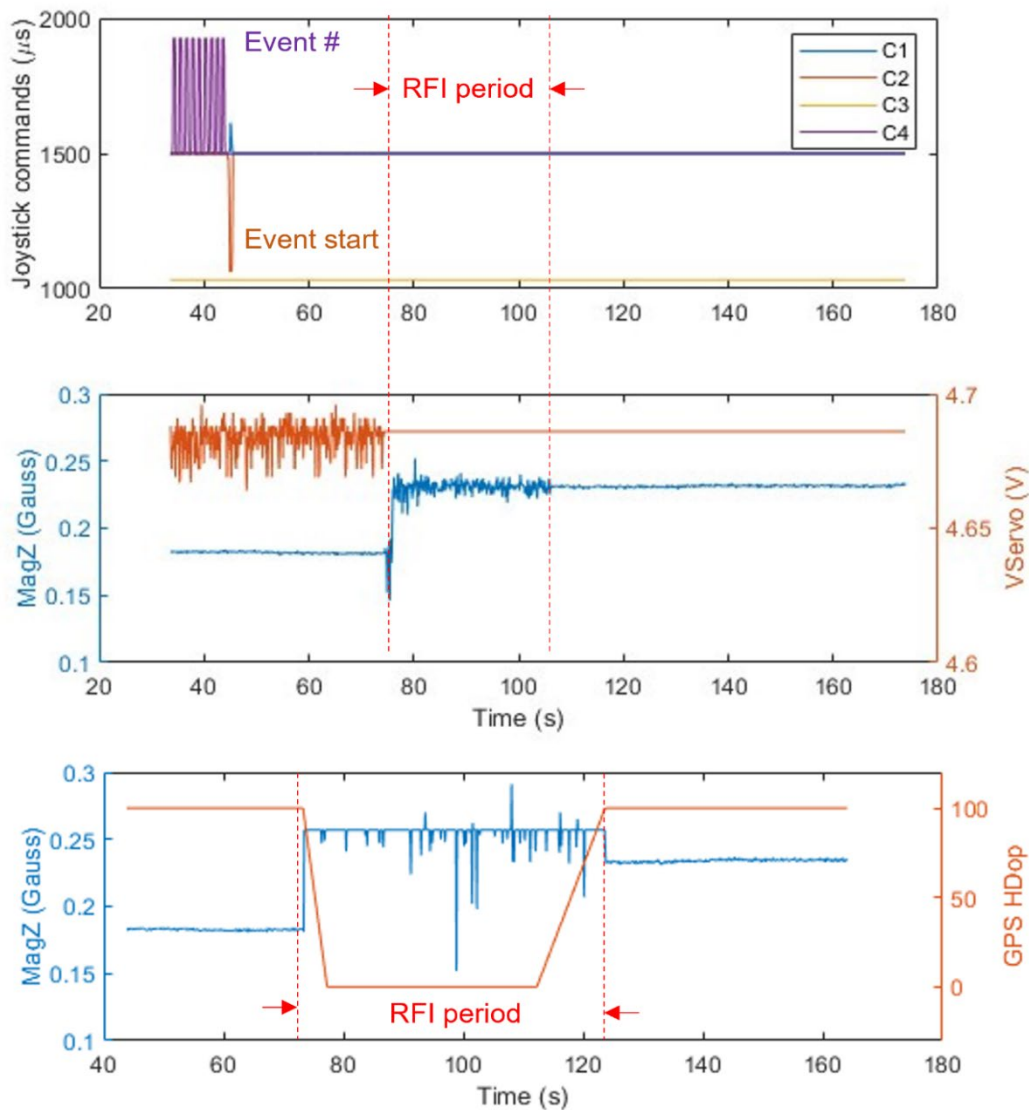


Figure 4-30. Significant back-door RFI effects on the compass, system power, GPS, and C2 links of the QwinOut F450 Standard model

Electric field strength thresholds associated with RFI signals were found to depend on frequency for both models. These thresholds were determined with measurement resolution of 1 dB for transmit power at the lower frequency boundary  $f_{LB}$ , middle  $f_{MID}$  and the upper frequency boundary  $f_{UB}$  of the frequency bands that have significant RFI effects, which are 180, 171 and 137 V/m at 123, 141.5 and 160 MHz, respectively for the Aurelia model, and 176, 116, and 113 V/m at 165, 202 and 242 MHz, respectively for the QwinOut model. The minimum bandwidth that has been tested with significant RFI effects is 1.5 MHz.

A variety of shielding tests were conducted to confirm and identify back-door RFI coupling paths. A few examples of these shielding tests are displayed in Figure 4-31. Back-door coupling paths have been identified through these shielding tests, which includes the Herelink box for the Aurelia model, and any conductive part of the QwinOut model except its antenna for command and telemetry.

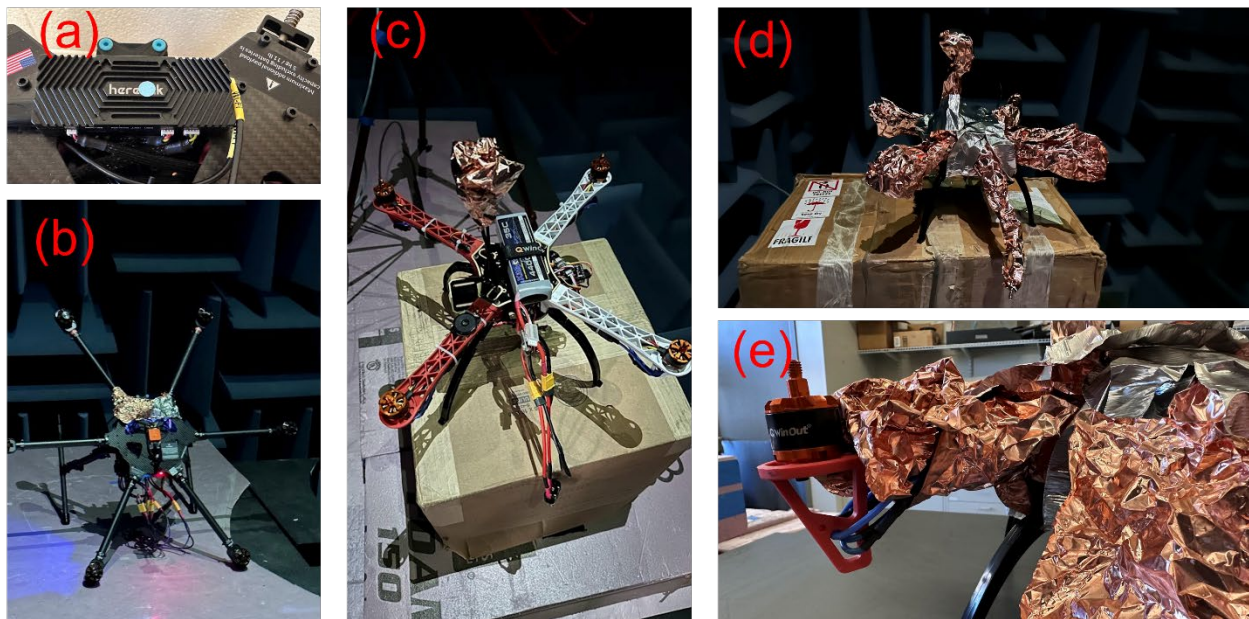


Figure 4-31. (a) The Herelink box on the Aurelia model; (b) the Herelink box shielded on the Aurelia model; (c) the GPS and compass disk of the QwinOut model shielded; (d) complete shielding of the QwinOut model except its antenna for commands and telemetry; (e) everything shielded except one motor and the antenna.

Table 4-6. Sumarized findings from VHF RFI and shielding tests

UAS model	Identified frequency range (MHz)	Electric Field Strength Threshold (V/m)			Minimum bandwidth tested (MHz)	RFI effects	Coupling path
		$f_{LB}$ (MHz) 123(A)/165(Q)	$f_{MID}$ (MHz) 141.5(A)/202(Q)	$f_{UB}$ (MHz) 160(A)/242(Q)			
Aurelia	123-160	180	171	137	1.5	C2 links disrupted, battery current change	Herelink box
QwinOut	165-242	176	116	113	1.5	C2 links, disrupted, Incorrect compass and GPS data, servo	Any conductive part of the UAS except the antenna

The findings from VHF RFI and shielding tests are summarized in Table 4-6. It should be noted that this table does not include the previous finding that for the Aurelia model, C2 links were also disrupted by the VHF RFI emissions between 60.5 and 88 MHz at the field strength of  $\sim 24$  V/m (see Figure 4-24). The VHF low band TV channels 3-6 fall in this frequency range. And the field strength of 24 V/m corresponds to a safe distance of 89 m according to Eq. (4), assuming the TV station transmitter power is equal to the standard value of 150 kW. The VHF high band channels 7-13 fall in the identified frequency range (165-242 MHz) that significant RFI effects on the QwinOut F450 model were observed. For channel 12, the threshold of electric field strength identified as 116 V/m at 202 MHz corresponds to a safe distance of 19 m according to Eq. (4), assuming the TV station transmitter power is also 150 kW.

#### 4.5 Flight Tests

Flight tests were performed using the QwinOut F450 model to assess the effects of front-door RFI on its C2 links in a real-world scenario. The purpose of flight tests was to verify the findings from previous static measurements and determine how the model would respond to significant front-door RFI signals in practice.

##### 4.5.1 Objectives of Flight Tests

Before each flight, the existing spectrum of environmental signals were measured to ensure no significant interference signals were present except our simulated RFI signals. Figure 4-32 shows a picture of the setup for these measurements and calibrations. The setup is similar to the setup in Figure 4-7. The distance between transmit and receive antennas was 12 ft.



Figure 4-32. Calibration setup (also refer to Figure 4-7).

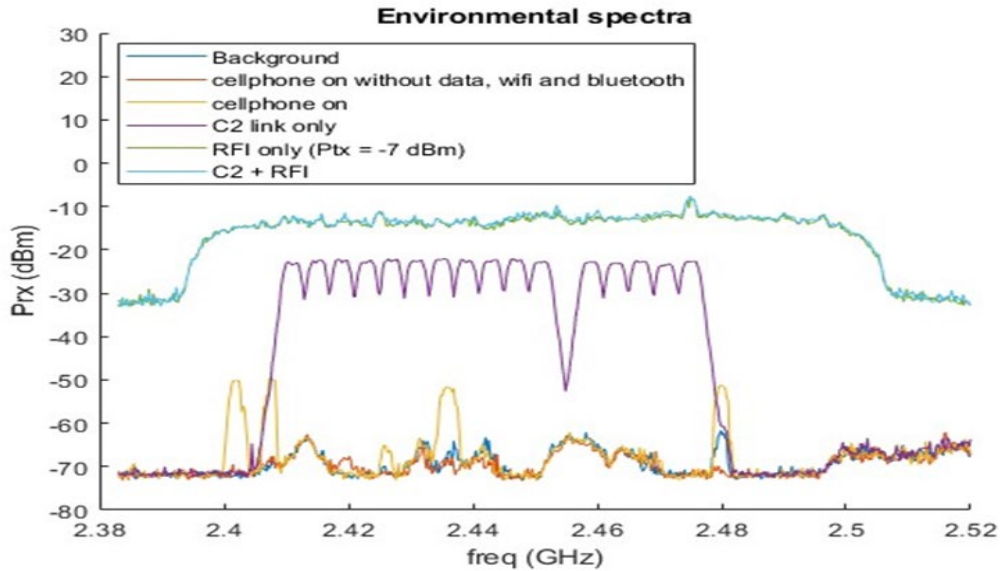


Figure 4-33. Environmental, C2 link, and simulated RFI signals

As shown in Figure 4-33, the environmental signals were recorded first with personal cellphones turned on. The C2 link signals, which were measured to be approximately -23 dBm, were also recorded with cellphones turned off as well as without RFI emissions; the background signal noise was below -50 dBm.

The purpose of calibrations was to determine the AGC values and ISR levels for each scenario. The RFI emission levels at the output of the SDR varied from -7 to -37 dBm with steps of -5 dBm (see Figure 4-34 top left). The RFI emission signals were recorded first with the cellphones turned off and without the C2 link signals. The average interference strength in the C2 link frequency band changes linearly with the RFI emission level, indicating no signal saturation in our devices (see Figure 4-34 top right). By comparing power levels of all signals (both simulated and background interference signals), it is clear that the measurements were not affected by the presence of operational personal cellphones for recording videos. In an abundance of caution, the cellphone data service, Wi-Fi, and Bluetooth were turned off during video recording, and the cellphones were turned off completely during recording flight data for analysis. The signals were then recorded in the presence of both the UAS C2 links and simulated RFI emissions present (see Figure 4-34 bottom).

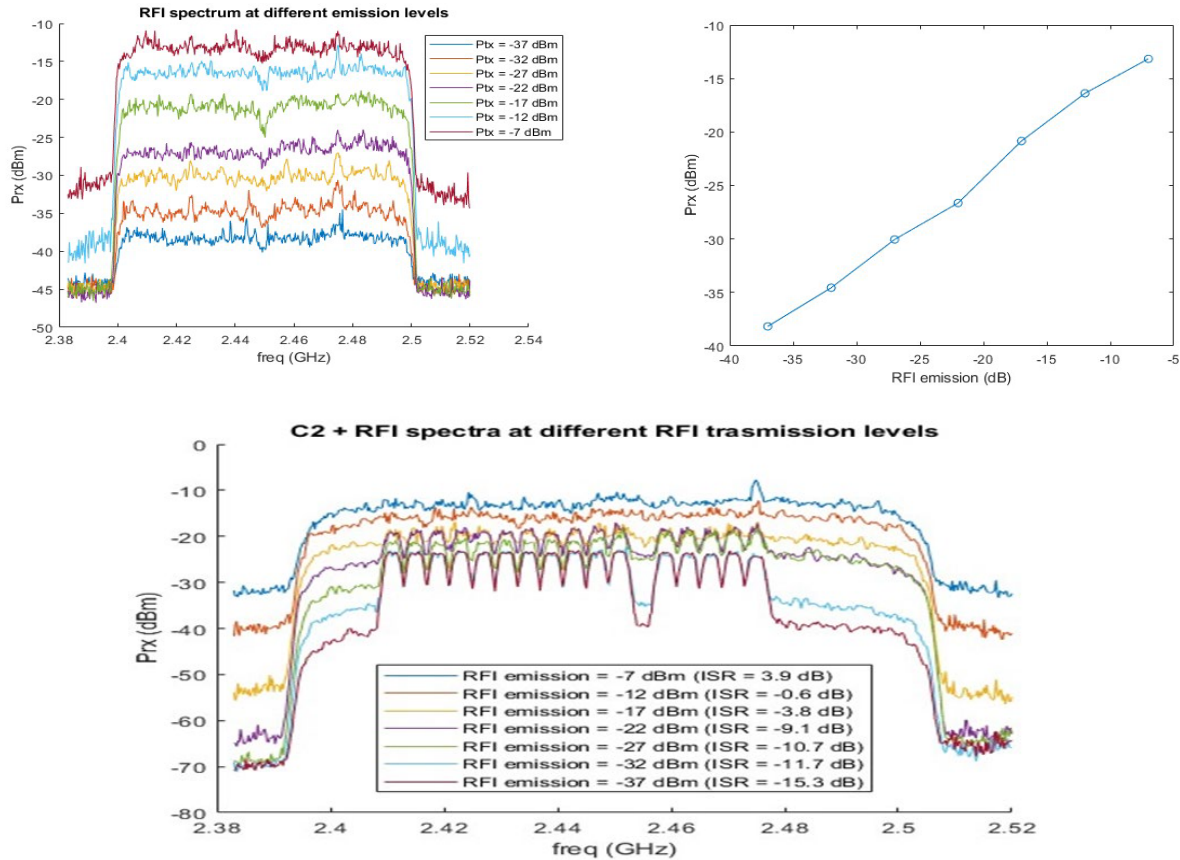


Figure 4-34. Calibration before flight tests. Top-left: RFI emissions at different strength levels (cellphones and C2 links turned off). Top-right: linear relation between RFI emissions and received signals. Bottom: Received signals with the presence of both the C2 links and RFI emissions.

The nonlinear AGC effects in C2 link strength were quantified between -32 dBm to -17 dBm and the ISR values at each transmit level were determined by taking out nonlinear AGC effects as below:

$$ISR = P_{rx\_rfi\_ref} - P_{c2-link} - AGC \quad (5)$$

Where  $P_{rx\_rfi\_ref}$  is a function of the SDR's transmit power  $P_{tx}$  determined from top-right panel of Figure 4-34,  $P_{c2-link} = -23 \text{ dBm}$  according to Figure 4-33, and the AGC gains were determined according to the bottom panel of Figure 4-34. The obtained AGC gains and calibrated ISRs are listed in Table 4-7 and Figure 4-35.

Table 4-7. Variable values used in ISR calculation

RFI emission level (dBm)	-37	-32	-27	-22	-17	-12	-7
Prx_rfi_ref (dBm)	-38.2	-34.6	-30.0	-26.6	-20.8	-16.4	-13.2
Pc2-link (dBm)	-22.9	-22.9	-22.9	-22.9	-22.9	-22.9	-22.9

<b>AGC (dB)</b>	0	0	3.5	5.3	5.8	5.8	5.8
<b>ISR (dB)</b>	-15.3	-11.7	-10.7	-9.1	-3.8	0.6	3.9

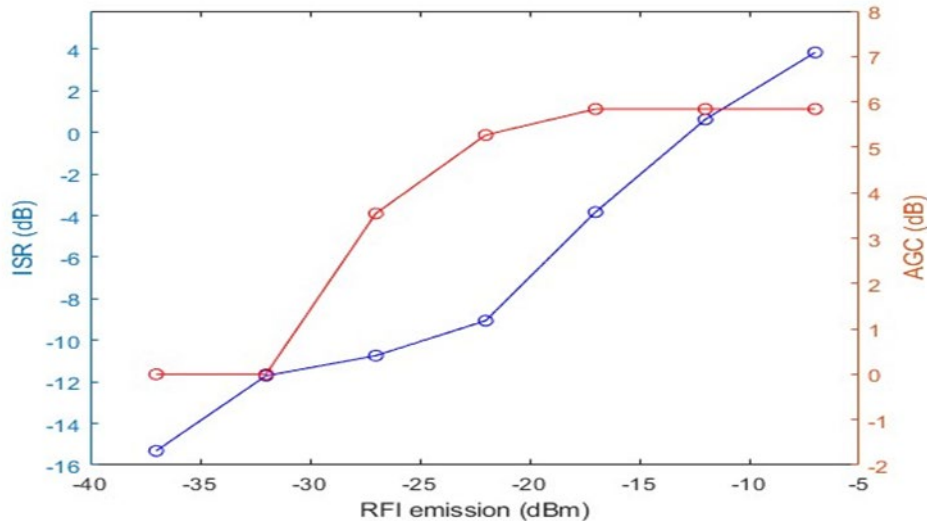


Figure 4-35. Determined AGC gains and ISRs versus the SDR's transmit power.

Four RFI emission levels (-7, -12, -17, -22 dBm) were tested during flights, corresponding to ISR = 3.9, 0.6, -3.8, -9.1 dB, respectively. Figure 4-36 presents a picture of the flight test setup, and a picture of the QwinOut F450 model during a test flight. During each flight, the UAS took off first without RFI emission. RFI was transmitted after it was controlled and kept at the desired position (at the same height as the transmit antenna and 12 ft away in front of it in position hold mode. Failsafe was set to Return To Launch (RTL) when the C2 link was disconnected by the interference emitted from the antenna. The RTL height was set to 5 meters. The failsafe was expected to be triggered by high RFI emission levels causing the UAS to climb to 5 meters above the ground and then land automatically.



Figure 4-36. Front-door RFI flight tests. Left: setup (also compare to Figure 4-32). Right: QwinOut F450 model during flight

#### 4.5.2 Flight Test Observations and Analysis

During the calibration process, it was clear if the emitted RFI would have significant effects on the C2 links by observing the RSSI shown on the remote control and by arming the UAS using the remote control. We noticed three different C2 link status conditions at all the RFI emission levels: 1) at high RFI emission levels, the UAS could not be armed and the RSSI shown on the remote control showed “NaN,” indicating that both the uplink and downlink were interrupted; 2) at moderate RFI emission levels, the UAS could be armed but the RSSI shown on the remote control showed “NaN,” indicating the uplink was working but the downlink was interrupted; 3) at low RFI emission levels, the UAS could be armed and the RSSN showed normal values on the remote control, indicating there was not significant RFI effects.

As shown in Figure 4-37 Figure 4-38 and Figure 4-39, failsafe was triggered at  $ISR = 3.9, 0.6$  and  $-3.8$  dB during test flights 1, 3 and 4 because the C2 links were interrupted by the emitted interference signals. (Failsafe\_Radio = 1 in the log files). The moments of takeoff, the start of RFI emission and the triggering of failsafe were marked in the plots of the controller histories and the UAS barometer altitudes above the ground. From the barometer altitude plots, we see the UAS climbed first and then landed automatically as expected according to the settings before the test flights. We also see that the time between the start of RFI emission and the triggering of failsafe varied as a function of  $ISR$  (8, 10, 41 seconds for  $ISR = 3.9, 0.6$  and  $-3.8$  dB, respectively). Although only three points were gathered, the trend of the time to trigger failsafe is to decrease as  $ISR$  increases as shown in Figure 4-40.

No significant RFI effects were observed in test flight 2 when the  $ISR$  level was set to  $-9.1$  dB. The observations in the calibrations and test flights are summarized in Table 4-8, which match very well with the results from previous static measurements summarized in Table 4-1.

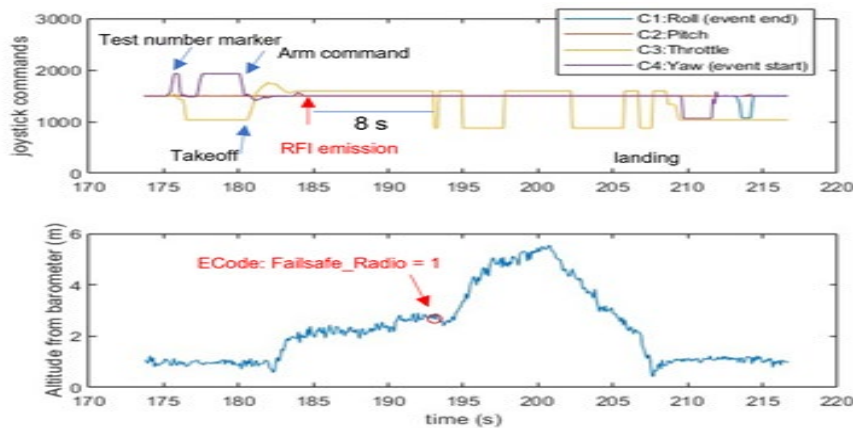


Figure 4-37. Data analysis from flight test 1 with  $ISR = 3.9$  dB

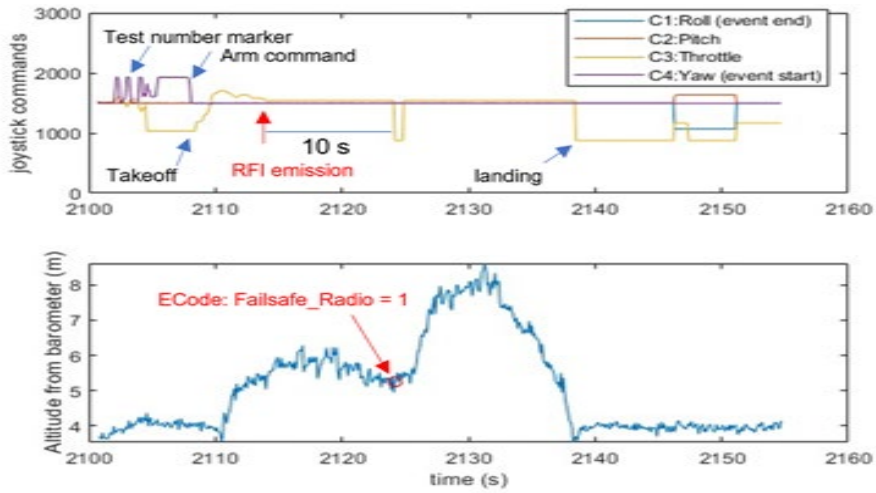


Figure 4-38. Data analysis from flight test 3 with ISR = 0.6 dB

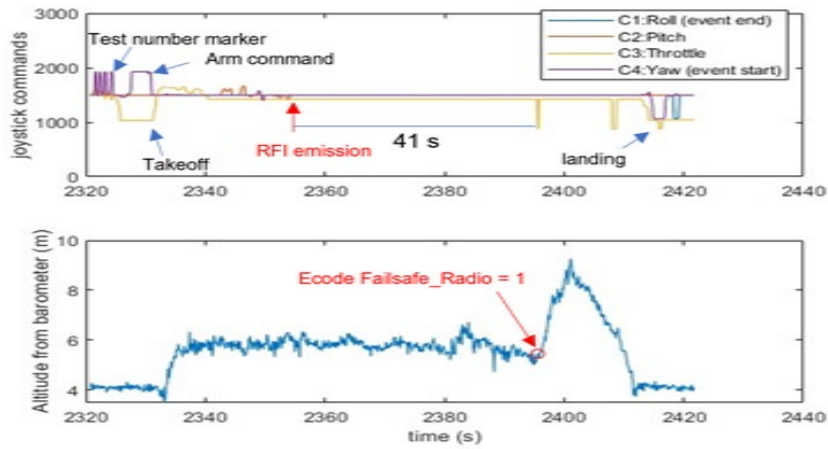


Figure 4-39. Data analysis from flight test 4 with ISR = -3.8 dB

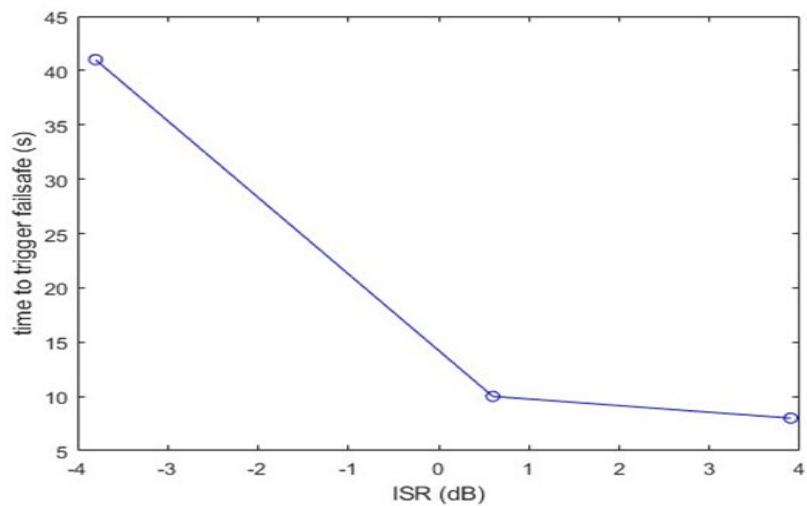


Figure 4-40. Time to trigger failsafe versus ISR

Table 4-8. Summary of calibration and flight test observations

	<b>ISR (dB)</b>	<b>3.9</b>	<b>0.6</b>	<b>-3.8</b>	<b>-9.1</b>	<b>-10.7</b>	<b>-11.7</b>	<b>-15.3</b>
<b>Calibration</b>	Remote Controller RSSI (Downlink)	Null	Null	Null	RSSI / Null	RSSI	RSSI	RSSI
	Be able to arm the UAS (Uplink)	No	Yes	Yes	Yes	Yes	Yes	Yes
<b>Flight Test</b>	C2 link status	D	D	D	C	--	--	--
	Failsafe triggered	Yes	Yes	Yes	No	--	--	--
	Time to trigger failsafe (s)	8	10	41	--	--	--	--

## 5 OBSERVATIONS AND RECOMMENDATIONS

### 5.1 Observations

#### 5.1.1 Power Transmission Lines

As expected, the magnetic fields associated with AC and DC power lines demonstrated a significant impact on magnetic compasses employed in UAS platforms. These magnetic fields did not cause any observable impacts to the Accelerometer, Gyroscope, GPS system, the batteries, and motors with measured data reported herein. Throughout this testing regimen, no impacts were observed on the remaining subsystems, including the C2 link, installed on-board multiple UAS platforms. The potential impacts of electric fields associated with these power lines were also examined in this work; no adverse impacts were identified for any UAS subsystems as a consequence of extensive electric field testing.

#### 5.1.2 RF Signals

A variety of fixed and active flight tests were performed to assess front-door and back-door effects of RFI on two different UAS platforms, the Aurelia X6 Standard and QwinOut F450. The following is a list of key findings from these tests:

- 1) ISR is a reliable parameter that can be used to assess the RFI susceptibility of the C2 links of UAS.
- 2) The C2 link associated with the Aurelia X6 Standard platform experienced several significant RFI effects as a consequence of several emissions that could be experienced in practice.
  - a. This C2 link overlaps with Wi-Fi channel 13, and was found to be susceptible to this in-band Wi-Fi signal with interruptions observed whenever the UAS was too close to a Wi-Fi access point. This interruption can be predicted on the basis of factors including ISR threshold, the ratio of Wi-Fi transmit power to the UAS remote control transmit power, and the ratio of the distance between the UAS and the Wi-Fi access point to the distance between the UAS and its remote control. It should be noted that Wi-Fi channel 13 is not used in the U.S.A. so this observation may have no effect in the NAS at the present time.

- b. These links were found to be susceptible to the signals of band 41 of 4G LTE and 5G NR which is adjacent to the third sub-band of the C2 link. This signal may be interrupted when the UAS approaches too closely to a cellular telephone transmit tower that transmits in band 41. The interruption can be predicted by factors such as ISR threshold, the ratio of the power level of the cellular telephone base station's unwanted emissions to the transmit power of the UAS remote control, and the ratio of the distance between the UAS and the base station to the distance between the UAS and its remote control.
  - c. The C2 link may be interrupted by VHF TV signals when the UAS gets too close to TV broadcast stations. For a typical TV transmitter power of 150 kW, the safety distance was found to be greater than 89m to avoid any back-door RFI effects
- 3) Signals in the VHF band may cause significant disruption to UAS sensors, especially the compass. For a typical TV transmitter power of 150kW, the safe distance was found to be 19m to avoid RFI caused by back-door effects on sensors.
  - 4) These two UAS platforms exhibited no significant adverse effects caused by radiation from ASR at a distance of 789m for the Aurelia X6 Standard and 1140 m for the QwinOut F450, assuming a typical ASR transmitter power of 25 kW and antenna gain of +34 dB.

## 5.2 Recommendations

Given the above findings, we have the following recommendations on UAS design, operation, safety, and testing that help to reduce adverse RFI effects:

- 1) One of the most significant findings of this work is the sensitivity of both UAS platforms to VHF interference. Because both UAS platforms exhibited sensitivity to different parts of this frequency band, it is necessary to test the C2 link associated with each prospective UAS platform for its sensitivity to VHF signals and to determine its safe distance from TV transmit antennas. This testing must include the entirety of the VHF band as follows:
  - a. VHF frequency sweep from 60.5 MHz to 335.5 MHz with a 55MHz bandwidth
  - b. Use a setup shown in Figure 4-15 to assess the sensitivity of each UAS platform to the entire VHF band
  - c. Once a region of the VHF band is identified as sensitive to RFI, the level of sensitivity should be assessed by varying the RFI power level and investigating signals obtained by the various on-board systems (such as C2 link, compass, GPS receiver, etc.)
- 2) From extensive experimental measurements in a controlled laboratory setting, it is clear that the commonly held safety level for magnetic fields of 180  $\mu$ T is overly restrictive. The team was not able to rigorously determine the maximum upper field strength for safe flight, the team recommends a threshold of at least 3,000  $\mu$ T.
- 3) All UAS should have adequate shielding of critical components to improve resilience to RFI. Components that require RF shielding include the C2 system (other than the antenna), GPS system (other than the antenna), and the compass.
- 4) Robust AGC circuitry should be employed in the C2 link to reduce the potential for RFI on the front-door C2 link.
- 5) Any C2 links that operate using the 2.4 GHz ISM band is likely to be sensitive to radiation from Wi-Fi access points and should operate with a significant distance from these points according to the results shown in Figure 4-19.

- 6) Any C2 link that operates using the 2.4 GHz ISM band is likely to be sensitive to radiation from 4G LTE or 5G NR using channel b41 or n41. When flying in a region with cellular radiation in these channels, the safe flight distance may be calculated using the Equation (2) and Figure 4-20.
- 7) Recommend a safe distance of at least 1,200 m from operating ASR for general purpose UAS. If closer flight is desired, each UAS platform must be characterized for its tolerance to ASR signals.
- 8) Flight near power lines has significant adverse impacts to compass/magnetometer performance. When a flight near power transmission lines is needed, alternative methods of determining direction than the compass/magnetometer is recommended.
- 9) Affordable laboratory testing setups that could be employed by UAS manufacturers and operators as described in section 2 are recommended to test any possible effects of strong magnetic and electric fields at lower frequencies.
- 10) The effects of the battery current changes due to long-time exposure to the VHF RFI emissions on UAS operation safety and performance need to be further investigated and evaluated.
- 11) Additional investigation into appropriate shielding against back-door signals in the VHF range is warranted.

## 6 REFERENCES

7

- [1] P. Kay, "EMC Considerations for Unmanned Aerial Vehicles," in *Handbook of Aerospace Electromagnetic Compatibility*, Wiley, 2018.
- [2] J. Jung, C. Ippolito, C. Rogers, R. Kerczewski, A. Downey and K. Matheou, "Small unmanned aircraft electromagnetic interference (EMI) initial assessment," in *2018 Integrated Communications, Navigation, Surveillance Conference (ICNS)*, Herndon VA, 2018.
- [3] J. Barnard, "Small UAV Command, Control and Communication Issues," 2007.
- [4] S. Bonter, D. Dunty and A. Mangrum, "C-Band and Ku-Band UAV Line-of-Sight Data Link EMC Analysis for Two Operational Scenarios," Office of the Assistant Secretary of Defense, 2004.
- [5] V. Rajamani and C. Bunting, "Overview of EMC issues for Unmanned Aircraft Systems".
- [6] W. Zhang, Y. Ning and S. Chunguang, "A method based on multi-sensor data fusion for UAV safety distance diagnosis," *Electronics*, vol. 8, no. 12, 2019.
- [7] T. Mooring, "FCC Online Table of Frequency Allocations," FEDERAL COMMUNICATIONS COMMISSION OFFICE OF ENGINEERING AND TECHNOLOGY POLICY AND RULES DIVISION, 2022.

- [8] L. C. Lavau, M. Suhrke and P. Knott, "Susceptibility of Sensors to IEMI Attacks," *2021 IEEE International Joint EMC/SI/PI and EMC Europe Symposium*, pp. 533-537, 2021.
- [9] Y. Chen, D. Zhang, E. Cheng and X. Wang, "Investigation on Susceptibility of UAV to Radiated IEMI," in *2018 IEEE International Symposium on Electromagnetic Compatibility and 2018 IEEE Asia-Pacific Symposium on Electromagnetic Compatibility (EMC/APEMC)*, Suntec City Singapore, 2022.
- [10] "fcc-tem-jm1," [Online]. Available: <https://www.fischercc.com/products/fcc-tem-jm1/>.
- [11] A. Pahl, K. U. Rathjen and S. Dickmann, "Intended Electromagnetic Interference with Motion Detectors," in *2021 IEEE International Joint EMC/SI/PI and EMC Europe Symposium*, Raleigh NC, 2021.
- [12] M. Skriver, A. Stengaard, U. P. Schultz and E. Ebeid, "Experimental Investigation of EMC Weaknesses in UAVs During Overhead Power Line Inspection," *2022 International Conference on Unmanned Aircraft Systems (ICUAS)*, pp. 626-635, 2022.
- [13] B. Guo, D. Yu, K. He, M. Chai, C. Zhou and D. Zhang, "Susceptibility Study of UAV GPS Positioning Module Under Electrostatic Discharge," in *2020 6th Global Electromagnetic Compatibility Conference (GEMCCON)*, XI'AN, China, 2020.
- [14] K. He, D. Yu, B. Guo, M. Chai, C. Zhou and D. Zhang, "An Equivalent Dynamic Test System for Immunity Characterization of the UAV Positioning Module Using Bulk Current Injection Method," *IEEE Letters on Electromagnetic Compatibility Practice and Applications*, vol. 2, no. 4, pp. 161-164, 2020.
- [15] J. Ge, L. Liu, Y. He and X. Cao, "Low Electromagnetic Interference Design and Simulation of Lithium Battery Powered UAV," in *2021 International Conference on Unmanned Aircraft Systems (ICUAS)*, Athens Greece, 2021.
- [16] N. Li, X. Liu, B. Yu, L. Li, J. Xu and Q. Tan, "Study on the environmental adaptability of lithium-ion battery powered UAV under extremen temperature conditions," *Energy*, vol. 219, 2021.
- [17] W. De Wilde, G. Cuypers, J.-M. Sleewaegen, R. Deurloo and B. Bougard, "GNSS Interference in Unmanned Aerial Systems," in *Ion. Org*, Portland OR, 2016.
- [18] R. Getz and B. Moeckel, "Understanding and eliminating emi in microcontroller applications," National Semiconductor, 1996.
- [19] S. Kaji, M. Kinugawa, D. Fujimoto and Y. Hayashi, "Data Injection Attack Against Electronic Devices With Locally Weakened Immunity Using a Hardware Trojan," *IEEE Transactions on Electromagnetic Compatibility*, vol. 61, no. 4, pp. 1115-1121, 2019.
- [20] R. Scully, "Electromagnetic Interference / Compatibility ( EMI / EMC ) Control Test and Measurement Facility User Test Planning Guide," NASA, Houston TX, 2011.

- [21] G. Petrov and A. Stancheva, "Problems related to EMC caused by low-altitude flying drones in urban environment," *E+E*, vol. 55, 2020.
- [22] RTCA, "Lightning Induced Transient Susceptibility," RTCA DO-160, 2022.
- [23] H. Rimal, A. Reatti, F. Corti, G. Lozito, S. Antonio, A. Fabia and E. Cardelli, "Protection From Indirect Lightning Effects for Power Converters in Avionic Environment: Modeling and Experimental Validation," *IEEE Transactions on Industrial Electronics*, vol. 68, no. 9, pp. 7850-7862, 2021.
- [24] K. Filik, S. Hajder and G. Masłowski, "Multi-stroke lightning interaction with wiring harness: Experimental tests and modelling," 4 2021. [Online].
- [25] P. Szczupak and T. Kossowski, "Response of Drone Electronic Systems to a Standardized Lightning Pulse," 2021. [Online]. Available: <https://www.mdpi.com/1996-1073/14/20/6547>.
- [26] F. A. M. Rizk, "Modeling of UHV and Double-Circuit EHV Transmission-Line Exposure to Direct Lightning Strikes," 2017. [Online]. Available: <http://ieeexplore.ieee.org/document/7515191/>.
- [27] S. Okabe, T. Tsuboi and J. Takami, "Analysis of aspects of lightning strokes to large-sized transmission lines," *IEEE Transactions on Dielectrics and Electrical Insulation*, vol. 18, no. 1, pp. 182-191, 2011.
- [28] T. Miyazaki, S. Okabe and S. Sekioka, "An Experimental Validation of Lightning Performance in Distribution Lines," *IEEE Transactions on Power Delivery*, vol. 23, no. 4, pp. 2182-2190, 2008.
- [29] P. Sun, W. Sima, M. Yang, J. Wu and J. Hua, "Accumulative Effect of Repeated Lightning Impulses on Transformer Insulation: Mechanism Analysis".
- [30] P. Yang, S. Chen and J. He, "Lightning Impulse Corona Characteristic of 1000-kV UHV Transmission Lines and Its Influences on Lightning Overvoltage Analysis Results," 2013. [Online]. Available: <http://ieeexplore.ieee.org/document/6588373/>.
- [31] C. Rourk, "A review of lightning-related operating events at nuclear power plants," *IEEE Transactions on Energy Conversion*, vol. 9, no. 3, pp. 636-641, 1994.
- [32] V. F. Hermosillo and V. Cooray, "Calculation of fault rates of overhead power distribution lines due to lightning-induced voltages including the effect of ground conductivity," *IEEE Transactions on Electromagnetic Compatibility*, vol. 37, no. 3, pp. 392-399, 1995.
- [33] R. G. Deshagani, T. Auditore, R. Rayudu and C. P. Moore, "Factors Determining the Effectiveness of a Wind Turbine Generator Lightning Protection System," *IEEE Transactions on Industry Applications*, vol. 55, no. 6, pp. 6585-6592, 2019.
- [34] A. De Conti, V. C. Oliveira, P. R. Rodrigues, F. H. Silveira, J. L. Silvino and R. Alipio, "Effect of a lossy dispersive ground on lightning overvoltages transferred to the low-voltage

- side of a single-phase distribution transformer," *Electric Power Systems Research*, vol. 153, pp. 104-110, 2017.
- [35] Y. Li, Ding, Qingqing, K. Li, S. Valtchev, S. Li and L. Yin, "A Survey of Electromagnetic Influence on UAVs from EHV Power Converter Stations and Possible Countermeasures," *Electronics*, vol. 10, no. 6, 2021.
- [36] M. Zhao, T. Xu, D. Zhang, X. Zhou, E. Cheng, X. Zhang, S. Gao and Y. Chen, "Implementation Method of Anti Electromagnetic Interference in Identical and Adjacent Frequency for the Data Link of UAV," in *IEEE MTT-S International Conference on Numerical Electromagnetic and Multiphysics Modeling and Optimization (NEMO)*, Hangzhou, China, 2020.
- [37] H. Li, "Inspection of Radiation Disturbance and Radiation Immunity of UAV," Heilongjiang University, 2017.
- [38] Y. Li, Q. Ding, K. Li, S. Valtchev, S. Li and L. Yin, "A Survey of Electromagnetic Influence on UAVs from an EHV Power Converter Stations and Possible Countermeasures," *Electronics*, vol. 10, no. 6, p. 701, 2021.
- [39] S. Liu, L. Zhu, M. Wei, X. Hu, L. Wang and G. Fan, "Research on long-range detection technology for corona discharge radiation signal," *High Voltage Engineering*, vol. 39, no. 12, pp. 2845-2851, 2013.
- [40] A. Chen and C. Chen, "Co-channel Interference and its Restraining Measures in Co-frequency Simulcast Systems," *Telecommun.*, vol. 49, pp. 18-22, 2009.
- [41] W. Zhang, Y. Ning and C. Suo, "A method based on multi-sensor data fusion for UAV safety distance diagnosis.," *Electronics*, vol. 8, no. 12, 2019.
- [42] X. D. Zhang, R. R. Hao and S. S. Liu, "Protection Circuit against Strong Electromagnetic Pulse Interference," Southeast University, Nanjing China, 2010.
- [43] Z. B. Qiu, J. J. Yan, W. J. Xu and C. P. Hang, "Hybrid prediction of the breakdown voltages of short air gaps with typical electrodes," *High Voltage Engineering*, vol. 44, 2018.
- [44] H. Tsuchiya, T. Enoto, S. Yamada, T. Yuasa, M. Kawaharada, T. Kitaguchi, M. Kokubun, H. Kato, M. Okano, S. Nakamura and K. Makishima, "Detection of High-Energy Gamma Rays from Winter Thunderclouds," *Physical Review Letters*, vol. 99, no. 16, p. 165002, 2007.
- [45] W. Radasky and E. Savage, "High-Frequency Protection Concepts," Metatech Corporation, Goleta CA, 2010.
- [46] F. Sabath, "What can be learned from documented intentional electromagnetic interference (iemi) attacks?," in *URSI General Assembly and Scientific Symposium*, Istanbul Turkey, 2011.

- [47] W. A. Radasky, C. E. Baum and M. W. Wik, "Introduction to the special issue on high-power electromagnetics (HPEM) and intentional electromagnetic interference (IEMI)," *IEEE Transactions on Electromagnetic Compatibility*, vol. 46, no. 3, pp. 314-321, 2004.
- [48] W. A. Radasky and R. Hoad, "Recent Developments in High Power EM (HPEM) Standards With Emphasis on High Altitude Electromagnetic Pulse (HEMP) and Intentional Electromagnetic Interference (IEMI)," *IEEE Letters on Electromagnetic Compatibility Practice and Applications*, vol. 2, no. 3, pp. 62-66, 2020.
- [49] S. Van de Beek and F. Leferink, "Robustness of a tetra base station receiver against intentional emi," *IEEE Transactions on Electromagnetic Compatibility*, vol. 57, no. 3, pp. 461-469, 2015.
- [50] V. Chamola, P. Kotesch, A. Agarwal, N. Gupta and M. Guizani, "A comprehensive review of unmanned aerial vehicle attacks and neutralization techniques," *Ad hoc Networks, Elsevier*, 2021.
- [51] H. Gantt, "Radio frequency interference and its use as a weapon," [infosecwriters.com](http://infosecwriters.com).
- [52] D. Kune, J. Backes, S. Clark, D. Kramer, M. Reynolds, K. Fu, Y. Kim and W. Xu, "Ghost Talk: Mitigating EMI Signal Injection Attacks against Analog Sensors," in *2013 IEEE Symposium on Security and Privacy*, Berkeley CA, 2013.
- [53] S. Kaji, M. Kinugawa, D. Fujimoto and Y. I. Hayashi, "Data injection attack against electronic devices with locally weakened immunity using a hardware Trojan.," *IEEE Transactions on Electromagnetic Compatibility*, vol. 61, no. 4, pp. 1115-1121, 2018.
- [54] P. Kay, "EMC Considerations for Unmanned Aerial Vehicles, Chapter 11," in *Handbook of Aerospace Electromagnetic Compatibility*, Wiley-IEEE Press, 2019.
- [55] H. Bragg, "C-band and Ku-band UAV line-of-sight data link EMC analysis for two operational scenarios," 2004.
- [56] "Air Accident Monthly Bulletins," United Kingdom Government, [Online]. Available: <https://www.gov.uk/government/collections/air-accident-monthly-bulletins> . [Accessed 11 June 2023].

## 8 APPENDIX A

Table A1. UAS Accidents compiled from AAIB between 2018 and 2021.

Publication date mm/dd/yyyy	Accident date mm/dd/yyyy	UAS model	Accident cause
03/10/2022	08/17/2021	DJI Matrice 300	suddenly unresponsive, cause unidentified
03/10/2022	11/21/2021	DJI Matrice M300	mechanical problem
02/10/2022	08/03/2021	DJI Matrice 300 RTK	mechanical problem
01/13/2022	07/20/2021	DJI Inspire 2	loss of link, failed to respond to any commands, cause unidentified
1/13/2022	10/14/2021	Evolve Dynamics	mechanical problem
12/9/2021	04/03/2021	Parrot Anafi USA	operation mistake, no GPS signal before takeoff
12/9/2021	03/02/2021	Prion Mk 3	loss of engine power due to a loose spark plug cap, limiting throttle lead to spin and stall
11/11/2021	04/19/2021	Brian Taylor AT6	loss of communication, cause unidentified
10/21/2021	12/29/2020	Tekever AR5 Evolution Mk 2, G-TEKV	sudden engine shutoff because of EMI
09/09/2021	04/18/2021	Parrot Anafi USA	abnormal solder connection
07/08/2021	02/19/2021	Parrot Anafi	mechanical: propeller bonding fault
06/10/2021	08/19/2021	DJI Mavic Pro 2	operation mistake
05/13/2021	12/02/2020	DJI Phantom 4 RTK	left rear propeller detached during flight
03/11/2021	09/21/2019	DJI Matrice 200 V1	unexpected activation of recovery parachute because of loss attachment
03/11/2021	11/29/2019	DJI Matrice 200 V1	unexpected activation of recovery parachute, cause unidentified
03/11/2021	07/04/2019	Alauda Airspeeder Mk II	loss of control, possible RFI
02/11/2021	10/06/2019	DJI Matrice 210	unexpected parachute activation, cause unidentified
01/14/2021	06/17/2020	Aeryon SkyRanger R60	operation mistake
01/14/2021	09/04/2020	Wingcopter 178 Heavylift	design imperfection: overheated rear electronic speed controller
12/10/2020	07/17/2020	Parrot Anafi	Structure problem, propeller failure
11/12/2020	06/29/2020	DJI Inspire 2	cause unidentified because of the wreckage was disposed after the accident, pilot observed propeller detached in landing
10/08/2020	05/20/2020	Believer	operation mistake: switch off radio control transmitter before the automatic flight control system engaged.
10/08/2020	07/08/2020	DJI Matrice M200	black-headed gull attack
09/10/2020	03/05/2020	DJI Phantom 4	operation mistake
09/10/2020	06/11/2020	Parrot Anafi Thermal	propeller failure

09/10/2020	04/24/2020	Yuneec H520	battery loose in turbulence
07/09/2020	12/13/2019	DJI M600 Pro	loss of control because of GPS-compass error caused by signal interference
06/11/2020	08/02/2020	DJI Inspire 2	loss of link, poor GPS and compass signals
06/11/2020	03/05/2020	DJI Matrice M210 V2	operation mistake: collide with trees
05/14/2020	10/01/2019	Aerialtronics Altura Zenith ATX8	EMC: compass interfered by high-voltage wires of railway
05/14/2020	11/18/2019	UAVE Prion Mk 3	design default: not big enough autopilot's elevator authority during landing
04/09/2020	09/18/2019	Velos Single Rotor	Electronic Speed Controller failure, cause not identified
03/12/2020	09/15/2019	DJI Phantom 4 PRO	collide with sea stack: the obstacle avoidance system did not detect it
01/09/2020	10/15/2018	DJI Matrice 210	Electronic Speed Controller failure, cause not identified
01/09/2020	01/19/2019	DJI Matrice 210	electronic speed controller had failed, likely as a result of water ingress it
01/09/2020	03/03/2019	DJI Matrice 210	No 3 (rear left) motor had failed
01/09/2020	03/18/2019	DJI Matrice 210	one of the motors failed
01/09/2020	04/20/2019	DJI Matrice 210	two motors failed
01/09/2020	06/11/2019	DJI Matrice 210	Electronic Speed Controller failure, cause not identified
01/09/2020	07/28/2019	DJI Matrice 210	propulsion error of the No. 2 motor but were unable to determine the reason for it
11/07/2019	10/15/2018	DJI Matrice 210	propeller blade failure in flight, a speed controller failure could not be ruled out
11/07/2019	09/04/2018	DJI Matrice 210	batteries' State of Charge (SOC) was indicating an erroneously high level of charge remaining
11/07/2019	10/26/2018	DJI Matrice 210	batteries' SOC was indicating an erroneously high level of charge remaining
11/07/2019	10/20/2018	DJI Matrice 210 RTK	batteries' SOC was indicating an erroneously high level of charge remaining
11/07/2019	07/18/2018	DJI Matrice 210 RTK	batteries' SOC was indicating an erroneously high level of charge remaining
11/07/2019	04/25/2019	DJI Phantom	operation mistake, buffer zones from trees not sufficient
11/07/2019	08/06/2019	Parrot	loss of control, cause unidentified
07/11/2019	01/14/2019	DJI Matrice 210RTK	operation mistake: overweight payload resulted in high load batteries
07/11/2019	02/07/2019	Evolve Dynamics Sky Mantis	loose batteries
05/09/2019	02/04/2019	DJI Matrice 100	operation mistake: too close to water surface

05/09/2019	02/18/2019	DJI Matrice 210	Electronic Speed Controller failure, cause not identified
05/09/2019	05/22/2018	DJI Phantom 3	structure failure
05/09/2019	06/17/2018	DJI Phantom 4 Pro	not respond to commands in hover mode, run out of batteries later.
04/11/2019	01/29/2019	DJI Matrice 210	a propulsion error in one of its four motors
03/14/2019	09/26/2018	Yuneec Typhoon H480	power loss

Table A2. List of potential sources of RFI to UAS.

Transmitter Type	Frequency bands (MHz)	Typical power (W)	Typical antenna main lobe gain	10 V/m distance in main beam (m)
Cell phone base station (2G - 5G)	600, 700,850, 1900, 2100, 2300,2500,3500,3700,5200, 26000,28000,38000, 60000	30	18	23.8
Broadcast FM, TV radio tower	FM 88-108; TV 54-88, 174-216, 470-806	150,000	0	212.1
Broadcast AM radio tower	0.54 -1.7	500,000	0	387.3
Wi-Fi hotspot	2400, 5000	1	10	1.7
Vehicle and fixed two-way radio	HF, VHF, UHF	25	2.2	3.5
small marine radar (pulse power)	S, X	2000	30	744.6
Telemetry link	L, S, C	1	5.2	1
Amateur radio shortwave transmitter	HF	100	2.2	7.1
Airport surveillance radar (ASR)	PSR, S (2700-2900) SSR, L (1030)	PSR:25,000(max),2100(avg) SSR:150-1500	34	4340

Table A3. RFI risk evaluation matrix.

Criteria	level	Rationale		
		Frequency closeness	Transmit power (10V/m Distance)	Level indexes
Likelihood	Improbable	Different Band (0)	Low (0)	0
	Rare		Medium (1)	1
	Infrequent		High (2)	2
	Rare	Adjacent Band (1)	Low (0)	1
	Infrequent		Medium (1)	2
	Often		High (2)	3
	Infrequent	In-Band (2)	Low (0)	2
	Often		Medium (1)	3
	frequent		High (2)	4

		Performance degradation	Loss of control	
<b>Impact</b>	Low	Possible	Unlikely	1
	Medium	Likely	Possible	2
	High	Likely	Likely	3
<b>Risk</b>	Negligible	Unlikely to suffer from RFI		0
	Minimal	RFI occurs rarely with possible performance degradation		1
	Minor	RFI occurs rarely with likely performance degradation and possible loss of control, or RFI occurs infrequently with possible performance degradation		2
	Major	RFI occurs often with possible performance degradation, or RFI occurs rarely with likely loss of control		3
	Hazardous	RFI occurs frequently with possible performance degradation		4
	Critical	RFI occurs infrequently with likely loss of control, or RFI occurs often with likely performance degradation and possible loss of control		6
		RFI occurs frequently with likely performance degradation and possible loss of control		8
	Very critical	RFI occurs often with likely loss of control		9
	Catastrophic	RFI occurs frequently with likely loss of control		12

Table A4. Multiple RFI scenario risk analysis.

Scenarios	Criteria	C2 link	Navigation Sensors		Flight Control Unit	Power management electronics	Overall risk index
			GPS	Accelerators, gyros and compass			
<b>Cell phone tower (S1)</b>	likelihood	3	1	1	1	1	
	Impact	3	3	2	2	2	
	Risk	9	3	2	2	2	18
<b>Wi-Fi hotspot (S2)</b>	likelihood	2	0	0	0	0	
	Impact	3	3	2	2	2	
	Risk	6	0	0	0	0	6
<b>AM broadcast tower (S3)</b>	likelihood	2	2	2	2	2	
	Impact	3	3	2	2	2	
	Risk	6	6	4	4	4	24
<b>FM &amp; TV broadcast tower (S4)</b>	likelihood	3	2	2	2	2	
	Impact	3	3	2	2	2	
	Risk	9	6	4	4	4	27
<b>ASR (S5)</b>	likelihood	3	2	2	2	2	
	Impact	3	3	2	2	2	
	Risk	9	6	4	4	4	27

Table A5. Measurement events to determine the VHF frequencies, signal bandwidth, and power that have significant back-door RFI effects on the Aurelia X6 Standard model.

<b>Frequency range search</b>				
<b>Event#</b>	<b>SDR <math>P_{tx}</math> (dBm)</b>	<b>RFI center frequency <math>F_c</math> (MHz)</b>	<b>RFI Bandwidth (MHz)</b>	<b>On-site observation of RFI effects</b>
<b>1</b>	-13	110	10	OK
<b>2</b>	-16	110	10	OK
<b>3</b>	-16	115	10	OK
<b>4</b>	-16	118	10	OK
<b>5</b>	-16	121	10	OK
<b>6</b>	-16	124	10	Disrupted C2 links
<b>7</b>	-16	122	10	OK
<b>8</b>	-16	123	10	Disrupted C2 links
<b>9</b>	-16	170	10	OK
<b>10</b>	-16	165	10	OK
<b>11</b>	-16	160	10	Disrupted C2 links
<b>12</b>	-16	163	10	OK
<b>13</b>	-16	162	10	OK
<b>14</b>	-16	162	10	OK
<b>15</b>	-16	161	10	OK
<b>Bandwidth determination</b>				
<b>1</b>	-16	141.5	5	Disrupted C2 links
<b>2</b>	-16	141.5	1	Disrupted C2 links
<b>3</b>	-16	141.5	0.5	Disrupted C2 links
<b>Power level determination</b>				
<b>1</b>	-22	141.5	1.5	OK
<b>2</b>	-19	141.5	1.5	OK
<b>3</b>	-16	141.5	1.5	Disrupted C2 links
<b>4</b>	-18	141.5	1.5	Disrupted C2 links
<b>5</b>	-22	123	1.5	OK
<b>6</b>	-19	123	1.5	OK
<b>7</b>	-16	123	1.5	Disrupted C2 links
<b>8</b>	-18	123	1.5	Disrupted C2 links
<b>9</b>	-22	160	1.5	OK
<b>10</b>	-19	160	1.5	Disrupted C2 links
<b>11</b>	-21	160	1.5	OK
<b>12</b>	-20	160	1.5	OK

Table A6. Measurement events to determine the VHF frequencies, signal bandwidth, and power that have significant back-door RFI effects on the QwinOut F450 model.

<b>Frequency range search</b>				
<b>Event#</b>	<b>SDR <math>P_{tx}</math></b> <b>(dBm)</b>	<b>RFI center</b> <b>frequency</b> <b><math>F_c</math> (MHz)</b>	<b>RFI Bandwidth</b> <b>(MHz)</b>	<b>On-site observation of RFI</b> <b>effects</b>
<b>1</b>	-12	239	10	Disrupted C2 links
<b>2</b>	-12	242	10	Disrupted C2 links
<b>3</b>	-12	245	10	OK
<b>4</b>	-12	244	10	OK
<b>5</b>	-12	243	10	OK
<b>6</b>	-12	165	10	Disrupted C2 links
<b>7</b>	-12	164	10	OK
<b>Bandwidth determination</b>				
<b>1</b>	-16	202	1.25	Disrupted C2 links
<b>2</b>	-16	202	1	Disrupted C2 links
<b>3</b>	-16	202	0.75	Disrupted C2 links
<b>4</b>	-16	202	0.5	Disrupted C2 links
<b>Power level determination</b>				
<b>1</b>	-17	242	1.5	Disrupted C2 links
<b>2</b>	-20	242	1.5	OK
<b>3</b>	-19	242	1.5	OK
<b>4</b>	-18	242	1.5	OK
<b>5</b>	-19	165	1.5	Disrupted C2 links
<b>6</b>	-22	165	1.5	OK
<b>7</b>	-21	165	1.5	OK
<b>8</b>	-20	165	1.5	OK
<b>9</b>	-19	202	1.5	Disrupted C2 links
<b>10</b>	-22	202	1.5	OK
<b>11</b>	-21	202	1.5	OK
<b>12</b>	-20	202	1.5	OK

## 9 APPENDIX B

### 9.1 Introduction

As the advancement of technology, the use of UAS has tremendously expanded from military applications to many non-military applications such as aerial photography, scientific survey, infrastructure inspection, forestry, agriculture, disaster relief, search and rescue, policing surveillance, product delivery, public and commercial formation show, sports and recreation; and more and more small and medium sized drones fly at low altitudes with various system and payload sensors that are highly integrated into limited avionics bay space and operate at different frequency bands. At the same time the regulatory authorities are squeezing frequency allocations closer and closer. As a result, the possibility of unpredictable performance and even loss of control of UAS due to interferences from ubiquitous electromagnetic emissions increases. UAS electromagnetic

compatibility has therefore become a critical consideration in UAS design and operation in order to reduce any potential safety risks and an important subject of investigation (Kay 2018; Jung, Ippolito, et al. n.d.; Barnard n.d.; Rajamani and Bunting, n.d.; Bonter and Dunty 2004).

Radio Frequency Interference (RFI) is a subset of a wider range of electromagnetic emissions. As part of the tasks of ASSURE A56 project, the objectives of literature review include:

- (1) Collect information about UAS incidents that might be related to electromagnetic emissions, especially the RF emissions.
- (2) Collect information about RFI sources that affect UAS safety, performance and operations.
- (3) Collect information of UAS susceptibility to RFI sources.
- (4) Collect information of RFI mitigation strategies.
- (5) Identify potential RFI risks and the gaps between the growing use of UAS and the existing design and operation policy and standards.
- (6) Make recommendations to inform Federal Aviation Administration (FAA) decisions and UAS industry standards based on literature review, and simulation and testing that follow after the literature review.

## **9.2 UAS Incidents**

To be controlled remotely, drones need to communicate with a Ground Control Station (GCS) through a Command and Control (C2) link. Interferences from electromagnetic emissions may cause C2 link loss of a drone, and the drone may drift away from its target, get lost, or crash. One such incident is the RQ-170 captured by Iran in December 2011 (Public Intelligence 2012). Environmental EMI from communications systems produces sufficient energy to disrupt C2 link and are responsible for 15 percent of Army UAS accidents between 2005 and 2009 according to a thesis investigation from the U.S. Army Command and General Staff College (Yochim 2010). An Alauda Airspeeder UAV lost control and crashed at the vicinity Goodwood West Sussex UK on 4 July 2019 during a demonstration flight at Goodwood aerodrome. The investigation was unable to establish the cause of the loss of control but noted that the system to immediately terminate a flight in such circumstances had also failed, and it was considered likely to have RFI (Skybrary 2021). Recent incidents because of sudden loss of C2 link without technical cause clearly identified (RFI is likely the reason) include (AAIB 2019; Taylor 2021; AAIB 2018; 2022b; 2022a).

RFI may disrupt drone navigation sensors including GPS, compass, gyros, and accelerometers and result in loss of control of the aircraft. A recent example of this kind of accident was reported that a non-military small drone (DJI Inspire 2) crashed in an operation to take photographs over a construction site on February 8, 2020 (AAIB 2020). According to the report, the site is close to Sampson House in central London and on the edge of a restricted airspace. The pilot had completed five successful flights over the same site on the day before the crash. Although pre-flight checks on the drone indicated that a full GPS signal had been acquired and that the 'home-point' had been set correctly, the logs showed a wrong 'home-point', and the GPS and compass had poor signal strength once the flight had commenced, and the drone became erratic and uncontrollable after takeoff before colliding with a concrete structure.

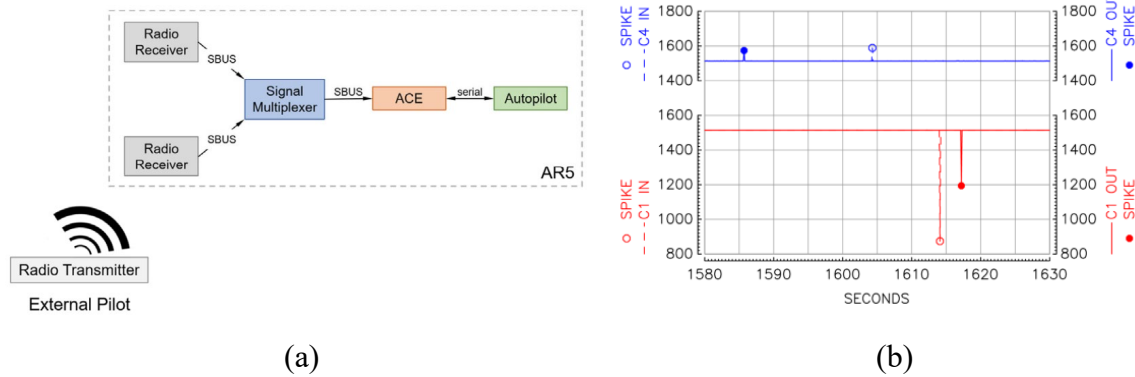


Figure B1. (a) EP control path; (b) Bit errors in SBUS from the aircraft log file of the June 2020 incident showing spikes on the control channels in and out of the autopilot for aileron and rudder.

Electromagnetic emissions from drone’s subsystems would interfere with its C2 link if Electromagnetic Compatibility were not considered carefully. Such incidents were reported in (AAIB 2021). According to the report, the Tekever AR5 Evolution UAS experienced two double engine shutdown incidents respectively in June and December 2020. The reason for the simultaneous shut down of both engines was likely to be a spurious ‘Ignition OFF’ command generated on the aircraft’s External Pilot (EP), also referred to as a Safety Pilot, controlling link through corruption of data provided to the autopilot from two radio receivers via a multiplexer. The presence of a single erroneous command was sufficient to cause the simultaneous engine shutdowns. This data corruption most likely originated from electrical noise as a result of electromagnetic interference originating from the Generator Power Unit (GPU), which affected the operation of the multiplexer. Figure B1 (a) illustrates the EP control link of the EP, receivers, Serial Data Bus (SBUS), Actuator Control Electronics (ACE), and the autopilot. Figure B1 (b) shows the bit errors identified from the log files within the data passed from the multiplexer via the ACE to the autopilot.

The team has reviewed Air Accident Monthly Bulletins (AAIB) published by the government of United Kingdom (AAIB 2015) for the past three years. As listed in Table B1, the team compiled the UAS accidents with field investigation reports for the report publication date, accident date, UAS model involved in accident, and accident cause identified. AAIB published 55 field investigation reports for UAS accidents happened between May 22, 2018 and November 21, 2021. There are a variety of UAS models involved in these accidents. There are 4 out of 55 events highlighted in red in Table B1 that RFI or EMC was identified or suspected as the accident cause. The accident causes were not determined for a significant number of accidents, among which 12 accidents are highlighted in yellow in the table. Either the C2 link, or susceptible components such as GPS, compass, and electronic speed controller were involved in these highlighted accidents in yellow, and therefore they might be caused by RFI or EMI. In most accident analysis, RFI or EMI causes were not considered because it requires much more efforts or the operators were not aware of them.

Table B1. UAS Accidents compiled from AAIB.

Publication date mm/dd/yyyy	Accident date mm/dd/yyyy	UAS model	Accident cause
03/10/2022	08/17/2021	DJI Matrice 300	suddenly unresponsive, cause unidentified
03/10/2022	11/21/2021	DJI Matrice M300	mechanical problem
02/10/2022	08/03/2021	DJI Matrice 300 RTK	mechanical problem
01/13/2022	07/20/2021	DJI Inspire 2	loss of link, failed to respond to any commands, cause unidentified
1/13/2022	10/14/2021	Evolve Dynamics	mechanical problem
12/9/2021	04/03/2021	Parrot Anafi USA	operation mistake, no GPS signal before takeoff
12/9/2021	03/02/2021	Prion Mk 3	loss of engine power due to a loose spark plug cap, limiting throttle lead to spin and stall
11/11/2021	04/19/2021	Brian Taylor AT6	loss of communication, cause unidentified
10/21/2021	12/29/2020	Tekever AR5 Evolution Mk 2, G-TEKV	sudden engine shutoff because of EMI
09/09/2021	04/18/2021	Parrot Anafi USA	abnormal solder connection
07/08/2021	02/19/2021	Parrot Anafi	mechanical: propeller bonding fault
06/10/2021	08/19/2021	DJI Mavic Pro 2	operation mistake
05/13/2021	12/02/2020	DJI Phantom 4 RTK	left rear propeller detached during flight
03/11/2021	09/21/2019	DJI Matrice 200 V1	unexpected activation of recovery parachute because of loss attachment
03/11/2021	11/29/2019	DJI Matrice 200 V1	unexpected activation of recovery parachute, cause unidentified
03/11/2021	07/04/2019	Alauda Airspeeder Mk II	loss of control, possible RFI

02/11/2021	10/06/2019	DJI Matrice 210	unexpected parachute activation, cause unidentified
01/14/2021	06/17/2020	Aeryon SkyRanger R60	operation mistake
01/14/2021	09/04/2020	Wingcopter 178 Heavylift	design imperfection: overheated rear electronic speed controller
12/10/2020	07/17/2020	Parrot Anafi	Structure problem, propeller failure
11/12/2020	06/29/2020	DJI Inspire 2	cause unidentified because of the wreckage was disposed after the accident, pilot observed propeller detached in landing
10/08/2020	05/20/2020	Believer	operation mistake: switch off radio control transmitter before the automatic flight control system engaged.
10/08/2020	07/08/2020	DJI Matrice M200	black-headed gull attack
09/10/2020	03/05/2020	DJI Phantom 4	operation mistake
09/10/2020	06/11/2020	Parrot Anafi Thermal	propeller failure
09/10/2020	04/24/2020	Yuneec H520	battery loose in turbulence
07/09/2020	12/13/2019	DJI M600 Pro	loss of control because of GPS-compass error caused by signal interference
06/11/2020	08/02/2020	DJI Inspire 2	loss of link, poor GPS and compass signals
06/11/2020	03/05/2020	DJI Matrice M210 V2	operation mistake: collide with trees
05/14/2020	10/01/2019	Aerialtronics Altura Zenith ATX8	EMC: compass interfered by high-voltage wires of railway
05/14/2020	11/18/2019	UAVE Prion Mk 3	design default: not big enough autopilot's elevator authority during landing
04/09/2020	09/18/2019	Velos Single Rotor	Electronic Speed Controller failure, cause not identified

03/12/2020	09/15/2019	DJI Phantom 4 PRO	collide with sea stack: the obstacle avoidance system did not detect it
01/09/2020	10/15/2018	DJI Matrice 210	Electronic Speed Controller failure, cause not identified
01/09/2020	01/19/2019	DJI Matrice 210	electronic speed controller had failed, likely as a result of water ingress it
01/09/2020	03/03/2019	DJI Matrice 210	No 3 (rear left) motor had failed
01/09/2020	03/18/2019	DJI Matrice 210	one of the motors failed
01/09/2020	04/20/2019	DJI Matrice 210	two motors failed
01/09/2020	06/11/2019	DJI Matrice 210	Electronic Speed Controller failure, cause not identified
01/09/2020	07/28/2019	DJI Matrice 210	propulsion error of the No. 2 motor but were unable to determine the reason for it
11/07/2019	10/15/2018	DJI Matrice 210	propeller blade failure in flight, a speed controller failure could not be ruled out
11/07/2019	09/04/2018	DJI Matrice 210	batteries' State of Charge (SOC) was indicating an erroneously high level of charge remaining
11/07/2019	10/26/2018	DJI Matrice 210	batteries' SOC was indicating an erroneously high level of charge remaining
11/07/2019	10/20/2018	DJI Matrice 210 RTK	batteries' SOC was indicating an erroneously high level of charge remaining
11/07/2019	07/18/2018	DJI Matrice 210 RTK	batteries' SOC was indicating an erroneously high level of charge remaining
11/07/2019	04/25/2019	DJI Phantom	operation mistake, buffer zones from trees not sufficient
11/07/2019	08/06/2019	Parrot	loss of control, cause unidentified

07/11/2019	01/14/2019	DJI Matrice 210RTK	operation mistake: overweight payload resulted in high load batteries
07/11/2019	02/07/2019	Evolve Dynamics Sky Mantis	loose batteries
05/09/2019	02/04/2019	DJI Matrice 100	operation mistake: too close to water surface
05/09/2019	02/18/2019	DJI Matrice 210	Electronic Speed Controller failure, cause not identified
05/09/2019	05/22/2018	DJI Phantom 3	structure failure
05/09/2019	06/17/2018	DJI Phantom 4 Pro	not respond to commands in hover mode, run out of batteries later.
04/11/2019	01/29/2019	DJI Matrice 210	a propulsion error in one of its four motors
03/14/2019	09/26/2018	Yuneec Typhoon H480	power loss

### 9.3 Sources of EMI

Figure B2 shows the classification of EMI types for three categories: system, environment, and cyber-attack. The former two categories can be considered as unintentional sources of interference while the latter addresses intentional sources of interference.

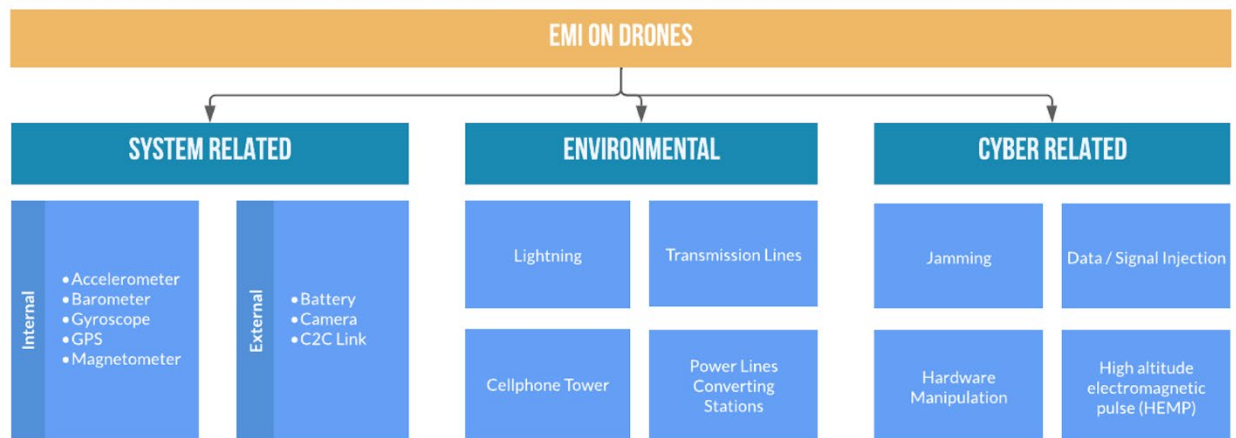


Figure B2. EMI categories based on system-related, environmental, and cyber causes.

#### 9.3.1 System

UAS often employ Inertial Measurement Unit (IMU) consisting typically of 1) gyroscope; 2) accelerometer; and 3) magnetometer to help determine the position in space and its orientation. Some difficulties in using IMU sensors for position determination are similar to those experienced in orientation determination. However, while position finding can rely at least in part on the GPS, orientation, often referred to as attitude and heading, can't be determined using GPS at least for relatively small aircraft. A brief overview below describes some general features and difficulties

in the navigation based on IMU using orientation determination as an example. Similar difficulties exist in using IMU for position finding.

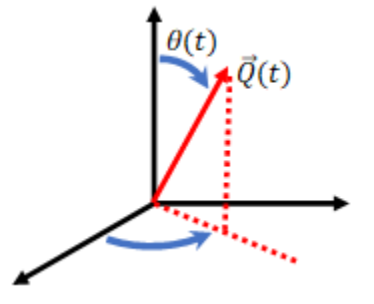


Figure B3. UAS Orientation in Space.

Ideally, an accurate gyroscope should be sufficient to find the orientation. The problem is that inertial sensors like gyroscopes often suffer from noise, bias and other problems associated with uncertain signal model parameters. As shown in Figure B3, if the UAS orientation in space is denoted by vector  $Q \rightarrow(t)$ , a gyroscope measures the angular velocity  $\omega \rightarrow t = dQ \rightarrow(t)/dt$ . In principle, the gyroscope signal should be just proportional to the angular velocity  $\omega \rightarrow t$ . Real signal model is more complex (Miao et al. 2014)(H. Wu et al. 2020)(Y. Wu, Journal, and 2016 2016)(Bonnet et al. n.d.). Often, the gyroscope signal model can be expressed by the equation:

$$\omega \rightarrow t = \bar{T} \bar{K} S \rightarrow Gt + b \rightarrow Gt + n \rightarrow Gt \quad (1)$$

In interpreting the signal, some difficulties can be caused by sensor component cross-sensitivity described by matrix  $\bar{T}$  and by different amplification (diagonal matrix  $\bar{K}$ ) for different angular velocity components. In many cases these difficulties can be dealt with through calibration. Bigger problems are caused by a broad-band (white-like) noise  $n \rightarrow Gt$  and by variable gyroscope bias  $b \rightarrow Gt$ . Integration of the angular velocity to find the orientation  $Q \rightarrow(t)$  turns the broad-band noise  $n \rightarrow Gt$  into a random-walk like noise. Consumer grade IMUs have gyroscopes whose integration yields about  $1^\circ/\text{hour}$  signal diffusion (Random Walk Noise). Bias  $b \rightarrow Gt$  can behave as a random signal although it is frequently caused by temperature variations. Consumer grade IMU gyroscopes employed in many smaller and mid-size UAS often have bias stability of the order of  $30^\circ/\text{hour}$ .

Given substantial possible random errors in estimating orientation using the gyroscope alone, an accelerometer is often used to help estimate the orientation. In principle, if the UAS position in space remains constant, it would be possible to use accelerometers to determine the UAS orientation because, without other accelerations, the accelerometers would be constantly indicating the direction of gravity. In general, of course, one is interested in finding the orientation of a moving UAS that could be accelerating in various directions. The sum of the gravity acceleration vector and other acceleration vector could still have the magnitude of the acceleration due to gravity making it often impossible to distinguish true direction of gravity for a moving aircraft. Thus, in fusion of gyroscope and accelerometer signals, care is needed when gravity direction is employed to update gyroscope determined orientation.

Given the difficulties of using gyroscope and accelerometer to find the UAS orientation reliably, a magnetometer can be used to provide direction and magnitude of the earth magnetic field as a directional reference. Maps of the earth magnetic field exists that would permit to determine the UAS orientation with respect to the field direction at any location. Such determination, however,

is hindered by two types of magnetic field “interference” effects: 1) magnetic field disturbances whose sources are internal to the UAS (on-board sources) and 2) magnetic field disturbances caused by sources that are external to UAS, may depend on the exact location of the UAS and may in some situations change over time.

Two different types of internal source interferences are often distinguished: 1) hard magnetic sources due to permanently magnetized objects onboard the UAS and 2) soft magnetic field sources due to objects that change their magnetization when the UAS re-orient. Internal UAS magnetic interferences can, ideally, be determined by calibration. However, such calibrations are not always performed properly by UAS operators. Furthermore, even when calibration is performed as specified by the UAS manufactures, it may not resolve some of the difficulties. This is due to the fact that the on-board sources include motors and actuators employing magnetic materials. During normal UAS operation, such actuators create magnetic fields that change in time and are different from fields that exist during a typical calibration procedures.

External to the UAS sources of the magnetic field disturbances can be caused by various man-made structures including building, bridges, buried pipes, and others. Power lines can cause not only magnetic field disturbances, but also strong electric fields that can interfere with many electronic components. The above structures are virtually permanent, but there also exist disturbances due to movable structures such as automobiles and trains. In contrast to the on-board sources, the external ones can’t be easily controlled unless they are mapped and known a priori. Such sources are another important reason for the difficulties that arise in using the earth magnetic field as the reference for determining the UAS orientation.

In summary, determining UAS orientation after even a few minutes of flight typically requires more than a gyroscope. Accelerometers and magnetometers are used in a sensor fusion process together with the gyroscope. This fact makes the determination of UAS orientation susceptible to interference from sources that create magnetic fields of relatively low frequency and from electric fields that can affect all the sensors in IMU. Furthermore, strong electric fields due to power lines and other sources can interfere directly with many IMU sensors and other electronic components in UAS.

#### **9.3.1.1 Radio Frequency**

When a UAV's frame is closely packed in a chassis with several electronic modules, it may suffer from EMI or “self-interference” from onboard sources. In an experiment by Watanabe and colleagues (Watanabe et al. n.d.), the test drone used two wireless communication modules: one with 2.4 GHz band used by remote controller, and another for Wi-Fi media data transmission to User Equipment (UE) such as smartphones. This drone has 2 Printed Circuit Boards (PCBs) which has six Integrated Circuits (IC), where three reference clock signals were provided by crystal oscillators at 12, 16, and 40 MHz. The measurement frequency range is 500 MHz to 6 GHz, which covers the bands used by cellular network systems. The drone and a measurement antenna were placed inside an anechoic box to reduce the impact of external cellular signals and measurement instruments on the drone's performance. The results from the experiment show that there was “self-interference” produced by the drone’s PCB at the 800 MHz frequency band. The chassis did not shield the external environment from this interference; frequencies of 864 and 868 MHz were identified to produce white noise that disrupted the operation of cellular-equipped UE.

### 9.3.1.2 Low Frequency

On-board sources of static and low frequency magnetic fields are typically classified as *hard* and *soft* sources (H. Wu et al. 2020)(Opromolla 2020)(Renk et al. n.d.)(Vitiello et al. 2021) (sometimes called hard and soft iron sources, although the sources might have nothing to do with the presence of iron itself). However, it does appear that such classification is somewhat incomplete. Introduction of another type of source that might be called *moving source* may be warranted.

*Hard Magnetic Sources.* Hard magnetic sources are those that are due to the magnetic materials on-board UAS that have at least some parts of their magnetization remaining fixed in the coordinate system of the UAS during a typical flight. As an example, hard magnetic sources have sometimes been associated with actuators or motors which often employ permanently magnetized parts.

*Soft Magnetic Sources.* Soft magnetic sources are those that are due to the magnetic material on board UAS that change at least some part of their magnetization with changing of the UAS orientation (attitude and heading). These might include ferromagnetic cores of actuators, structural parts of UAS that might include magnetizable steel and others. The most often identified reason for changes in the magnetization of the soft sources with UAS orientation is the change in the direction of the earth magnetic field with respect to the UAS.

This classification of on-board sources of magnetic fields is typical but does not always accurately describe all possible on-board magnetic field sources as pointed out by some authors (Opromolla 2020). This is due to the fact that some sources that might appear to be hard prior to flight and at some times during flight, start to move relative to the UAS. Similarly, some soft source might actually change their position and orientation during flight. This might happen, for example, as a result of operation of motors and actuators.

### 9.3.1.3 Magnetic

EMI is a form of radiation that covers the electromagnetic spectrum and is comprised of alternating electrical and magnetic fields. EMI is distinct from RFI, as the latter is produced by frequencies in the radio spectrum and comprises of a portion of the electromagnetic spectrum. Depending on the application, radio frequencies used for communication will vary from magnitudes of a few kHz to larger GHz (Federal Communications Commission 2021). EMI can be produced intentionally by malicious threat actors (i.e., *intentional EMI*) or by external factors (i.e., *unintentional EMI*). This report classifies unintentional sources of EMI under system-related and environmental factors and intentional sources of EMI from cyber threats.

Because of the limited space available, it can be difficult to design and operate a UAV for a variety of tasks. The carrier is more susceptible to electromagnetic compatibility concerns due to the physical proximity of the onboard components. UAV electronic systems causing inadvertent interference are a major issue because they occur within the navigation bands. The electromagnetic interference caused by onboard components is discussed in later sections.

*Battery:* Drone batteries are responsible for the operation and have a significant impact on their overall performance because some of the functions performed by drones require a lot of energy. As a result, drone batteries are just as important as the drone's build and capabilities. The two most common lithium compounds are Lithium Polymer (LiPo) and lithium-ion.

EMI from a lithium-ion battery-powered UAV can be classified into two types: 1) EMI unrelated to UAV maneuver and 2) EMI connected to UAV maneuver. High-frequency EMI from airborne electronic equipment is the main cause of the former. The latter refers to the electricity-generated low-frequency electromagnetic field, which includes EMI from wires and lithium batteries. Through low EMI design, the average EMI generated by lithium battery is 177.3 nT. In terms of the UAV itself, flight heading, and throttle can have an impact on EMI at the magnetic compass. During the flight (Ge et al. n.d.), the EMI of UAV is continuous in the time domain and overlapping in the frequency domain. The parts such as the lithium-powered battery (Assuming that UAV uses one 6S lithium battery) and electrified wires related to UAV maneuver appears as low-frequency interference in the frequency domain, When the EMI is greater than 50nT, it will affect the magnetic compass, which in turn will affect the flight trajectory of the system, resulting in heading measurement error cause collision (Ge et al. n.d.).

When lithium-ion batteries are exposed to extremely high temperatures (above 70 °C) or extremely cold temperatures (below 25 °C), their lifetime and discharging capacity can be severely reduced or even destroyed (N. Li et al. n.d.).

*Camera:* Drone cameras are useful for surveillance, crowd monitoring, and even threat detection. This type of surveillance is also necessary for border surveillance to prevent criminal activity and alert authorities. One of the sources of interference in the carrier is imaging systems in unmanned applications. Light Detection and Ranging (LIDAR) + Red Green Blue (RGB) cameras, Full Frame aerial cameras, and thermal cameras are the most often utilized cameras for power line inspection. The navigation antenna is frequently located with other electronics in the carrier that are less than 3 meters away from the camera, which is prone to digital noise (Cuypers et al. 2016) in terms of shot noise affecting the image quality. When the receiver's gain was adjusted and the camera was turned on, the in-band noise reported by the receiver rose by 12 dB.

*Barometer & Magnetometer Sensor:* By connecting the barometer and magnetometer sensors to the same microprocessor and enclosing them in an open Transverse Electromagnetic (TEM) cell, the susceptibility of these sensors was investigated within certain limits set by IEC 61000-4-20. Because the TEM waveguide can only illuminate one electromagnetic field polarization, the Device Under Test (DUT) must be rotated to investigate others. Continuous Wave signals with a frequency range of 10 MHz–7.5 GHz were transmitted with a one-second interval and a step size of 10 MHz and gradually incremented. RF source was turned off for about five seconds to observe the behavior of these sensors under Intentional Electromagnetic Interference (IEMI) exposure and compared it to normal conditions. The magnetometer sensor was affected in the range of 300–500 MHz, according to the findings. The temperature readings from the barometer sensor were incorrect at various frequencies, while the pressure displayed similar behavior with small variations at the same frequencies (Y. Chen et al. n.d.). The summary of frequency ranges affected are listed in the Table B2.

Table B2. Barometer and magnetometer sensors affected ranges and field strengths.

Sensor	Frequency Range (in MHz)	Field Strength (V/m)
Barometer	500	80
	800-1200	160
	2500-2800	100
	5600-6500	100
	7200-7400	100
Magnetometer	300-500	50
	1800-1900	300

*Accelerometer & Gyroscope Sensor:* The accelerometer can estimate the tilt by measuring the direction of gravity relative to the sensor (pitch and roll). A gyroscope, on the other hand, keeps the drone balanced by measuring the rate of rotation. Gyroscopes are mechanical devices in which a mounted wheel spins on an axis that can move in any direction. They are used to keep a reference point or provide stability. The interference susceptibility of two sensors (accelerometer and gyroscope) was investigated. In an FCC-TEM-JM1 cell, an Arduino board (GY-521) with MPU6050 (3-axis accelerometer and 3-axis gyroscope) was set up. The sensor and Arduino board were both reset before the measurement. After 15 minutes, the signal generator is turned on, with a 10 dBm output and a sine wave of the selected frequency between 5 MHz and 1 GHz.

In the frequency range between 280 MHz and 330 MHz, an occasional failure occurred during the establishing of data communication (*i.e., missing ACK bit where sensor do not reach to I2C communication*). In the same frequency range, the Arduino got crashed occasionally (Pahl et al. n.d.).

*GPS Sensor:* The GPS module is one of several that aid in the transmission of position and altitude data, both of which are necessary for the UAV to function properly. Because the GPS module is more sensitive, a lower Electro-Static Discharge (ESD) voltage interference could cause the GPS module to fail or even be damaged. Induced EMI is one of the side effects of an ESD. Data errors, and temporary resets can be caused by ESD-induced EMI in the presence of mission critical equipment.

The experiment was carried out in a shielded room with a GPS receiving antenna on the outside and a GPS transmitting antenna on the inside, with the GPS enhanced transmitting device having a GPS receiving antenna on the outside and a GPS transmitting antenna on the inside. The first GPS receiving antenna receives GPS signals, while the second GPS transmitting antenna sends them out, and the two antennas are connected by SMA coaxial cables. This method boosts the GPS signal's strength in the shielded room. The GPS module (*uBlox - NEO-M8N chip*) and propeller blades are removed from the UAV and placed on a rubber table. An ESD simulator model NSG437 was used to simulate the actual electrostatic discharge. The charge on the GPS module decays to less than 10% of the peak value when the discharge mode and number of discharges are set to repeat discharge and 10 times, respectively, and the discharge interval is greater than 1 second (Guo et al. n.d.).

Another experiment was carried out with three GPS module chips chosen and given the numbers 1519, 6248, and 6656, respectively. The ESD Generator was set to repeat mode, with the discharge

interval set to 1s and the number of discharges set to 10, and it was discovered that the ESD threshold of the GPS module is below 3500V for the Chip #1519. The ESD threshold of the GPS module is around 3200V, according to chips #6248 and #6656. The UAV system behaves abnormally when exposed to a 3100V electrostatic discharge voltage (Guo et al. n.d.).

Kai He and colleagues (He et al. n.d.) conducted a series of immunity tests on GPS modules using the Bulk Current Injection (BCI) method bounded by the test environment. According to ISO 11452-4 and IEC 62132-3, BCI tests should be conducted in a shielding room with the UAV remaining stationary. The GPS module (uBlox - NEO-M8N chip) was tested according to the IEC 62132-3 standards and the results show that the GPS positioning module is sensitive in the 450MHz to 800MHz range (He et al. n.d.).

*Adjacent RF Channel - Differential and Common-Mode Coupling:* Unintentional electromagnetic coupling is troublesome. It can result in electromagnetic interferences—both external and internal interference. In electromagnetic coupling causing interference, the source components conduct or radiate electromagnetic signals to interfere with components in the same circuit or neighboring circuit. At high frequencies, the common-mode coupling is more active.

- Various EMI shielding techniques, such as Faraday cages, are introduced in RF and microwave circuits to reduce electromagnetic coupling between circuit components.
- Conductors and cables connected will be sharing a common mode impedance, then voltage drops can interfere with the electronic components and cause Electromagnetic disturbances (“Understanding and Eliminating EMI in Microcontroller... - Google Scholar” n.d.).

### **9.3.1.4 Cyber**

#### *9.3.1.4.1 Hardware manipulation*

Though not a source of IEMI, hardwired attacks can exacerbate or amplify the power of external EMI carried out locally on the hardware by inserting a malicious component onboard the UAV that weakens the system. For instance, Kaji et al. (Kaji et al. 2019a) insert a Hardware Trojan (HT) on an IC to create a zone of heightened receptivity to electromagnetic waves which are about 1/100<sup>th</sup> of the electric power of a conventional High-Power Electromagnetic (HPEM). The insertion of this HT weakens the device immunity, induces electromagnetic waves of a specific frequency, and paves the way for attacks like arbitrary data injection. If electromagnetic waves similar to an HPEM is produced from outside the device/system, a current or voltage is induced at zones with weakened immunity. According to the authors, the time required to mount this HT onto a target device like a UAV’s flight computer is approximately three minutes for an experienced attacker.

### **9.3.2 Environmental**

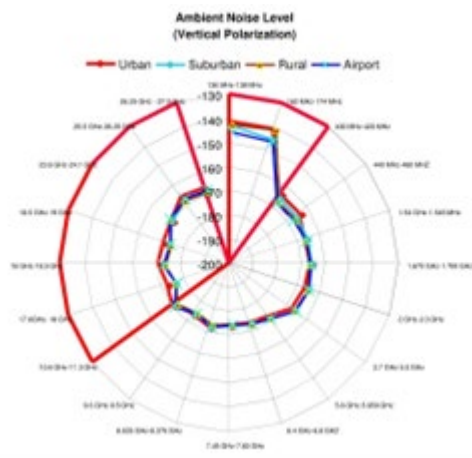
#### **9.3.2.1 Radio Frequency**

Radio frequency emissions are ubiquitous in the world, such as from cell phone towers, broadcast of TV, AM and FM radios, two-way radio, Wi-Fi hotspot, various radars, telemetry, etc. These emissions can enter the circuits of UAS electronics to disturb its operation as RFI. Figure B4 presents the summarized results of RF noise floor measured by the National Oceanic and Atmospheric Administration (NOAA) National Weather Service for frequency bands between 136MHz and 37.1GHz over urban, suburban, rural and airport areas in the U.S. in 2004 and 2005

(Leck 2006), and measured by the National Aeronautics and Space Administration (NASA) in the US in 2002 and 2003 for GPS L1 band (1563.42 – 1587.42 MHz), the Unified S-Band (2025 – 2110 MHz), the 2.4 GHz Industrial, Scientific, and Medical (ISM) Band (2400 – 2482.50 MHz), and the 23.6 - 24.0 GHz Passive Sensing Band at 8 representative sites (Enge, Akos, and Do 2004). These measurements indicate that higher level of radio activities occur at urban area, airport and harbor compared to a rural area.

According to the pathway by which RFI enters the circuits of UAS electronics, RFI can be divided into front door RFI and back door RFI (Kay 2018). Front door RFI occurs when an UAS suffers interference from RF sources that enter its circuits via a pathway that is designed to receive RF energy, such as an antenna/receiver. The front door RFI can be in-band or adjacent band signals. The investigation by (Y. Chen et al. n.d.) shows that even the radiated electric field is lower than 1 V/m, the UAS C2 link can be disrupted when the frequency of radiated continuous wave is the same as or close to the frequency of the data link. The investigation also shows that for harmonic signals generated by nonlinear devices such as amplifiers cause high bitter error rate and lead to the data link unlocked.

Back door RFI occurs when an UAS suffers interference from RF sources that enter its circuits via a pathway that is not designed to receive RF energy, such as through capacitive coupling of RF electrical field. Because the electronics of a small UAS are lightweight and inexpensive, it is possible that it will suffer back door RFI if it is close to the RF sources where the RF electric field strength is greater than 10 to 30 V/m. Table B3 lists some potential sources of RFI to UAS, and their frequency bands, typical power, typical antenna main lobe gain, and the distance where the RF electric field strength equals 10 V/m (Kay 2018). The distances given in Table B3 are not the ranges for small drones to fail. Any particular drone may fail at lower field intensities or tolerate higher field strength. Although 2G has been superseded by newer technologies of 3G, 4G and 5G, 2G networks are still used in many parts of Europe, Africa, Central America, and South America.



(a)

Measurement Site	GPS L1 Band	Unified S Band	ISM 2.4 GHz Band
Urban I	-111.0	-109.2	-83.1
Urban II	-111.5	-111.4	-82.2
Rural I	-132.1	-111.8	-85.1
Rural II	-132.1	-111.7	-87.1
Airport I	-132.5	-77.4	-82.2
Airport II	-132.3	-132.0	-82.5
Harbor I	-132.9	-106.9	-87.4
Harbor II	-111.9	-110.9	-83.8

\*Note: The power measurements by a horizontally polarized horn antenna in dBm/MHz.

Table 1. Average Received Power

(b)

Figure B4. Results of Ambient RF Noise Floor Measurements (a) by NOAA; (b) by NASA.

Table B3. List of Potential Sources of RFI to UAS.

<b>Transmitter Type</b>	<b>Frequency bands (MHz)</b>	<b>Typical power (W)</b>	<b>Typical antenna main lobe gain</b>	<b>10 V/m distance in main beam (m)</b>	<b>Impacted Systems</b>
Cell phone base station (2G -5G)	600, 700,850, 1900, 2100, 2300,2500,3500,3700,5200, 26000,28000,38000, 60000	30	18	23.8	C2 link
Broadcast FM,TV radio tower	FM 88-108; TV 54-88, 174-216, 470-806	150,000	0	212.1	
Broadcast AM radio tower	0.54 -1.7	500,000	0	387.3	
Wi-Fi hotspot	2400, 5000	1	10	1.7	Onboard ICs, UAV motion controller, C2 link
Vehicle and fixed two-way radio	HF,VHF, UHF	25	2.2	3.5	
Small marine radar (pulse power)	S,X	2000	30	744.6	
Telemetry link	L,S,C	1	5.2	1	
Amateur radio shortwave transmitter	HF	100	2.2	7.1	
Airport surveillance radar (ASR)	PSR, S(2700-2900) SSR, L(1030)	PSR:25,000(max),2100(avg) SSR:150-1500	34	4340	

### 9.3.2.2 Low Frequency

#### 9.3.2.2.1 Transmission Line Inspection Applications

Due to the prevalence of drone platforms in transmission line inspections and a significant increase in accidents during such inspections compared to other drone environments, it can be concluded that modern commercial drone platforms have high risks in the electromagnetic field generated by transmission lines.

Although there are clear effects of the magnetic and electric fields of power lines on drone components, particularly the positioning sensors, these require the fusing of different sensor data. Figure B5 provides screenshots from a video where DJI showcases its M200 series drones as power line inspection tools (DJI 2017a). In this video, it is noted that a special high precision navigation system is used to handle electromagnetic interference from the power lines. The positioning system used is the Differential-Real Time Kinematic, Global Navigation Satellite System (D-RTK GNSS). The system enables up to 1 centi-meter positioning accuracy, using differential error correction by having two antenna arrays mounted on the drone.



Figure B5. Drones in close proximity to transmission lines for inspection (DJI 2017a).

#### 9.3.2.2.2 Selected Practical UAS Incidents Related to Power Lines

Drone accident reporting systems have been developed by both government (ASRS, n.d.) and private organizations (Report Drone Accident 2022). It is important to note that since drone accident reporting systems depend heavily on self-reporting, they only include a small sample set of all the crashes that have occurred. Typically, the reports, especially those submitted to federal databases, will be from commercial drone users, or law enforcement agencies which require reporting in their operating procedures. Incidents can be classified into two categories 1) accidents where the power lines are deemed as a direct cause of the accident, and 2) situations where power lines or electromagnetic interferences may affect the drone's operation. Several of these accidents are discussed in detail below.

For example, an accident in the Philippines where a drone makes contact with a power line (Report Drone Accident 2021a), is shown in Figure B6. It is evident from the resulting crashed drone that the power line melted the drones' propellers during contact. What is unclear from the report is

whether the drone navigation or obstacle avoidance systems had caused or contributed to the accident.



Figure B6. Drone damaged from physical contact with a powerline (Lee and Choi 2017).

In another example, (Report Drone Accident 2021b) a drone has similar contact with a powerline but is able to recover in flight without any damage to the drone or the line, as shown in Figure B7. This result suggests the necessity to characterize different lines when determining their danger to drones.



Figure B7. Drone hits a power line and recovers (D. Chen et al. n.d.).

The drone is also used to inspect a guy wired tower, as shown in Figure B8 (Report Drone Accident 2020a). In this mission, the drone was in an automatic mode, and the control was lost in 10 minutes. During this accident, the drone detected the upward wire, but it continued to hit the wire and hung on the wire. After losing control, the drone fell on the ground from 10-20 feet height, and it was totally destroyed. There is no clear reason for this accident. The possible guess from the operator could be the wind or the loss of GPS signal.



Figure B8. Drone hits guy tower line (left) and crashes (right) (Dong et al. n.d.).

In (Report Drone Accident 2020b), the ParaZero system is a system designed to deploy a parachute if the drone is detected to be crashing. this is done to reduce the damage to the drone and other property and injury two individuals on the ground. As shown in Figure B9, it uses independent accelerometers and gyroscopes to determine if the drone is falling. If a falling event is detected the system deploys the parachute and ejects the battery. This failure demonstrates that even if drone control algorithms are designed to counteract or EMI radiation from power lines, a characterization of the effects is still necessary to ensure that third party accessories will not malfunction and cause crashes.



Figure B9. Third party drone parachute system ParaZero erroneously deploys. Last frame that was captured from the video feed (left) before the crash (right) (Report Drone Accident 2020b).

Although optical sensors can enable 3D positioning, an excellent obstacle avoidance, they also have vulnerabilities as demonstrated in (Heron 2022). The drone's flight control algorithm is designed such that when an object is detected close to the lower side of the drone the drone increases altitude. Since in this case the obstruction was physically coupled to the drone the altitude continued to rise indefinitely until the drone depleted its battery and crashed.



Figure B10. Drone is attached to another drone resulting in obstacle avoidance algorithm indefinitely continuing to increase drone altitude until it depletes batteries crashes (Heron 2022).

From the previous examples, they clearly show that there exist drone accidents directly have the involvement of power lines. The searched examples are provided in Table B4.

Table B4. Examples of drone accidents with involvement of power lines.

<b>Date</b>	<b>Drone Make/Model</b>	<b>Cause</b>	<b>Components</b>	<b>Reference</b>
12/9/2021	DJI Mavic 2	The drone (front left propeller) contacted the transmission line and crashed in the rice fields.	Obstacle avoidance system	(Report Drone Accident 2021a)
3/26/2021	DJI Mavic 2 Pro Enterprise Dual	Drone hits unseen power line, drone recovered, no damage to drone or powerline	Obstacle avoidance system	(Report Drone Accident 2021b)
4/20/2020	Unknown	Transmission line inspection in controlled airspace; UAV pilot flew above 50 feet altitude limit.	Human Error	(ASRS, n.d.)
8/20/2020	DJI Matrice 200	Pilot claims drone autopilot gave throttle command that resulted in the drone hitting a guy tower line and crashing	Autopilot system	(Report Drone Accident 2020a)
10/09/2020	DJI Matrice 200 V2	Third party accessory ParaZero erroneously deployed a parachute, and ejected batteries causing the drone to crash	Parazero Parachute system IMU	(Report Drone Accident 2020b)
3/15/2022	DJI Matrice	Drone payload interfered with ground facing optical sensors, causing loss of control and crash.	Optical rangefinder/flight control algorithm	(Heron 2022)

9.3.2.2.3 *External Sources of Static and Low Frequency Magnetic Field Disturbances.*

*Relatively Constant Local Distortion of the Earth’s Magnetic Field.* Direction and magnitude of the earth’s magnetic field can often be viewed as being known within typical area of UAS flight. However, many man-made structures that have various magnetic materials within them can distort this field causing the resulting field to have direction and magnitude not only different from the earth’s magnetic field, but also varying spatially often by more than 10% within several meters. Buildings, bridges, underground pipes, cell towers, and many other relatively permanent man-made structures cause such distortions. There has been a relatively limited effort to describe general features of such magnetic field distortions and to model them (Yamazaki et al. n.d.). Figure B11 is taken as an example of modeling efforts from (Yamazaki et al. n.d.).

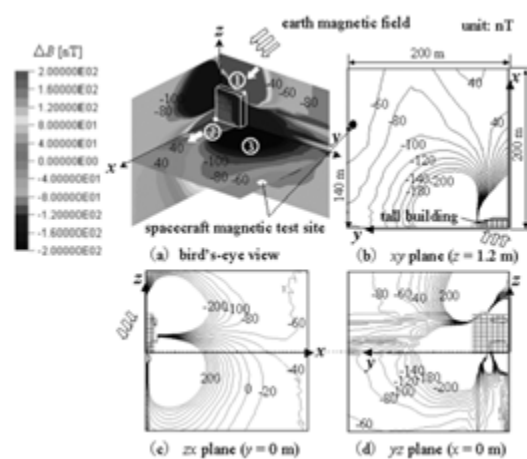


Figure B11. Magnetic disturbance due to the planned tall building. (a) Bird's eye view. (b) xy plane ( $z=12\text{m}$ ). (c) zx plane ( $y=0\text{m}$ ). (d) yz plane ( $x=0\text{m}$ ).

*Local and Slowly Time Varying Distortion of the Earth's Magnetic Field.* Earth's magnetic field can also be distorted by object that are man-made, but not permanently located. An example could be a car or a train. Distortions of the Earth magnetic field cause by such objects have also been modeled (Stojanovic et al. n.d.), but also received relatively little attention in the UAS related literature.

*Weather Phenomena.* Some weather-related phenomena can cause substantial magnetic field distortions within a relatively short period of time. Lightning, for example, can directly induce large magnetic field (Gaynutdinov and Chermosentsev 2017) within a short period of less than one second. The lightning field can also depend on the presence of nearby man-made structures (A. Zhang et al. 2009).

#### 9.3.2.2.4 EMI from Indirect Lightning Strikes

EMI produced from external environmental conditions such as lightning are associated with electricity and are a type of low-frequency interference that does not ionize the surrounding fluid (air). Lightning produces an electric current between the sky and the ground and this produces an electromagnetic field (United States Environmental Protection Agency 2022) that can make onboard components susceptible to transients (or oscillations) (Deppisch 2011). Depending on the external material of the aircraft, lightning strikes can either cause significant damage only at the point of contact, or to the entire aircraft and on-board components. According to Petrov and Stancheva (Petrov and Stancheva 2020), 20% of unprotected aircrafts that do not have any type of lightning protection reported seeing major failures of electrical components compared to just 3% of aircrafts that do have a lightning protection mechanism in place. One standard that addresses the induced (indirect) effects of lightning on avionics and airborne equipment is the Radio Technical Commission for Aeronautics (RTCA) DO-160 (RTCA 2022). The tests in DO-160 standard assess how damage- and upset-tolerant avionics are to lightning-induced transients.

Findings from research literature have attempted to quantify the indirect effects of lightning on avionics. Rimal and colleagues (Rimal et al. n.d.) have shown that induced currents and voltages generated by two lightning waveforms with a "level 4 amplitude" on MOSFET, diodes, and

inductors can easily exceed the tolerable limits for each component; this can upset or damage the equipment

### 9.3.2.3 Magnetic

#### 9.3.2.3.1 EMI from converter stations

Origin/Cause: The major component of a High Voltage Direct Current (HVDC) transmission system is the converter station. Its function is to complete the interface between AC and DC power systems. The switching of the converter station's valves (power electronics converter) is the principal source of electromagnetic emission from the HVDC converter station. When the converter valves are working, they open and close in an alternate, causing rapid transients in the switching voltage and internal current of the valves. The transmission of energy spreads a wide and continuous spectrum of noise characterized as electromagnetic emission (Y. Li et al. 2021).

Effects/Impacts: The data link allows the UAV to interact with the ground control terminal and exchange information. Through the uplink remote control link, the control terminal transmits control commands to the drone, and through the downlink telemetry link, the drone status parameters and task collection information are relayed back to the control terminal. Lock-state refers to the state in which a UAV's data link is operational. The lock-state is interrupted during exposure to large external EMI, and this is known as a lost-link situation (Zhao et al. n.d.).

#### c) On UAV Data Link Communication

A UAV was used in a microwave anechoic chamber to conduct a radiation interference experiment. When the interference field strength reaches 10 V/m at frequencies of 80 MHz to 1000 MHz and 1000 MHz to 2750 MHz, communication between the drone and the ground is disrupted, and the controller is unable to control the steering stepper motor (H. Li 2017).

Another experiment was carried out on a UAV as a continuous radiation of IEMI radiated susceptibility test. The results show that when the frequency of the radiated continuous wave is the same as or close to the frequency of the UAV's data link, even if the radiated electric field is less than 1 V/m, the data link of the UAV used to communicate with the ground control station can be disrupted. Harmonics produced by nonlinear units, such as amplifiers, in the continuous wave emission system produce sensitive frequencies such as 1/2, 1/3, 1/4, and 1/5 times the working frequency, causing the data link to be disrupted (Y. Chen et al. n.d.).

#### d) On UAV Navigation and Positioning System

The GPS positioning accuracy of line-following drones will be affected by corona discharge, insulator pollution flashover, and electromagnetic scattering in the environment of HVDC converter stations. Polluted insulators have a partial discharge frequency range of 1 MHz to 10,000 MHz, which overlaps with the GPS L1 and L2 frequency bands (H. Li 2017). The partial discharge power of contaminated insulators ranges from -70 dBm to -10 dBm. GPS positioning accuracy is under the L1 and L2 frequency bands, and it will suffer obvious interference if the power exceeds -40 dBm. When an abnormal discharge occurs in power equipment (such as corona discharge (Liu and Zhu 2013) or flashover discharge), co-channel interference (A. Chen and Chen 2009) will degrade GPS positioning accuracy if the generated electromagnetic wave signal frequency is the same as the GPS signal frequency and reaches a certain signal strength.

### 9.3.2.3.2 *EMI from Transmission Lines*

#### a) Electric Field on UAV

Experimentation was conducted with a quadrotor UAV inspection model on 500 kV and 220 kV high-voltage overhead transmission lines and simulated experiments. The patrol UAV's maximum field strength is scanned at a distance of 0.5–12 meters from the wire in the experiment. The maximum field strength of the surface of the 220 kV voltage class overhead transmission line is reduced as the distance from the conductor increases, and the field strength and distance are nearly inversely proportional. The distortion field strength varies similarly to the distance between the edge conductor's outer side and the middle line.

At a distance of 1 m, the maximum field strength had an amplitude of about 150 kV/m, and at a distance of 3.5 m, the field strength is attenuated to 40 kV/m. The maximum field strength and field strength change rate of the UAV surface gradually decreases as the distance between the UAV and the 500 kV voltage class overhead transmission line increases.

The maximum field strength is 180 kV/m when the UAV is 1 m away from the side conductor, and it is attenuated to 50 kV/m when the distance is 5 m. The electric field distortion of the 500 kV voltage level has a greater influence on the surface of the UAV than the 220 kV voltage level, but the variation of the field strength with distance and the rate of change of the field strength are similar (W. Zhang et al. n.d.).

The maximum electric field strength that can resist electromagnetic interference in the electronic components that make up the UAV flight control system and inspection system, as well as the sensor's conditioning circuit and protection circuit, is generally 50 kV/m (X. D. Zhang, Hao, and Liu 2010) (Qiu et al. 2018). As a result, the maximum electric field strength of the UAV surface must be less than 50 kV/m to operate the UAV and collect normal environmental data. This electric field strength value is used as the normal inspection operation of the unmanned aerial vehicle's safety field strength threshold in this paper.

#### **Effects of Power Lines on UAS Flight and Navigation**

There is not much literature that analyzes effects of power line currents and voltages on UAS. Results from few papers found so far are summarized below.

Electric field distribution near UAS was modelled in (D. Chen et al. n.d.)(Dong et al. n.d.)(W. Zhang et al. n.d.). Examples of computed fields based on finite element analysis (FEA) are shown in Figure B12 for 500kV lines where the electric field distribution over a UAS is also illustrated. Some references note that there is a common threshold of 50kV/m for electronic components. In case of UAS, some testing of the electric field effects has been carried out using a special test rig (Burghardt and Garbe 2017). It was noted that the flight controller unit which integrated sensor input and sent signals to the motor control unit was sensitive to field as low as 5kV/m.

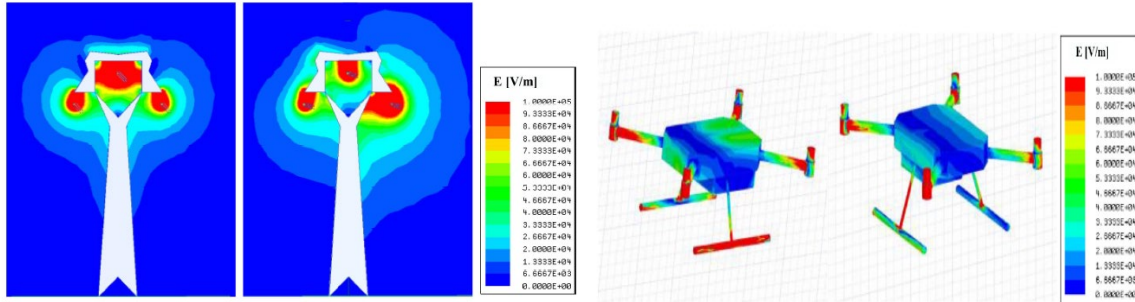


Figure B12. Simulated electric field distribution of 500kV power lines and the effects on drones (D. Chen et al. n.d.).

In details, the electric field distortion in the nearby environment close to drones are also analyzed in reference (W. Zhang et al. n.d.), which is illustrated in Figure B13. In this example, the drone is located right below the transmission line. It clearly shows that the electric field distribution is significantly affected by the distance to the power line. Also, the geometry of the drone itself can affect the fields. The field has also been analyzed at different power line voltages, 220kV and 500kV. In some power systems, the voltage level could be further increased to 1000kV range. It can be easily estimated that the field emission issue will be a critical concern.

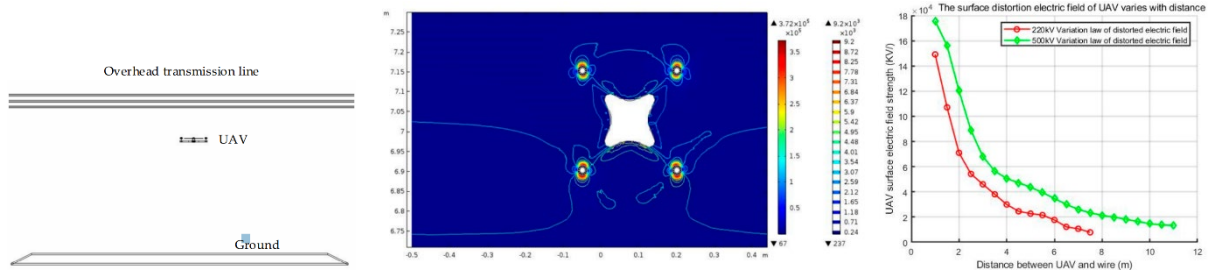


Figure B13. Simulated electric field distribution considering different power line voltages (W. Zhang et al. n.d.).

In addition to the electric field, magnetic field modeling for UAS in proximity with power lines were also carried out in (W. Zhang et al. n.d.). Some examples are illustrated in Figure B14. The following experimental observations were made in (W. Zhang et al. n.d.). With an electric field of 70-80kV/m: 1) UAS starts to shake; 2) UAS response to control signals is delayed; 3) Image transmission has streaks, snowflakes, or black screen. Meanwhile, with a magnetic field of 200-210 $\mu$ T: 1) UAS starts to shake; 2) Magnetometer is disturbed; 3) UAV slowly drift towards the power line; 4) Abnormal data transmission. These are severe impacts that might damage the safe operation of the UAS system.

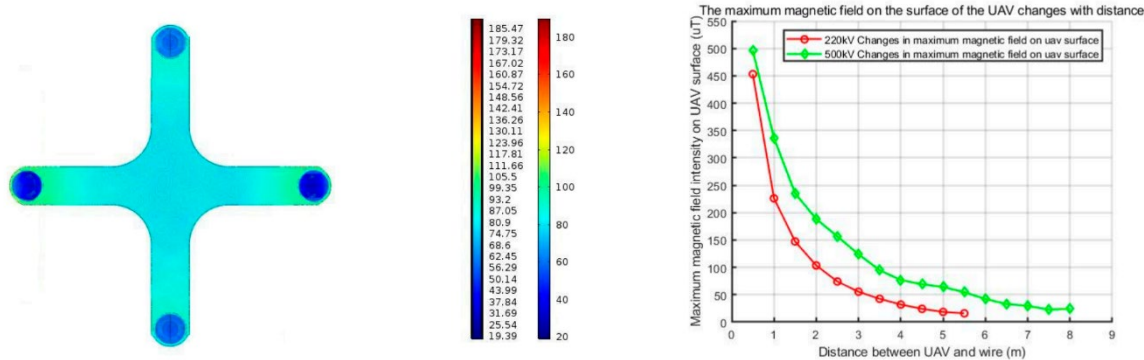


Figure B14. Simulated magnetic field distribution considering different power line voltages (W. Zhang et al. n.d.).

### 9.3.2.3.3 External Components (Ground Control Station)

#### A) Motion Controller

A new device was introduced which allows the UAV to be controlled via natural hand motions. The motion controller can operate at both 2.4 and 5.8 GHz and can automatically select the best transmission channel. According to DJI, in order to avoid the interference, any external wireless devices should not utilize same frequency as the motion controller (DJI 2021).

#### B) Communication and Control Link (C2 Link)

According to Jung and colleagues (Jung, Ippolito, et al. n.d.) experiments were conducted to characterize the RF environment at altitudes up to 400 ft. to better understand how sUAS C2 links performs under EMI tests. DJI S1000 drone underwent pre-compliance radiated emissions testing in the Return to Lands (RTL) RFI/EMI shielded enclosure in a semi-anechoic chamber which was equipped with absorber that completely covers all walls and ceiling adding an additional -15dB to -50dB of attenuation from 450 MHz to 40 GHz. The tests were carried out with a double ridge guide horn receiving antenna that was built to MIL-STD requirements for frequencies ranging from 700 MHz to 10 GHz. An Anritsu MS2035B Vector Network Analyzer + Spectrum Analyzer was used to calibrate the test configuration and analyze emissions. Measurements were done in the frequency bands of 700 MHz-930 MHz, 1700 MHz- 1800 MHz, 1900 MHz-2700 MHz, and 5700 MHz-5950 MHz to enhance precision and better resolve spurious signals. During the test, EMI signals in the band of interest were calculated at high and low RPM conditions with top, bottom and rear orientation in the RF test lab enclosure.

EMI signals in the bands of interest were not detected in the low RPM scenario. In the rear orientation a small vicinity of EMI signal was observed when testing in the frequency range of 900 MHz–2700 MHz band in the DJI S1000 drone. The probable reason for this EMI signal could be the WiFi network installed in the building. They aren't a concern because they don't fall within the LTE spectrum (Jung, Ippolito, et al. n.d.).

EMI signals in the bands of interest were not detected in the high RPM scenario. The measurements are carried out for the four frequency ranges where no additional EMI signals are detected.

Table B5. Intentional sources of EMI based on system components.

S/N	Components	Remarks	Range	Occurrence	References
-----	------------	---------	-------	------------	------------

Battery	Charging / Discharging cycles of batteries are reduced during extreme high or low temperature.	177.3nT (Interference in low EMI Design)	Low-Medium <sup>2</sup>	(Ge et al. n.d.)(N. Li et al. n.d.)
Camera	To avoid interference, placement of camera in the UAV body frame is important.	While switching on the camera, the in-band noise reported by the receiver increased with 12dB	Low <sup>1</sup>	(Cuypers et al. 2016)
Barometer & Magnetometer	Sensor value and status error were noticed during exposure to IEMI.	<ul style="list-style-type: none"> <li>Barometer Ranges - 500, 800-1200, 2500-2800, 5600-6500, 7200-7400 (in MHz)</li> <li>Magnetometer Ranges - 300-500, 1800-1900 (in MHz)</li> </ul>	Low <sup>1</sup>	
Accelerometer & Gyroscope	Due to interference the communication signal is lost between the controller and sensors.	Missing ACK bit in the controller in the frequency range between 280 MHz – 380 MHz	Low <sup>1</sup>	(Pahl et al. n.d.)
GPS	Probability of ESD Events is one of the main causes leading to reduction in GPS reliability.	<ul style="list-style-type: none"> <li>3200 V (ESD Threshold)</li> <li>450MHz to 800MHz (GPS Sensitive Range)</li> </ul>	Low <sup>1</sup>	(Guo et al. n.d.)(He et al. n.d.)

<sup>1</sup>Low – Individual component placement and calibration are carefully evaluated; hence the occurrence is low.

<sup>2</sup>Medium – Various factors contributing to EMI occurrence (wiring, external temperature, vibration).

#### **9.3.2.4 Cyber**

EMI is produced by alternating electric and magnetic fields. Typical sources of interference include onboard UAS components (camera, rotors, flight controller) and environmental causes (cellphone towers, emissions from power lines). These sources come under a broader category of unintentional EMI. However, IEMI from threats external to the UAS also exists as any communication system using wireless links (i.e., full duplex communication in the case of UAS) is susceptible to EMI. As defined by a report from Metatech Corporation (W. Radasky and Savage 2010), IEMI is the “intentional malicious generation of electromagnetic energy introducing noise or signals into electric and electronic systems, thus disrupting, confusing or damaging these systems for terrorist or criminal purposes”. Sources of IEMI are small, highly mobile, and freely available in the commercial market and are not easy to detect as they don’t leave verifiable traces; the complexity of internal circuitry adds to the latter issue, and users of systems under IEMI attacks are likely to attribute the interference to faulty hardware (Sabath 2011). IEMI attacks can have either of the following two characteristics:

##### c) Narrowband:

Narrowband attacks use frequencies that are close to the center frequency, typically with a bandwidth within 1% of the center frequency (W. A. Radasky, Baum, and Wik 2004a) and are powerful.

##### d) Wideband:

Wideband or Ultra-Wideband attacks are based on the use of short, non-continuous pulses spread across a range of frequencies. Though not as powerful as narrowband signals, they can be used to find a system’s vulnerability to different frequencies.

Through these attacks means, IEMI can be maliciously targeted at a UAS via the following attacks:

##### i) High-altitude Electromagnetic Pulses (HEMP)

Although much less likely than other IEMI attacks, HEMPs are electromagnetic pulses that produced a nuclear event outside the earth’s atmosphere, typically above an altitude of 30 km (W. A. Radasky and Hoad 2020a). These pulses come under the category of HPEM where electromagnetic signals are channeled at peak strength. Radasky and colleagues (W. A. Radasky, Baum, and Wik 2004a) state that computers and other systems using microprocessors appear to be vulnerable to radiated EMI that have amplitudes of 30 V/m or above in the narrowband fields. In addition to being fairly easy to produce, narrowband interference is a greater threat to UAVs than wideband frequencies as since a narrowband waveform is close to the center frequency, the electrical energy is delivered in a substantially small frequency and is thus of greater power. Of course, the experiment setups and quality of equipment shielding/enclosures will to some degree determine how these systems would respond to such interference.

##### ii) Jamming

Any system that relies on electronic hardware can be damaged or disrupted by electromagnetic signals given that these signals are powerful enough. The antennae on terminal equipment such as the ground station controllers and the UAV itself serve as easy entry points for IEMI. When IEMI is coupled via an antenna, it is termed as front door coupling. Experiments performed by Beek and Leferink (van de Beek and Leferink 2015) shows that regardless of any base station or wireless receiver that is equipped with a bandpass filter, front door coupled EMI that is produced by IEMI sources that are from Out-Of-Band frequencies (i.e., frequencies that are outside the passband of the front-end filter) need to be at a certain magnitude to cause receiver saturation. However, in-band frequencies from an IEMI source can saturate the front end of a receiver and lead to decreased signal sensitivity. Jamming attacks can use narrowband or wideband frequencies (Chamola et al. 2020). An example of a wideband interference weapon is the Transient Electromagnetic Device (TED). TEDs do not work with a specific frequency but rather operate in a wide spectrum range and are attractive options to an attacker as they don't require much skill to build, require much less power to operate, and are smaller in size than narrowband weapons (Grant, n.d.).

iii) Data/Signal injection

Analog sensors such as temperature or air quality sensors that can be deployed onboard a UAV can serve as an entry point for attacks like a signal injection. Analog sensors that operate on circuits in the order of a few millivolts and produce signals in the Very Low Frequency (VLF) band (1 Hz – 30 kHz) are vulnerable to interference and signal injection at much lower power levels. According to Kune and colleagues (Kune et al. 2013), manipulating sensor readings with EMI-based sources requires an adversary to identify a suitable emission frequency as each component has a certain frequency by which a signal can pass with little attenuation. Another side-effect of EMI to analog sensor circuits is the loss of accuracy in sensor readings (Sino 2011). Narrowband frequencies can damage modern electronic equipment at amplitudes of 0.5kV/m for a frequency of 1 GHz (W. Radasky and Savage 2010).

Table B6 summarizes the common cyber attacks that cause EMI. Occurrences are assigned based on the ease by which components can be obtained and attacks can be executed.

Table B6. Intentional sources of EMI from common cyber attacks.

	<b>Attack</b>	<b>Remark</b>	<b>Affected Range</b>	<b>Occurrence</b>	<b>References</b>
<b>Cyber</b>	High-altitude electromagnetic pulse (HEMP)	Typically produced by super high-power, high-energy emissions such as those from nuclear detonation.	Narrowband frequencies of < 1 Hz.	Low <sup>1</sup>	(W. Radasky and Savage 2010)(W. A. Radasky, Baum, and Wik 2004b)(W. A. Radasky and Hoard 2020b)
	Jamming	Antennae onboard UAVs	Deployed using	Medium <sup>2</sup>	(van de Beek and Leferink

		and a source of IEMI that targets these antennae (front door coupling) using in-band operating frequencies.	wideband frequencies.		2015)(Chamola et al. 2020)(Grant, n.d.)
	Data/Signal injection	EMI is ‘injected’ in analog sensors as they are sensitive to EMI due to heightened sensor receptivity (mV-level sensitivity).	Wideband frequencies or narrowband frequencies of 1 GHz.	Medium <sup>2</sup>	(W. Radasky and Savage 2010)(Kune et al. 2013)(Sino 2011)
	Hardware manipulation	Insertion of malicious hardware component(s) amplifies EMI to the entire system	-	Low-Medium	(Kaji et al. 2019b)

<sup>1</sup>Low – Likely to be used in military-level situations that call for high impact weaponry. There is a fairly high degree of complexity for execution.

<sup>2</sup>Medium – Subject to use in situations where components are easy to obtain. There is a low complexity for execution.

## 9.4 Susceptibility

### 9.4.1 Radio Frequency

In terms of the susceptibility of unintentional RFI in UAS operation environments, the team considers the following important UAS subsystem/components that are important to the Guidance, Navigation and Control of UAS. These subsystem/components have been investigated as the vulnerable victims in the cyber-attack scenarios (Kim et al. 2012).

#### (1) C2 link, transmitters, receivers, and GCS

Currently the frequency bands used by many drones are at 433MHz, 869MHz, 900MHz, 2400MHz and 5800MHz, which share with ISM bands. As a result, the drone C2 link is most susceptible in urban areas. C-band and Ku-band are used for UAS satellite links. In order to assure the reliability and robustness of C2 link to support a large number of UAS operating whenever and wherever, allocations of frequency bands especially to UAS are under consideration. Two frequency ranges considered likely to be applied to LOS UAS Control and Non-Payload Communications (CNPC) links are in L-Band (960-1164 MHz) and C-Band (5030-5091 MHz), and existing satellite networks operating in the Fixed Satellite Service (FSS) in the frequency bands at 14/12 GHz (Ku-band) and 30/20 GHz (Ka-band) have potential spectrum capacity to meet the requirements for

UAS BLOS CNPC links. The aggregate effect of many Fixed Service (FS) transmitters, while constrained to operate within their required limits, will have the potential to impact the performance of the Beyond Line of Sight (BLOS) CNPC link (Kerczewski et al. n.d.).

UAS C2 link consists of uplink and downlink. The uplink from Ground Control Station (GCS) to the UAS sends commands to control the aircraft flight, and the downlink from UAS to GCS sends telemetry information about the status of the aircraft and the on-board sensors. The required bit rate bandwidth for each link depends on the number of parameters, the number of bits of each parameter, coding scheme for transmission error detection and correction, and the maximum update rate during critical moments such as takeoff, collision avoidance and landing (Barnard n.d.). Because C2 link is most susceptible to RFI and critical to UAS safe operation, a redundant C2 link is recommended for the Uncrewed Aircraft System Traffic Management (UTM) under development (Jung, Nag, et al. n.d.).

The susceptibility of UAS C2 link varies with the distance between the UAV and its GCS. When the UAS is near the GCS, the communication signal is too strong to be interfered, and when the UAS is far away from the GCS, the communication signal is weak and the link is more vulnerable to interference.

Transmitters and receivers are designed to intercept RF signals in specified frequency band, and therefore are very sensitive to any in-band RFI. Although front door RFI are most mitigated through careful frequency planning and management, it is still possible for a drone to suffer from front door RFI through adjacent channel leakage. In addition, because the C2 link of many drones operates at either 2.4GHz or 5.8GHz, they are susceptible to emissions from many industrial, scientific, and medical devices, Wi-Fi and 5G cell phone towers because these emissions are in the same frequency bands. The Department of Defense (DoD) Joint Spectrum Center conducted an electromagnetic compatibility analysis in 2004 to determine the potential for EMI between the UAV Line-of-Sight Data Link Terminal and the Communications-Electronics (C-E) environment for two Predator operational scenarios: Southern Border Vehicle Intrusion and Northern Maritime Border Security (NMBS). This analysis included the C-bands of 4400 – 4940 and 5250 – 5850, and Ku-band of 14400 – 15350 MHz used by Predator for the transmitters and receivers of its C2 links. The analysis found each frequency band had a potential interference between the UAS terminals and various C-E systems in the environment. Environmental systems analyzed included radar systems (fixed and mobile), terrestrial microwave links, telemetry systems, satellite downlink systems, radio astronomy telescopes and troposcatter systems (Bonter and Dunty 2004).

(2) Navigation sensors such as GPS, gyros, accelerometers, magnetic compass

According to (Eliardsson et al. 2017), the L-band for GPS is relatively pristine and quiet in terms of spectral noise, therefore a GPS receiver is mainly susceptible to intentional jamming and spoofing attacks. In the jamming scenario, attackers generate interference in the L1 band, making the UAS unable to receive the legitimate positioning signals. In the spoofing case, attackers generate and transmits fake GPS signals to divert the UAS from its original trajectory. A more recent EMI measurement in GPS L1-band in Europe show approximately 15 significant interference events in most active sites close to the major roads or city centers (Eliardsson et al. 2017).

Gyros, accelerometers, and magnetic compasses are not directly susceptible to RFI, but they are likely to suffer back door RFI from related circuits. They may also suffer EMI disturbances from onboard electric rotors and electronic systems and external sources such as large metal infrastructures and high voltage power lines.

### (3) Flight Control Unit with autopilot and electric speed controller

Flight Control Units with autopilot and electric speed controllers are likely to suffer back door RFI from related circuits.

### (4) Power management electronics

Power management electronics are likely to suffer back door RFI from related circuits.

The susceptibility of drones to back door RFI is a function of frequency and the drone dimensions, illumination time, and direction dependent. For example, a small drone of 0.5m may not be susceptible to FM radio which wavelength is around 3m because it behaves more like a short dipole than a matched antenna; In contrast, a medium size drone of 3m may be susceptible to FM radio because it behaves as a matched antenna to intercept the RF field with good coupling efficiency. The same small drone may be susceptible to cell phone tower emissions at 2GHz as the signal wavelength is 0.15 m. Most electronic circuits have higher immunity to continuous RFI. In the case of a search radar that emits short pulses at low duty cycle, the victim circuits of a drone may not have enough time to respond to the interference before it has ceased. So, it is possible a drone may require 100 v/m field strength of a pulsed RFI to bring about a failure, which occurs at 77 m from the source in the example of marine radar given in Table B3 (Kay 2018). The circuit boards, wires, and other components of a drone will have directional properties in its abilities to receive RF signal. This directionality is related to the electrical length - the ratio between the wavelength of the impinging energy and the dimension of the victim, which affect the beam width and nulls of the receiving pattern.

#### **9.4.2 Low Field Environment**

Proximity to transmission lines will have an effect on the drone's sensor readings. In both academic literature (W. Zhang et al. n.d.) and anecdotal accounts (DJI 2017b), the effects described are violent shaking, inaccurate magnetometer readings, drifting towards the power line, and loss or weakening of the transmission signal with ground control.

Determining absolute drone orientation in a high magnetic interference environment such as near a power line is exceptionally challenging. Typically, an inertial measurement unit (IMU) on most drone's gyroscope, and accelerometer and magnetometer data are used to determine position in 3D space. Gyroscopes suffer from drift bias, requiring filtering techniques and data from other sensors to compensate this error (Passaro et al. n.d.).

To combat the above limitations, the following methods have been proposed:

**GPS** can also be used to derive orientation, but this requires the object to be moving. A dual GPS and magnetometer set up, offers a redundant and more robust approximation of position in 3D space. This strategy has been proposed in (Gowda et al. 2016) and used commercially in products such as DJI D-RTK GNSS.

**Optical sensors** can also be used to determine positioning in 3D space. These include stereoscopic cameras and time of flight sensors, coupled with machine vision and optical flow algorithms. Some challenges arise when relying on these sensors in power line applications. The power line is often not detected as an obstacle resulting in a crash (Report Drone Accident 2021a). Some research has been conducted using computer vision techniques to approximate the position of the lines even if they are not seen (Hui et al. 2018). Although promising, the strategies are not implemented in most existing drone platforms.

Table B7. Analysis of component susceptibility of transmission line interference.

<b>Component</b>	<b>Known susceptibility points</b>	<b>Existing mitigation strategies</b>	<b>Risk (low/medium/high)</b>	<b>References</b>
Body/frame	Physical contact with power line	Obstacle avoidance techniques	Low	(Siebler et al. 2020)(Report Drone Accident 2022)(Report Drone Accident 2021a)
Magnetometer	Proximity to magnetic field emissions results in false heading readings	Sensor fusion-differential sensors, GPS derived orientation	High	
Gyroscope	Accumulates error over time; requires input from other sensors to re calibrate	Sensor fusion - GPS or magnetometer data	Medium	
Accelerometer	Error is accumulated when using accelerometer data to determine velocity and distance moved	Sensor fusion – with optical sensor data	Medium	
Optical sensors	Sensor accuracy is diminished if the drone is shaky; less capabilities at night	Sensor fusion – GPS, Accelerometer, and Gyroscope	High	
Motors	Generate EMI	Software calibration	Low	
Electronic speed controller (ESC)	None known	N/A	Low	
Battery	None known	N/A	Low	
Flight controller	Drone flight characteristics	Actively, using sensor data and	Medium	

	heavily dependent on flight controller algorithms	reducing dependence on sensors based on perceived error		
GNSS/GPS receivers	Relies on magnetic field sensor for orientation; poor signal quality near tall structures [24]	Sensor fusion - differential receivers, optical receivers [24], [25]	High	
TX/RX ground control module	Susceptible to interference (both jamming, and unintentionally)	Return to home function (RTH); spectrum hopping	High	

## 9.5 Conclusion

The impact of EMI on small UAS has the potential to cause significant physical harm and property damage if no regulations are put in place to mitigate its effects. Causes of EMI can be categorized as RF, static and low-frequency, and cybersecurity related. These three categories allow for appropriate regulation to be developed for each that will assure safe flight in the most diverse scenarios. The research team has developed risk analysis matrix in each area that will drive the subsequent experimental test phase of the project.

## 9.6 REFERENCES

- AAIB. 2015. "Air Accident Monthly Bulletins." Air Accidents and Serious Incidents. 2015. <https://www.gov.uk/government/collections/air-accident-monthly-bulletins>.
- . 2018. "AAIB Bulletin: 5/2019 DJI Phantom 4 EW/G2018/06/28," 10–27.
- . 2019. "AAIB Bulletin: 11/2019 Parrot EW/G2019/08/11," 2019.
- . 2020. "AAIB Bulletin: 6/2020 DJI Inspire 2 AAIB-26456," no. Figure 1: 96–98.
- . 2021. "AAIB Bulletin: 11/2021 G-TEKV AAIB-27083," 1–16.
- . 2022a. "AAIB Bulletin: 1/2022 DJI Inspire 2 AAIB-27505," 51–52.
- . 2022b. "AAIB Bulletin: 3/2022 DJI Matrice 300 AAIB-27593," 76–77.
- ASRS. n.d. "Aviation Safety Reporting System." <https://asrs.arc.nasa.gov/index.html>.
- Barnard, J. n.d. "Small UAV Command, Control and Communication Issues." *Barnardmicrosystems.Com*. Accessed March 23, 2022. [https://barnardmicrosystems.com/media/presentations/IET\\_UAV\\_C2\\_Barnard\\_DEC\\_2007.pdf](https://barnardmicrosystems.com/media/presentations/IET_UAV_C2_Barnard_DEC_2007.pdf).
- Beek, Stefan van de, and Frank Leferink. 2015. "Robustness of a TETRA Base Station Receiver Against Intentional EMI." *IEEE Transactions on Electromagnetic Compatibility* 57 (3): 461–69. <https://doi.org/10.1109/TEM.2015.2406732>.
- Bonnet, S, C Bassompierre, C Godin, ... S Lesecq - Sensors and Actuators A, and undefined 2009. n.d. "Calibration Methods for Inertial and Magnetic Sensors." *Elsevier*. Accessed March 23, 2022. <https://www.sciencedirect.com/science/article/pii/S0924424709004324>.
- Bonter, Steve, and Diana Dunty. 2004. "C-Band and Ku-Band UAV Line-Of-Sight Data Link EMC Analysis for Two Operational Scenarios," no. JSC-PR-04-054. <https://info.publicintelligence.net/JSC-04-054.pdf>.
- Burghardt, F, and H Garbe. 2017. "Development of a Test Rig to Measure the EM-Susceptibility of an Unmanned Aerial Vehicle." *Ieeexplore.Ieee.Org*, 19–26. <https://ieeexplore.ieee.org/abstract/document/8105013/>.
- Chamola, Vinay, Pavan Kotesh, Aayush Agarwal, and Navneet Gupta. 2020. "A Comprehensive Review of Unmanned Aerial Vehicle Attacks and Neutralization Techniques," no. January.
- Chen, A, and C Chen. 2009. "Co-Channel Interference and Its Restraining Measures in Co-Frequency Simulcast Systems." *Telecommunication Engineering*. 2009. [https://scholar.google.com/scholar?hl=en&as\\_sdt=0%2C35&q=Co-channel+Interference+and+its+Restraining+Measures+in+Co-frequency+Simulcast+Systems&btnG=](https://scholar.google.com/scholar?hl=en&as_sdt=0%2C35&q=Co-channel+Interference+and+its+Restraining+Measures+in+Co-frequency+Simulcast+Systems&btnG=).
- Chen, DQ, XH Guo, ... P Huang - IEEE Letters on, and undefined 2020. n.d. "Safety Distance Analysis of 500kv Transmission Line Tower Uav Patrol Inspection." *Ieeexplore.Ieee.Org*. Accessed March 23, 2022a. <https://ieeexplore.ieee.org/abstract/document/9309320/>.
- . n.d. "Safety Distance Analysis of 500kv Transmission Line Tower Uav Patrol Inspection." *Ieeexplore.Ieee.Org*. Accessed March 23, 2022b. <https://ieeexplore.ieee.org/abstract/document/9309320/>.

- Chen, Y, D Zhang, ... E Cheng - 2018 IEEE International, and undefined 2018. n.d. "Investigation on Susceptibility of UAV to Radiated IEMI." *Ieeexplore.Ieee.Org*. Accessed March 23, 2022a. <https://ieeexplore.ieee.org/abstract/document/8393875/>.
- . n.d. "Investigation on Susceptibility of UAV to Radiated IEMI." *Ieeexplore.Ieee.Org*. Accessed March 23, 2022b. <https://ieeexplore.ieee.org/abstract/document/8393875/>.
- Cuyppers, Gert, K U Leuven, Wim de Wilde, Jean-Marie Sleewaegen, Richard Deurloo, and Bruno Bougard. 2016. "GNSS Interference in Unmanned Aerial Systems." *Ion.Org*. <https://doi.org/10.33012/2016.14674>.
- Deppisch, Richard. 2011. "Electromagnetic Interference / Compatibility ( EMI / EMC ) Control Test and Measurement Facility User Test Planning Guide." *Configurations*, 1–33.
- DJI. 2017a. "DJI, DJI – M200 Series– Powerline Inspection Tool." 2017. <https://www.youtube.com/watch?v=Bj5ByZKVNao>.
- . 2017b. "How Far to Stay Away from High Power Lines???" DJI Forum. 2017. <https://forum.dji.com/thread-116061-1-1.html>.
- . 2021. "User Manual." *Database 3304*: 1–148.
- Dong, X, F Qu, Y Li, Z Wu, ... Z Chen - ... Conference on the, and undefined 2018. n.d. "Electric Field Simulation and Discharge Distance Measurement between UAV and Overhead Line." *Ieeexplore.Ieee.Org*. Accessed March 23, 2022. <https://ieeexplore.ieee.org/abstract/document/8401098/>.
- Eliardsson, Patrik, Mikael Alexandersson, Michael Pattinson, Steve Hill, Åsa Waern, Yeqiu Ying, and Dimitrios Fryganiotis. 2017. "Results from Measuring Campaign of Electromagnetic Interference in GPS L1-Band." In *2017 International Symposium on Electromagnetic Compatibility - EMC EUROPE 2017, EMC Europe 2017*. <https://doi.org/10.1109/EMCEurope.2017.8094660>.
- Enge, Per, Dennis Akos, and Juyong Do. 2004. "Measurements of Man-Made Spectrum Noise Floor." *National ...*, no. November. [http://corporations.ic.gc.ca/epic/internet/insmt-gst.nsf/vwapj/smse00205-novatel-nasa01.pdf/\\$FILE/smse00205-novatel-nasa01.pdf](http://corporations.ic.gc.ca/epic/internet/insmt-gst.nsf/vwapj/smse00205-novatel-nasa01.pdf/$FILE/smse00205-novatel-nasa01.pdf).
- Federal Communications Commission. 2021. "FCC Online Table of Frequency Allocations." *Office of Engineering and Technology*.
- Gaynutdinov, RR, and SF Chermosentsev. 2017. "Electromagnetic Stability of an Unmanned Aerial Vehicle at the Indirect Effect of a Lightning Discharge." *Ieeexplore.Ieee.Org*. <https://ieeexplore.ieee.org/abstract/document/8109917/>.
- Ge, J, L Liu, Y He, X Cao - 2021 International Conference on, and undefined 2021. n.d. "Low Electromagnetic Interference Design and Simulation of Lithium Battery Powered UAV." *Ieeexplore.Ieee.Org*. Accessed March 23, 2022. <https://ieeexplore.ieee.org/abstract/document/9476833/>.
- Gowda, Mahanth, Justin Manweiler, Ashutosh Dhekne, Romit Roy Choudhury, and Justin D Weisz. 2016. "Tracking Drone Orientation with Multiple GPS Receivers." *DL.Acm.Org* 0 (1): 280–93. <https://doi.org/10.1145/2973750.2973768>.
- Grant, Helen. n.d. "Radio Frequency Interference and Its Use as a Weapon." *Infosec Writers*, 1–11.

- Guo, B, D Yu, K He, M Chai, ... C Zhou - 2020 6th Global, and undefined 2020. n.d. "Susceptibility Study of UAV GPS Positioning Module Under Electrostatic Discharge." *Ieeexplore.Ieee.Org*. Accessed March 23, 2022. <https://ieeexplore.ieee.org/abstract/document/9456739/>.
- He, K, D Yu, B Guo, M Chai, ... C Zhou - IEEE Letters on, and undefined 2020. n.d. "An Equivalent Dynamic Test System for Immunity Characterization of the UAV Positioning Module Using Bulk Current Injection Method." *Ieeexplore.Ieee.Org*. Accessed March 23, 2022. <https://ieeexplore.ieee.org/abstract/document/9256287/>.
- Heron, Ken. 2022. "How to CRASH \$10,000 Worth of Drones in 60-Seconds." 2022. <https://www.youtube.com/watch?v=81bCAWcwW1Q>.
- Hui, X, J Bian, X Zhao, M Tan - International Journal of, and undefined 2018. 2018. "Vision-Based Autonomous Navigation Approach for Unmanned Aerial Vehicle Transmission-Line Inspection." *Journals.Sagepub.Com* 15 (1). <https://doi.org/10.1177/1729881417752821>.
- Jung, J, C Ippolito, ... C Rogers - 2018 Integrated, and undefined 2018. n.d. "Small Unmanned Aircraft Electromagnetic Interference (EMI) Initial Assessment." *Ieeexplore.Ieee.Org*. Accessed March 23, 2022. <https://ieeexplore.ieee.org/abstract/document/8384835/>.
- Jung, J, S Nag, HC Modi - 2019 IEEE/AIAA 38th Digital Avionics, and undefined 2019. n.d. "Effectiveness of Redundant Communications Systems in Maintaining Operational Control of Small Unmanned Aircraft." *Ieeexplore.Ieee.Org*. Accessed March 23, 2022. <https://ieeexplore.ieee.org/abstract/document/9081782/>.
- Kaji, Shugo, Masahiro Kinugawa, Daisuke Fujimoto, and Yu Ichi Hayashi. 2019a. "Data Injection Attack Against Electronic Devices with Locally Weakened Immunity Using a Hardware Trojan." *IEEE Transactions on Electromagnetic Compatibility* 61 (4): 1115–21. <https://doi.org/10.1109/TEM.C.2018.2849105>.
- . 2019b. "Data Injection Attack Against Electronic Devices with Locally Weakened Immunity Using a Hardware Trojan." *IEEE Transactions on Electromagnetic Compatibility* 61 (4): 1115–21. <https://doi.org/10.1109/TEM.C.2018.2849105>.
- Kay, Paul. 2018. "EMC Considerations for Unmanned Aerial Vehicles." *Handbook of Aerospace Electromagnetic Compatibility*, December, 603–19. <https://doi.org/10.1002/9781119082880.CH11>.
- Kerczewski, Robert J, James H Griner, William D Bishop, David W Matolak, and Jeffrey D Wilson. n.d. "Progress on the Development of the UAS C2 Link and Supporting Spectrum—from LOS to BLOS." *Ieeexplore.Ieee.Org*. Accessed March 23, 2022. <https://ieeexplore.ieee.org/abstract/document/7943926/>.
- Kim, Alan, Brandon Wampler, James Goppert, Inseok Hwang, and Hal Aldridge. 2012. "Cyber Attack Vulnerabilities Analysis for Unmanned Aerial Vehicles." *AIAA Infotech at Aerospace Conference and Exhibit 2012*. <https://doi.org/10.2514/6.2012-2438>.
- Kune, Denis Foo, John Backes, Shane S. Clark, Daniel Kramer, Matthew Reynolds, Kevin Fu, Yongdae Kim, and Wenyan Xu. 2013. "Ghost Talk: Mitigating EMI Signal Injection Attacks against Analog Sensors." *Proceedings - IEEE Symposium on Security and Privacy*, 145–59. <https://doi.org/10.1109/SP.2013.20>.

- Leck, R. 2006. "Results of Ambient RF Environment and Noise Floor... - Google Scholar." World Meteorological Organization. 2006. [https://scholar.google.com/scholar?hl=en&as\\_sdt=0%2C35&q=Results+of+Ambient+RF+Environment+and+Noise+Floor+Measurements+Taken+in+the+U.S.+in+2004+and+2005&btnG=](https://scholar.google.com/scholar?hl=en&as_sdt=0%2C35&q=Results+of+Ambient+RF+Environment+and+Noise+Floor+Measurements+Taken+in+the+U.S.+in+2004+and+2005&btnG=).
- Lee, Jung Keun, and Mi Jin Choi. 2017. "A Sequential Orientation Kalman Filter for AHRS Limiting Effects of Magnetic Disturbance to Heading Estimation." *Journal of Electrical Engineering and Technology* 12 (4): 1675–82. <https://doi.org/10.5370/JEET.2017.12.4.1675>.
- Li, H. 2017. "Inspection of Radiation Disturbance and Radiation Immunity of UAV."
- Li, N, X Liu, B Yu, L Li, J Xu, Q Tan - Energy, and undefined 2021. n.d. "Study on the Environmental Adaptability of Lithium-Ion Battery Powered UAV under Extreme Temperature Conditions." *Elsevier*. Accessed March 23, 2022. <https://www.sciencedirect.com/science/article/pii/S0360544220325883>.
- Li, Yanchu, Qingqing Ding, Keyue Li, Stanimir Valtchev, Shufang Li, Liang Yin, Teresa Donateo, and Mohamed Benbouzid. 2021. "A Survey of Electromagnetic Influence on UAVs from EHV Power Converter Stations and Possible Countermeasures. *Electronics* 2021, 10, 701." *Mdpi.Com*. <https://doi.org/10.3390/electronics10060701>.
- Liu, S, and L Zhu. 2013. "Research on Long-Range Detection Technology for Corona Discharge Radiation Signal."
- Miao, Cunxiao, Qingdong Zhang, Jiancheng Fang, and Xusheng Lei. 2014. "Design of Orientation Estimation System by Inertial and Magnetic Sensors." *Proceedings of the Institution of Mechanical Engineers, Part G: Journal of Aerospace Engineering* 228 (7): 1105–13. <https://doi.org/10.1177/0954410013485523>.
- Opromolla, Roberto. 2020. "Magnetometer Calibration for Small Unmanned Aerial Vehicles Using Cooperative Flight Data." *Sensors (Switzerland)* 20 (2). <https://doi.org/10.3390/s20020538>.
- Pahl, A, KU Rathjen, ... S Dickmann - Joint EMC/SI/PI and EMC, and undefined 2021. n.d. "Intended Electromagnetic Interference with Motion Detectors." *Ieeexplore.Ieee.Org*. Accessed March 23, 2022. <https://ieeexplore.ieee.org/abstract/document/9559187/>.
- Passaro, Vittorio M N, Antonello Cuccovillo, Lorenzo Vaiani, Martino de Carlo, and Carlo Edoardo Campanella. n.d. "Gyroscope Technology and Applications: A Review in the Industrial Perspective." *Mdpi.Com*. Accessed March 23, 2022. <https://doi.org/10.3390/s17102284>.
- Public Intelligence. 2012. "Lost-Links and Mid-Air Collisions: The Problems With Domestic Drones." *News*. 2012. <https://publicintelligence.net/the-problems-with-domestic-drones/>.
- Qiu, Z.B., J.J. Yan, W.J. Xu, and C.P. Hang. 2018. "Hybrid Prediction of the Breakdown Voltages of Short Air Gaps with Typical Electrodes." *High Voltage Engineering*, 44.
- Radasky, William A., Carl E. Baum, and Manu W. Wik. 2004a. "Introduction to the Special Issue on High-Power Electromagnetics (HPEM) and Intentional Electromagnetic Interference (IEMI)." *IEEE Transactions on Electromagnetic Compatibility* 46 (3): 314–21. <https://doi.org/10.1109/TEM.2004.831899>.

- . 2004b. “Introduction to the Special Issue on High-Power Electromagnetics (HPEM) and Intentional Electromagnetic Interference (IEMI).” *IEEE Transactions on Electromagnetic Compatibility* 46 (3): 314–21. <https://doi.org/10.1109/TEMC.2004.831899>.
- Radasky, William A, and Richard Hoad. 2020a. “Recent Developments in High Power EM (HPEM) Standards with Emphasis on High Altitude Electromagnetic Pulse (HEMP) and Intentional Electromagnetic Interference (IEMI).” *IEEE Letters on Electromagnetic Compatibility Practice and Applications* 6423 (c): 62–66.
- . 2020b. “Recent Developments in High Power EM (HPEM) Standards with Emphasis on High Altitude Electromagnetic Pulse (HEMP) and Intentional Electromagnetic Interference (IEMI).” *IEEE Letters on Electromagnetic Compatibility Practice and Applications* 6423 (c): 62–66.
- Radasky, William, and Edward Savage. 2010. “Intentional Electromagnetic Interference (IEMI) and Its Impact on the U.S. Power Grid.” *Metatech Corporation*, no. 805: 11–12.
- Rajamani, Vignesh, and Chuck Bunting. n.d. “Overview of EMC Issues for Unmanned Aircraft Systems.”
- Renk, EL, M Rizzo, W Collins, ... F Lee - IEEE Control Systems, and undefined 2005. n.d. “Calibrating a Triaxial Accelerometer-Magnetometer-Using Robotic Actuation for Sensor Reorientation during Data Collection.” *Ieeexplore.Ieee.Org*. Accessed March 23, 2022. <https://ieeexplore.ieee.org/abstract/document/1550155/>.
- Report Drone Accident. 2020a. “DJI Matrice 200 - Accident - 2020-08-20.” 2020. <https://reportdroneaccident.com/1016/dji-matrice-200-accident-2020-08-20/>.
- . 2020b. “DJI Matrice 200 V2 ParaZero - Accident - 2020-10-09 - Analysis.” 2020. <https://reportdroneaccident.com/1145/dji-matrice-200-v2-accident-2020-10-09-analysis/>.
- . 2021a. “DJI Mavic 2 - Incident - 2021-12-09.” 2021. <https://reportdroneaccident.com/2182/dji-mavic-2-incident-2021-12-09/>.
- . 2021b. “DJI Mavic 2 Pro Enterprise Dual - Accident - 2021-03-26 - Video.” 2021. <https://reportdroneaccident.com/1597/dji-mavic-2-pro-enterprise-dual-accident-2021-03-26-video/>.
- . 2022. “Drone Accident Submissions.” 2022. <https://reportdroneaccident.com/drone-accident-submissions/>.
- Rimal, HP, A Reatti, F Corti, ... GM Lozito - IEEE Transactions, and undefined 2020. n.d. “Protection From Indirect Lightning Effects for Power Converters in Avionic Environment: Modeling and Experimental Validation.” *Ieeexplore.Ieee.Org*. Accessed March 13, 2022. <https://ieeexplore.ieee.org/abstract/document/9162560/>.
- RTCA. 2022. “Lightning Induced Transient Susceptibility.” DO-160. 2022. <https://do160.org/lightning-induced-transient-susceptibility/>.
- Sabath, Frank. 2011. “What Can Be Learned from Documented Intentional Electromagnetic Interference ( IEMI ) Attacks ? 2 . Documented Criminal Usage of Electromagnetic Tools 3 . Analysis of Documented IEMI Attacks,” 3–6.

- Siebler, B, S Sand, UD Hanebeck - IEEE Sensors Journal, and undefined 2020. 2020. "Localization with Magnetic Field Distortions and Simultaneous Magnetometer Calibration." *Ieeexplore.Ieee.Org* XX: 1. <https://doi.org/10.1109/JSEN.2020.3024073>.
- Sino, Henri. 2011. "Electromagnetic Interference ( EMI ) Filtering Reduces Errors in Precision Analog Applications," 1–3.
- Skybrary. 2021. "UAV, Vicinity Goodwood West Sussex UK, 2019." Accidents and Incidents. 2021. <https://skybrary.aero/accidents-and-incidents/uav-vicinity-goodwood-west-sussex-uk-2019>.
- Stojanovic, Milan, Jana Vracar, Ljubomir Vracar, M Stojanović, J Vračar, I N Dimitriu, and Lj Vračar. n.d. "Simulation of the Earth's Magnetic Field Distortion Induced by a Vehicle." *Ieeexplore.Ieee.Org*. Accessed March 23, 2022. <https://doi.org/10.1109/MIEL52794.2021.9569087>.
- Taylor, Brian. 2021. "AAIB Bulletin: 11/2021 Brian Taylor AT6 AAIB-27212," 101–2.
- "Understanding and Eliminating EMI in Microcontroller... - Google Scholar." n.d. Accessed March 23, 2022. [https://scholar.google.com/scholar?hl=en&as\\_sdt=0%2C35&q=%E2%80%AFUnderstanding+and+Eliminating+EMI+in+Microcontroller+Applications+&btnG=](https://scholar.google.com/scholar?hl=en&as_sdt=0%2C35&q=%E2%80%AFUnderstanding+and+Eliminating+EMI+in+Microcontroller+Applications+&btnG=).
- United States Environmental Protection Agency. 2022. "Electric and Magnetic Fields from Power Lines." Neighborhood. 2022. <https://www.epa.gov/radtown/electric-and-magnetic-fields-power-lines>.
- Vitiello, Federica, Flavia Causa, Roberto Opromolla, Giancarmine Fasano, and Aboelmagd Noureldin. 2021. "Onboard and External Magnetic Bias Estimation for UAS through CDGNSS/Visual Cooperative Navigation." *Mdpi.Com*. <https://doi.org/10.3390/s21113582>.
- Watanabe, K, M Aoi, ... M Komatsu - 2021 Asia-Pacific, and undefined 2021. n.d. "Measurements of Electromagnetic Emission Nearby a Compact Drone." *Ieeexplore.Ieee.Org*. Accessed March 23, 2022. <https://ieeexplore.ieee.org/abstract/document/9597146/>.
- Wu, H, X Pei, J Li, H Gao, Y Bai - Measurement and Control, and undefined 2020. 2020. "An Improved Magnetometer Calibration and Compensation Method Based on Levenberg–Marquardt Algorithm for Multi-Rotor Unmanned Aerial Vehicle." *Journals.Sagepub.Com* 53 (4): 276–86. <https://doi.org/10.1177/0020294019890627>.
- Wu, Y, S Luo - IEEE Sensors Journal, and undefined 2016. 2016. "On Misalignment between Magnetometer and Inertial Sensors." *Ieeexplore.Ieee.Org* 16 (16). <https://doi.org/10.1109/JSEN.2016.2582751>.
- Yamazaki, K, K Kato, K Ono, ... H Saegusa - IEEE Transactions, and undefined 2003. n.d. "Analysis of Magnetic Disturbance Due to Buildings." *Ieeexplore.Ieee.Org*. Accessed March 23, 2022. <https://ieeexplore.ieee.org/abstract/document/1233353/>.
- Yochim, JA. 2010. "The Vulnerabilities of Unmanned Aircraft System Common Data Links to Electronic Attack." <https://apps.dtic.mil/sti/citations/ADA525301>.

- Zhang, AM, DP Dong, FR He, ... MR Chen - Journal of Lightning, and undefined 2009. 2009. "Effect of Nearby Buildings on Electromagnetic Fields from Lightning." *Benthamopen.Com* 1: 52–60. <https://benthamopen.com/ABSTRACT/JLR-1-52>.
- Zhang, W, Y Ning, C Suo - Electronics, and undefined 2019. n.d. "A Method Based on Multi-Sensor Data Fusion for UAV Safety Distance Diagnosis." *Mdpi.Com*. Accessed March 23, 2022a. <https://doi.org/10.3390/electronics8121467>.
- . n.d. "A Method Based on Multi-Sensor Data Fusion for UAV Safety Distance Diagnosis." *Mdpi.Com*. Accessed March 23, 2022b. <https://doi.org/10.3390/electronics8121467>.
- Zhang, X.D., R.R. Hao, and S.S. Liu. 2010. "Protection Circuit against Strong Electromagnetic Pulse Interference." *Southeast University*.
- Zhao, M, T Xu, D Zhang, ... X Zhou - 2020 IEEE MTT-S, and undefined 2020. n.d. "Implementation Method of Anti Electromagnetic Interference in Identical and Adjacent Frequency for the Data Link of UAV." *Ieeexplore.Ieee.Org*. Accessed March 23, 2022. <https://ieeexplore.ieee.org/abstract/document/9343564/>.